

Title	Germanium tin nanowires: synergy at the nanoscale
Authors	Doherty, Jessica
Publication date	2018
Original Citation	Doherty, J. A. 2018. Germanium tin nanowires: synergy at the nanoscale. PhD Thesis, University College Cork.
Type of publication	Doctoral thesis
Rights	© 2018, Jessica Anne Doherty. - <a href="http://creativecommons.org/licenses/by-nc-nd/3.0/">http://creativecommons.org/licenses/by-nc-nd/3.0/</a>
Download date	2023-05-05 06:59:55
Item downloaded from	<a href="http://hdl.handle.net/10468/8290">http://hdl.handle.net/10468/8290</a>

# **Germanium Tin Nanowires: Synergy at the Nanoscale**

Jessica Anne Doherty, BSc. (Hons)

School of Chemistry,  
University College Cork, Ireland.



**Presented for the degree of Doctor of Philosophy to the National  
University of Ireland**

Supervisor: Prof. Justin D. Holmes

Head of School: Prof. Justin D. Holmes

**2018**

## TABLE OF CONTENTS

---

<b>Declaration.....</b>	<b>vi</b>
<b>Abstract.....</b>	<b>vii</b>
<b>Common Abbreviations and Acronyms: .....</b>	<b>xi</b>
<b>Acknowledgements .....</b>	<b>xiii</b>
<b>Dedication .....</b>	<b>xv</b>
<b>1. Progress on GeSn Alloy Semiconductors: from Thin Films to the Nanoscale .....</b>	<b>2</b>
1.1. Abstract.....	2
1.2. Introduction.....	3
1.3. Theoretical Perspective of $\text{Ge}_{1-x}\text{Sn}_x$ .....	6
1.3.1. Band Structure of $\text{Ge}_{1-x}\text{Sn}_x$ .....	6
1.3.2. Theoretical Insight into the Properties of $\text{Ge}_{1-x}\text{Sn}_x$ .....	9
1.4. Growth of GeSn Materials .....	10
1.4.1. Thin Films .....	11
1.4.2. Nanostructures .....	12
1.5. Properties .....	23
1.5.1. Optical.....	23
1.5.2. Electrical .....	28
1.6. Applications .....	32
1.6.1. Electronic .....	32
1.6.2. Optoelectronics .....	33
1.6.3. Photonics.....	34
1.6.4. Other Applicaitons .....	37
1.7. Conclusion and Outlook.....	38
1.7.1. Thesis Summary.....	39
1.8. References .....	41

<b>2. Non-equilibrium Induction of Tin in Germanium: Towards Direct Bandgap <math>\text{Ge}_{1-x}\text{Sn}_x</math> Nanowires .....</b>	<b>54</b>
2.1. Abstract .....	54
2.2. Introduction .....	55
2.3. Experimental .....	58
2.3.1. Method .....	58
2.3.2. Characterisation .....	59
2.4. Results .....	61
2.5. Discussion .....	82
2.6. Conclusion .....	86
2.7. References .....	88
2.8. Appendix .....	94
<b>3. Influence of Growth Kinetics on Sn Incorporation in Direct Bandgap <math>\text{Ge}_{1-x}\text{Sn}_x</math> Nanowires .....</b>	<b>105</b>
3.1. Abstract .....	105
3.2. Introduction .....	106
3.3. Experimental .....	109
3.3.1. Method .....	109
3.3.2. Characterisation .....	110
3.4. Results and Discussion .....	112
3.5. Conclusion .....	136
3.6. References .....	139
3.7. Appendix .....	146
<b>4. Direct Bandgap <math>\text{Ge}_{1-x}\text{Sn}_x</math> (<math>x = 0.10</math>) Nanowires in Photodetection .....</b>	<b>158</b>
4.1. Abstract .....	158

4.2. Introduction.....	159
4.3. Results and Discussion .....	161
4.4. Conclusion .....	170
4.5. References.....	172
4.6. Appendix.....	179
4.6.1. Experimental .....	179
4.6.2. Characterisation .....	180
4.6.3. Figures.....	181
4.6.4. References.....	182
<b>5. Germanium Tin Nanowires as Anode Materials for High Performance Li-Ion Batteries ..</b>	<b>184</b>
.....	
5.1. Abstract.....	184
5.2. Introduction.....	185
5.3. Results and Discussion .....	186
5.4. Conclusion .....	195
5.5. References.....	197
5.6. Appendix.....	202
5.6.1. Experimental .....	202
5.6.2. Characterisation .....	203
5.6.3. Figures.....	204
5.6.4. References.....	206
<b>6. One-Step Fabrication of GeSn Branched Nanowires .....</b>	<b>208</b>
6.1. Abstract.....	208
6.2. Introduction.....	209
6.3. Results and Discussion .....	211
6.4. Conclusion .....	227
6.5 References.....	229

6.6. Appendix.....	238
6.6.1. Experimental.....	238
6.6.2. Characterisation .....	239
6.6.3. Figures.....	240
6.6.4. References.....	245
<b>7. Supercritical Fluid Growth of High Sn Content <math>\text{Ge}_{1-x}\text{Sn}_x</math> (<math>x &gt; 0.3</math>) Nanowires .....</b>	<b>247</b>
7.1. Abstract.....	247
7.2. Introduction.....	248
7.3. Experimental.....	250
7.3.1. Method .....	250
7.3.2. Characterisation .....	250
7.4. Results and Discussion .....	251
7.5. Conclusion .....	259
7.6. References.....	261
<b>8. Conclusions and Future Outlook.....</b>	<b>266</b>
8.1. Conclusions and Future Outlook .....	266
8.2. References.....	269
<b>9. Appendix - Dissemination .....</b>	<b>273</b>
9.1. Publication List .....	273
9.1.1. Publications arising directly from this thesis.....	273
9.1.2. Co-authored Publications.....	274
9.1.3. Conference Presentations.....	275

## **Declaration**

---

I, Jessica Doherty, certify that this thesis is my own research and I have not obtained a degree in University College Cork or elsewhere on the basis of this PhD Thesis.

---

Jessica Doherty

## Abstract

---

The race to create alternative, Si compatible, scalable, tuneable device materials over the past number of years has led to a focus on group IV elements. Alloying group IV semiconductors, such as Ge or Si with group IV metals such as Sn and Pb, can lead to direct bandgap semiconductors, as in III-V materials, but with the distinct advantage over III-Vs of being Si compatible. A direct bandgap group IV semiconductor would be beneficial for the development of mid-IR optoelectronic devices such as photodetectors. However, due to the lattice mismatch between Ge and Sn,  $\text{Ge}_{1-x}\text{Sn}_x$  thin films often experience large amounts of strain. Compressive strain shifts the energy gap to lower wavelengths, therefore, in order to achieve a direct bandgap, more Sn incorporation is necessary. A promising solution to overcome strain induced in GeSn thin films is the move towards 1-D GeSn nanostructures; nanowire morphology allows for increased strain relaxation compared to thin films due to free sidewall facets. This thesis aims to demonstrate the advancements in  $\text{Ge}_{1-x}\text{Sn}_x$  nanowires, and branched nanostructures, and their application in various fields and devices.

Chapter 1 presents a review of the recent advances in  $\text{Ge}_{1-x}\text{Sn}_x$  materials, with a focus on recent advances in the field, in particular concerning nanostructures *i.e.* nanowires and nanoparticles. I aim to summarise the recent developments in the growth and characterisation of  $\text{Ge}_{1-x}\text{Sn}_x$  films and nanostructures, and their application in electronic, optoelectronic and other devices. I will briefly discuss the theoretical insights on  $\text{Ge}_{1-x}\text{Sn}_x$  material to provide an essential historical starting point for what has become an increasingly popular material. The growth and properties of  $\text{Ge}_{1-x}\text{Sn}_x$  thin films will also be considered, as this material has been reported on sporadically over the last 30 years prior to the popularisation of  $\text{Ge}_{1-x}\text{Sn}_x$ .



Chapter 2 describes the growth of  $\text{Ge}_{1-x}\text{Sn}_x$  nanowires with  $x = 0.09$ . The addition of an annealing step close to the Ge-Sn eutectic temperature (230 °C) during cool-down further facilitated the excessive dissolution of Sn in the nanowires. Sn was distributed throughout the Ge nanowire lattice with no metallic Sn segregation or precipitation at the surface or within the bulk of the nanowires. The non-equilibrium incorporation of Sn into the Ge nanowires was attributed to a kinetic trapping model for impurity incorporation at the triple-phase boundary during growth.

Chapter 3 details the incorporation of this same high Sn content ( $x = 0.09$ ) without the use of a eutectic anneal, thereby increasing the relative atomic ordering. This Sn incorporation was achieved by altering the growth parameters of the system to increase the nanowire growth rate, thereby confirming solute trapping as the mechanism of Sn inclusion. The profound impact of growth kinetics on the incorporation of Sn; from 7 to 9 at. %; in  $\text{Ge}_{1-x}\text{Sn}_x$  nanowires was clearly apparent, with the fastest growing nanowires (of comparable diameter) containing a higher amount of Sn. The participation of a kinetic dependent, continuous Sn incorporation process in the single-step VLS nanowire growth resulted in improved ordering of the  $\text{Ge}_{1-x}\text{Sn}_x$  alloy lattice; as opposed to a randomly ordered alloy. The amount of Sn inclusion and the Sn impurity ordering in  $\text{Ge}_{1-x}\text{Sn}_x$  nanowires has a profound effect on the quality of the light emission (narrowing of the photoluminescence spectra) and on the directness of the band gap as confirmed by temperature dependent photoluminescence study and electron energy loss spectroscopy.

Chapter 4 reports the functionality of these  $\text{Ge}_{1-x}\text{Sn}_x$  nanowires in optoelectronics as photodetectors ( $x = 0.105$ ). The structural and optical quality of these high Sn content  $\text{Ge}_x\text{Sn}_{1-x}$  nanowires was investigated to determine their applicability and functionality in photodetector devices. The as-grown  $\text{Ge}_{1-x}\text{Sn}_x$  nanowires were single crystalline with a direct bandgap of 0.59 eV, as determined from photoluminescence spectroscopy. These highly crystalline direct bandgap  $\text{Ge}_{1-x}\text{Sn}_x$

nanowires, with narrow emission widths, uniform morphologies and chemical homogeneity were found to be ideal candidates for photodetectors due to their high responsivity and broad range photoresponse.

Chapter 5 also explores the functionality of  $\text{Ge}_{1-x}\text{Sn}_x$  nanowires, this time with lower Sn incorporation ( $x = 0.048$ ), in energy storage as Li-ion anode materials.  $\text{Ge}_{1-x}\text{Sn}_x$  nanowires were predominantly seeded from the  $\text{Au}_{0.80}\text{Ag}_{0.20}$  catalysts with negligible amount of growth also catalysed from stainless steel substrate. The electrochemical performance of the  $\text{Ge}_{1-x}\text{Sn}_x$  nanowires as an anode material for Li-ion batteries was investigated *via* galvanostatic cycling and detailed analysis of differential capacity plots.

Chapter 6 informs on the development of  $\text{Ge}_{1-x}\text{Sn}_x$  branched nanostructures. A growth mechanism is proposed for these novel nanostructures; with trunk components comprised of 4.4 at. % Sn and branches containing 8.0 at. % Sn; fabricated in a one step growth. The trunks are seeded from  $\text{Au}_{0.80}\text{Ag}_{0.20}$  nanoparticles followed by the epitaxial growth of secondary branches (diameter  $\sim 50$  nm) from the excess of Sn on the sidewalls of the trunks, as determined by scanning transmission electron microscopy (STEM) and energy dispersive X-ray (EDX) analysis. The nanowires, with  $\langle 111 \rangle$  directed GeSn branches oriented at  $\sim 70^\circ$  to the trunks, have no apparent defects or change in crystal structure at the trunk-branch interface; structural quality is retained at the interface with epitaxial crystallographic relation. These  $\text{Ge}_{1-x}\text{Sn}_x$  nanostructures are also explored as anode materials for Li-ion batteries, as their increased charge carrier pathways, mechanical strength and surface area result in increased capacities over conventional nanowires.

Chapter 7 depicts the influence of pressure on the growth  $\text{Ge}_{1-x}\text{Sn}_x$  nanowires. A move to a supercritical fluid growth regime results in the incorporation of colossal amounts of Sn in the Ge

nanowire lattice, with  $0.1 \leq x \leq 0.35$ . Sn incorporation in the  $\text{Ge}_{1-x}\text{Sn}_x$  nanowires was found to be strongly diameter dependent, with small diameter nanowires containing higher amounts of Sn relative to nanowires with larger diameters. A colossal Sn content of 35 at. % was achieved in  $\text{Ge}_{1-x}\text{Sn}_x$  nanowires with diameters of  $\sim 20$  nm. EDX analysis of the  $\text{Ge}_{1-x}\text{Sn}_x$  nanowires verified the homogeneous distribution of Sn throughout the nanowires, even for the high Sn content nanowires, without apparent clustering or segregation of Sn.

Finally, Chapter 8 details the conclusions of this thesis, and a future outlook for  $\text{Ge}_{1-x}\text{Sn}_x$  nanowires is provided.

## **Common Abbreviations and Acronyms:**

---

<b>1-D:</b>	One dimensional
<b>2-D:</b>	Two dimensional
<b>3-D:</b>	Three dimensional
<b>at. %:</b>	Atomic percent
<b>ATBS:</b>	Allyltributylstannane
<b>CVD:</b>	Chemical Vapour Deposition
<b>DCP:</b>	Differential Capacity Plot
<b>DPG:</b>	Diphenylgermane
<b>EDX:</b>	Energy dispersive x-ray
<b>EELS:</b>	Electron Energy Loss Spectroscopy
<b>Ge:</b>	Germanium
<b>HR:</b>	High Resolution
<b>IR:</b>	Infra-red
<b>Li-ion:</b>	Lithium ion
<b>OCV:</b>	Open Circuit Voltage
<b>PL:</b>	Photoluminescence
<b>SCF:</b>	Supercritical Fluid

<b>SEM:</b>	Scanning Electron Microscopy
<b>Si:</b>	Silicon
<b>SFLS:</b>	Supercritical Fluid-Liquid-Solid
<b>Sn:</b>	Tin
<b>STEM:</b>	Scanning Transmission Electron Microscopy
<b>TAT:</b>	Tetraallyltin
<b>TEM:</b>	Transmission Electron Microscopy
<b>TET:</b>	Tetraethyltin
<b>UV:</b>	Ultra-violet
<b>VLS:</b>	Vapour Liquid Solid
<b>VSS:</b>	Vapour Solid Solid

## **Acknowledgements**

---

I honestly never thought the day would come for me to write my acknowledgements. There are many people to whom I owe thanks. Firstly, thank you to my supervisor Prof. Justin Holmes, for giving me the opportunity to work with him in the MCAG. I never would have guessed when I started my summer project in 2013 that I would become part of the MCAG and have the chance to work with such wonderful people for the last few years. Your guidance and support have been invaluable, and your understanding during this stressful time is a testament to your character and leadership. I couldn't have wished for a more encouraging and dedicated supervisor. Thank you also to the man who I have shadowed around the lab for the last four (plus) years – Dr. Subhajit Biswas. Without you, there is no way I would be writing this today. Your tireless encouragement and involvement in my research have made me into a better researcher. Your good humour, boundless knowledge and straight-talking nature are traits which I admire in you immensely, and have appreciated every step of the way.

I would also like to thank everyone in the MCAG for their help and support, and for lending me an ear when I can't stop talking. To Gill, who would always indulge me in a chat, and who is an inspiration to me as a woman in the field. To John, for being a font of knowledge of all things 115, and all things Simpsons. To those who were here before me; Olan, Mark, Róisín, Anushka, Elaine, Hugh, and especially Dave McN, Shelly, Colm O'R, Tim and Colm G for all of their patience and guidance on collaborative work. To those who will be here after me; Alex, Adria, Fionán, Mai, Debarati, Noel, Luke, Shane and Eadaoin – thank you for always listening to me. I know I talk a lot. Not to forget Karzan and Tandra, I wish you and your families the best of all things. And of course, thank you to Darragh, Giuseppe, Maart and Sally. You really are some of my closest friends, and I couldn't have imagined doing this without you. To my housemates over

the years, Niamh, Niamh, Eamonn and Sean – thanks for putting up with me! And to all of the Ultra Cool Super Friends, for keeping me sane and bringing the fun when I needed it. Particularly “The Friendship Enterprise”, Thomas and Tosh, who went through this with me.

I also express my gratitude to all the staff of the School of Chemistry for their assistance. To those in the office, for always helping me and putting up with an endless barrage of emails from me. I am grateful to the lads in the workshop, for all the help they gave me, all the wire cut and all the cells un-stuck, and especially for calling me Maureen O’Hara. Thanks of course to Tina and Denis in the stores, for supplies and for a chat. No better woman to talk to about a holiday. And of course, thanks are due to Trevor Carey. No better man to talk to about anything! You and Ian have been rocks during the last few years, and know I can always count on you both.

Finally, I would like to thank my family. To my extended family, particularly Rosie, Mamie, Matty, Madge and my Nanny and Grandad, thank you for putting up with my infrequent visits. To my Mam, Anne, for always chatting to me on the phone about normal things. You keep me sane. To my Dad, Paul, for always chatting to me about work things. You keep me grounded. To Keith and Eoghan, for being there for me always. You are two amazing brothers. To Donovan, my flower – you have held my hand every step of the way and I can never repay you. I cannot put into words how grateful I am to you, and to your family. I am so lucky to be surrounded by the people who I love, and who love me. I am so very grateful to you all.

## Dedication

---

*Dedicated to my Dad*



# **Chapter 1**

## **Progress on GeSn Alloy Semiconductors: from Thin Films to the Nanoscale**

This chapter is intended to be published as a review article in 2019.

Consequently, sections of the chapter such as the abstract and introduction may contain repeating concepts and paragraphs.

Doherty, J.; Biswas, S.; Gallucio, E.; Broderick, C.; Duffy, R.;  
O'Reilly, E.; Holmes, J. D. Progress on GeSn Alloy  
Semiconductors: from Thin Films to the Nanoscale

# **1. Progress on GeSn Alloy Semiconductors: from Thin Films to the Nanoscale**

---

## **1.1. Abstract**

Group IV alloys have attracted interest in the drive to create Si compatible, direct bandgap materials for implementation in complementary metal oxide semiconductor (CMOS), and indeed beyond CMOS devices. The lack of a direct bandgap in Si and Ge hinders their incorporation into optoelectronic and photonic devices, without the induction of undesirable strain. Alloying of Ge with Sn represents a novel solution to the lack of light emission in group IV compounds, with an indirect-to-direct bandgap transition predicted for Sn incorporation greater than 6.5 at. %. Here, I review the recent advances in the growth and application of  $\text{Ge}_{1-x}\text{Sn}_x$  materials. A brief overview of theoretical band structure calculations for  $\text{Ge}_{1-x}\text{Sn}_x$  is reported, along with some as of yet unreported calculations regarding the predicted effect band-mixing has on the photoluminescence properties of  $\text{Ge}_{1-x}\text{Sn}_x$  alloys. The optical and electrical properties for both  $\text{Ge}_{1-x}\text{Sn}_x$  thin films and strain-relaxed one dimensional (1-D) nanostructures are reported and recent key findings and applications are outlined.

## 1.2. Introduction

The race to create alternative, Si compatible, scalable, tuneable device materials over the past number of years has led to a focus on group IV elements. Alloying group IV semiconductors, such as Ge or Si with group IV metals such as Sn and Pb, can lead to direct bandgap semiconductors, as in III-V materials, but with the distinct advantage over III-Vs of being Si compatible. A number of researchers have reported both theoretically and experimentally that a direct bandgap can be achieved in Ge by alloying the semiconductor with Sn,<sup>1,2</sup> lowering the separation between indirect (L) and direct ( $\Gamma$ ) valleys (140 meV in bulk Ge) in the conduction band of Ge.<sup>3</sup> A direct bandgap group IV semiconductor would be beneficial for efficient band-to-band tunnelling devices, such as a tunnelling field effect transistor (TFET),<sup>4,5</sup> for lasing platforms<sup>6,7</sup> and for the development of mid-IR photonic devices, such as waveguide amplifiers and multi-wavelength light sources.<sup>8</sup> Figure 1.1(a) denotes the historical  $\text{Ge}_{1-x}\text{Sn}_x$  benchmarks up to 2015, as reported by Wirths et al.<sup>9</sup>

There have been many reports in the literature on  $\text{Ge}_{1-x}\text{Sn}_x$  thin films and their applications in electronics,<sup>10</sup> optoelectronics<sup>11,12</sup> and photonics.<sup>7</sup> However, due to the lattice mismatch between Ge and Sn, thin films often experience large amounts of strain. Compressive strain shifts the energy gap to lower wavelengths, therefore, in order to achieve a direct bandgap, more Sn incorporation is necessary.<sup>13,14</sup> This higher incorporation of Sn then becomes increasingly difficult to achieve due to the low equilibrium solubility of Sn in Ge (< 1 at. %) and the tendency for Sn to segregate at high growth temperatures.<sup>15,16</sup> Some solutions have been proposed to reduce strain incorporation in  $\text{Ge}_{1-x}\text{Sn}_x$  films; introducing a Ge buffer layer,<sup>6</sup> or increasing  $\text{Ge}_{1-x}\text{Sn}_x$  layer thickness.<sup>17,18</sup> A promising solution to overcome strain induced in  $\text{Ge}_{1-x}\text{Sn}_x$  thin films is the move towards 1-D  $\text{Ge}_{1-x}\text{Sn}_x$  nanostructures; a nanowire morphology allows for increased strain

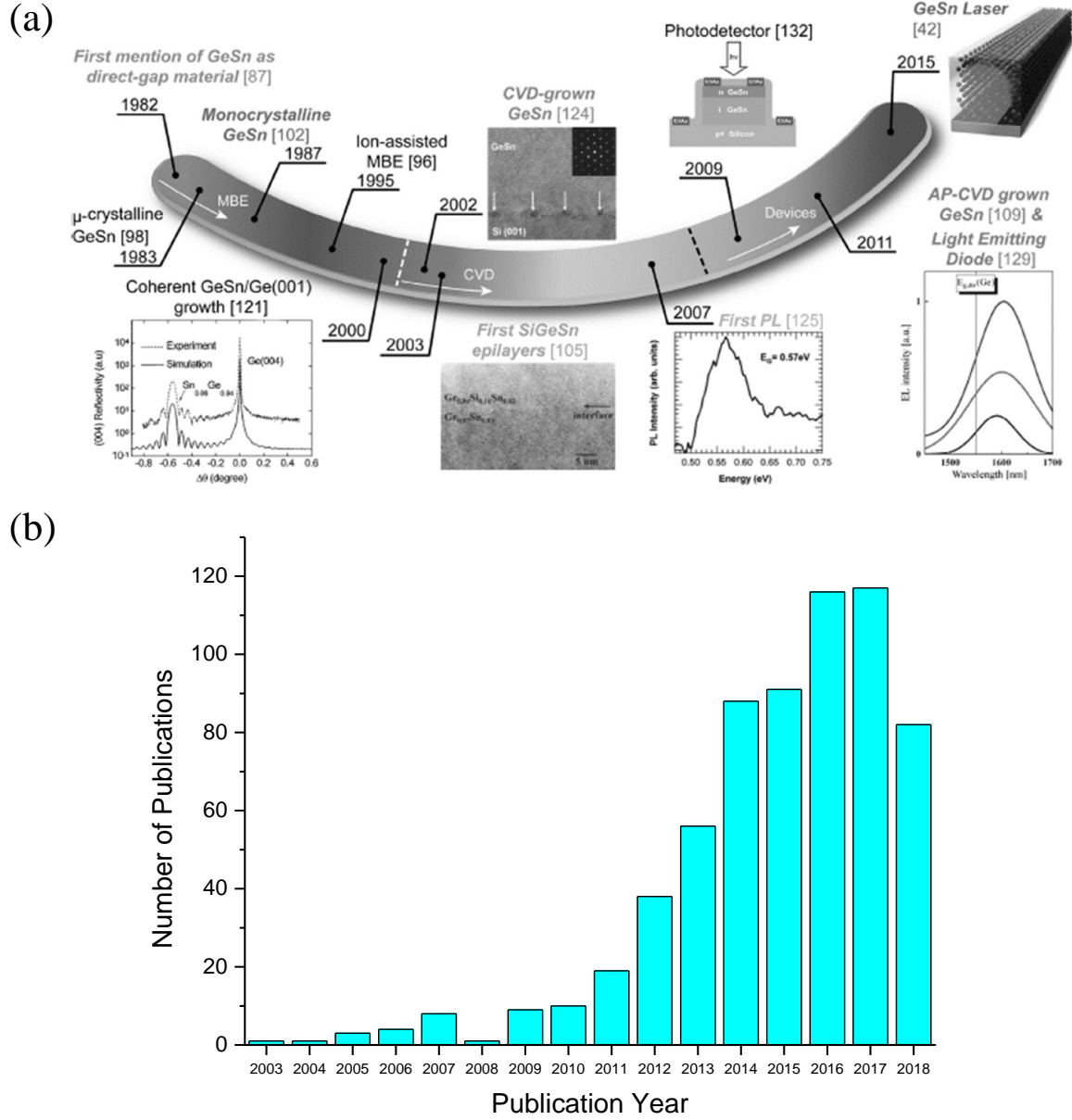


**Figure 1.1:** Recent advances in  $\text{Ge}_{1-x}\text{Sn}_x$  and increase in popularity. (a) Timeline of historical  $\text{Ge}_{1-x}\text{Sn}_x$  benchmarks reprinted from S. Wirths *et al.*, *Progress in Crystal Growth and Characterisation of Materials* **2016**, 62, 1.<sup>9</sup> (b) relaxation compared to thin films due to free sidewall facets.<sup>19</sup> The move from  $\text{Ge}_{1-x}\text{Sn}_x$  thin films to nanowires also reduces the Sn required to achieve a direct bandgap as the compressive strain is effectively relaxed. However, greatly decreasing nanostructure size can also result in increased quantum effects – resulting in a blue shift of bandgap energies. While this will result in an

increased amount of Sn incorporation necessary to transition to a direct bandgap, it may also result in a semiconductor which emits at a higher energy (*i.e.* the visible range).

This review aims to summarise the recent developments in the growth and characterisation of  $\text{Ge}_{1-x}\text{Sn}_x$  films and nanostructures, and their application in electronic, optoelectronic and other devices. I have noted the lack of a comprehensive review of  $\text{Ge}_{1-x}\text{Sn}_x$  materials and applications since 2015.<sup>15</sup> Thus, due to a surge in number of reports in the last five years (Figure 1(b)), this review will primarily focus on the growth and application of recent  $\text{Ge}_{1-x}\text{Sn}_x$  nanostructures. This review will also highlight the optical and electronic properties of the novel  $\text{Ge}_{1-x}\text{Sn}_x$  nanostructures and focus on the recent development in  $\text{Ge}_{1-x}\text{Sn}_x$  device fabrication. Firstly, however, I will briefly discuss the theoretical insights on  $\text{Ge}_{1-x}\text{Sn}_x$  materials to provide an essential historical starting point for what has become an increasingly popular material. The growth and properties of  $\text{Ge}_{1-x}\text{Sn}_x$  thin films will also be considered, as this material has been reported on periodically over the last 30 years prior to the popularisation of  $\text{Ge}_{1-x}\text{Sn}_x$ . There were no reports of 1-dimensional (1D)  $\text{Ge}_{1-x}\text{Sn}_x$  nanostructures until 2003,<sup>20</sup> with sporadic reports following that until 2015.<sup>21</sup> The most promising  $\text{Ge}_{1-x}\text{Sn}_x$  nanostructures will also be discussed in terms of their growth and characterisation, such as nanowires and nanoparticles.

### 1.3. Theoretical Perspective of $\text{Ge}_{1-x}\text{Sn}_x$

The knowledge that  $\text{Ge}_{1-x}\text{Sn}_x$  alloys would exhibit a direct bandgap was not determined experimentally, rather, it was long predicted theoretically.<sup>22,23</sup> This prediction predates the growth of crystalline  $\text{Ge}_{1-x}\text{Sn}_x$  alloys<sup>24,25</sup> and was a key component in the motivation behind fabricating  $\text{Ge}_{1-x}\text{Sn}_x$  alloys with sufficient Sn incorporation to produce a direct bandgap. Many of the early theory reports on  $\text{Ge}_{1-x}\text{Sn}_x$  are specific to bulk  $\text{Ge}_{1-x}\text{Sn}_x$ , reporting a large Sn incorporation to produce a direct bandgap, *e.g.* in 1989 Mader et al.<sup>23</sup> reported the requirement of  $0.26 \leq x \leq 0.74$  for direct bandgap  $\text{Ge}_{1-x}\text{Sn}_x$ . As this review aims to focus on recently reported nanostructures, only relevant theoretical aspects of the material will be reported here. Following from the prediction that a relatively low amount of Sn was required to produce a direct bandgap transition in nanoscale  $\text{Ge}_{1-x}\text{Sn}_x$ , some growth methods were theorised for  $\text{Ge}_{1-x}\text{Sn}_x$ , as well as thermal stability, optical properties, mobility and tunability predictions.<sup>23,26,27</sup> In this section, I will focus on the theoretical modelling of the  $\text{Ge}_{1-x}\text{Sn}_x$  band structure, followed by a brief outline of the theorised properties of  $\text{Ge}_{1-x}\text{Sn}_x$ .

#### 1.3.1. Band Structure of $\text{Ge}_{1-x}\text{Sn}_x$

Since the first report of  $\text{Ge}_{1-x}\text{Sn}_x$  as a direct bandgap material in the literature three decades ago,<sup>22</sup> there have been many major advances in the computational methods and techniques used. The band gap of the  $\text{Ge}_{1-x}\text{Sn}_x$  alloy is expected to undergo an indirect-to-direct transition, since the direct band gap in Ge has a value of 0.81 eV, while  $\alpha$ -Sn has a negative (-0.4 eV) direct bandgap.<sup>26</sup> From initial predictions of over 20 at. % Sn incorporation required to achieve direct bandgap (Figure 1.2),<sup>28</sup> the theoretical prediction of the Sn content required has shifted continuously towards lower values.<sup>28-30</sup> A simple linear interpolation between Ge and  $\alpha$ -Sn places the crossover at  $x = 0.2$ ; which agrees remarkably well with the early electronic structure calculations using the virtual crystal approximation (VCA). Band structure calculations of  $\text{Ge}_{1-x}\text{Sn}_x$  confirm that the

reduction of the energy gap in the  $\Gamma$  state occurs at a more pronounced rate than the reduction of the L state. Due to the already narrow energy separation of these two states in Ge (140 meV), the  $\Gamma$  valley rapidly becomes the lowest available conduction band, resulting in a direct bandgap transition. A commonly accepted value of the Sn content necessary to transition from an indirect to direct bandgap in strain free Ge is no less than 6.5 at. %.<sup>31</sup> Many theoretical predictions have also included the influence of strain on a  $\text{Ge}_{1-x}\text{Sn}_x$  system; as tensile strain is known to induce Ge to behave as a direct bandgap semiconductor.<sup>32,33</sup> Another important factor to consider when estimating the band structure, and thus the Sn content required to transition from an indirect to direct bandgap in Ge, is the size confinement effect. Upon scaling to increasingly small sizes (*e.g.* nanoparticles), the quantum confinement effects will dominate and the Sn content required will increase dramatically.<sup>34</sup>

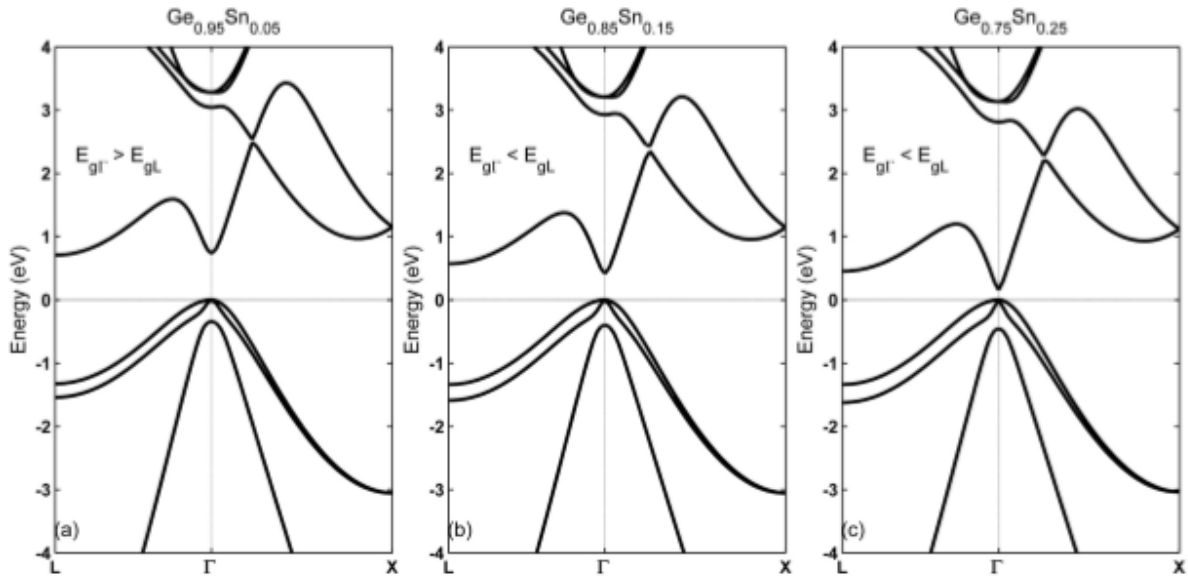


**Figure 1.2:** Calculated band structure for  $\text{Ge}_{1-x}\text{Sn}_x$  with (a) 5% Sn, (b) 15% Sn, and (c) 25% Sn. Reprinted from Gupta *et al. Journal of Applied Physics*, **2013**, 113, 073707.<sup>28</sup>

When discussing theoretical calculations these generally fall into two types: (i) simple models based on the virtual crystal approximation, and related approximations, in which each atom is

treated as having the properties of an average " $\text{Ge}_{1-x}\text{Sn}_x$ " atom, and (ii) direct atomistic calculations, in which the Ge and Sn atoms are treated explicitly. While both of these approaches predict an indirect to direct gap transition, the former type of models explicitly omit the mismatch in covalent radii and chemical properties, and hence omit alloy effects such as band mixing. Since Ge has a relatively "weak" indirect band gap (the direct band gap is only 140 meV larger than the indirect band gap) band mixing effects are prominent and have a marked effect on the nature of the states at the conduction band edge, particularly for Sn compositions  $< 10\%$ .

Direct atomistic calculations include these band mixing effects, but they do not appear to have been interrogated in significant detail in the literature. However, recent calculations suggest that band mixing effects are indeed prominent to the extent that calculations of the electronic, optical and transport properties must include such effects in order to quantitatively predict technologically important material properties.<sup>35,36</sup> In particular, many theoretical analyses, even those based on direct atomistic calculations, treat the  $\text{Ge}_{1-x}\text{Sn}_x$  alloy as having distinct L and  $\Gamma$  states in the interpretation of the band structure, the energy of which decreases with increasing Sn composition (with the energy of the  $\Gamma$  states decreasing faster, hence giving rise to a direct band gap).

As yet unpublished calculations ("Comparison of first principles and semi-empirical models of the structural and electronic properties of  $\text{Ge}_{1-x}\text{Sn}_x$  alloys", Broderick et al., submitted 2018) show that having distinct L and  $\Gamma$  is not the case, but instead that the conduction band edge states in general are a strongly hybridised mixture of Ge L and  $\Gamma$  states. This is evidenced in pressure-dependent measurements, where the pressure coefficient of the  $\text{Ge}_{1-x}\text{Sn}_x$  band gap evolves continuously from the low pressure coefficient associated with the indirect Ge  $\Gamma$ -L band gap, towards the higher pressure coefficient associated with the direct Ge  $\Gamma$ - $\Gamma$  band gap. As such, the evolution of a direct band gap is continuous with increasing Sn composition, with Ge  $\Gamma$  character transferring



continuously to the  $\text{Ge}_{1-x}\text{Sn}_x$  conduction band edge states (which start out as purely L-like at  $x = 0$ ) between  $x = 0$  and 10 %. This demonstrates that although many simple theoretical models based on the virtual crystal and related approximations correctly predict the formation of a direct band gap, they omit band mixing effects which are likely important for the material properties of  $\text{Ge}_{1-x}\text{Sn}_x$  (“Comparison of first principles and semi-empirical models of the structural and electronic properties of  $\text{Ge}_{1-x}\text{Sn}_x$  alloys”, Broderick et al., submitted 2018). Much of the early theoretical work on  $\text{Ge}_{1-x}\text{Sn}_x$  was carried out using VCA, which negates the impact of Sn positioning within the lattice. A move toward empirical atomistic (AT) rather than VCA has revealed band structure calculations with much stronger bandgap bowing,<sup>37</sup> indicating the atomistic effects on  $\Gamma - \text{L}$  crossover. As the theoretical understanding of the  $\text{Ge}_{1-x}\text{Sn}_x$  material progresses, and as the growth control of  $\text{Ge}_{1-x}\text{Sn}_x$  nanomaterials becomes increasingly more precise, the effect of Sn positioning within the Ge lattice will become an important aspect of  $\text{Ge}_{1-x}\text{Sn}_x$  characterisation.

### **1.3.2. Theoretical Insight into the Properties of $\text{Ge}_{1-x}\text{Sn}_x$**

The optical, thermal, and electrical properties of  $\text{Ge}_{1-x}\text{Sn}_x$  have been investigated and reported throughout the last 30 years; in many instances predating the experimental verification of the same. Due to the progression towards a direct bandgap with increasing Sn content in  $\text{Ge}_{1-x}\text{Sn}_x$  materials, the optical properties of  $\text{Ge}_{1-x}\text{Sn}_x$  have been widely considered and investigated. A detailed theoretical analysis of the optical properties of  $\text{Ge}_{1-x}\text{Sn}_x$  was reported before experimental data was produced,<sup>38</sup> potentially fuelling the desire to produce a single crystalline, direct bandgap  $\text{Ge}_{1-x}\text{Sn}_x$  material. The optical properties of  $\text{Ge}_{1-x}\text{Sn}_x$  are of particular importance due to the indirect to direct transition undergone by Ge upon sufficient incorporation of Sn ( $> 6.5$  at. % Sn).<sup>28,31,35</sup> Theoretically, the bandgap can be tuned between 0.6 eV and 0.0 eV by altering the Sn inclusion in the  $\text{Ge}_{1-x}\text{Sn}_x$  material.<sup>28</sup> The tunability of this bandgap is a valuable commodity in both optoelectronics and photonics, making  $\text{Ge}_{1-x}\text{Sn}_x$  materials particularly suited for incorporation in

photodiodes; covering the broad mid-IR range. In terms of electrical properties, theoretical studies of  $\text{Ge}_{1-x}\text{Sn}_x$  show similar or enhanced values of electron mobilities and concentrations compared with doped Ge counterparts.<sup>39</sup> Wang et al.<sup>40</sup> modelled  $\text{Ge}_{1-x}\text{Sn}_x/\text{Si}_y\text{Ge}_{1-x-y}\text{Sn}_x$  staggered heterojunction n-channel tunnelling field effect transistors (hetero-NTFETs) using a non-local empirical pseudopotential method. Hetero-NTFETs theoretically exhibited a steeper subthreshold swing, a higher ON-state current, and a larger ON-OFF current ratio compared with  $\text{Ge}_{1-x}\text{Sn}_x$  homojunction n-channel tunnelling FET devices.<sup>40</sup> Sant and Schenk performed modelling analysis of  $\text{Ge}_{1-x}\text{Sn}_x/\text{Si}_y\text{Ge}_{1-x-y}\text{Sn}_x$  hetero tunnel FETs, but also explored the role of strain.<sup>41</sup> Their simulations of  $\text{Ge}_{1-x}\text{Sn}_x/\text{Si}_y\text{Ge}_{1-x-y}\text{Sn}_x$  hetero-TFETs determined that compressive strain in  $\text{Ge}_{1-x}\text{Sn}_x$  widens the design space for TFET applications while tensile strain reduces it. Haehnel et al.<sup>42</sup> explored the influence of drain doping, short channel, and Sn content in p-channel Ge(Sn) heterojunction band-to-band tunnelling FETs. In their work they investigated the influence of a reduction of the channel length down to 15 nm on transistor performance.<sup>42</sup>

#### 1.4. Growth of GeSn Materials

From the first reported growth of microcrystalline  $\text{Ge}_{1-x}\text{Sn}_x$  by Oguz et al.<sup>24</sup> to the present day, fabrication of  $\text{Ge}_{1-x}\text{Sn}_x$  materials has been dominated by thin films. In recent years, however, there has been an emergence of new  $\text{Ge}_{1-x}\text{Sn}_x$  nanomaterials, such as nanowires and nanoparticles. Although the focus of this review is towards new nanostructures (*i.e.* nanowires and nanoparticles), it would be remiss not to detail some of the recent work on the growth and fabrication of  $\text{Ge}_{1-x}\text{Sn}_x$  thin films.

#### 1.4.1. Thin Films

Reports of  $\text{Ge}_{1-x}\text{Sn}_x$  thin films have been detailed extensively in the literature, and as such, will not be the focal point of this review. However, the understanding of the growth techniques used in the fabrication of  $\text{Ge}_{1-x}\text{Sn}_x$  thin films provides a starting point for the fabrication of  $\text{Ge}_{1-x}\text{Sn}_x$  nanostructures (such as nanowires and nanoparticles).

The growth of  $\text{Ge}_{1-x}\text{Sn}_x$  thin films has been reported using many fabrication techniques, including chemical vapour deposition (CVD), molecular beam epitaxy (MBE), radio frequency sputtering, solid phase epitaxy and co-evaporation of Ge and Sn *via* physical vapour deposition (PVD).<sup>43–51</sup> The use of MBE dominated early  $\text{Ge}_{1-x}\text{Sn}_x$  growth,<sup>20,24,25,52</sup> with a shift to CVD growth occurring in the early 2000's.<sup>26,45,53–56</sup> To obtain above equilibrium Sn incorporation, non-equilibrium, low temperature techniques are preferred.<sup>47,57</sup> This effort has led to the growth of  $\text{Ge}_{1-x}\text{Sn}_x$  thin films with Sn incorporation far in excess of the equilibrium ( $x \geq 0.10$ ).<sup>6,14,17</sup> However, due to the large lattice mismatch between Ge and Sn and the inability of films to accommodate strain, the incorporation of Sn into  $\text{Ge}_{1-x}\text{Sn}_x$  thin films leads to high compressive strain.<sup>53,58–60</sup> As the presence of compressive strain causes the fundamental energy gap to blue-shift to lower wavelengths, more Sn incorporation is necessary to achieve a direct bandgap.<sup>13,14,59,60</sup> However, due the incredibly low equilibrium solubility of Sn in Ge (< 1 at. %) and the tendency for Sn to segregate at high growth temperatures, this task becomes increasingly difficult.<sup>15,16</sup> The inclusion of a Ge buffer layer<sup>6,44,45</sup> has been proven to increase the relaxation of  $\text{Ge}_{1-x}\text{Sn}_x$  thin films, which decreases the Sn required to achieve a direct bandgap. Conley *et al.*<sup>45</sup> used cross-sectional TEM to investigate the strain induced in their 76 nm  $\text{Ge}_{1-x}\text{Sn}_x$  ( $x = 0.032$ ) thin film grown on a 675 nm Ge buffer layer (Figure 1.3). An alternative choice of buffer layer is relaxed  $\text{In}_y\text{Ga}_{1-y}\text{P}$ , which results in  $\text{Ge}_{1-x}\text{Sn}_x$  thin film experiencing tensile strain, thus resulting in decrease in the fundamental energy gap.<sup>61</sup> Another interesting approach to the generation of a group IV direct

bandgap materials was reported by Shimura et al.,<sup>47</sup> where a  $\text{Ge}_{1-x}\text{Sn}_x$  thin film was used as a buffer layer to grow a tensile strained Ge layer; the  $\text{Ge}_{1-x}\text{Sn}_x$  thin film ( $x = 0.07$ ) induced tensile strain in the subsequent Ge layer, resulting in a direct bandgap material. As the thickness of the  $\text{Ge}_{1-x}\text{Sn}_x$  layer increases, the induced strain in the layer has been observed to decrease<sup>17,18</sup>. Hence, growing a suitably thick  $\text{Ge}_{1-x}\text{Sn}_x$  thin film can result in strain relaxation and a lowering of the energy gap. A unique growth technique employed by Tran et al.<sup>62</sup> involved the use of ion implantation and pulsed laser melting (PLM) to incorporate Sn into a Ge thin film, as this method was speculated to provide a more effective pathway for strain relaxation. The use of ion implantation and PLM resulted in the formation of indirect single crystalline  $\text{Ge}_{1-x}\text{Sn}_x$  thin films with  $x = 0.06$ .

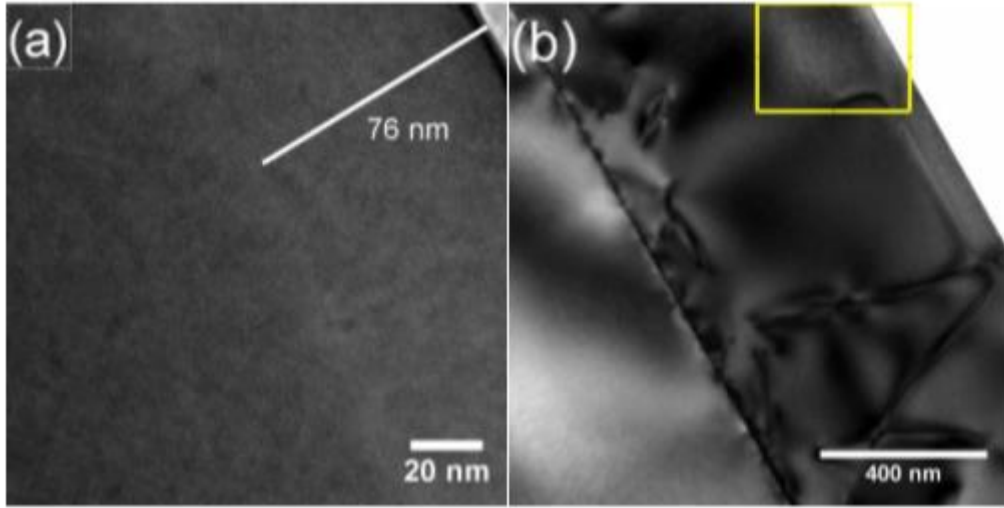


**Figure 1.3:** XTEM of sample with  $x = 3.2\%$  Sn. 76 nm  $\text{Ge}_{1-x}\text{Sn}_x$  film grown on relaxed Ge buffer layer with an approximately 675 nm thickness. Reprinted from Conley *et al.*, *Conference Record of the IEEE Photovoltaic Specialists Conference*, **2013**, 1346-1349.<sup>45</sup>

#### 1.4.2. Nanostructures

The increasing demand for group IV compatible semiconductors has led to increased interest in group IV alloy nanostructures. In particular,  $\text{Ge}_{1-x}\text{Sn}_x$  nanowires and nanoparticles are of interest

due to their unique bandgap chemistry *i.e.* the ability to transition from an indirect to direct bandgap, narrow bandgap, *etc.* and potential use in optoelectronic, electronic and energy storage applications. Typically, these nanostructures have been fabricated on Group IV (Si or Ge) substrates. Here I detail recent reports on the fabrication of nanoscale  $\text{Ge}_{1-x}\text{Sn}_x$  alloys.

#### **1.3.2.1. Nanowires**

The fabrication of  $\text{Ge}_{1-x}\text{Sn}_x$  nanowires has been reported for homogeneous, conventional nanowires and Ge/ $\text{Ge}_{1-x}\text{Sn}_x$  core/shell nanowires. Despite the first reported fabrication of  $\text{Ge}_{1-x}\text{Sn}_x$  nanowires in 2003,<sup>20</sup> the surge in popularity of  $\text{Ge}_{1-x}\text{Sn}_x$  nanowires is a recent development. The first recent report on the synthesis of  $\text{Ge}_{1-x}\text{Sn}_x$  nanowires was by Barth et al., and expanded upon by Seifner et al.,<sup>21</sup> detailing the fabrication of nanowires with  $x = 0.125$  by solution based, microwave assisted growth. These nanowires, grown using Sn as a growth catalyst, were non-uniform in terms of diameter, with increasing Sn content along the wire with diminishing nanowire diameter. A three stage growth regime was proposed for the two  $\text{Ge}_{1-x}\text{Sn}_x$  nanowire types reported (Figure 1.4), with the metallic Sn seed consumed as the reaction progressed. Seifner et al.<sup>63</sup> expanded their study by pushing the limit of the Sn incorporation in the nanowires grown *via* microwave assisted method, achieving  $\text{Ge}_{1-x}\text{Sn}_x$  nanowires with up to  $x = 0.28$ .<sup>63</sup> These nanowires, grown with a modified microwave approach at 140 °C using Ge (II) and Sn (II) hexamethylsilylamides, exploited a thermal treatment to induce further Sn incorporation into their as grown  $\text{Ge}_{1-x}\text{Sn}_x$  nanowires ( $x = 0.17$ ). Microwave synthesis was utilised as it results in high crystallinity at lower temperatures, with a homogeneous distribution of temperature. The thermal stability of these  $\text{Ge}_{1-x}\text{Sn}_x$  nanowires with and without the presence of the Sn seed was also investigated; revealing the diffusion of metallic Sn clusters through the  $\text{Ge}_{1-x}\text{Sn}_x$  nanowires at temperatures where the material composition was non-homogeneous. We have also reported the CVD growth of  $\text{Ge}_{1-x}\text{Sn}_x$  nanowires with a high Sn content ( $x > 0.06$ ) *via* conventional vapour-liquid-solid (VLS) growth.<sup>64</sup>

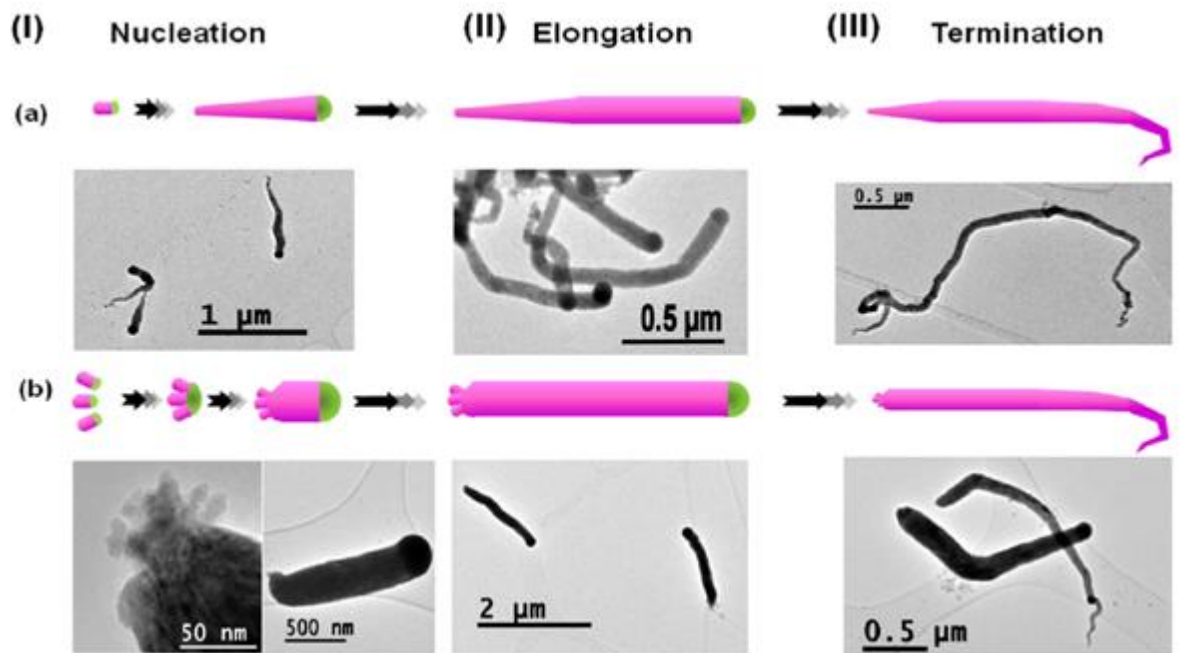


**Figure 1.4:** Schematic for microwave assisted growth of  $\text{Ge}_{1-x}\text{Sn}_x$  nanowires ( $x = 0.125$  and TEM images to illustrate the structural features (Ge in purple; Sn in green). (a) Describes the growth *via* homogeneous nucleation with diameter expansion and accumulation of Sn at the growth front. (b) Represents the pre-nucleation of  $\text{Ge}_{1-x}\text{Sn}_x$  nanowires by an additional heat treatment and nucleus formation *via* oriented attachment leading to a quickly settling nanowire diameter at the nucleation (I) stage. The elongation (II) is a phase where the nanowire grows along its axis with a constant diameter due to constant Sn supply and consumption caused by incorporation in the Ge matrix. The termination (III) includes shrinkage in nanowire diameter and the consumption of the tin growth seed. Reprinted from M. Seifner *et al.*, *Chemistry of Materials*, **2015**, 27, 17.<sup>21</sup>

Using Au and  $\text{Au}_{1-x}\text{Ag}_x$  metal catalysts and employing a post-growth step anneal,  $\text{Ge}_{1-x}\text{Sn}_x$  ( $x = 0.09$ ) nanowires were fabricated.<sup>64</sup> Evidence of “random” alloy ordering however, prompted the removal of the post-growth step anneal, i.e. single step growth. To attain the same high Sn content without the use of a eutectic anneal, the growth parameters of the  $\text{Ge}_{1-x}\text{Sn}_x$  nanowires were altered to increase the growth rate.<sup>65</sup> Faster growth kinetics resulted in high Sn incorporation into the nanowires and  $\text{Ge}_{1-x}\text{Sn}_x$  nanowires with 9 at. % were fabricated (Figure 1.5). These nanowires

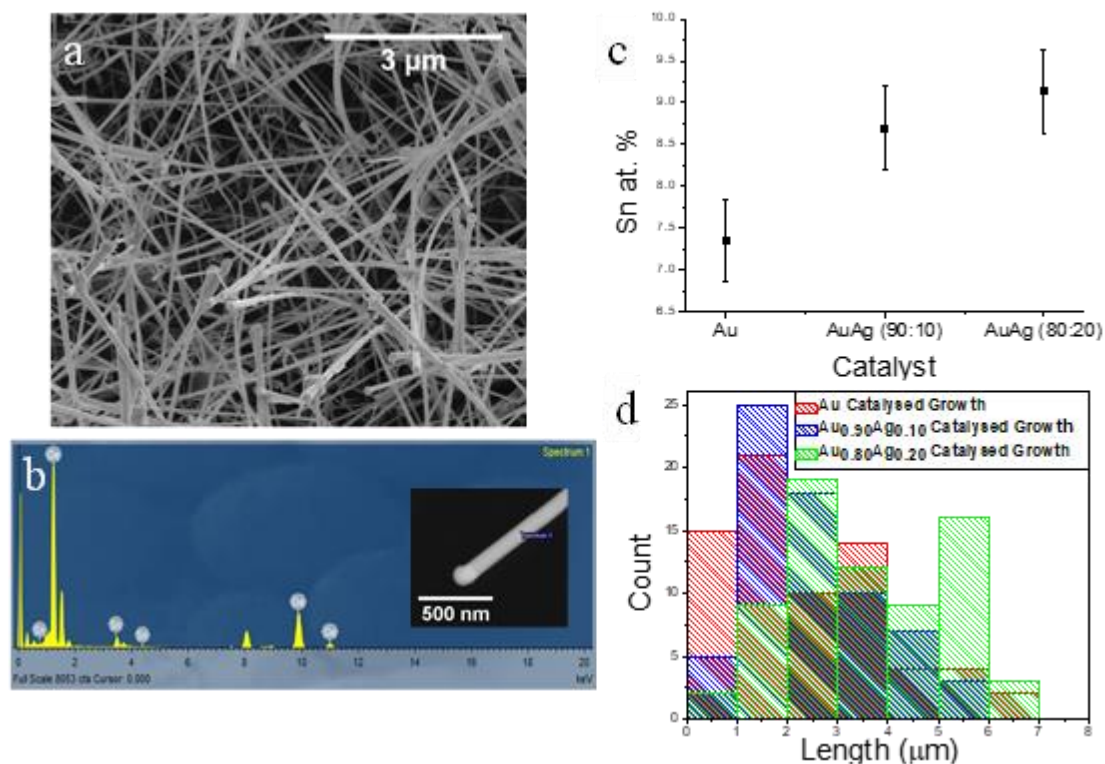


**Figure 1.5:** Investigation of the impact of growth kinetics on Sn incorporation in  $\text{Ge}_{1-x}\text{Sn}_x$  nanowires. (a) SEM image of  $x = 0.09$   $\text{Ge}_{1-x}\text{Sn}_x$  nanowires, displaying negligible Sn clusters. (b) Energy dispersive X-ray (EDX) spectrum showing high Sn incorporation and the absence of Au or Ag impurities from the  $\text{Au}_{0.80}\text{Ag}_{0.20}$  nanoparticle catalysts. (c) and (d) display the relationship between growth kinetics and Sn incorporation; with the faster growth rate resulting in both longer nanowires and an increased Sn content. Reprinted from J. Doherty *et al.*, *Journal of Materials Chemistry C*, **2018**, 6.<sup>65</sup>

displayed increased atomic ordering when compared to  $\text{Ge}_{1-x}\text{Sn}_x$  nanowires with the same Sn content, grown by a two-step process; as determined by Raman, TEM and photoluminescence analysis. We have also observed the unique growth of  $\text{Ge}_{1-x}\text{Sn}_x$  nanostructures – branched nanowires with heterogeneously Sn concentration from “trunk” (4.4 at. % Sn) to “branch” (8.0 at. % Sn) (Chapter 6). These novel heterostructures, seen in Figure 1.6, are grown in an  $\text{Au}_{0.80}\text{Ag}_{0.20}$  catalysed VLS growth process in which excess Sn on the sidewall is utilised as the catalyst for the



secondary growth of smaller branches (diameter  $\sim 50$  nm), ordered along the nanowire trunk (diameter  $\sim 200$  nm). These branch nanowires are ordered in the  $\langle 111 \rangle$  orientation along the

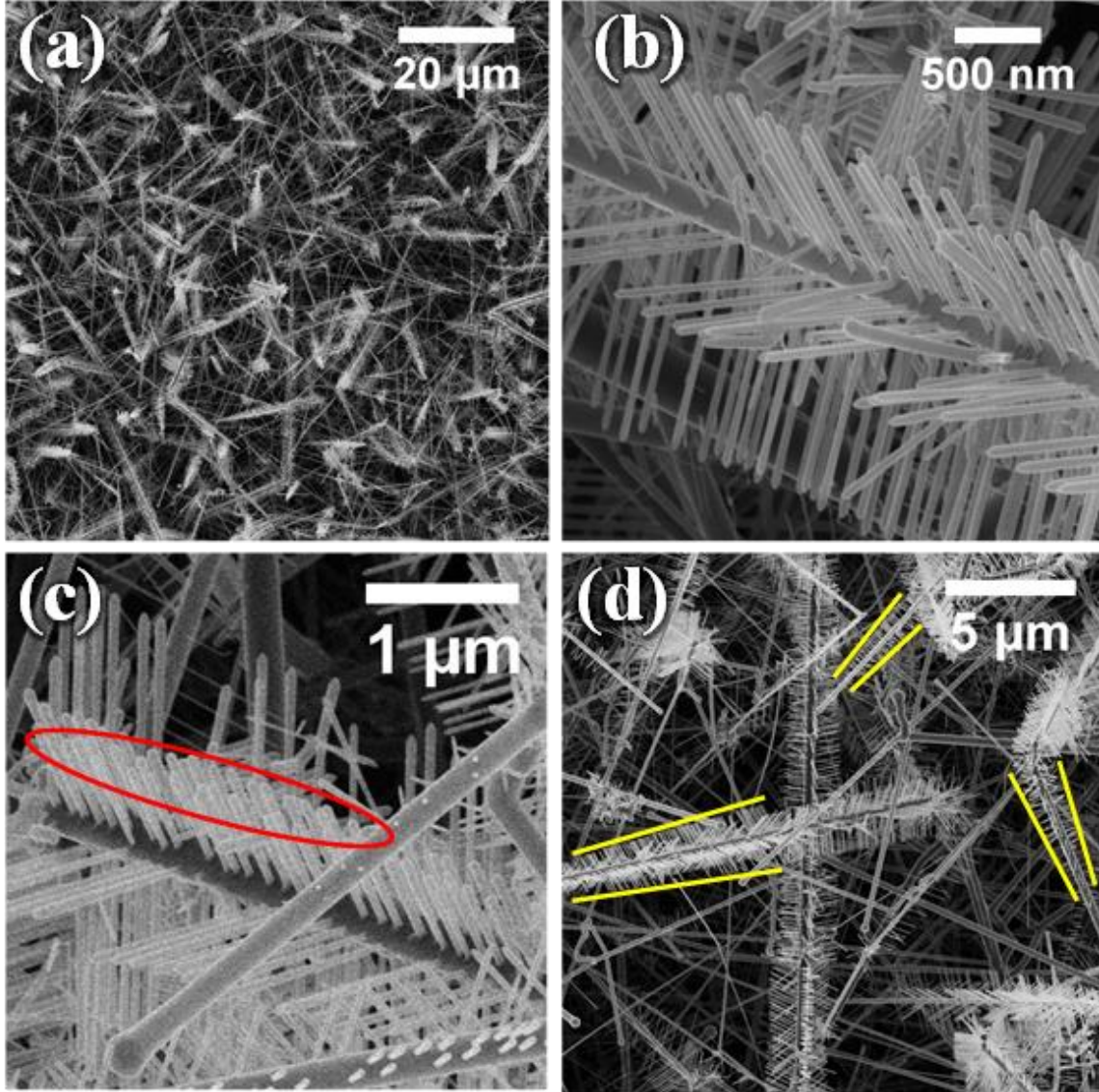


**Figure 1.6:** SEM images of  $\text{Ge}_{1-x}\text{Sn}_x$  branched nanostructures grown on Si substrate at 440 °C with a typical growth time of 2hr. The high yield of branched nanostructures with respect to conventional nanowires is apparent in (a), and the uniformity is clearly apparent in (b). The presence of nanoparticle seeds on the branched nanowires is not clear in all cases (b), however nanoparticle seeds on the tips of the branched nanowires is clearly visible in (c). The changing length of branched nanowires along the main nanowire trunk is observed in (d), with longer branches seen toward the end of the nanowire trunk and shorter branches closer to the nanowire tip. The yellow lines are provided as a guides for the eye.



nanowire trunk at an angle of  $\sim 70^\circ$ . Deposition and migration of Sn on to the nanowire sidewall forms Sn droplets which act as the catalyst for the secondary growth of the branch nanowires. The wetting of the nanowire trunk by Sn, originating from the original seeds, was pinpointed as the primary source of Sn. The formation of these novel 3D  $\text{Ge}_{1-x}\text{Sn}_x$  nanostructures, can potentially trigger different electron band transitions in a single structure, i.e. the 4.4 at. % Sn nanowire trunk acting as an indirect bandgap semiconductor with the 8.0 at. % Sn branches behaving as a direct bandgap semiconductor.

There have also been several recent research articles on Ge/ $\text{Ge}_{1-x}\text{Sn}_x$  core/shell nanowires, with at least one report per year since 2016.<sup>19,66,67</sup> These nanowires are typically comprised of a Sn-rich  $\text{Ge}_{1-x}\text{Sn}_x$  shell surrounding a pure Ge nanowire, often with increasing Sn content radially outward from the Ge core. Meng et al. reported in 2016 the growth of Ge/ $\text{Ge}_{1-x}\text{Sn}_x$  core shell nanowires through low temperature CVD.<sup>66</sup> A Au nanoparticle catalyst was used, as per standard VLS growth, employing germane ( $\text{GeH}_4$ ) and tin(IV) chloride ( $\text{SnCl}_4$ ) precursors (Figure 1.7). These core/shell nanowires displayed tapering near the tips of the nanowires and inverse tapering along the lengths of nanowires, with a majority of nanowires (60 %) growing in the  $\langle 111 \rangle$  direction. The nanowires had 7 at. % Sn incorporated into the  $\text{Ge}_{1-x}\text{Sn}_x$  shell, while the Ge core had a small amount of Sn incorporation ( $\sim 1$  at. %). In another report on Ge/ $\text{Ge}_{1-x}\text{Sn}_x$  core/shell nanowires, Assali et al.<sup>67</sup> utilised EDX measurements, correlated with atom probe tomography (ATP), of a cross sectional area of their nanowires to determine the Sn distribution in the shell (Figure 1.8). Using a similar growth process to Meng et al.,<sup>66</sup> with identical catalysts and precursor, Ge/ $\text{Ge}_{1-x}\text{Sn}_x$  core/shell nanowires with 13 at. % Sn were produced. The EDX and ATP analysis display a “sunburst-like” geometry of Sn rich areas of the  $\text{Ge}_{1-x}\text{Sn}_x$  shell along the  $\{112\}$  side facets compared to  $\{110\}$  facets. The Sn-rich region increased sharply from the Ge core to 8 at. % in the

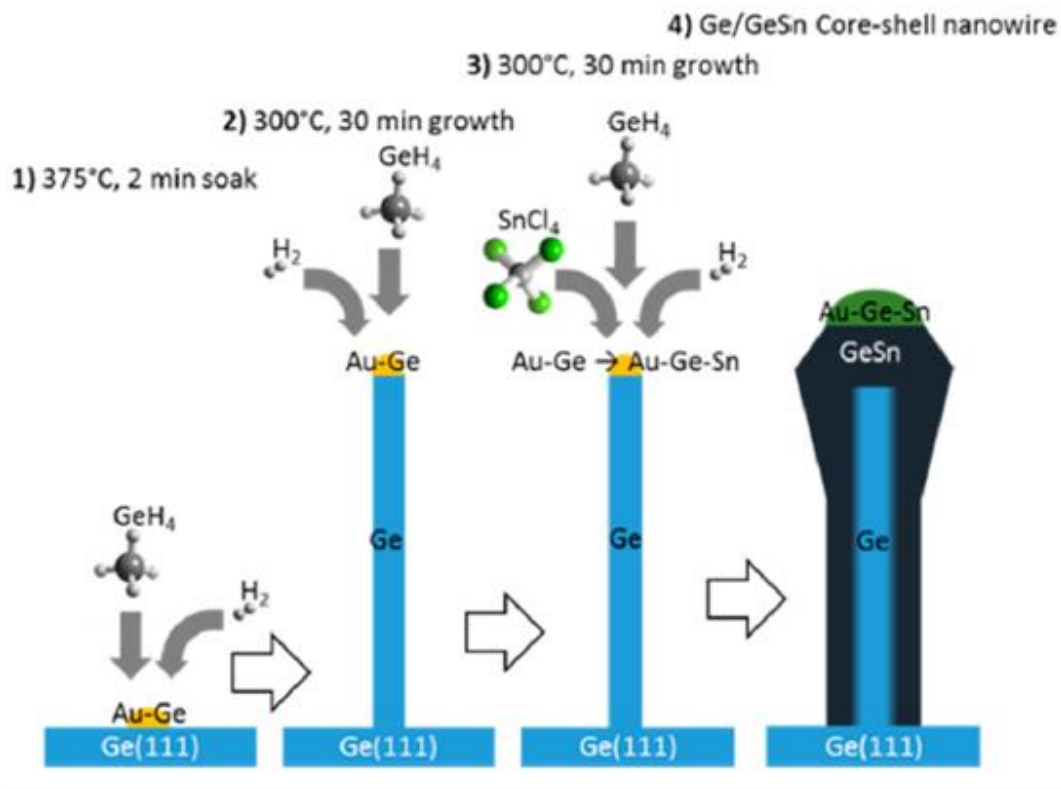


**Figure 1.7:** Growth schematic for core/shell nanowires at four different growth stages. Reprinted from A. Meng *et al.*, *Nano Letters*, **2016**, 16.<sup>66</sup>

shell, which gradually increases to 13 at. % toward the outer edge of the shell. A linear profile of this change in Sn content can be seen in Figure 1.8(f). The critical strain for these core/shell nanowires with sunburst geometry was further explored by Albani *et al.*<sup>19</sup> on nanowires with 10.5 % Sn incorporation in the outmost region of the Ge<sub>1-x</sub>Sn<sub>x</sub> shell. Increased Sn content in thick Ge layers has been reported to induce further strain relaxation.<sup>19</sup>

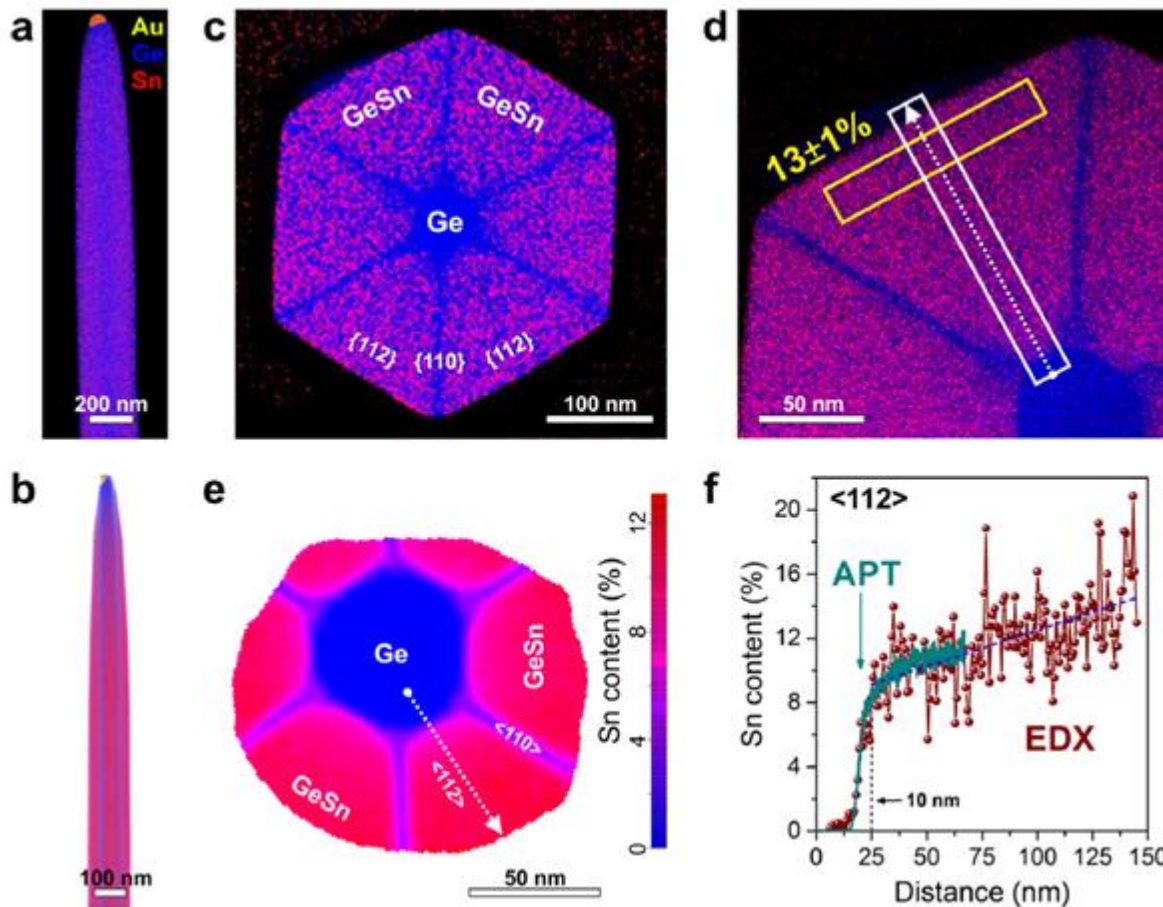


**Figure 1.8:** Radial Sn incorporation in a Ge/Ge<sub>1-x</sub>Sn<sub>x</sub> core-shell nanowire. (a) EDX compositional map and (b) APT image showing the Ge/Ge<sub>0.87</sub>Sn<sub>0.13</sub> core/shell structure. A uniform Sn distribution is observed in the Ge<sub>1-x</sub>Sn<sub>x</sub> shell along the NW growth axis, while no axial growth of Ge<sub>1-x</sub>Sn<sub>x</sub> is present. (c) and (d) Cross-sectional EDX compositional maps showing a ~120 nm thick Ge<sub>1-x</sub>Sn<sub>x</sub> shell, with enhanced Sn incorporation on the {112} side-facets compared to the {110} facets. The integrated tangential composition profile in the yellow rectangle provides an average Sn content of  $13 \pm 1\%$ , while the radial line-profile (white dashed arrow) is shown in (f). (e) APT measurements showing the Ge core and the inner portion of the Ge<sub>1-x</sub>Sn<sub>x</sub> shell. The line-profile (dashed arrow) is shown in (f). (f) Plot of the Sn content as a function of the distance along the radial direction for EDX and APT measurements. After a 10 nm transition region from the Ge core into the Ge<sub>1-x</sub>Sn<sub>x</sub> shell, the Sn content gradually increases toward the outer portion of the shell. The blue dashed line is the linear fit of the EDX profile.

Reprinted from S. Assali *et al.*, *Nano Letters*, **2017**, 17.<sup>67</sup>

While all of the above  $\text{Ge}_{1-x}\text{Sn}_x$  nanowire growth techniques make use of bottom-up growth regimes, it is important to note that  $\text{Ge}_{1-x}\text{Sn}_x$  nanowires have also been fabricated by top-down methods.<sup>68–71</sup> The top-down fabrication of  $\text{Ge}_{1-x}\text{Sn}_x$  nanowires typically involves the bottom-up growth of a  $\text{Ge}_{1-x}\text{Sn}_x$  layer on a Ge buffer layer. The presence of this Ge buffer layer presents a unique opportunity to create  $\text{Ge}_{1-x}\text{Sn}_x/\text{Ge}$  nanowire heterostructures with a precisely controlled interface. This precise control is as of yet under-developed, however selective dry etching of Ge over  $\text{Ge}_{1-x}\text{Sn}_x$  has been demonstrated by Gupta et al. (Figure 1.9).<sup>71</sup> Dry etching of the Ge buffer substrate was used to achieve a strain free, direct bandgap  $\text{Ge}_{1-x}\text{Sn}_x$  layer ( $x = 0.08$ ). A combination of wet and dry etching has recently shown promise as a route to the top-down fabrication of  $\text{Ge}_{1-x}\text{Sn}_x$

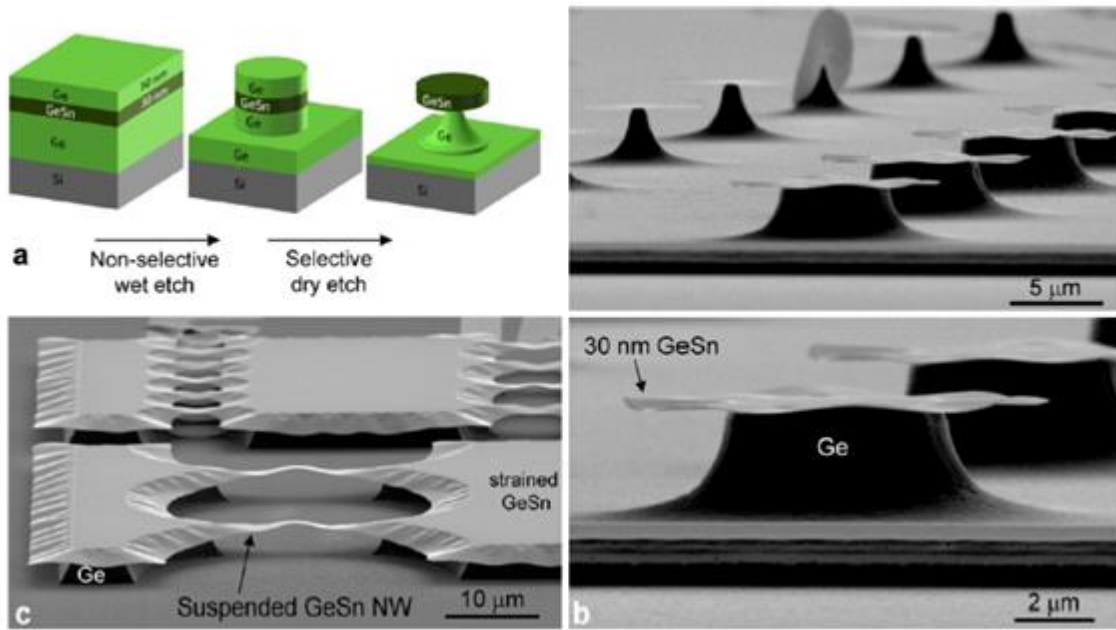


**Figure 1.9:** (a) Key steps in the process flow for fabrication of  $\text{Ge}_{1-x}\text{Sn}_x$  undercut structures on sample B. (b) SEM images of  $\text{Ge}_{1-x}\text{Sn}_x$  microdisks fabricated on sample B using the process flow shown in (a). Note that the  $\text{Ge}_{1-x}\text{Sn}_x$  layer is only 30 nm thick. (c) SEM image of suspended  $\text{Ge}_{1-x}\text{Sn}_x$  nanowires. Even though the length of the suspended region is greater than 15 μm, the wires do not collapse onto the substrate. These SEM images prove the high resistance of  $\text{Ge}_{1-x}\text{Sn}_x$  to  $\text{CF}_4$  plasma etching. Reprinted from S. Gupta *et al.*, *Nano Letters*, **2013**, 13.<sup>71</sup>

$_x\text{Sn}_x$  nanowires, however, the dry etch is significantly dependent on the Sn content of the  $\text{Ge}_{1-x}\text{Sn}_x$  layer.<sup>70</sup> Hence, detailed calibration of this technique is required for future, reproducible, tuneable  $\text{Ge}_{1-x}\text{Sn}_x$  nanowire production.

#### **1.3.2.2. Nanocrystals**

$\text{Ge}_{1-x}\text{Sn}_x$  nanocrystals (also referred to in the literature as nanoparticles, quantum dots and nanodots) provide an alternative nanostructure for  $\text{Ge}_{1-x}\text{Sn}_x$  alloys, although their diminished size results in an increase in fundamental bandgaps due to quantum confinement effects.<sup>72</sup> A high degree of both tunability in terms of Sn incorporation and size results in a broad range of energy gaps; suitable for further implementation in solar cells, optical detectors and biosensors.<sup>72–74</sup> The growth of  $\text{Ge}_{1-x}\text{Sn}_x$  nanocrystals has been reported by using a number of varying techniques.

A solution based approach has been detailed by Ramasamy et al.,<sup>73</sup> utilising a host of readily available precursors. Through their use of several precursors, they determined that a highly reactive Ge precursor and a relatively inert Sn precursor, or a pair of precursors that formed a complex in situ which could be reduced to  $\text{Ge}_{1-x}\text{Sn}_x$  nanocrystals, were required in order to synthesise a non-trivial amount of  $\text{Ge}_{1-x}\text{Sn}_x$  nanocrystals. The resulting  $\text{Ge}_{1-x}\text{Sn}_x$  nanocrystals were found to be quasi-spherical in shape, with mean diameters between 5 – 15 nm; the variation in diameter is due to the precise technique by which the  $\text{Ge}_{1-x}\text{Sn}_x$  nanocrystals were synthesised. By using a low growth temperature of 200 °C,  $\text{Ge}_{1-x}\text{Sn}_x$  nanocrystals with  $x = 0.42$  were fabricated; an increase in growth temperature in this system resulted in a decrease in Sn incorporation in the  $\text{Ge}_{1-x}\text{Sn}_x$  nanocrystals. This colossal Sn incorporation is necessary in  $\text{Ge}_{1-x}\text{Sn}_x$  nanocrystals to induce a direct bandgap, as quantum confinement effects increase the fundamental energy gap. The tunability of the bandgaps has been explored by Esteves et al.,<sup>72</sup> where  $\text{Ge}_{1-x}\text{Sn}_x$  nanocrystals were fabricated by a solution-based process as illustrated in the scheme shown in Figure 1.10, with

germanium diiodide and tin dichloride used as the Ge and Sn precursors respectively. By holding the mixture at a temperature of 300 °C for 0 and 10 minutes post growth,  $\text{Ge}_{1-x}\text{Sn}_x$  nanocrystals of varying sizes were produced (4.1 – 4.6 nm for 0 minutes and 15 – 17 nm for 10 minutes post growth). The resulting 15 – 17 nm  $\text{Ge}_{1-x}\text{Sn}_x$  nanocrystals,  $0.05 \leq x \leq 0.279$  were not shown to contain any metallic Sn clustering, despite their high Sn impurity. The smaller  $\text{Ge}_{1-x}\text{Sn}_x$  nanocrystals, 4.1 – 4.6 nm were synthesised to explore confinement effects. These  $\text{Ge}_{1-x}\text{Sn}_x$  nanocrystals, however, were not as Sn rich as their larger counterparts, with  $x \leq 0.116$ . While this Sn content was markedly lower than in the larger  $\text{Ge}_{1-x}\text{Sn}_x$  nanocrystals, it was nonetheless substantial Sn inclusion. The size effects of the optical properties of these  $\text{Ge}_{1-x}\text{Sn}_x$  nanocrystals will be discussed later in the article.

An alternative method for the synthesising  $\text{Ge}_{1-x}\text{Sn}_x$  nanocrystals was reported by Cho et al.,<sup>74</sup> who described the use of gas-phase laser photolysis to produce  $\text{Ge}_{1-x}\text{Sn}_x$  nanocrystals with  $x = 0.05 - 0.4$ . However, the  $\text{Ge}_{1-x}\text{Sn}_x$  nanocrystals with a high Sn content ( $x \geq 0.1$ ) were found to contain significant amounts of tetragonal phase Sn metal. The  $\text{Ge}_{1-x}\text{Sn}_x$  nanocrystals were produced by

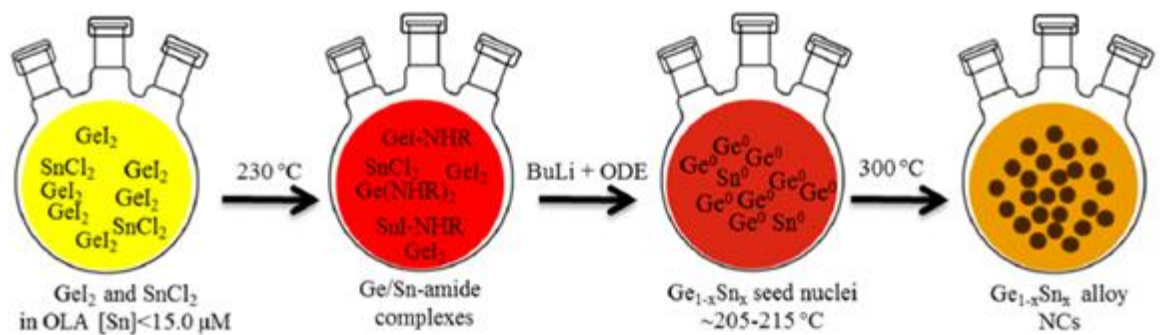


**Figure 1.10:** An Illustration of the synthesis of  $\text{Ge}_{1-x}\text{Sn}_x$  alloy nanocrystals. Fast chemical co-reduction of precursor halides dissolved in oleylamine (OLA), followed by the growth of resulting alloy nuclei at 300 °C has been successfully utilised to produce homogeneous  $\text{Ge}_{1-x}\text{Sn}_x$  nanoalloys. Reprinted from R. Esteves *et al.*, *Chemistry of Materials*, **2015**, 27.<sup>72</sup>

focussing a Nd:YAG pulsed laser into a reactor containing tetramethyl germanium and tetramethyl tin under vacuum. The presence of an increasing amount of metallic Sn was noted for increasing Sn content, as determined by X-ray diffraction (XRD) measurements; the larger the value of  $x$ , the larger the observed  $\beta$ -phase Sn peak. These  $\text{Ge}_{1-x}\text{Sn}_x$  nanocrystals with  $x = 0.05$  were explored as anode materials for Li-ion batteries and will be discussed later in the article.

As with  $\text{Ge}_{1-x}\text{Sn}_x$  nanowires, there are, as of yet, far fewer reports on the top-down fabrication-of  $\text{Ge}_{1-x}\text{Sn}_x$  nanocrystals compared to bottom-up growth. Bartolomeo et al.<sup>75</sup> detailed the bottom-up growth of  $\text{Ge}_{1-x}\text{Sn}_x$  nanocrystals on top-down patterned Si nanopillars.<sup>76</sup> These  $\text{Ge}_{1-x}\text{Sn}_x$  nanocrystals, grown by MBE, were reported to have Sn contents roughly in line with the expected equilibrium solubility of 1 at. %, but this may be an overestimation due to the propensity of Sn to segregate into metallic Sn at the high growth temperature of 750 °C. Despite this low Sn incorporation, these  $\text{Ge}_{1-x}\text{Sn}_x$  nanocrystals displayed field emission current with good stability.

## 1.5. Properties

### 1.5.1. Optical

Incorporating Sn into the Ge lattice has been predicted to show enhanced absorption in the near infrared region. There are many theoretical reports regarding the predicted optical properties of  $\text{Ge}_{1-x}\text{Sn}_x$  alloys with varying Sn content and strain incorporation.<sup>28,29,35,38,77</sup> However, for the purpose of this review, only the experimentally obtained optical properties will be discussed. The induction of Sn is also expected to result in increased carrier mobilities over both Ge and Si.<sup>1,78</sup> There is an increased responsivity in  $\text{Ge}_{1-x}\text{Sn}_x$  photodetectors compared to photodetectors comprised of pure Ge.<sup>12,16,46,79</sup> Importantly, sufficient Sn incorporation can enable Ge to transition

to a direct bandgap material.<sup>6,14,63–65,80</sup> All of these things provide potential to enable to co-integration of infrared optoelectronics and electronic devices based solely on group IV materials.

There are many methods for characterising the optical properties of a material. Regarding  $\text{Ge}_{1-x}\text{Sn}_x$ , photoluminescence studies have been at the forefront of optical characterisation. Photoluminescence (PL) studies are useful in determining the size of a bandgap, as well as whether the transition is direct, indirect or mixed.<sup>13,80</sup> PL has also been utilised to observe differences in the bandgap of doped and undoped  $\text{Ge}_{1-x}\text{Sn}_x$  by Al Kabi et al. (Figure 1.11).<sup>13</sup> Through PL studies, it has been ascertained that increased compressive strain in the  $\text{Ge}_{1-x}\text{Sn}_x$  alloys, typically observed in  $\text{Ge}_{1-x}\text{Sn}_x$  layers due to the lattice mismatch between the  $\text{Ge}_{1-x}\text{Sn}_x$  layer and the layer from which it is grown (typically a Ge buffer layer), results in an increase in the Sn quantity required to produce a direct band transition.<sup>59,60,81,82</sup> To determine where a band transition is direct or indirect using PL temperature dependent studies are essential. There is a distinct change in the relationship between intensity and temperature from indirect to direct bandgap. A direct bandgap will result in an inverse relationship between temperature and intensity, with increasing temperature leading to decreased PL intensity,<sup>14,64,65,80</sup> which can be attributed to a reduced transfer of electrons from the  $\Gamma$  to L valleys by thermal activation.<sup>83</sup> Thus, the increase in the intensity of the PL peak with decreasing temperature for direct bandgap  $\text{Ge}_{1-x}\text{Sn}_x$  is attributed to the higher population of the  $\Gamma$  valley. With increasing temperature, the fast diffusion of photocarriers toward surfaces and interfaces leads to non-radiative surface and interface recombination respectively, reducing the radiative transition rate. A monotonical decrease in the PL intensity with increase in temperature; which is typical behaviour seen in direct bandgap semiconductors,<sup>6,60,84–86</sup> confirms a direct bandgap for  $\text{Ge}_{1-x}\text{Sn}_x$ . Due to the gradual transition of  $\text{Ge}_{1-x}\text{Sn}_x$  alloys from an indirect to a direct bandgap, a certain degree of band mixing can also be observed for  $\text{Ge}_{1-x}\text{Sn}_x$  alloys through PL



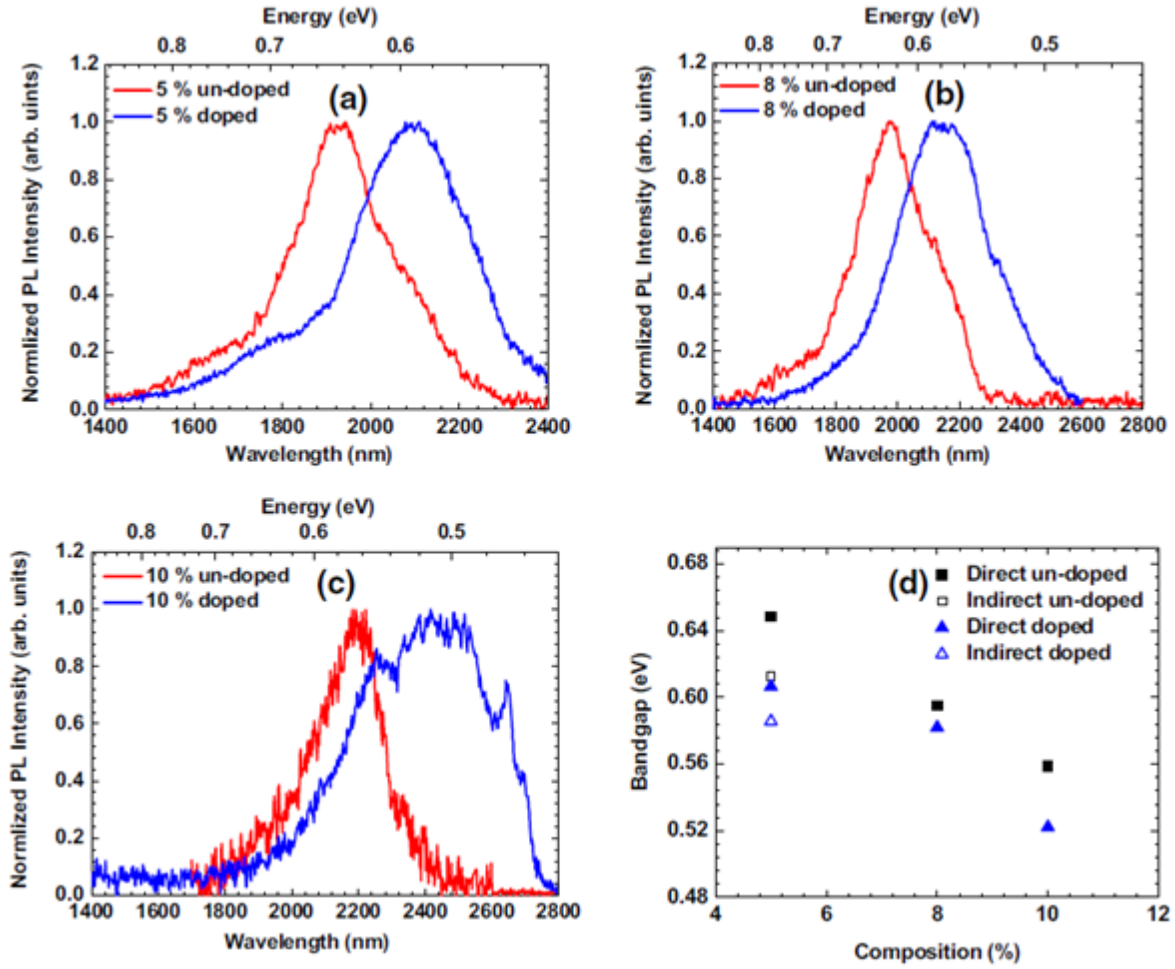


**Figure 1.11:** Comparison of the normalised PL spectra between unintentionally doped and n-doped  $\text{Ge}_{1-x}\text{Sn}_x$  samples with Sn compositions of (a) 5 at.% (b) 8 at.%, and (c) 10 at.% at room temperature. The indirect and direct bandgap shrinkages are summarised in (d). Reprinted from S. Al-Kabi *et al.*, *Journal of Electronic Materials*, **2016**, 45, 4.<sup>13</sup>

studies. Unusually, broad PL line-widths for  $\text{Ge}_{1-x}\text{Sn}_x$  alloys can sometimes be observed, which can be attributed to band mixing participation from both direct and indirect transitions resulting in an overlap of their PL peaks, as the indirect transition is shifted to lower energies. The determination of the activation energy for non-radiative transition from low temperature PL is also possible, with typical values for the activation energy of  $\text{Ge}_{1-x}\text{Sn}_x$  dependent on both  $x$ , and the

relative atomistic order.<sup>65</sup> PL studies have also been employed to investigate the difference in bandgap energies between doped and undoped  $\text{Ge}_{1-x}\text{Sn}_x$ .<sup>13</sup> Doped  $\text{Ge}_{1-x}\text{Sn}_x$  demonstrates a band transition with a decreased energy separation compared to undoped  $\text{Ge}_{1-x}\text{Sn}_x$  with the same Sn incorporation, for both direct and indirect samples (Figure 1.11).

Solid-state diffuse reflectance near infra-red (NIR) spectroscopy, in conjunction with the Kubelka-Munk (KM) remission function (to obtain pseudo-absorption from reflectance) has also been carried out on  $\text{Ge}_{1-x}\text{Sn}_x$  materials to determine bandgaps from reflectance data, particularly on  $\text{Ge}_{1-x}\text{Sn}_x$  nanocrystals of varying Sn content and sizes ( $0.00 \leq x \leq 0.116$  and 3.4 – 4.6 nm respectively) by Esteves et al. This investigation provided a deeper understanding of the impact of confinement effects on  $\text{Ge}_{1-x}\text{Sn}_x$  (Figure 1.12).<sup>72</sup> The bandgaps obtained from KM analysis were indicative of

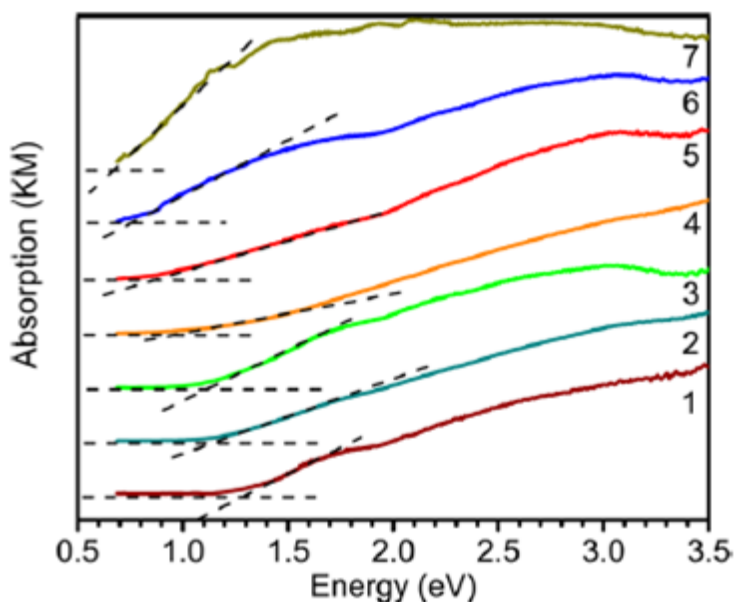


**Figure 1.12:** Diffuse reflectance spectra (converted to absorbance using the Kubelka–Munk (KM) remission function) of 3.6–4.3 nm  $\text{Ge}_{1-x}\text{Sn}_x$  alloy nanocrystals as a function of Sn composition:  $x = 0.000$  (spectrum 1),  $x = 0.033$  (spectrum 2),  $x = 0.056$  (spectrum 3),  $x = 0.077$  (spectrum 4),  $x = 0.088$  (spectrum 5),  $x = 0.092$  (spectrum 6), and  $x = 0.116$  (spectrum 7). Reprinted from R. Esteves *et al.*, *Chemistry of Materials*, **2015**, 27.<sup>72</sup>

the strong effect of quantum confinement in  $\text{Ge}_{1-x}\text{Sn}_x$  nanocrystals; an energy gap of 0.95 eV was observed for  $\text{Ge}_{1-x}\text{Sn}_x$  nanocrystals ( $x = 0.116$ ) which was a 0.15 eV increase when compared to the fundamental direct bandgap of bulk Ge (0.80 eV). This blue shift towards higher energies was expected upon dramatically decreasing the size of the nanostructure.

Spectroscopic ellipsometry is another technique that has been used to characterise the refractive index, extinction coefficient and dielectric properties of  $\text{Ge}_{1-x}\text{Sn}_x$  thin films (or substrates densely covered in nanostructures).<sup>3,27,39,62</sup> The technique can be employed for both crystalline and amorphous materials and can be used to examine any difference in optical properties upon crystallisation of the material. Lieten et al.<sup>87</sup> used spectroscopic ellipsometry to explore the differences in refractive index and extinction coefficient for amorphous and crystalline  $\text{Ge}_{1-x}\text{Sn}_x$  thin films ( $x = 0.045$ ).<sup>87</sup>

The determination of the nature of a band transition, be it direct or indirect, can also be determined through the use of Tauc Plots. These Tauc plots can be generated through many of the techniques outlined above; photocurrent measurements,<sup>88</sup> IR absorption,<sup>63</sup> and spectroscopic ellipsometry<sup>87</sup> to name a few. Tauc plots can be used to measure the optical gap, or bandgap, in amorphous and crystalline materials. Once created, a Tauc plot provides an easily interpreted insight into the nature of the band gap. The standard procedure for Tauc plots involves plotting  $(\alpha \cdot h\nu)^2$  vs  $h\nu$ , where  $\alpha$  represents the absorption coefficient and  $h\nu$  the photon energy. If a straight line fit is obtained, the band gap is determined to be direct in nature. A straight line plotting  $(\alpha \cdot h\nu)^{1/2}$  vs  $h\nu$  reveals an indirect transition, as derived by Tauc et. al..<sup>89</sup> The nature of the band transition (*i.e.* direct or indirect) has been determined for  $\text{Ge}_{1-x}\text{Sn}_x$  nanowires using Tauc plots (Figure 1.13).<sup>63</sup> Tauc plots can also be used to observe multiple energy transitions in a single sample, *i.e.* a sample containing energy transitions from both the indirect and direct components. Tauc plots can also

be used to determine contributions from heavy hole and light hole components of the band transitions in  $\text{Ge}_{1-x}\text{Sn}_x$ . As  $\text{Ge}_{1-x}\text{Sn}_x$  is predicted to transition gradually from indirect to direct, a certain degree of band mixing is expected here, as in PL studies. However, due to the band-mixing effects present in  $\text{Ge}_{1-x}\text{Sn}_x$  materials, Tauc plots may not be the most suitable technique in determining the nature of the bandgap.

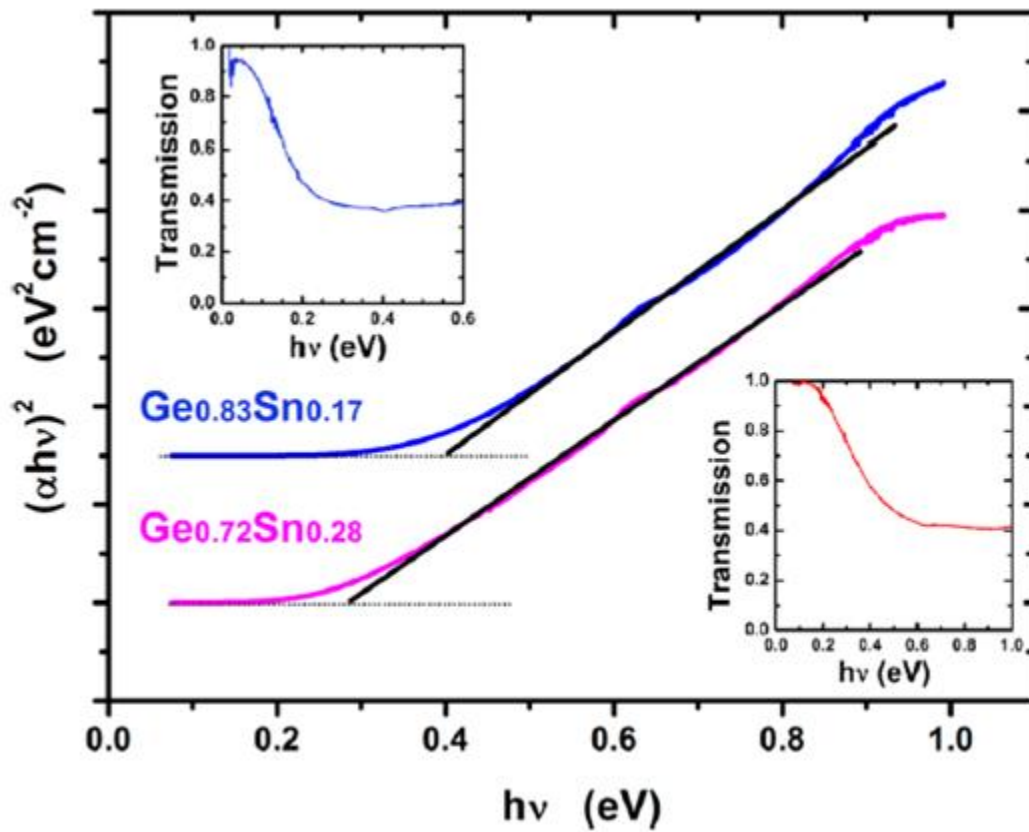


**Figure 1.13:** Tauc plot from IR absorption (insets) used to determine the direct bandgap energy of the nanorods and nanowires. Reprinted from M. Seifner *et al.*, *Chemistry of Materials*, **2017**, 29.<sup>63</sup>

### 1.5.2. Electrical

The incorporation of Sn into a Ge lattice results in changes in the physical properties of the material. Theoretical studies of the electrical properties of  $\text{Ge}_{1-x}\text{Sn}_x$  show some similar or

enhanced values of electron mobilities and concentrations compared with doped Ge counterparts.<sup>39</sup> Typical Ge p- and n- type dopants are also used as  $\text{Ge}_{1-x}\text{Sn}_x$  dopants.<sup>90</sup> D'Costa et al.<sup>39</sup> reported hole mobilities comparable to pure Ge with similar doping levels for carrier concentrations in the order of  $> 10^{18} \text{ cm}^{-3}$  for their  $\text{Ge}_{1-x}\text{Sn}_x$  thin films ( $x = 0.02$ ). Wang et al.<sup>91</sup> demonstrated high-mobility of strained  $\text{Ge}_{0.958}\text{Sn}_{0.042}$  p-channel MOSFETs with ammonium sulphide surface passivation. A  $\sim 10 \text{ nm}$  thick fully-strained single crystalline  $\text{Ge}_{1-x}\text{Sn}_x$  layer was epitaxially grown on Ge (100) as the channel layer. The as-grown  $\text{Ge}_{1-x}\text{Sn}_x$  layer was unintentionally p-doped with a concentration of  $\sim 5 \times 10^{16} \text{ cm}^{-3}$ .  $(\text{NH}_4)_2\text{S}$  surface passivation was performed for the  $\text{Ge}_{1-x}\text{Sn}_x$  surface, followed by gate stack formation.  $\text{Ge}_{0.958}\text{Sn}_{0.042}$  devices had a peak effective mobility of  $509 \text{ cm}^2/\text{Vs}$ .<sup>91</sup> Lei et al.<sup>92</sup> also assessed the impact of sulphur passivation on the gate stack quality in  $\text{Ge}_{1-x}\text{Sn}_x$  devices. At a high inversion carrier density ( $N_{\text{inv}}$  of  $1 \times 10^{13} \text{ cm}^{-2}$ ), sulphur passivation increased the effective mobility by 25 % in  $\text{Ge}_{0.83}\text{Sn}_{0.17}$  p-MOSFETs.<sup>92</sup> Fang et al.<sup>93</sup> used solid phase epitaxially grown  $\text{Ge}_{1-x}\text{Sn}_x$  to assess the eligibility of using direct  $\text{O}_2$  plasma treatments on  $\text{Ge}_{1-x}\text{Sn}_x$  surfaces for passivation of GeSn N-MOSFETs. The  $\text{O}_2$  plasma treatment formed a  $\text{Ge}_{1-x}\text{Sn}_x\text{O}_n$  film on the surface which was covered by in situ  $\text{Al}_2\text{O}_3$  for the gate stack in  $\text{Ge}_{1-x}\text{Sn}_x$  MOS devices. The benefit of the surface passivation was evidenced by low interface trap density of  $1.62 \times 10^{11} \text{ cm}^{-2}\text{eV}^{-1}$ , resulting in  $\text{Ge}_{1-x}\text{Sn}_x$  N-MOSFETs with a peak electron mobility of  $518 \text{ cm}^2/\text{Vs}$ .<sup>93</sup> Lei et al.<sup>92,93</sup> produced the world's first  $\text{Ge}_{1-x}\text{Sn}_x$  p-FinFETs formed on  $\text{Ge}_{1-x}\text{Sn}_x$ -on-insulator (GSOI), with channel lengths down to  $50 \text{ nm}$  and fin width down to  $20 \text{ nm}$ . In comparison with other reported  $\text{Ge}_{1-x}\text{Sn}_x$  p-FETs, a low subthreshold slope (SS) of  $79 \text{ mV/decade}$  at  $V_{\text{DS}} = -0.5 \text{ V}$  was achieved (Figure 1.14).<sup>94,95</sup> Schulte-Braucks et al.<sup>5</sup> also systematically studied  $\text{Ge}_{1-x}\text{Sn}_x$  n-FETs, from individual process modules to complete devices. High-k gate stacks and NiGeSn metallic contacts for source and drain were characterised, over a range of  $0 - 14.5 \text{ at. \%}$

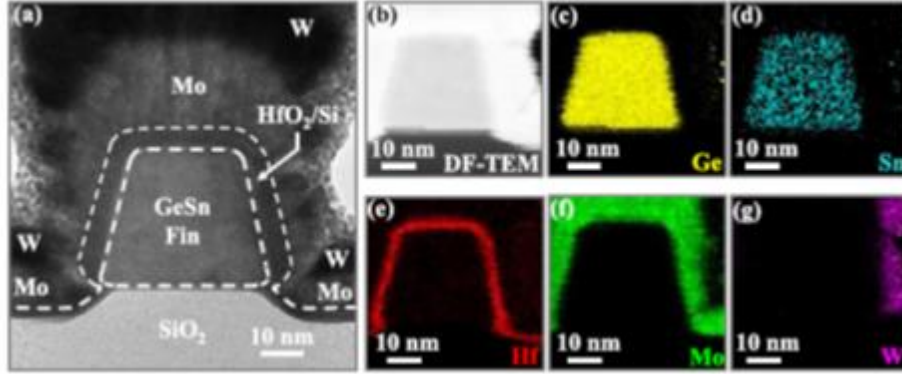


**Figure 1.14:** (a) HR-XTEM image of a  $\text{Ge}_{1-x}\text{Sn}_x$  FinFET ( $W_{\text{Fin}} = 25$  nm and  $H_{\text{Fin}} = 35$  nm) cut across the gate line. Smooth  $\text{Ge}_{1-x}\text{Sn}_x$  fin sidewall was realised with a sidewall angle of  $\sim 78^\circ$ . (b) STEM image and EDX elemental mappings of (c) Ge, (d) Sn, (e) Hf, (f) Mo, and (g) W showing the contour of the  $\text{Ge}_{1-x}\text{Sn}_x$  fin. The Sn composition in the  $\text{Ge}_{1-x}\text{Sn}_x$  fin was  $\sim 7.8\%$  from the energy dispersive X-ray analysis spot scan, which was consistent with X-ray diffraction data. Reprinted from Lei *et al.*, *IEEE Transactions on Electronic Devices*, **2018**, 65, 9.<sup>95</sup>

Sn-content  $\text{Ge}_{1-x}\text{Sn}_x$  alloys. Negative differential resistance in  $\text{Ge}_{0.87}\text{Sn}_{0.13}$  tunnel-diodes were demonstrated at cryogenic temperatures.<sup>5</sup> Wirths et al.<sup>96</sup> investigated Ni(SiGeSn) metal contact formation for Sn compositions from 6 to 9 at.% and quaternary NiSiGeSn alloys, formed on SiGeSn ternaries with large Si/Sn compositions ratios.<sup>96</sup> Tensile strained single-crystal  $\text{Ge}_{1-x}\text{Sn}_x$  on insulator (GSOI) was obtained by Liu et al. using self-organised seeding lateral growth. P-MOSFETs were fabricated and a low field peak hole mobility of  $383 \text{ cm}^2\text{V}^{-1}\text{s}^{-1}$  was obtained, which indicated the high quality of this GSOI structure.<sup>97</sup>

Han et al.<sup>98</sup> fabricated  $\text{Ge}_{1-x}\text{Sn}_x$  quantum well (QW) p-type tunnel-FETs (TFETs) and pMOSFETs on Si.  $\text{Ge}_{1-x}\text{Sn}_x$  quantum well (QW) pMOSFETs on Si(111) demonstrated a high effective hole mobility of  $505 \text{ cm}^2/\text{Vs}$ , related to high crystallinity of the  $\text{Ge}_{1-x}\text{Sn}_x$  material. They also reported that  $\text{Ge}_{1-x}\text{Sn}_x$  QW pTFETs on Si(111) outperformed the devices on Si(001) on SS and ON-state current.<sup>98</sup> Cong et al.<sup>99</sup> fabricated a multilayer graphene and  $\text{Ge}_{1-x}\text{Sn}_x/\text{Ge}$  QW heterostructure as a

Si-based light source. Specially designed  $\text{Ge}_{0.9}\text{Sn}_{0.1}/\text{Ge}$  QWs were used as the active layer, which achieved a PL peak at 2050 nm.<sup>99</sup> Huang et al.<sup>100</sup> fabricated compressively strained  $\text{Ge}_{1-x}\text{Sn}_x$  QW channels sandwiched by Ge sacrificial layers grown using CVD. The stacked  $\text{Ge}_{0.93}\text{Sn}_{0.07}$ -channel p-gate-all-around FET had a record high for  $\text{Ge}_{1-x}\text{Sn}_x$  pFETs of  $I_{\text{ON}} = 1975 \mu\text{A}/\mu\text{m}$  width at  $-1 \text{ V}$ .<sup>100</sup>

Photoresponse and photoconductivity are also imperative to determine the optoelectronic properties of  $\text{Ge}_{1-x}\text{Sn}_x$ . Unsurprisingly, the addition of Sn results in the photoresponse of  $\text{Ge}_{1-x}\text{Sn}_x$  alloys to shift to lower energies (longer wavelengths) than their pure Ge counterparts.<sup>101</sup> Naturally, this can be predicted as the lower energies are expected due to the reducing energy of the  $\Gamma$  valley. Due to the presence of band mixing,  $\text{Ge}_{1-x}\text{Sn}_x$  alloys have a broad spectral response, across all telecommunications bands.<sup>46,102,103</sup> Temperature dependent photoresponse studies, conventionally taken at a specified wavelength (1550 nm), reveal that temperature and responsivity have an inverse relationship (the responsivity at a given wavelength is increased with decreasing temperature) which can be attributed to decreased phonon scattering.<sup>88,101,104</sup> Again, this is not unlike the behaviour noted in PL studies, where an increase in temperature resulted in a decrease in intensity. This behaviour is not observed for pure Ge devices, in fact the opposite is observed, with decreasing temperature the bandgap of Ge is increased and shifted to higher energies, thus a less intense absorption is observed at a wavelength of 1550 nm. A strong spectral response has been observed for  $\text{Ge}_{1-x}\text{Sn}_x$  thin films ( $0.045 < x < 0.052$ ) compared to pure Ge thin films, or indeed, for samples with  $x > 0.052$  which showed similar magnitudes at 1550 nm.<sup>88</sup> This consistency of responsivity of  $\text{Ge}_{1-x}\text{Sn}_x$  devices with increasing  $x$  indicates that a photodetector comprised of  $\text{Ge}_{1-x}\text{Sn}_x$  will be of equal, or greater, quality than a Ge photodetector. Hart et al.<sup>88</sup> also reported that their  $\text{Ge}_{1-x}\text{Sn}_x$  layer ( $x = 0.113$ ) displayed a dark conductivity three times higher

than their Ge reference.<sup>88</sup> In fact, it was noted that at room temperature, the dark conductance increased with increasing Sn content.

## 1.6.Applications

With the unique, and often remarkable, qualities that  $\text{Ge}_{1-x}\text{Sn}_x$  alloys possess, their integration into many varied devices is possible. Their direct bandgap, with sufficient Sn incorporation, is essential for implementation in optoelectronic and photonic devices such as lasers and photodetectors;<sup>6,7,104–106</sup> and the high mobility of  $\text{Ge}_{1-x}\text{Sn}_x$  over Ge or Si is beneficial for electronic devices such as TFETs.<sup>10,107,108</sup> The characteristics of  $\text{Ge}_{1-x}\text{Sn}_x$  nanostructures discussed in the previous section, as well as those not mentioned in this review such as tensile strength, *etc.*, make  $\text{Ge}_{1-x}\text{Sn}_x$  a desirable material for use in electronic, optoelectronic, photonic and energy storage devices.

### 1.6.1. Electronic

There have been a multitude of semiconductor applications for  $\text{Ge}_{1-x}\text{Sn}_x$  materials recently reported in the literature. For example, negative-capacitance FETs (NC-FETs) for steep slope switches have been studied by Zhou et al., where they explored the negative differential resistance and hysteresis reduction in planar Ge pFETs,<sup>109,110</sup> using a  $\text{HfZrO}_x$  gate stack. The same group produced a highly impressive  $\text{Ge}_{1-x}\text{Sn}_x$  (4 at. % Sn) based ferroelectric NC-FET with a sub-20 mV/dec subthreshold slope. The stack in this case was comprised of a metal-ferroelectric-metal-insulator.<sup>111</sup> Liu et al.<sup>110</sup> designed a heterojunction-enhanced n-channel tunnelling field-effect-transistor with a  $\text{Ge}_{1-x}\text{Sn}_x/\text{Ge}_{1-y}\text{Sn}_y$  ( $x > y$ ) heterojunction located in the channel region. At a supply voltage of 0.3 V, a >300 % ON-state current enhancement was demonstrated in a  $\text{Ge}_{0.92}\text{Sn}_{0.08}/\text{Ge}_{0.94}\text{Sn}_{0.06}$  FET, compared to a  $\text{Ge}_{0.92}\text{Sn}_{0.08}$  homogeneous structured FET, due to a steeper average subthreshold slope.<sup>112</sup> Wang et al.<sup>111</sup> reported the demonstration of high-



performance  $\text{Ge}_{1-x}\text{Sn}_x$  metal-semiconductor-metal photodetectors and  $\text{Ge}_{1-x}\text{Sn}_x$  pFinFETs on an advanced  $\text{Ge}_{1-x}\text{Sn}_x$ -on-insulator platform. The detection range of the  $\text{Ge}_{1-x}\text{Sn}_x$  photodetector was beyond 2  $\mu\text{m}$ , with responsivities of 0.39 and 0.10 A/W at 1550 nm and 2003 nm, respectively.  $\text{Ge}_{1-x}\text{Sn}_x$  pFinFETs with fin width scaled down to 15 nm were also fabricated on the GSOI platforms, exhibiting a small SS of 93 mV/decade, and a high drive current of 176  $\mu\text{A}/\mu\text{m}$ .<sup>113</sup> Other examples of impressive process module development have included the work by Buca et al. who recently studied gate stack and Ni(SiGeSn) metal contact formation on low bandgap strained (Si)Ge(Sn) semiconductors.<sup>114</sup> Quintero et al. also studied the stanogermanide system, involving Ni- $\text{Ge}_{1-x}\text{Sn}_x$  based materials. They evaluated the impact of the addition of 10 at. % of Pt in Ni thin films. At an alloy formation temperature of 360 °C, a stable  $(\text{Ni}_{1-y}\text{Pt}_y)(\text{Ge}_{1-x}\text{Sn}_x)$  phase was obtained.<sup>115</sup> Recently Prucnal et al.<sup>114</sup> studied ex situ n+ doping of  $\text{Ge}_{1-x}\text{Sn}_x$  alloys realised by P implantation into  $\text{Ge}_{1-x}\text{Sn}_x$  alloy layers grown by molecular beam epitaxy followed by flash lamp annealing. They showed that carrier concentration of up to  $1 \times 10^{19} \text{ cm}^{-3}$  could be achieved without affecting the Sn distribution.<sup>116</sup> For further reading on the electronic properties of  $\text{Ge}_{1-x}\text{Sn}_x$ , Gupta et al.<sup>117</sup> presented a comprehensive overview of the state of the art in Ge and  $\text{Ge}_{1-x}\text{Sn}_x$  transistor research in their 2014 review article. Key material challenges involved in fabrication, such as gate stack formation and achieving low-resistance contacts to transistor source/drain regions were reviewed.<sup>117</sup>

### 1.6.2. Optoelectronics

Use of  $\text{Ge}_{1-x}\text{Sn}_x$  thin films in photodetectors<sup>16,101,105,118,119</sup> and photodiodes<sup>104</sup> has become increasingly popular during recent years. The tunability of the bandgap in  $\text{Ge}_{1-x}\text{Sn}_x$ , and its compatibility with Si platforms, allows for the facile implementation of  $\text{Ge}_{1-x}\text{Sn}_x$  nanomaterials into optoelectronic devices.  $\text{Ge}_{1-x}\text{Sn}_x$  thin films are expected to have increased photoconductivity and broader photoresponse than their pure Ge counterparts,<sup>29</sup> and have been predicted to exhibit

greater carrier mobilities.<sup>39,78</sup>  $\text{Ge}_{1-x}\text{Sn}_x$  photodetectors have been demonstrated using  $\text{Ge}_{1-x}\text{Sn}_x$  thin films with varying Sn amounts, exhibiting a shift to lower energies with Sn addition, as well as increased dark conductivity.<sup>101,102,104,106,119</sup> Mathews et al. fabricated n-i- $\text{Ge}_{1-x}\text{Sn}_x$ /p-Si photodiode detectors with  $\text{Ge}_{0.98}\text{Sn}_{0.02}$  active layers and found that even at low Sn concentrations the detector quantum efficiencies were higher than comparable pure-Ge device designs.<sup>120</sup> The research of Chang et al.<sup>121</sup> proposed the use of  $\text{Ge}_{1-x}\text{Sn}_x$  heterojunction phototransistors as efficient optical receivers on Si substrates. Their designs used n-Ge/p- $\text{Ge}_{1-x}\text{Sn}_x$ /n- $\text{Ge}_{1-x}\text{Sn}_x$  layers pseudomorphically grown on Si wafers *via* a Ge virtual substrate, compatible with CMOS technology.<sup>121</sup> However, due to the lattice mismatch between Ge and Sn, thin films often experience large amounts of strain. Compressive strain shifts the energy gap to lower wavelengths, which results in higher amounts of Sn incorporation to achieve a direct bandgap.<sup>13,14</sup> A promising solution to the strain induction in  $\text{Ge}_{1-x}\text{Sn}_x$  thin films is the move towards 1-D  $\text{Ge}_{1-x}\text{Sn}_x$  nanostructures; a nanowire morphology allows for increased strain relaxation over thin films due to the free sidewall facets.<sup>19</sup> We have recently implemented  $\text{Ge}_{1-x}\text{Sn}_x$  ( $x = 0.1$ ) nanowires as efficient photodetector materials with increased photosensitivity compared to  $\text{Ge}_{1-x}\text{Sn}_x$  thin films (Chapter 4).

### 1.6.3. Photonics

$\text{Ge}_{1-x}\text{Sn}_x$  has been put forward as a suitable gain material in lasing applications<sup>35,77,122</sup> and recently there have been several reports of  $\text{Ge}_{1-x}\text{Sn}_x$  lasers.<sup>6,7,123</sup> Wirths et al.<sup>6</sup> demonstrated lasing in partially strain-relaxed  $\text{Ge}_{1-x}\text{Sn}_x$  ( $x = 0.126$ ) thin films; the use of power dependent PL studies and a Fabry-Perot waveguide were employed to observe clear lasing under optical pumping. The  $\text{Ge}_{1-x}\text{Sn}_x$  films were fabricated by CVD on virtual Ge substrates to increase strain relaxation. A threshold excitation density of  $\sim 325 \text{ kW/cm}^2$  at 100 K was observed. Von den Driesch et al.<sup>122</sup> explored  $\text{Ge}_{1-x}\text{Sn}_x/\text{Si}_y\text{Ge}_{1-x}\text{Sn}_x$  group IV heterostructure lasers, where different types of double

heterostructures and multi-quantum wells were epitaxially grown with varying well thicknesses and barriers.<sup>124</sup> Al-Kabi et al.<sup>7</sup> and Stange et al.<sup>123</sup> each reported the fabrication of  $\text{Ge}_{1-x}\text{Sn}_x$  lasers in the year 2016. The laser produced by Al-Kabi et al.,<sup>7</sup> utilising a strain relaxed  $\text{Ge}_{1-x}\text{Sn}_x$  ( $x = 0.0895$ ) thin film grown on a Ge buffer layer, was fabricated in a low cost regime with commercially available precursors, *i.e.* a “manufacture ready” process.<sup>7</sup> This process development is of significant importance for the future of  $\text{Ge}_{1-x}\text{Sn}_x$  and its place in photonic devices. Stange et al.<sup>123</sup> sought to improve lasing temperature and threshold of  $\text{Ge}_{1-x}\text{Sn}_x$  lasers by fabricating  $\text{Ge}_{1-x}\text{Sn}_x$  microdisks ( $x = 0.125$ ). These microdisks were produced by forming a  $\text{Ge}_{1-x}\text{Sn}_x$  layer on a Ge buffer layer; the buffer was then selectively etched to manufacture a  $\text{Ge}_{1-x}\text{Sn}_x$  microdisk on a Ge pedestal (Figure 1.15). This etching of the Ge buffer layer was crucial in increasing the optical confinement in the  $\text{Ge}_{1-x}\text{Sn}_x$  laser, as the large refractive index contrast between  $\text{Ge}_{1-x}\text{Sn}_x$  and air results in an improvement of the optical properties. This unique approach resulted in a  $\text{Ge}_{1-x}\text{Sn}_x$  laser which was usable up to temperatures of 130 K; the highest temperature yet reported.

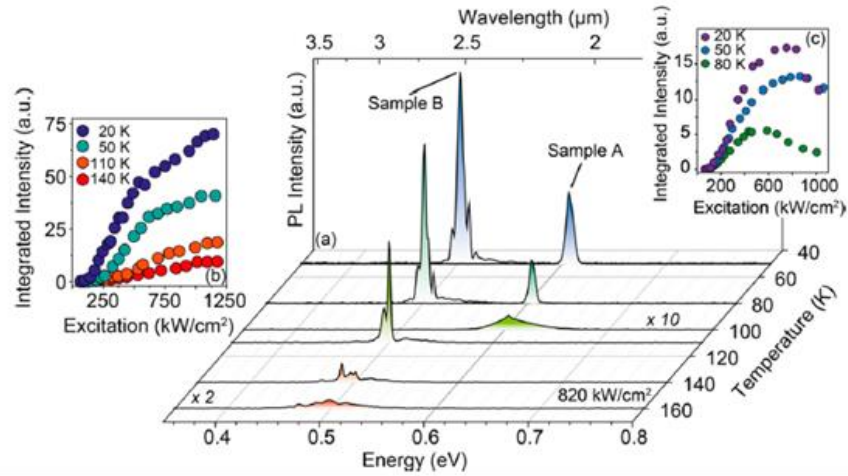
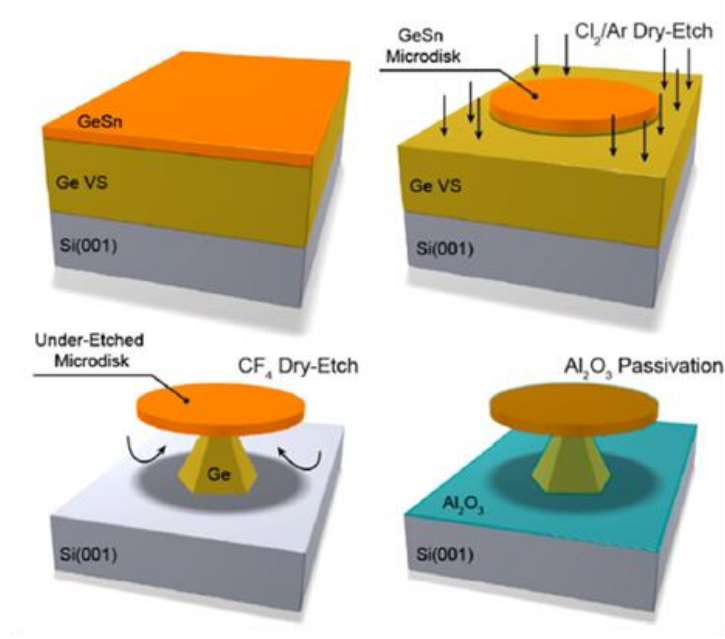


**Figure 1.15:**  $\text{Ge}_{1-x}\text{Sn}_x$  microdisk lasers. (Top) Fabrication of  $\text{Ge}_{1-x}\text{Sn}_x$  microdisks, schematic representation of the fabrication flow and of 8  $\mu\text{m}$  diameter  $\text{Ge}_{0.875}\text{Sn}_{0.125}$  microdisks with the underlying Ge virtual substrate (VS) undercut by 3.6  $\mu\text{m}$ . (Bottom) Power and temperature dependence for different Sn contents. (a) Temperature-dependent spectra of 8  $\mu\text{m}$  diameter microdisks from samples A ( $x = 0.085$ ) and B ( $x = 0.125$ ) at 820  $\text{kW}/\text{cm}^2$ . Light-in and light-out curves at different temperatures for (b) sample B and (c) sample A. Reprinted from D. Stange *et al.*, *ASC Photonics*, **2016**, 3.<sup>123</sup>

#### 1.6.4. Other Applications

Due to its increased mobility,  $\text{Ge}_{1-x}\text{Sn}_x$  alloys can also be utilised in energy storage devices, such as batteries.  $\text{Ge}_{1-x}\text{Sn}_x$  nanostructures have shown promise as anode materials for Li-ion batteries using nanoparticles<sup>74,125,126</sup>, nanowires (Chapter 5) and branched nanostructures (Chapter 6). The incorporation of just 5 at. % Sn in  $\text{Ge}_{1-x}\text{Sn}_x$  nanocrystals resulted in a non-trivial increase in specific capacities in Li-ion battery.<sup>74</sup> The  $\text{Ge}_{1-x}\text{Sn}_x$  nanocrystals maintained a capacity of 1010 mA h g<sup>-1</sup> and a coulombic efficiency of 96.8 %, compared to capacities of 800 mA h g<sup>-1</sup> for pure Ge nanocrystals of comparable size and structure (Figure 1.16). However, the increasing Sn composition resulted in a decrease in capacities due to the tendency of metallic Sn to segregate. Further to  $\text{Ge}_{1-x}\text{Sn}_x$  nanocrystals,  $\text{Ge}_{1-x}\text{Sn}_x$  nanowires and branched nanostructures have also been explored as anode materials for Li-ion batteries (Chapter 6). The  $\text{Ge}_{1-x}\text{Sn}_x$  ( $x = 0.048$ ) nanowires, grown by conventional CVD and displayed high capacities ( 921 mAh/g) and excellent coulombic efficiencies. Following this,  $\text{Ge}_{1-x}\text{Sn}_x$  branched nanostructures revealed themselves to also be capable anode materials. Particularly, the unique combination of the morphology of  $\text{Ge}_{1-x}\text{Sn}_x$  branched nanostructures resulted in exceptionally high capacities because of the increased charge carrier pathways and surface area, and the incorporation of Sn into the nanostructure.

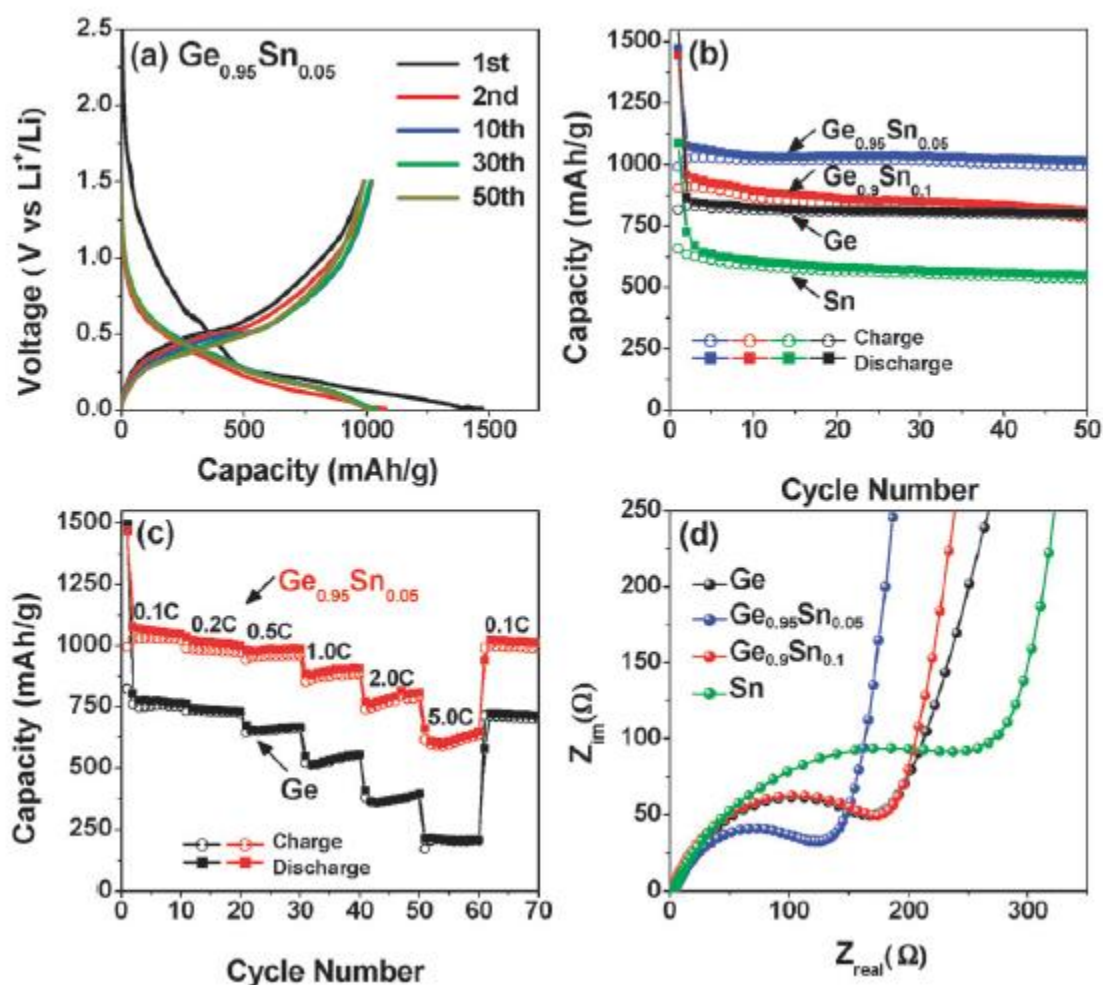


**Figure 1.16:** Charge and discharge voltage profiles of a half cell using  $\text{Ge}_{0.95}\text{Sn}_{0.05}$  nanocrystals for 1, 2, 10, 30, and 50 cycles tested between 0.01 and 1.5 V, at a rate of 0.1 C. (b) Charge-discharge capacity vs. cycle number for half cells of Ge (ref. 15),  $\text{Ge}_{0.95}\text{Sn}_{0.05}$ ,  $\text{Ge}_{0.9}\text{Sn}_{0.1}$ , and Sn nanocrystals at a rate of 0.1 C. (c) Cycling performance of Ge and  $\text{Ge}_{0.95}\text{Sn}_{0.05}$  NCs as the rate is increased from 0.1 C to 5.0 C. (d) Nyquist plots of Ge,  $\text{Ge}_{0.95}\text{Sn}_{0.05}$ ,  $\text{Ge}_{0.9}\text{Sn}_{0.1}$ , and Sn nanocrystals. Reprinted from Y. Cho *et al.*, *Phys.Chem. Chem. Phys.*, **2013**, 15.<sup>74</sup>

## 1.7. Conclusion and Outlook

In order to address the drive to create Si compatible, direct bandgap materials for implementation in complementary metal oxide semiconductor (CMOS), and indeed beyond CMOS, devices, group IV alloys have becoming of increasing interest. Alloying of Ge with Sn represents a novel solution

to the lack of light emission in group IV compounds, with an indirect to direct bandgap transition predicted for Sn incorporation greater than 6.5 at. %. This review details the recent advances in the growth methods and physical properties of  $\text{Ge}_{1-x}\text{Sn}_x$  materials, with a focus on the recent shift in interest toward  $\text{Ge}_{1-x}\text{Sn}_x$  nanostructures. This shift stems from the ability of  $\text{Ge}_{1-x}\text{Sn}_x$  1-D nanostructures to fully or partially relax strain, due to the free sidewall facets, compared to the comparatively strained  $\text{Ge}_{1-x}\text{Sn}_x$  thin films. Varying growth methods for both  $\text{Ge}_{1-x}\text{Sn}_x$  thin films and nanostructures were detailed. The optical and electronic properties, both theoretically and experimentally obtained, were also reported, with evidence of direct bandgaps, high carrier mobilities, optical gain and broad photoresponse across the mid-IR.

The future of  $\text{Ge}_{1-x}\text{Sn}_x$  nanostructures is a broad and varied one, with potential for integration into photonic, optoelectronic, electronic and energy storage devices to name but a few. The development of high quality, uniform and stable  $\text{Ge}_{1-x}\text{Sn}_x$  alloy materials; especially in nanoforms; is crucial to its successful implementation in large scale applications. Intentional doping of  $\text{Ge}_{1-x}\text{Sn}_x$  nanostructures will also be imperative in furthering the implementation of  $\text{Ge}_{1-x}\text{Sn}_x$  nanostructures in devices. While some research is already underway, *in-situ* incorporation of dopants<sup>43</sup> and *ex-situ* post growth,<sup>116</sup> *i.e.* ion implantation and pulsed laser annealing,<sup>90</sup> will need to be thoroughly explored and exploited. The tunable bandgap, optical emission, scalability and high carrier mobilities of  $\text{Ge}_{1-x}\text{Sn}_x$  nanostructures provide one route towards ensuring the future of Si compatible device fabrication.

### 1.7.1. Thesis Summary

To address the under-representation of  $\text{Ge}_{1-x}\text{Sn}_x$  nanowires in the literature, this thesis will focus on my contribution to the advancements in  $\text{Ge}_{1-x}\text{Sn}_x$  nanowires, and branched nanostructures.

Chapter 2 describes the growth of  $\text{Ge}_{1-x}\text{Sn}_x$  nanowires with  $x = 0.09$ . This high Sn incorporation was facilitated by the use of a step anneal at the eutectic temperature post growth, and by a solute trapping model of impurity incorporation. However, the step anneal resulted in an apparent degree of “disorder” on the atomic scale. Chapter 3 details the incorporation of this same high Sn content ( $x = 0.09$ ) without the use of a eutectic anneal, thereby increasing the relative atomic ordering. This Sn incorporation was achieved by altering the growth parameters of the system to increase the nanowire growth rate, thereby confirming solute trapping as the mechanism of Sn inclusion. Chapter 4 reports the functionality of these  $\text{Ge}_{1-x}\text{Sn}_x$  nanowires in optoelectronics as photodetectors ( $x = 0.105$ ). The photoresponse of  $\text{Ge}_{1-x}\text{Sn}_x$  nanowires are proven to be comparable alternatives to pure Ge devices. Chapter 5 also explores the functionality of  $\text{Ge}_{1-x}\text{Sn}_x$  nanowires, this time with lower Sn incorporation ( $x = 0.048$ ) in energy storage as Li-ion anode materials, with high capacities ( $> 900 \text{ mAh/g}$ ) and excellent retention. Chapter 6 informs on the development of  $\text{Ge}_{1-x}\text{Sn}_x$  branched nanostructures. A growth mechanism is proposed for these novel nanostructures; with trunk components comprised of 4.4 at. % Sn and branches containing 8.0 at. % Sn; fabricated in a one step growth. These  $\text{Ge}_{1-x}\text{Sn}_x$  nanostructures are also explored as anode materials for Li-ion batteries, as their increased charge carrier pathways, mechanical strength and surface area result in increased capacities over conventional nanowires. Chapter 7 depicts the influence of pressure on the growth  $\text{Ge}_{1-x}\text{Sn}_x$  nanowires. A move to a supercritical fluid growth regime results in the incorporation of colossal amounts of Sn in the Ge nanowire lattice, with  $0.1 \leq x \leq 0.35$ . An apparent dependence of the Sn content with nanowire diameter is briefly explored in Chapter 7. Finally, Chapter 8 details the conclusions of this thesis, and a future outlook for  $\text{Ge}_{1-x}\text{Sn}_x$  nanowires is provided.



## 1.8. References

- 1 J. D. Sau and M. L. Cohen, *Phys. Rev. B - Condens. Matter Mater. Phys.*, 2007, **75**, 1–7.
- 2 D. W. Jenkins and J. D. Dow, *Phys. Rev. B*, 1987, **36**, 7994–8000.
- 3 V. Richard D’Costa, W. Wang, Q. Zhou, E. Soon Tok and Y. C. Yeo, *Appl. Phys. Lett.*, , DOI:10.1063/1.4862659.
- 4 A. M. Ionescu and H. Riel, *Nature*, 2011, **479**, 329–337.
- 5 C. Schulte-Braucks, S. Glass, E. Hofmann, D. Stange, N. von den Driesch, J. M. Hartmann, Z. Ikonc, Q. T. Zhao, D. Buca and S. Mantl, *Solid. State. Electron.*, 2017, **128**, 54–59.
- 6 S. Wirths, R. Geiger, N. V. Den Driesch, G. Mussler, T. Stoica, S. Mantl, Z. Ikonc, M. Luysberg, S. Chiussi, J. M. Hartmann, H. Sigg, J. Faist, D. Buca and D. Grützmacher, 2015, 1–5.
- 7 S. Al-Kabi, S. A. Ghetmiri, J. Margetis, T. Pham, Y. Zhou, W. Dou, B. Collier, R. Quinde, W. Du, A. Mosleh, J. Liu, G. Sun, R. A. Soref, J. Tolle, B. Li, M. Mortazavi, H. A. Naseem and S. Q. Yu, *Appl. Phys. Lett.*, , DOI:10.1063/1.4966141.
- 8 R. Soref, *Nat. Photonics*, 2010, **4**, 495–497.
- 9 S. Wirths, D. Buca and S. Mantl, *Prog. Cryst. Growth Charact. Mater.*, 2016, **62**, 1–39.
- 10 H. Wang, Y. Liu, G. Han, Y. Shao, C. Zhang, Q. Feng, J. Zhang and Y. Hao, *IEEE Trans. Electron Devices*, 2017, **64**, 2804–2811.
- 11 Y.-H. Peng, H. H. Cheng, V. I. Mashanov and G.-E. Chang, *Appl. Phys. Lett.*, 2014, **105**, 231109.
- 12 J. Werner, M. Oehme, M. Schmid, M. Kaschel, A. Schirmer, E. Kasper and J. Schulze,

- Appl. Phys. Lett.*, 2011, **98**, 1–3.
- 13 S. Al-Kabi, S. A. Ghetmiri, J. Margetis, W. Du, A. Mosleh, M. Alher, W. Dou, J. M. Grant, G. Sun, R. A. Soref, J. Tolle, B. Li, M. Mortazavi, H. A. Naseem and S. Q. Yu, *J. Electron. Mater.*, 2016, **45**, 2133–2141.
  - 14 S. A. Ghetmiri, W. Du, J. Margetis, A. Mosleh, L. Cousar, B. R. Conley, A. Nazzal, G. Sun, R. a Soref, J. Tolle, B. Li, H. a Naseem, S. A. Ghetmiri, W. Du, J. Margetis, A. Mosleh, L. Cousar, J. Tolle, B. Li, H. a Naseem and S. Yu, , DOI:10.1063/1.4898597.
  - 15 S. Zaima, O. Nakatsuka, T. Asano, T. Yamaha, S. Ike, A. Suzuki, K. Takahashi, Y. Nagae, M. Kurosawa, W. Takeuchi, Y. Shimura and M. Sakashita, *2016 IEEE Photonics Soc. Summer Top. Meet. Ser. SUM 2016*, 2016, **16**, 37–38.
  - 16 S. Su, B. Cheng, C. Xue, W. Wang, Q. Cao, H. Xue, W. Hu, G. Zhang, Y. Zuo and Q. Wang, *Opt. Express*, 2011, **19**, 6400.
  - 17 I. S. Yu, T. H. Wu, K. Y. Wu, H. H. Cheng, V. I. Mashanov, A. I. Nikiforov, O. P. Pchelyakov and X. S. Wu, *AIP Adv.*, , DOI:10.1063/1.3656246.
  - 18 W. Wang, Q. Zhou, Y. Dong, E. S. Tok and Y.-C. Yeo, *Appl. Phys. Lett.*, 2015, **106**, 232106.
  - 19 M. Albani, S. Assali, M. A. Verheijen, S. Koelling, R. Bergamaschini, F. Pezzoli, E. P. A. M. Bakkers and L. Miglio, *Nanoscale*, 2018, **10**, 7250–7256.
  - 20 R. Ragan, C. C. Ahn and H. a. Atwater, *Appl. Phys. Lett.*, 2003, **82**, 3439–3441.
  - 21 M. S. Seifner, F. Biegger, A. Lugstein, J. Bernardi and S. Barth, *Chem. Mater.*, 2015, **27**, 6125–6130.
  - 22 P. C. H. L. Goodman, *IEE PROC.*, 1982, **129**, 189–192.

- 23 K. A. Mäder, A. Baldereschi and H. von Känel, *Solid State Commun.*, 1989, **69**, 1123–1126.
- 24 S. Oguz, W. Paul, T. F. Deutsch, B. Y. Tsaur and D. V. Murphy, *Appl. Phys. Lett.*, 1983, **43**, 848–850.
- 25 S. I. Shah, J. E. Greene, L. L. Abels, Q. Yao and P. M. Raccah, *J. Cryst. Growth*, 1987, **83**, 3–10.
- 26 M. R. Bauer, J. Tolle, C. Bungay, A. V. G. Chizmeshya, D. J. Smith, J. Menéndez and J. Kouvetakis, *Solid State Commun.*, 2003, **127**, 355–359.
- 27 M. Bauer, J. Taraci, J. Tolle, A. V. G. Chizmeshya, S. Zollner, D. J. Smith, J. Menendez, C. Hu and J. Kouvetakis, *Appl. Phys. Lett.*, 2002, **81**, 2992–2994.
- 28 S. Gupta, B. Magyari-Köpe, Y. Nishi and K. C. Saraswat, *J. Appl. Phys.*, 2013, **113**, 0–7.
- 29 R. A. Soref and L. Friedman, *Superlattices Microstruct.*, 1993, 14, 189–193.
- 30 N. Amrane, S. Ait Abderrahmane and H. Aourag, *Infrared Phys. Technol.*, 1995, **36**, 843–848.
- 31 W. J. Yin, X. G. Gong and S. H. Wei, *Phys. Rev. B - Condens. Matter Mater. Phys.*, 2008, **78**, 1–4.
- 32 D. S. Sukhdeo, D. Nam, J.-H. Kang, M. L. Brongersma and K. C. Saraswat, *Photonics Res.*, 2014, **2**, A8.
- 33 D. Saladukha, M. B. Clavel, F. Murphy-Armando, G. Greene-Diniz, M. Grüning, M. K. Hudait and T. J. Ochalski, *Phys. Rev. B*, 2018, **97**, 1–12.
- 34 M. Singh, M. Goyal and K. Devlal, *J. Taibah Univ. Sci.*, ,

DOI:10.1016/j.jtusci.2017.06.007.

- 35 B. Dutt, H. Lin, D. S. Sukhdeo, B. M. Vulovic, S. Gupta, D. Nam, K. C. Saraswat and J. S. Harris, *IEEE J. Sel. Top. Quantum Electron.*, , DOI:10.1109/JSTQE.2013.2241397.
- 36 M. P. Polak, P. Scharoch and R. Kudrawiec, *J. Phys. D. Appl. Phys.*, 2017, **50**, 195103.
- 37 P. Moontragoon, Z. Ikonić and P. Harrison, *Semicond. Sci. Technol.*, 2007, **22**, 742–748.
- 38 A. Zaoui, M. Ferhat, M. Certier, B. Khelifa and H. Aourag, *Infrared Phys. Technol.*, 1996, **37**, 483–488.
- 39 V. R. D’Costa, J. Tolle, J. Xie, J. Menéndez and J. Kouvetakis, *AIP Conf. Proc.*, 2009, **1199**, 57–58.
- 40 H. Wang, G. Han, Y. Liu, S. Hu, C. Zhang, J. Zhang and Y. Hao, *IEEE Trans. Electron Devices*, 2016, **63**, 303–310.
- 41 S. Sant and A. Schenk, *IEEE J. Electron Devices Soc.*, 2015, **3**, 164–175.
- 42 D. Haehnel, I. A. Fischer, A. Hornung and A. Koellner, 2014, **62**, 1–8.
- 43 B. Vincent, F. Gencarelli, H. Bender, C. Merckling, B. Douhard, D. H. Petersen, O. Hansen, H. H. Henrichsen, J. Meersschart, W. Vandervorst, M. Heyns, R. Loo and M. Caymax, *Appl. Phys. Lett.*, 2011, **99**, 2–5.
- 44 C. L. Senaratne, J. D. Gallagher, L. Jiang, T. Aoki, D. J. Smith, J. Menéndez and J. Kouvetakis, *J. Appl. Phys.*, 2014, **116**, 133509.
- 45 B. R. Conley, A. Mosleh, S. A. Ghetmiri, H. a Naseem, J. Tolle and S. Yu, *2013 IEEE 39th Photovolt. Spec. Conf.*, 2013, 1346–1349.

- 46 S. Kim, N. Bhargava, J. Gupta, M. Copping and J. Kolodzey, *Opt. Express*, 2014, **22**, 11029.
- 47 Y. Shimura, N. Tsutsui, O. Nakatsuka, A. Sakai and S. Zaima, *Thin Solid Films*, 2010, **518**, S2–S5.
- 48 H. Pérez Ladrón De Guevara, A. G. Rodríguez, H. Navarro-Contreras and M. A. Vidal, *Appl. Phys. Lett.*, 2003, **83**, 4942–4944.
- 49 R. R. Lieten, J. W. Seo, S. Decoster, A. Vantomme, S. Peters, K. C. Bustillo, E. E. Haller, M. Menghini and J. P. Locquet, *Appl. Phys. Lett.*, , DOI:10.1063/1.4790302.
- 50 M. Kim, W. Fan, J. H. Seo, N. Cho, S. C. Liu, D. Geng, Y. Liu, S. Gong, X. Wang, W. Zhou and Z. Ma, *Appl. Phys. Express*, , DOI:10.7567/APEX.8.061301.
- 51 H. Mahmodi, M. R. Hashim, M. Kim, W. Fan, J.-H. Seo, Z. Liu, J. Wen, X. Zhang, T. Maeda, W. Jevasuwan, H. Hattori, H. Z. Xi, B. Y. Man, C. S. Chen, R. Yoshimine, K. Toko, T. Suemasu, N. Chen, G. Lin, L. Zhang, C. Li, S. Chen, W. Huang, J. Xu and J. Wang, *Jpn. J. Appl. Phys.*
- 52 P. Kringhoj and R. G. Elliman, *Appl. Phys. Lett.*, 1994, **65**, 324–326.
- 53 A. Mosleh, S. A. Ghetmiri, B. R. Conley, M. Hawkridge, M. Benamara, A. Nazzal, J. Tolle, S.-Q. Yu and H. A. Naseem, *J. Electron. Mater.*, 2014, **43**, 938–946.
- 54 T. S. S. Wirths, D. Buca, A.T. Tiedemann, B. Holländer, P. Bernardy and and S. M. D. Grützmacher, *ECS Trans.*, 2012, **50**, 885–893.
- 55 S. Zollner, N. V. Edwards, E. Duda, J. Tolle, J. Taraci, M. R. McCartney, J. Menendez, G. Wolf, D. J. Smith and J. Kouvetakis, 2002, **1**, 8010.

- 56 M. R. Bauer, C. S. Cook, P. Aella, J. Tolle, J. Kouvetakis, P. a. Crozier, a. V. G. Chizmeshya, D. J. Smith and S. Zollner, *Appl. Phys. Lett.*, 2003, **83**, 3489–3491.
- 57 S. Su, W. Wang, B. Cheng, W. Hu, G. Zhang, C. Xue, Y. Zuo and Q. Wang, *Solid State Commun.*, 2011, **151**, 647–650.
- 58 S. Su, D. Zhang, C. Xue and B. Cheng, *Appl. Surf. Sci.*, 2015, **340**, 132–137.
- 59 Y. Zhou, W. Dou, W. Du, T. Pham, S. A. Ghetmiri, S. Al-Kabi, A. Mosleh, M. Alher, J. Margetis, J. Tolle, G. Sun, R. Soref, B. Li, M. Mortazavi, H. Naseem and S. Q. Yu, *J. Appl. Phys.*, 2016, **120**, 1–8.
- 60 D. Stange, S. Wirths, N. Von Den Driesch, G. Mussler, T. Stoica, Z. Ikonc, J. M. Hartmann, S. Mantl, D. Grützmacher and D. Buca, *ACS Photonics*, 2015, **2**, 1539–1545.
- 61 W. Wang, W. K. Loke, T. Yin, Z. Zhang, V. R. D’Costa, Y. Dong, G. Liang, J. Pan, Z. Shen, S. F. Yoon, E. S. Tok and Y.-C. Yeo, *J. Appl. Phys.*, 2016, **119**, 125303.
- 62 T. T. Tran, D. Pastor, H. H. Gandhi, L. A. Smillie, A. J. Akey, M. J. Aziz and J. S. Williams, *J. Appl. Phys.*, 2016, **119**, 0–8.
- 63 M. S. Seifner, S. Hernandez, J. Bernardi, A. Romano-Rodriguez and S. Barth, *Chem. Mater.*, 2017, **29**, 9802–9813.
- 64 S. Biswas, J. Doherty, D. Saladukha, Q. Ramasse, D. Majumdar, M. Upmanyu, A. Singha, T. Ochalski, M. A. Morris and J. D. Holmes, *Nat. Commun.*, , DOI:10.1038/ncomms11405.
- 65 J. Doherty, S. Biswas, D. Saladukha, Q. Ramasse, T. S. Bhattacharya, A. Singha, T. J. Ochalski and J. D. Holmes, *J. Mater. Chem. C*, 2018, 8738–8750.
- 66 A. C. Meng, C. S. Fenrich, M. R. Braun, J. P. McVittie, A. F. Marshall, J. S. Harris and P.

- C. McIntyre, *Nano Lett.*, 2016, **16**, 7521–7529.
- 67 S. Assali, A. Dijkstra, A. Li, S. Koelling, M. A. Verheijen, L. Gagliano, N. von den Driesch, D. Buca, P. M. Koenraad, J. E. M. Haverkort and E. P. A. M. Bakkers, *Nano Lett.*, 2017, **17**, 1538–1544.
- 68 X. Gong, G. Han, S. Su, R. Cheng, P. Guo, F. Bai, Y. Yang, Q. Zhou, B. Liu and K. H. Goh, *2013 Symp. VLSI Circuits*, 2013, 34–35.
- 69 M. Noroozi, B. Hamawandi, M. S. Toprak and H. H. Radamson, *ULIS 2014 - 2014 15th Int. Conf. Ultim. Integr. Silicon*, 2014, 125–128.
- 70 C. K. Shang, V. Wang, R. Chen, S. Gupta, Y. C. Huang, J. J. Pao, Y. Huo, E. Sanchez, Y. Kim, T. I. Kamins and J. S. Harris, *Appl. Phys. Lett.*, , DOI:10.1063/1.4941800.
- 71 S. Gupta, R. Chen, Y. C. Huang, Y. Kim, E. Sanchez, J. S. Harris and K. C. Saraswat, *Nano Lett.*, 2013, **13**, 3783–3790.
- 72 R. J. A. Esteves, M. Q. Ho and I. U. Arachchige, *Chem. Mater.*, 2015, **27**, 1559–1568.
- 73 K. Ramasamy, P. G. Kotula, A. F. Fidler, M. T. Brumbach, J. M. Pietryga and S. A. Ivanov, *Chem. Mater.*, 2015, **27**, 4640–4649.
- 74 Y. J. Cho, C. H. Kim, H. S. Im, Y. Myung, H. S. Kim, S. H. Back, Y. R. Lim, C. S. Jung, D. M. Jang, J. Park, S. H. Lim, E. H. Cha, K. Y. Bae, M. S. Song and W. Il Cho, *Phys. Chem. Chem. Phys.*, 2013, **15**, 11691–11695.
- 75 A. Di Bartolomeo, M. Passacantando, G. Niu, V. Schlykow, G. Lupina, F. Giubileo and T. Schroeder, *Nanotechnology*, , DOI:10.1088/0957-4484/27/48/485707.
- 76 J. Bauer, Y. Yamamoto, P. Zaumseil, O. Fursenko, K. Schulz, G. Kozłowski, M. A.

- Schubert, T. Schroeder and B. Tillack, *Microelectron. Eng.*, 2012, **97**, 169–172.
- 77 R. Ranjan and M. K. Das, *Opt. Quantum Electron.*, 2016, **48**, 1–11.
- 78 P. Zaumseil, O. Nakatsuka, S. Zaima and T. Schroeder, *Mater. Sci. Semicond. Process.*, 2017, **57**, 48–53.
- 79 R. Roucka, S.-Q. Yu, J. Tolle, Y.-Y. Fang, S.-N. Wu, J. Menendez and J. Kouvetakis, *LEOS 2007 - IEEE Lasers Electro-Optics Soc. Annu. Meet. Conf. Proc.*, 2007, 178–179.
- 80 D. Stange, S. Wirths, N. Von Den Driesch, G. Mussler, T. Stoica, Z. Ikonc, J. M. Hartmann, S. Mantl, D. Grützmacher and D. Buca, *ACS Photonics*, 2015, **2**, 1539–1545.
- 81 B. Schwartz, M. Oehme, K. Kosteck, D. Widmann, M. Gollhofer, R. Koerner, S. Bechler, I. a Fischer, T. Wendav, E. Kasper, J. Schulze and M. Kittler, *Opt. Lett.*, 2015, **40**, 3209–3212.
- 82 E. Kasper and M. Oehme, *Jpn. J. Appl. Phys.*, 2015, **54**, 1–5.
- 83 D. Saladukha, J. Doherty, S. Biswas, T. J. Ochalski and J. D. Holmes, *Silicon Photonics Xii*, 2017, **10108**, 101081C.
- 84 S. Biswas, J. Doherty, D. Saladukha, Q. Ramasse, D. Majumdar, M. Upmanyu, A. Singha, T. Ochalski, M. A. Morris and J. D. Holmes, *Nat. Commun.*, 2016, **7**, 11405.
- 85 F. Pezzoli, A. Giorgioni, D. Patchett and M. Myronov, *ACS Photonics*, 2016, **3**, 2004–2009.
- 86 M. Y. Ryu, T. R. Harris, Y. K. Yeo, R. T. Beeler and J. Kouvetakis, *Appl. Phys. Lett.*, 2013, **102**, 1–5.
- 87 R. R. Lieten, C. Fleischmann, S. Peters, N. M. Santos, L. M. Amorim, Y. Shimura, N.



- Uchida, T. Maeda, S. Nikitenko, T. Conard, J.-P. Locquet, K. Temst and a. Vantomme, *ECS J. Solid State Sci. Technol.*, 2014, **3**, P403–P408.
- 88 J. Hart, T. Adam, Y. Kim, Y. C. Huang, A. Reznicek, R. Hazbun, J. Gupta and J. Kolodzey, *J. Appl. Phys.*, , DOI:10.1063/1.4942851.
- 89 J. Tauc, *Mat. Res. Bull.*, 1968, **3**, 37–46.
- 90 K. Takahashi, M. Kurosawa, H. Ikenoue, M. Sakashita, O. Nakatsuka and S. Zaima, .
- 91 L. Wang, S. Su, W. Wang, X. Gong, Y. Yang, P. Guo, G. Zhang, C. Xue, B. Cheng, G. Han and Y. C. Yeo, *Solid. State. Electron.*, 2013, **83**, 66–70.
- 92 D. Lei, W. Wang, Z. Zhang, J. Pan, X. Gong, G. Liang, E. S. Tok and Y. C. Yeo, *J. Appl. Phys.*, 2016, **119**, 0–9.
- 93 Y. C. Fang, K. Y. Chen, C. H. Hsieh, C. C. Su and Y. H. Wu, *ACS Appl. Mater. Interfaces*, 2015, **7**, 26374–26380.
- 94 D. Lei, K. H. Lee, S. Bao, W. Wang, S. Masudy-panah, S. Yadav, A. Kumar, Y. Dong, Y. Kang, S. Xu, Y. Wu, Y. Huang, H. Chung, S. S. Chu, S. Kuppurao, C. S. Tan, X. Gong and Y. Yeo, 2017, 198–199.
- 95 Y.-C. Lei, D., Lee, K.H., Bao, S., Wang, W., Masudy-Panah, S., Yadav, S., Kumar, A., Dong, Y., Kang, Y., Xu, S., Wu, Y., Huang, Y.-C., Chung, H., Chu, S.S., Kuppurao, S., Tan, C.S., Gong, X., Yeo, *IEEE Trans. Electron Devices*, 2018, 1–8.
- 96 D. Wirths, S., Troitsch, R., Mussler, G., Zaumseil, P., Hartmann, J.M., Schroeder, T., Mantl, S., Buca, *Trans. E C S Soc. Electrochem.*, 2014, **64**, 107–112.
- 97 Z. Liu, J. Wen, X. Zhang, C. Li, C. Xue, Y. Zuo, B. Cheng and Q. Wang, *J. Phys. D. Appl.*

- Phys.*, 2015, **48**, 1–6.
- 98 G. Han, Y. Wang, Y. Liu, C. Zhang, Q. Feng, M. Liu, S. Zhao, B. Cheng, J. Zhang and Y. Hao, *IEEE Electron Device Lett.*, 2016, **37**, 701–704.
  - 99 H. Cong, F. Yang, C. Xue, K. Yu, L. Zhou, N. Wang, B. Cheng and Q. Wang, *Small*, 2018, **14**, 1704414.
  - 100 Y. S. Huang, F. L. Lu, Y. J. Tsou, H. Y. Ye, S. Y. Lin, W. H. Huang and C. W. Liu, *IEEE Electron Device Lett.*, 2018, **39**, 1274–1277.
  - 101 J. Zheng, S. Wang, Z. Liu, H. Cong, C. Xue, C. Li, Y. Zuo, B. Cheng and Q. Wang, *Appl. Phys. Lett.*, 2016, **108**, 1–5.
  - 102 S. J. Su, C. L. Xue, B. W. Cheng, W. Wang, G. Z. Zhang, Y. H. Zuo and Q. M. Wang, *IEEE Int. Conf. Gr. IV Photonics GFP*, 2011, 33–35.
  - 103 D. Zhang, C. Xue, B. Cheng, S. Su, Z. Liu, X. Zhang, G. Zhang, C. Li and Q. Wang, *Appl. Phys. Lett.*, 2013, **102**, 98–102.
  - 104 T. Pham, W. Du, H. Tran, J. Margetis, J. Tolle, G. Sun, R. A. Soref, H. A. Naseem, B. Li and S.-Q. Yu, *Opt. Express*, 2016, **24**, 4519.
  - 105 H. Cong, C. Xue, J. Zheng, F. Yang, K. Yu, Z. Liu, X. Zhang, B. Cheng and Q. Wang, *IEEE Photonics J.*, , DOI:10.1109/JPHOT.2016.2607687.
  - 106 S. Xu, Y.-C. Huang, K. Hong Lee, W. Wang, Y. Dong, D. Lei, S. Masudy-Panah, C. S. Tan, X. Gong and Y.-C. Yeo, *Opt. Express*, 2018, **26**, 17312–17320.
  - 107 S. Gupta, R. Chen, B. Vincent, D. Lin, B. Magyari-Kope, M. Caymax, J. Dekoster, J. S. Harris, Y. Nishi and K. C. Saraswat, *ECS Trans.*, 2013, **50**, 937–941.

- 108 Y. Yang, K. Lu Low, W. Wang, P. Guo, L. Wang, G. Han and Y. C. Yeo, *J. Appl. Phys.*, , DOI:10.1063/1.4805051.
- 109 J. Zhou, G. Han, J. Li, Y. Liu, Y. Peng, J. Zhang, Q. Q. Sun, D. W. Zhang and Y. Hao, *IEEE Electron Device Lett.*, 2018, **39**, 622–625.
- 110 J. Zhou, G. Han, Y. Peng, Y. Liu, J. Zhang, Q. Q. Sun, D. W. Zhang and Y. Hao, *IEEE Electron Device Lett.*, 2017, **38**, 1157–1160.
- 111 J. Zhou, Y. Peng, G. Han, Q. Li, Y. Liu, J. Zhang, M. Liao, Q. Q. Sun, D. W. Zhang, Y. Zhou and Y. Hao, *IEEE J. Electron Devices Soc.*, 2017, **6**, 41–48.
- 112 M. Liu, Y. Liu, H. Wang, Q. Zhang, C. Zhang, S. Hu, Y. Hao and G. Han, *IEEE Trans. Electron Devices*, 2015, **62**, 1262–1268.
- 113 W. Wang, D. Lei, Y. Huang, K. H. Lee, W. Loke, Y. Dong, S. Xu, C. S. Tan, H. Wang, S. Yoon, X. Gong and Y. Yeo, *Opt. Express*, 2018, **26**, 10305.
- 114 D. Buca, C. Schulte-Braucks, N. Von Den Driesch, A. T. Tiedemann, U. Breuer, J. M. Hartmann, P. Zaumseil, S. Mantl and Q. T. Zhao, *2018 18th Int. Work. Junction Technol. IWJT 2018*, 2018, **2018–Janua**, 1.
- 115 A. Quintero, P. Gergaud, J. Aubin, J. M. Hartmann, N. Chevalier, J. P. Barnes, V. Loup, V. Reboud, F. Nemouchi and P. Rodriguez, *J. Appl. Phys.*, 2018, **124**, 0–10.
- 116 S. Prucnal, Y. Berencén, M. Wang, L. Rebohle, R. Böttger, I. A. Fischer, L. Augel, M. Oehme, J. Schulze, M. Voelskow, M. Helm, W. Skorupa and S. Zhou, *Semicond. Sci. Technol.*, , DOI:10.1088/1361-6641/aabe05.
- 117 S. Gupta, X. Gong, R. Zhang, Y. C. Yeo, S. Takagi and K. C. Saraswat, *MRS Bull.*, 2014,

- 39**, 678–686.
- 118 J. Werner, M. Oehme, A. Schirmer, E. Kasper and J. Schulze, *Thin Solid Films*, 2012, **520**, 3361–3364.
  - 119 M. Oehme, M. Schmid, M. Kaschel, M. Gollhofer, D. Widmann, E. Kasper and J. Schulze, *Appl. Phys. Lett.*, , DOI:10.1063/1.4757124.
  - 120 J. Mathews, R. Roucka, J. Xie, S. Q. Yu, J. Meéndez and J. Kouvetakis, *Appl. Phys. Lett.*, 2009, **95**, 1–4.
  - 121 G. E. Chang, R. Basu, B. Mukhopadhyay and P. K. Basu, *IEEE J. Sel. Top. Quantum Electron.*, , DOI:10.1109/JSTQE.2016.2553447.
  - 122 K. P. Homewood and M. A. Lourenço, *Nat. Photonics*, 2015, **9**, 78–79.
  - 123 D. Stange, S. Wirths, R. Geiger, C. Schulte-Braucks, B. Marzban, N. V. Den Driesch, G. Mussler, T. Zabel, T. Stoica, J. M. Hartmann, S. Mantl, Z. Ikonik, D. Grützmacher, H. Sigg, J. Witzens and D. Buca, *ACS Photonics*, 2016, **3**, 1279–1285.
  - 124 N. von den Driesch, D. Stange, D. Rainko, I. Povstugar, P. Zaumseil, G. Capellini, T. Schröder, T. Denneulin, Z. Ikonik, J. M. Hartmann, H. Sigg, S. Mantl, D. Grützmacher and D. Buca, *Adv. Sci.*, 2018, **5**, 1–7.
  - 125 M. G. Kim and J. Cho, *J. Electrochem. Soc.*, 2009, **156**, A277.
  - 126 M. I. Bodnarchuk, K. V. Kravchyk, F. Krumeich, S. Wang and M. V. Kovalenko, *ACS Nano*, 2014, **8**, 2360–2368.

## Chapter 2

### Non-equilibrium Induction of Tin in Germanium: Towards Direct Bandgap Ge<sub>1-x</sub>Sn<sub>x</sub> Nanowires

This chapter has been published as a peer-reviewed article in Nature Communications. Consequently, sections of the chapter such as the abstract and introduction may contain repeating concepts and paragraphs. My contribution to the paper concerned the growth and elemental characterisation of the nanowires. I also analysed the photoluminescence and electron energy loss spectra.

Biswas, S.; Doherty, J.; Saladukha, D.; Ramasse, Q.; Majumdar, D.; Upmanyu, M; Singha, A.; Ochalski, T. J.; Morris, M. A.; Holmes, J. D. Non-equilibrium Induction of Tin in Germanium: Towards Direct Bandgap Ge<sub>1-x</sub>Sn<sub>x</sub> Nanowires *Nature Comm.*, **2016**, 7, 11405.

## **2. Non-equilibrium Induction of Tin in Germanium: Towards Direct Bandgap $\text{Ge}_{1-x}\text{Sn}_x$ Nanowires**

---

### **2.1. Abstract**

The development of non-equilibrium group IV nanoscale alloy is critical to achieving new functionalities, such as the formation of a direct bandgap in a conventional indirect bandgap elemental semiconductor. Here, we describe the fabrication of uniform diameter, direct bandgap  $\text{Ge}_{1-x}\text{Sn}_x$  alloy nanowires, with a Sn incorporation up to 9.2 at. %, far in excess of the equilibrium solubility of Sn in bulk Ge, through a conventional catalytic bottom-up growth paradigm employing noble metal and metal alloy catalysts. Metal alloy catalysts permitted a greater inclusion of Sn in Ge nanowires compared to conventional Au catalysts, when employed during vapour-liquid-solid growth. The addition of an annealing step close to the Ge-Sn eutectic temperature (230 °C) during cool-down further facilitated the excessive dissolution of Sn in the nanowires. Sn was distributed throughout the Ge nanowire lattice with no metallic Sn segregation or precipitation at the surface or within the bulk of the nanowires. The non-equilibrium incorporation of Sn into the Ge nanowires can be understood in terms of a kinetic trapping model for impurity incorporation at the triple-phase boundary during growth.

## 2.2. Introduction

Direct bandgap semiconductor materials are needed for new device architectures such as band-to-band tunnelling (BTBT) tunnel FETs (TFET)<sup>1</sup>, optical interconnects<sup>2</sup> and for the development of group IV photonics<sup>3, 4</sup> because these technological modules are based on the direct transition of carriers between energy bands. However, a major problem arises with bulk Si and Ge in photonics, optoelectronics and TFET devices as they are indirect bandgap semiconductors, that is the lowest-energy transition from the valence to the conduction band involves a change in crystal momentum.<sup>5</sup> Although highly-doped, tensile strained Ge results in enhanced direct gap light emission, due to raising of the Fermi level, the doping levels and induced strain required are not practical for many post-CMOS devices. III-V compound semiconductors, for example InP, GaAs, InAs *etc.*, offer a solution for integrating direct bandgap materials as on-chip photonic and electronic components. However, the monolithic integration of direct bandgap group IV semiconductor materials is expected to lead to lower production costs and higher reliability than hybrid III-V-on-Si approaches.<sup>6</sup> Sn-based group IV alloys are predicted to be tunable direct gap semiconductor materials.<sup>7</sup> Apart from the direct transition of carriers, group IV alloy systems have also been predicted to exhibit high electron and hole mobilities and low carrier effective masses, making them ideal material platforms for co-integration of optoelectronic and high speed electronic devices.<sup>7</sup>

Considering group IV elements, on moving from Si to Ge to Sn, the conduction band at  $k = 0$  drops in energy until, in grey tin, the material acquires a direct (and vanishing) bandgap at  $k = 0$ .<sup>5</sup> A direct band system from group IV elements is likely to require the presence of Sn.<sup>8, 9</sup> Especially for Ge, the small energy separation of 140 meV between the indirect (L) and direct ( $\Gamma$ ) conduction

band valleys can be overcome by alloying with Sn. Theoretical modelling<sup>10</sup> as well as photoluminescence experimental studies<sup>11</sup> have found unstrained  $\text{Ge}_{1-x}\text{Sn}_x$  to transition to a direct bandgap material at an alloy composition of no less than 6.5 at. % Sn, although some contradiction regarding this value exists,<sup>6,12,13</sup> with the range of Sn incorporation to obtain a direct band transition predicted to be between 6.5-10 at. %. However, fundamental challenges (low solubility, metallic Sn segregation, lattice mismatch *etc.*) restrict the growth of Sn-based Si and Ge alloys with a high Sn content ( $> 8$  at. %) in any nanoform, *e.g.* thin film, nanowire *etc.*<sup>14-15</sup>

In recent years, considerable effort has been employed to grow  $\text{Ge}_{1-x}\text{Sn}_x$  films on Si substrates, where the lattice mismatch with Si is fully relieved by periodic misfit dislocations at the interface with no dislocations into the films.<sup>16</sup> Recent advances in chemical *vapour* deposition (CVD) techniques have made it possible to grow binary  $\text{Ge}_{1-x}\text{Sn}_x$  and ternary  $\text{Si}_x\text{Ge}_y\text{Sn}_{1-x-y}$  group IV thin film semiconductor alloys using low temperature epitaxy.<sup>17-19</sup> However, minimal effort has been applied to fabricate group IV direct bandgap materials in one-dimensional (1-D) nanoform to keep track with the miniaturisation of Si-based nanoelectronics and to take advantage of their 1-D geometry for new age field-effect transistor (FET) devices (finFET, gate-all-around (GAA) FET *etc.*). Top-down processing to fabricate good quality (single crystalline, straight, uniform diameter nanowire with no Sn segregation)  $\text{Ge}_{1-x}\text{Sn}_x$  nanowires is limited due to under-developed surface and etch chemistries, although encouraging results (with  $\sim 8$  at. % Sn incorporation) were recently reported on the fabrication of suspended  $\text{Ge}_{1-x}\text{Sn}_x$  nanowires through competitive etching between  $\text{Ge}_{1-x}\text{Sn}_x$  and Ge layers.<sup>20,21</sup> Using bottom-up growth paradigms, Ge and  $\text{Ge}_{1-x}\text{Sn}_x$  nanowires were synthesized by utilising low melting point Sn metal catalysts, but these techniques produced



nanowires either with insufficient Sn incorporation<sup>22</sup> or low quality (bending and kinking) crystals with non-significant luminescence.<sup>23</sup>

Based on thermodynamic limitations, a non-equilibrium growth scenario influenced by the kinetics of the system is required to incorporate a sufficient amount, far from equilibrium, of Sn into a one-dimensional Ge lattice to achieve a direct bandgap transition. The triple-phase boundary at the catalyst-nanowire interface in a bottom-up growth process is known to be a feasible pathway for impurity incorporation in a one-dimensional lattice and can act as a localized non-equilibrium centre for excessive impurity dissolution.<sup>24, 25</sup> A kinetics dependent framework was predicted to be responsible for the extraordinary incorporation of impurity adatoms from the catalyst tip.

Here, we report the application of a three phase bottom-up growth protocol to fabricate highly crystalline, uniform diameter, direct bandgap  $\text{Ge}_{1-x}\text{Sn}_x$  nanowires with considerable ( $x > 0.09$ ) Sn incorporation; around 10 times the equilibrium solubility. Third-party metal catalysts (Au or AuAg alloy) were used to guide the non-equilibrium incorporation of Sn adatoms into the precipitated Ge bi-layers, where the impurity Sn atoms become trapped with the deposition of successive layers, thus giving an extraordinary Sn content in the alloy nanowires.

## 2.3. Experimental

### 2.3.1. Method

Continuous-flow reactions for nanowire growth were carried out in a toluene medium using a liquid-injection chemical vapour deposition (LICVD) technique. Metal nanoparticles were spin-coated onto a Si (001) substrate and loaded into a stainless steel micro reactor cell, connected to metal tubing (For a schematic representation of the set-up, see Figure 2.3.1.1.). The catalyst nanoparticle concentration in each case was fixed at  $40 \mu\text{mole cm}^{-3}$ . The density and distribution of these nanoparticles was not studied pre-growth as the reaction temperature is far above the melting point of these nanoparticles. Solutions of (DPG) and allyltributylstannane (ATBS) in anhydrous toluene were prepared in an  $\text{N}_2$  glove box with a typical Ge precursor concentration of  $10 \mu\text{mole ml}^{-1}$  and varying Sn concentrations. The concentration of DPG in toluene was fixed at  $10 \mu\text{mol ml}^{-1}$  whereas tin precursor concentrations were varied from  $1\text{--}2 \mu\text{mol ml}^{-1}$  for the incorporation of different amounts of Sn in the  $\text{Ge}_{1-x}\text{Sn}_x$  nanowires. A precursor solution was loaded into a Hamilton sample-lock syringe inside a nitrogen-filled glovebox. Prior to injection, the coated Si substrate was annealed for 15 min at  $440^\circ\text{C}$  under a flowing  $\text{H}_2/\text{Ar}$  atmosphere inside a tube furnace to bring the substrate to growth temperature under inert atmosphere. The precursor solution was then injected into the metal reaction cell using a high pressure syringe pump at a rate of  $0.025 \text{ ml min}^{-1}$ . A  $\text{H}_2/\text{Ar}$  flow rate of  $0.5 \text{ ml min}^{-1}$  was maintained during the entire growth period. A typical nanowire growth time was 2 hr. An additional annealing step was also introduced during the cool down process where the substrate was kept at  $230^\circ\text{C}$  for 2 hr under a  $\text{H}_2/\text{Ar}$  flowing atmosphere. The reaction cell was allowed to cool to room temperature and

disassembled to access the growth substrate. Nanowires were washed with dry toluene and dried under N<sub>2</sub> flow for further characterisation.

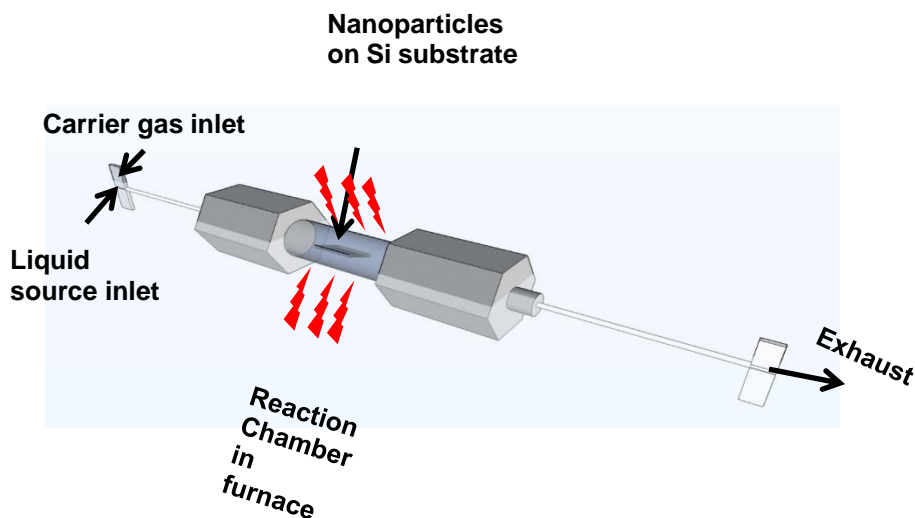


**Figure 2.3.1.1.:** Schematic of stainless steel reaction vessel, used in all reactions.

### 2.3.2. Characterisation

Bottom-up grown Ge<sub>1-x</sub>Sn<sub>x</sub> nanowires were imaged on an FEI Helios NanoLab 600i scanning electron microscope (SEM). All energy dispersive X-ray (EDX) measurements were recorded in high angle annular dark-field (HAADF) mode in the FEI Helios NanoLab 600i operating at 20 kV and 1.4 nA with an attached Oxford X-Max 80 detector. Error in the EDX measurements indicates standard deviation in EDX measurements measured over 50 nanowires. Transmission electron microscopy (TEM) analysis was done in a JEOL JEM-2100 operating at 200 kV in bright field condition for imaging. High resolution Scanning TEM imaging and electron energy loss spectroscopy (EELS) mapping was done using Nion UltraSTEM100 microscope, operated at 100 kV. Probe-forming optics were adjusted to deliver a 0.9 Å probe, with 120 pA beam current and

31 mrad convergence semi-angle. EELS data was acquired on a Gatan Enfina spectrometer, at 1 eV per channel to capture both the Sn and Ge edges simultaneously. As a result, the effective energy resolution was limited to 2.5 eV by the detector point spread function (approx. 3 pixels), even though the cold field emission gun of the instrument had a native energy width of 0.35 eV in the operating conditions. Raman scattering measurements were performed in a backscattering geometry using a micro-Raman setup consisting of a spectrometer (model LabRAM HR, Jobin Yvon) and a Peltier-cooled charge-coupled device (CCD) detector. An air cooled He-Ne laser of wavelength 633 nm was used as an excitation source. The PL measurements were performed using a confocal configuration. Samples were cooled to 7 K using a Helium cryostat. Low temperature PL is preferred due to the minimisation of thermal activation of carriers to non-radiative recombination centres. A pulsed titanium-sapphire 800 nm laser was used as an excitation source. Laser frequency was 76 MHz and pulse width was 300 fs. The laser beam was focused down to a 50  $\mu\text{m}$  spot and the power was measured to be 500 mW. For temperature and power dependent experiments, the structures were encased in a liquid He and liquid nitrogen cryostat respectively equipped with KBr window and cooled to desired temperature. The PL emission was collected by a monochromator and then sent to a thermoelectrically cooled, photoconductive, extended-range InGaAs detector, sensitive in the mid-IR spectral range from 1.2 to 2.6  $\mu\text{m}$  and facilitated by CaF<sub>2</sub> optical components. Lock-in and chopper was used as a standard noise-cancellation tool.

## 2.4. Results

**Growth of group IV alloy nanowires.** Participation of Au and AuAg alloy seeds in the bottom-up growth of Ge nanowires has been well documented by our group in previous reports.<sup>26-28</sup> Similarly, for the growth of  $\text{Ge}_{1-x}\text{Sn}_x$  nanowires, we have used dodecanethiol-stabilized phase pure Au and  $\text{Au}_{0.90}\text{Ag}_{0.10}$  alloy nanoparticles.<sup>29</sup> These small colloidal alloy nanoparticles were deposited onto silicon (001) substrates (with native oxide) and dried at 180 °C under vacuum, leading to the desorption of the surfactant molecules from the surface of the particles.<sup>30</sup> A liquid injection chemical vapour deposition (LICVD) technique, using toluene as the solvent phase, was adopted for growing the  $\text{Ge}_{1-x}\text{Sn}_x$  nanowires at 440 °C on the surface of Si(001) substrates. Diphenylgermane (DPG) was used as the Ge source whereas allyltributylstannane (ATBS) was used as the tin precursor. Similar decomposition kinetics and solubility of the tin and germanium precursors provoked the choice of DPG and ATBS, where the Sn precursor has a slightly higher boiling point (360 °C at atm. pressure) than the Ge precursor (325 °C at atm. pressure). The choice of Au and AuAg catalysts and the growth temperature was driven by the Au-Ge and Au-Ag-Ge phase diagrams,<sup>30</sup> where a faster growth rate of Ge nanowires is expected using AuAg catalysts.<sup>27</sup> A faster Ge growth rate provides the opportunity to incorporate more Sn into the Ge lattice, as per the solute trapping relationship in which impurity incorporation is dependent on the growth velocity of the nanowire, with less chance of segregating on the surface or within the bulk.<sup>31</sup> At our growth temperature (440 °C) Au-Sn or Ag-Sn phase diagrams predict the formation of eutectic liquid alloys (Au-Sn-Ge or AuAg-Sn-Ge) with enormous Sn intakes in the catalyst, without any window for the precipitation of Sn layers.<sup>32</sup>

Both Au and AuAg nanoparticles successfully catalysed the growth of Ge nanowires after a 2 hr time period, as determined by scanning electron microscopy (SEM), see Figures 2.1(a) and (b). The absence (or very little amount) of particulate deposits, as a byproduct, on the nanowire surfaces and within the samples in general verifies the controlled growth of the nanowires. The grown nanowires were straight without any observed kinks, bends or curling. A Ge and Sn precursor mixture containing 15 at. % Sn was used as the injection solution for the growth of the nanowires shown in Figures 2.1(a) and (b). The lengths of the nanowires grown from both Au and

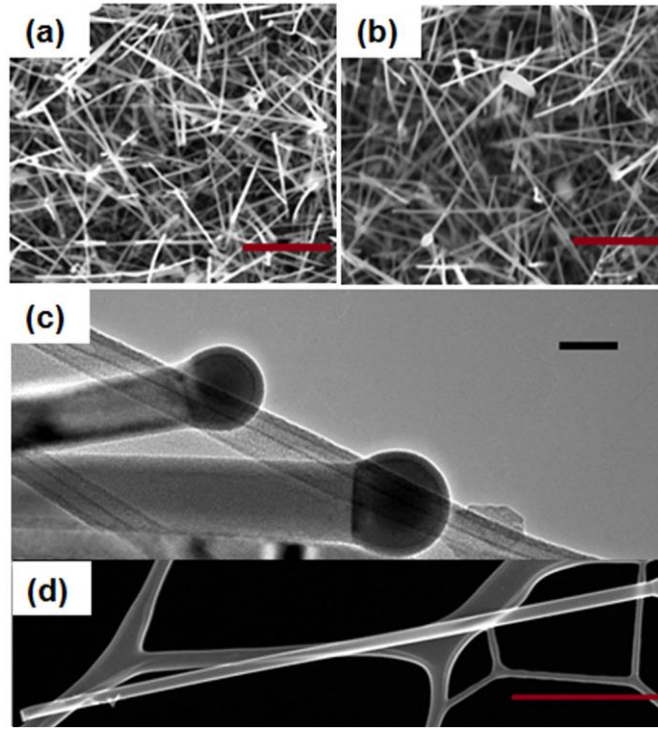


**Figure 2.1: Morphological examination of alloy nanowires with SEM.** SEM images of catalyzed  $\text{Ge}_{1-x}\text{Sn}_x$  nanowires grown using 15 at. % of Sn containing solution with: (a) Au (b)  $\text{Au}_{0.90}\text{Ag}_{0.10}$  catalysts (scale bar denotes 1  $\mu\text{m}$ ). TEM image in (c) confirms the participation of VLS growth mechanism with dark-contrast spherical seed at the tip of the nanowire with AuAg catalysts from precursor solution containing 15 at. % Sn. Scale bar, 100 nm. HAADF STEM image in part (d) confirms uniform nanowire diameter along the length with negligible tapering. Scale bar, 1  $\mu\text{m}$ .

AuAg seeds were in the order of 1-3  $\mu\text{m}$ , whereas their diameters were between 30-70 nm; with a mean diameter of 45.3 and 38.5 nm for Au and AuAg-seeded nanowires respectively. The bright-field transmission electron microscopy (TEM) image in Figure 2.1(c) confirms the participation of catalytic vapour-liquid-solid (VLS) nanowire growth, as the dark-contrasted partially spherical metal seed can be seen at the tip of the nanowire in the image. A thin amorphous shell can also be observed on top of the nanoparticle seed, but the nanowire diameter is determined by the dimension of the metal seed at the tip. A flat interface was observed after growth between the nanoparticle seed and nanowire, without any lateral side facets at the tri-junction. The nanowires were fairly straight, with no or very little indication of tapering from the seed to the end of the nanowire as shown in the dark-field scanning transmission electron microscopy (STEM) image in Figure 2.1(d). Metal seeds at the nanowire tips were pinned at the interface, where the contact angle between the interface and the edge of the seed was larger than in the growth of Ge nanowires with Au or AuAg seeds,<sup>27, 28</sup> due to the relatively low surface energy of Sn-rich metal catalyst seeds. Participation of different growth regimes with foreign Au and AuAg metal catalysts was confirmed by the fact that nanowires synthesised without any noble metal seeds, that is self-seeded growth from Sn seeds, resulted in the formation of very short nanowires (200-300 nm in length), with prominent tapering from the seed-nanowire interface to the very end of the nanowire (2.8. Appendix Figure A2.1).

**Elemental analysis of alloy nanowires through EDX.** As the primary objective of this work was to fabricate direct bandgap  $\text{Ge}_{1-x}\text{Sn}_x$  nanowires with a high Sn content, it is essential to explore the quantitative and qualitative incorporation of Sn in the nanowire body. Energy dispersive x-ray (EDX) analysis and high resolution electron energy loss spectroscopy (EELS) provide the means

to investigate the chemical environment in the bulk of the alloy nanowire and also at the atomic scale. The composition of the nanowires and the distribution of elements within them were estimated through EDX point measurements and elemental mapping in STEM. For nanowires grown from pure Au catalysts, the amount of Sn in the injecting solution was varied from 10-20 at. %, resulting in a gradual increase in the actual Sn concentration in the nanowires. Very low amounts of Sn (mean concentration of 1.5 at. %) was determined in nanowires using an injecting solution of 10 at. % Sn. Increasing the Sn concentration in the injecting solution to 15 and 20 at. % resulted in the incorporation of Sn in the nanowires at levels of 6 and 9 at. % respectively. These values of Sn concentrations are much higher (almost 6 and 9 times) than the extrapolated bulk equilibrium solid solubility of Sn in Ge.<sup>31</sup> Although a higher assimilation of Sn in the Ge nanowires was achieved with an injection solution of 20 at. % Sn, this high Sn concentration also resulted in homogeneous nucleation of metallic Sn as spherical clusters (2.8. Appendix Figure A2.2). Hence, under our reaction conditions, an initial Sn concentration of 15 at. % was determined to be ideal to obtain  $\text{Ge}_{1-x}\text{Sn}_x$  nanowires with substantial Sn incorporation and with negligible secondary nucleation of unwanted spherical particulates in the sample. With the aim of including more Sn into the 1-D Ge lattice,  $\text{Au}_{0.90}\text{Ag}_{0.10}$  alloy nanoparticle catalysts were used as seeds rather than pure Au, as the alloy seeds have been previously shown to favour faster growth kinetics for phase pure Ge nanowire growth.<sup>27</sup> To avoid spherical metallic Sn clusters in the sample, injection solutions with 15 at. % of Sn were employed. A slight increase in the Sn incorporation in the Ge nanowires from 6.0 ( $\pm 0.5$ ) to 6.6 ( $\pm 0.6$ ) at. % (error bars are defined in Method section) was observed when using AuAg alloy rather than pure Au seeds respectively. For an accurate estimation of the amount of Sn included in each nanowire sample, EDX point measurements were performed on 50 different nanowires and mean values computed. An example



of a point EDX measurement taken of a  $\text{Ge}_{1-x}\text{Sn}_x$  nanowire grown from AuAg seed is shown in Figure A2.3 of 2.8. Appendix. The distribution of Sn in the alloy nanowires grown with AuAg seeds was uniform along the length and width of the nanowires, without any segregation near the catalyst-nanowire interface or at the nanowire surfaces (2.8. Appendix Figure A2.3 and A2.4). Elemental EDX mapping from a AuAg seeded  $\text{Ge}_{1-x}\text{Sn}_x$  nanowire also confirmed uniform Sn distribution in the entire nanowire volume (2.8. Appendix Figure A2.5). The uniform axial and radial distribution of Sn and the minimal tapering of our nanowires also rules out the diffusion of Sn through the nanowire sidewalls as a possible incorporation mechanism. The strong incorporation and uniform distribution of Sn atoms confirms the continuous dissolution of Sn atoms throughout the growth process at the seed-nanowire growth interface.

To achieve a higher concentration of Sn in the  $\text{Ge}_{1-x}\text{Sn}_x$  nanowires, a step cooling method was utilized, where the initial injection of the solution at the growth temperature (440 °C) was followed by an annealing step for 2 hr at 230 °C during the cool down. Motivation to introduce a step cooling at 230 °C was driven by two reasons: a small window in the Sn rich side of the Au-Sn phase diagram at 230 °C and the bulk Ge-Sn eutectic temperature at around 230 °C. This step cooling technique further forces a colossal amount of Sn (an example is shown in Figure 2.2(a)), with an average concentration of 9.2 ( $\pm 0.8$ ) at. % (with a AuAg growth promoter and 15 at. % Sn injecting solution), into the nanowire while keeping the nanowire morphology intact (SEM image in 2.8. Appendix Figure A2.6). The extraordinary amount of Sn incorporation as measured *via* EDX analysis was also supported through x-ray diffraction (XRD) measurements (2.8. Appendix Figure A2.8.). The amount of Sn in the nanowires was calculated as 9.8% from Vegard's law which is an empirical law that relates the substitution of a guest ion into the host lattice with the

experimentally observed degree of lattice change (as per the relationship  $\alpha_{A_{1-x}B_x} = (1 - x)\alpha_A + x\alpha_B$  where  $\alpha$  is the lattice parameter of the pure constituent (A or B) and  $x$  is the molar fraction of B). A plot showing the mean Sn concentration in  $\text{Ge}_{1-x}\text{Sn}_x$  alloy nanowires as a function of different growth conditions can be seen in Figure 2.2(b). To confirm the homogeneity of Sn dissolution in the nanowire, that is to rule out the formation of Sn precipitates or cluster formations in the core or on the surfaces of the nanowires after step annealing, EDX elemental mapping was performed on  $\text{Ge}_{1-x}\text{Sn}_x$  nanowires with the highest Sn incorporation, *i.e.* a mean concentration of 9.2 at. %. Elemental mapping of a particular nanowire with a Sn concentration of 9.4 at. % is shown in Figure 2.2(c). The elemental maps show a homogeneous distribution of Sn in the core of the nanowires without any surface segregation or precipitation near the seed-nanowire interface after step annealing at 230 °C. A high density of Sn was observed at the spherical tips of the nanowires, as confirmed from EDX mapping in Figure 2.2(c) and the line scan in Figure 2.2(d), confirming the participation of a Sn rich alloy seed (Sn alloyed with Au or AuAg) in VLS nanowire growth. An elemental EDX linescan of Ge and Sn along the nanowire axis clearly demonstrated the homogeneity of Sn incorporation along the nanowire length even after the step annealing process, thus confirming the continuous dissolution of Sn throughout the nanowire length (part of Figure 2.2(d)). The uniformity of Sn dissolution in the alloy nanowires at the highest average Sn concentration was further confirmed through EDX point scans at different lengths along the nanowires (2.8. Appendix Figure A2.8). Even the radial Sn concentration detected by EDX demonstrates (2.8. Appendix Figure A2.9 shows the radial line profile for a nanowire selected from the sample with highest Sn content, that is with stepdown cooling) a flat profile (“U” shape profile indicates surface segregation), thus again indicating uniform distribution of Sn without any clustering of Sn near nanowire side facets.

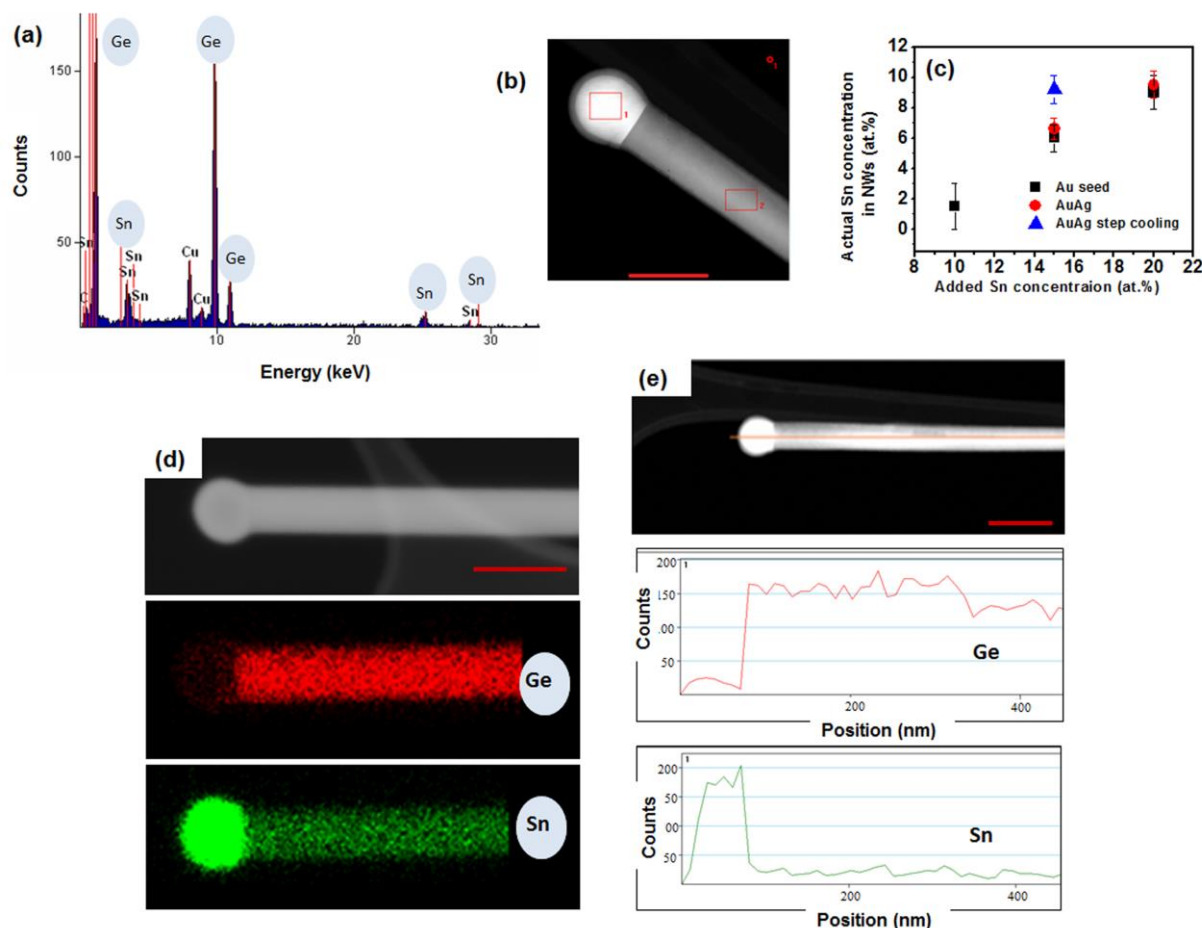


**Figure 2.2: EDX analysis of  $\text{Ge}_{1-x}\text{Sn}_x$  nanowires.** (a) EDX spectrum recorded from the body of an alloy nanowire (selected from the sample with 9.2 at. % average Sn incorporation) showing the presence of both Ge and Sn. This particular nanowire is shown in part (b). Scale bar, 50 nm. Variations in Sn concentration with different catalysts and growth conditions are demonstrated in the part (c). Error bar indicates standard deviation in EDX measurements measured over 50 nanowires. (d) Dark field HAADF image and EDX mapping for Ge and Sn in a  $\text{Ge}_{1-x}\text{Sn}_x$  nanowire with 9.4 at. % of Sn. HAADF image with the uniform distribution of Ge and Sn and Sn rich catalyst is confirmed from EDX mapping and also from HAADF image and EDX linescan in part (e). Red curve denotes linescan for Ge whereas green curve for Sn. Scale bar denotes 50 nm and 100 nm in part (d) and (e) respectively.

**Atomic resolution Sn mapping through EELS.** The uniform distribution of Sn atoms throughout the nanowires also suggests a single atomic pathway for Sn impurity incorporation. The local distribution of Sn in the nanowires is a fine criterion to determine impurity incorporation and diffusion modes in the nanowires. The possible formation of Sn precipitates in the nanowire bulk or near the nanowire surface suggests multiple impurity incorporation pathways where the impurities are diffused to the preferred lattice sites such as crystal defects. Also, the formation of local metallic Sn segments and Sn-Sn dimers could quench efficient emission from these materials due to the creation of dark trapping sites for charge carriers. To confirm the sparse distribution of Sn in the Ge lattice of the nanowires, we have probed the spatial arrangement of Sn through high resolution EELS, in a STEM. The spatial arrangement of dissolved Sn in a nanowire sample with the highest Sn incorporation (mean concentration of  $9.2 (\pm 0.8)$  at. %), as determined by EDX measurements were traced (error bars are defined in Method section). Two EELS maps were acquired at two vastly different heights along the wires, to make sure Sn was not only present at certain areas of each nanowire, such as close to the catalyst. Maps were de-noised by principal components analysis and the background was removed by fitting a power law over a region immediately in front of the core loss edges. The signal was then integrated over a 120 eV window above the onset of the Sn  $M_{4,5}$  and Ge  $L_{2,3}$  edges. HAADF images and the corresponding EELS chemical profile recorded from the rectangular box region are depicted in Figures 2.3(a) and (b). The HAADF survey image in Figure 2.3(a) was acquired from the bulk of the nanowire to avoid strongly oxidized edges (and the overlap with the Sn edge) and the HAADF image shown in Figure 2.3(b) was acquired closer to the edge of the wire. Both data sets were representative of the whole nanowire. Atomically resolved EELS spectral images highlight the incorporation of Sn in the core of the Ge nanowires. The sparse distribution of Sn in the Ge host lattice is clearly observed in the

lattice resolved EELS maps. No apparent sign of Sn precipitation was detected in the nanowires from EELS mapping, thus confirming the distribution of Sn atoms throughout the  $\text{Ge}_{1-x}\text{Sn}_x$  1-D lattice. The Sn EELS M-edge is quite delocalised, thus making it very difficult to resolve Sn as part of the Ge-Sn dumb-bell due to inelastic scattering. A single Sn atom will look blurry and 'delocalised', especially when the maps are taken over relatively thick regions of the wires as the Sn atom may be buried deep inside the lattice and further scattering will give the impression of a poor image. So the proximity effect of Sn atoms in the lattice may represent as Sn clusters in high resolution mapping (Figure 2.3(a) and (b)) with a smaller field of view. Low resolution EELS mapping from  $\text{Ge}_{1-x}\text{Sn}_x$  nanowires also confirmed the sparse distribution of Sn without any formation of metallic Sn hotspots (2.8. Appendix Figure A2.10). Hence Sn was distributed uniformly throughout the lengths of the nanowires, but randomly at the atomic scale (as seen in Figure A2.2 and Figure A2.10 in Appendix), without any phase separation. To assess precisely the catalyst-nanowire interface sharpness, EELS chemical maps (recorded from the rectangular red box denoted in the HAADF image attached to the map) and profiles were recorded by moving the electron probe serially across the interface along the line indicated by the red arrow and recording the Ge  $L_{2,3}$  and Sn  $M_{4,5}$  EELS edges (Figure 2.3(c)). The red shaded area in the linescan (Figure 2.3(c)) corresponds to the same spatial extent indicated on the HAADF image. EELS spectral images for Ge and Sn and chemical line profiles confirm the very Sn rich composition of the catalyst seed with sharp composition variation at the seed-nanowire interface. The oscillations of the integrated EELS intensities follow the oscillations of the simultaneously recorded HAADF signal, in both the nanowire and in the seed regions. Random, non-uniform fluctuation of the Sn signal in the line profiles of the nanowire region also suggests random  $\text{Ge}_{1-x}\text{Sn}_x$  alloy formation with high Sn incorporation. The frequency of the HAADF oscillation signal increased in the

catalyst thus confirming a much narrower inter-planar spacing in the lattice of the catalyst than the nanowire. Abrupt composition fluctuations at the seed-nanowire interface confirmed a continuous trapping and dissolution process for Sn impurity incorporation rather than a Sn layer precipitation and diffusion process.

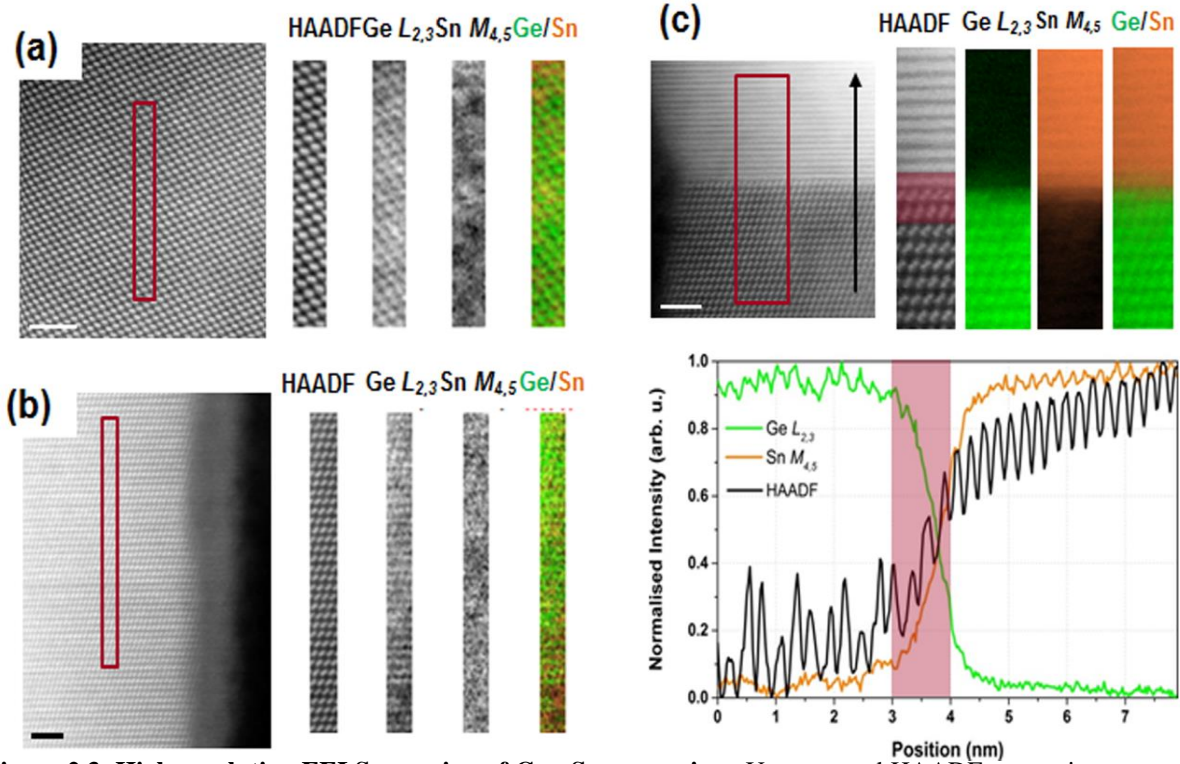


**Figure 2.3: High-resolution EELS mapping of  $\text{Ge}_{1-x}\text{Sn}_x$  nanowires.** Unprocessed HAADF survey image recorded from the center (a) and near the edge (b) of a  $\text{Ge}_{1-x}\text{Sn}_x$  nanowire with a Sn incorporation of 9 at. % (area of interest highlighted). Corresponding EELS map for Ge and Sn is also attached along with the simultaneously acquired HAADF image (Green: Ge and orange: Sn). For the EELS map, after de-noising by principal components analysis, the background was removed by fitting a power law over a region immediately in front of the core loss edges. The signal was then integrated over a 120 eV window above the onsets of the Sn  $M_{4,5}$  and Ge  $L_{2,3}$  edges. (c) HAADF survey image of a seed-nanowire interface region with the Ge and Sn EELS map recorded from the highlighted region. Another section of part (c) shows a linescan acquired subsequently in the same region. The red shaded area in the linescan corresponds to the same spatial extent indicated on the HAADF image. Scale bar, 2 nm for all the HAADF images.

**Structural characterisation of nanowires *via* STEM and HRTEM.** Impurity atoms (Sn in our case) in nanowires can induce structural defects, such as twins and stacking faults and these defects can act as preferential sites for subsequent impurity accumulation.<sup>33</sup> In other scenarios, pre-formed stacking faults in nanowires due to interface engineering, can also act as preferred sites for the segregation of foreign atoms from catalyst nanoparticles.<sup>34</sup> Hence, it is very important to probe the structural quality of the alloy nanowires to estimate the mode for impurity incorporation in Ge. Also nanowires with defects are not suitable for nanoelectronic devices as stacking faults and twin boundaries can encourage electron scattering.<sup>35</sup> A bright field high-resolution transmission electron microscopy (HRTEM) image (Figure 2.4(a)) confirms the high crystallinity of a single  $\text{Ge}_{1-x}\text{Sn}_x$  nanowire with a 9.2 at. % Sn incorporation and with a 2-3 nm amorphous oxide coating. Fast Fourier transform (FFT) analysis showed a pseudo hexagonal symmetry and the reflections can be assigned to the high-order Laue zone diffraction of  $\{111\}$  and  $\{002\}$  planes in group IV crystals.<sup>36</sup> FFT and HRTEM images depict an interplanar spacing ( $d$ ) between  $\{111\}$  planes in the nanowire to be 0.323 nm, which is very close to the  $d$  value for bulk diamond Ge crystal (JCPDS 04-0545). An increase in the  $d$  value from bulk Ge is expected with the incorporation of large amounts of Sn in Ge lattice. However this discrepancy may arise from the fact that this particular nanowire could only be aligned to a relatively minor zone axis. Figure 2.4(b) shows a

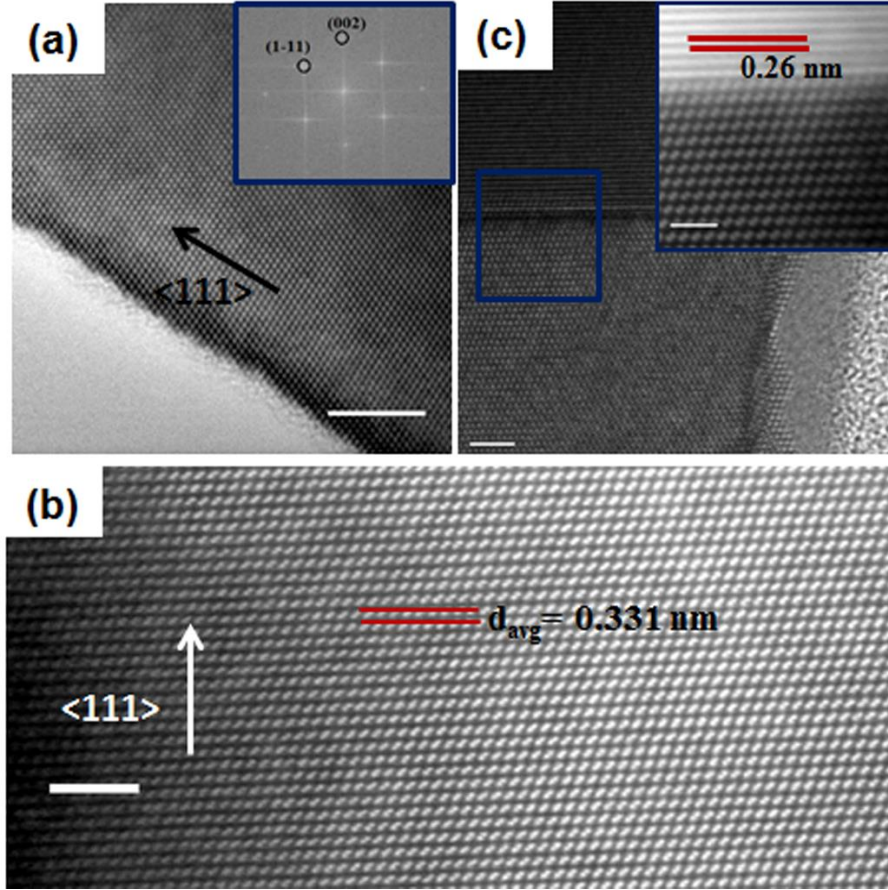


**Figure 2.4: Structural study of alloy nanowires with HRTEM and STEM.** (a) HRTEM image of highly crystalline  $\text{Ge}_{1-x}\text{Sn}_x$  nanowire (9.1 at. % Sn incorporation). Scale bar, 5 nm. FFT pattern in the inset confirms the crystallinity and growth orientation of the alloy nanowire. (b) Lattice-resolved STEM HAADF image recorded from the core of the alloy nanowire showing the single crystalline nature with an inter-planer spacing of 0.33 nm. Scale bar, 2 nm. (c) High resolution HAADF image of a seed-nanowire interface (magnified image in the inset) shows abrupt catalyst-nanowire interface with no precipitation of metallic Sn. Scale bar, 2 nm and 1 nm for the inset.

high resolution STEM image of another nanowire from the sample with the highest Sn incorporation using the HAADF mode. The image was recorded with  $\langle 110 \rangle$  zone axis alignment. Generally, the crystal structure of the  $\text{Ge}_{1-x}\text{Sn}_x$  alloy nanowires, with various Sn incorporations, exhibited a bulk diamond cubic crystal structure with a 3C lattice arrangement without any stacking faults and twin boundaries, with  $\langle 111 \rangle$  being the dominant growth direction. Although



there is a large lattice mismatch between the components (Ge and Sn) of the alloy,<sup>31</sup> the epitaxial mismatch in the nanowires is compensated by elastic deformation near the hetero-interface and relieved at the nanowire surfaces,<sup>37</sup> thus maintaining highly crystalline nanowires. The liquid eutectic catalyst at the tip of the nanowires can also naturally accommodate elastic strain. Atomic-scale randomness in Sn incorporation in the Ge lattice, as observed through EELS mapping, can generate varied local lattice distortion and spacing at an Ångström scale. To compensate the effect of random alloying on the  $d$  value, we have calculated the inter planner spacing of 50 successive lattice planes (over >15 nm length) and determined the average  $d$  value to be 0.331 nm, which is slightly above the bulk 3C-Ge value (2.8. Appendix Figure A2.11). Bright-field STEM imaging (Figure 2.4(c)) of the interface between the  $\text{Ge}_{1-x}\text{Sn}_x$  nanowires and the metallic tips confirmed the sharp nature of the interface, with no tailing effect or segregation of metal at the interface. For STEM imaging, stacks of images were acquired sequentially at high scanning speed to minimize drift and instabilities and were aligned and summed for a high signal-to-noise ratio. An atomic-resolution view of a catalyst-nanowire interface area, indicated by the blue box in Figure 2.4(c), is depicted in the HAADF image in the inset of Figure 2.4(c). The sharp contrast in the HAADF intensity at the interface clearly suggests the abrupt nature of the interface. A lattice spacing of 0.26 nm was measured at the metallic tip which is relatively close to metallic Sn (JCPDS cards #04-0673), thus further confirming the formation of a Sn rich alloy at the tip.

**Structural and compositional analysis through Raman spectroscopy.** Raman scattering is an effective tool to estimate the structural and chemical environment in the core of a nanowire. Raman spectroscopy was employed to accurately probe the local chemical bonding environment and also to estimate the amount of Sn in the alloy nanowire samples. Figure 2.5(a) shows the

Raman spectra of alloy nanowires with different Sn concentrations and for reference a spectrum from bulk Ge. The strong peak around  $302\text{ cm}^{-1}$  in bulk Ge is attributed to the Ge-Ge LO mode. The Ge-Ge Raman peak progressively shifts to a lower energy with increasing Sn concentration (as determined by EDX measurements). A red shift of  $1.2$  to  $5.9\text{ cm}^{-1}$  of the Ge-Ge LO mode was observed for a variation in the Sn concentration from  $1.5$  to  $9.2\text{ at. \%}$ , compared to bulk Ge. We

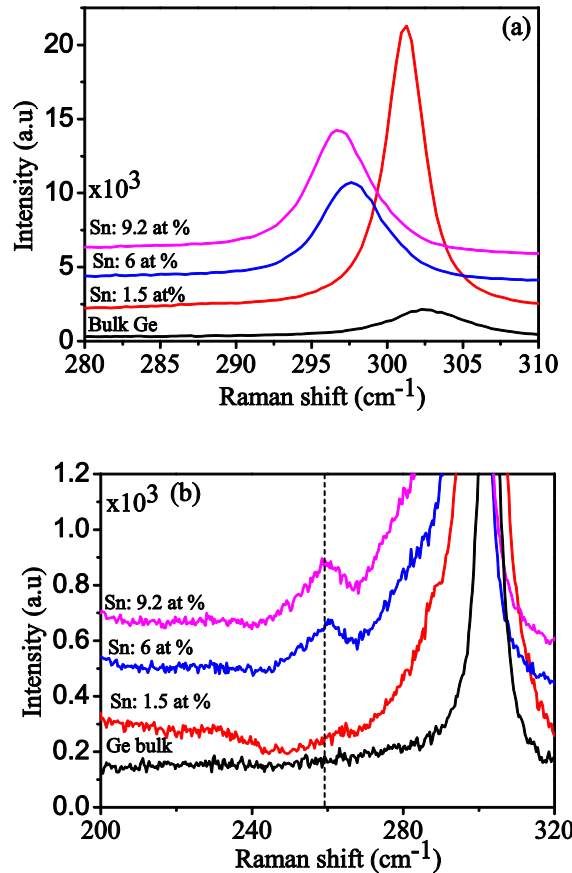


**Figure 2.5: Confirmation of  $\text{Ge}_{1-x}\text{Sn}_x$  alloy formation with Raman analysis.** Raman spectra of bulk Ge and  $\text{Ge}_{1-x}\text{Sn}_x$  nanowires (where  $x = 0.06$  and  $0.092$ ) within the range (a)  $280\text{--}310\text{ cm}^{-1}$  and (b)  $200\text{--}320\text{ cm}^{-1}$ . Vertical line in part (b) represents position of Ge-Sn vibration. The inset of Figure 5(a) shows the downshift of Ge-Ge LO mode as a function of Sn percentage. Experimental data are represented with dots which fits (straight line) well with the linear expression,  $\omega(x) = \omega_0 + \Delta\omega x$ .

could not compare the Raman shift to a sample of pure Ge nanowires, as the similar growth conditions without any Sn yielded Ge nanowires of entirely different dimensions and morphology.<sup>27</sup> In the alloy nanowires, apart from the Ge-Ge LO peak, additional modes due to Ge-Sn bonds appeared at around  $260\text{ cm}^{-1}$ , as shown in Figure 2.5(b). The presence of a Ge-Sn vibrational mode indicates the formation of  $\text{Ge}_{1-x}\text{Sn}_x$  alloys, where an increase in the intensity ratio between Ge-Sn and Ge-Ge LO modes with increasing Sn content, implies a larger substitution of Sn in the Ge lattice for  $\text{Ge}_{1-x}\text{Sn}_x$  nanowires. The origin of the Ge-Ge frequency shift in the Raman spectra of the  $\text{Ge}_{1-x}\text{Sn}_x$  alloys is due to compositional variations and strain effects. Participation of compressive and tensile strain towards the Raman shift is not justified for nanowire samples, as due to the large surface area, strain can be effectively released for these nanostructures. Compositional variations can originate from two factors: (i) mass disorder and (ii) bond distortion. The Ge-Ge LO mode progressively shifts towards a lower frequency with an increasing Sn concentration as displayed in the inset of Figure 2.5(a). We have fitted the Raman peak shift ( $\Delta\omega$ ) against Sn composition ( $x$ ), as determined through EDX analysis, with a linear expression,  $\omega(x) = \omega_0 + \Delta\omega x$ , and the obtained value of  $\Delta\omega$  was found to be  $-(64.3 \pm 0.1)\text{ cm}^{-1}$ . This value is consistent with the value of  $-(68 \pm 5)\text{ cm}^{-1}$  reported by Li et al., who assumed that their alloy films were completely strain free.<sup>38</sup> The linear correlation between the Raman peak shift and the Sn concentration (determined by EDX) in the alloy nanowires further validates the high Sn content in  $\text{Ge}_{1-x}\text{Sn}_x$  nanowires. Compared to a few other recent reports, a discrepancy in the  $\Delta\omega$  value and Raman shift is observed for the 9.2 at. % Sn containing nanowire sample with a relatively smaller shift in the Ge-Ge LO peak.<sup>21, 39</sup> This downshift in Raman frequency may arise from the random alloying affect<sup>38</sup>, instead of a spontaneous ordering, as observed in our nanowire sample through high resolution EELS and TEM measurement.

**Photoluminescence study of alloy nanowires: towards a direct bandgap.** As there are contradictions regarding the amount of Sn needed in  $\text{Ge}_{1-x}\text{Sn}_x$  thin films and bulk alloy to obtain a direct bandgap, it is essential to investigate the emission characteristics of strain free bottom-up grown  $\text{Ge}_{1-x}\text{Sn}_x$  alloy nanowires. Bandgap information on  $\text{Ge}_{1-x}\text{Sn}_x$  alloys was extracted through photoluminescence (PL) measurements at low temperature. A PL study to probe the bandgap characteristics of  $\text{Ge}_{1-x}\text{Sn}_x$  nanowire samples was conducted on samples cooled to 7 K, using a He cryostat. PL spectra of two nanowire samples (with an average Sn concentration of 6 and 9.2 at. %) recorded at 7 K is shown in Figure 2.6(a). The PL spectrum for the nanowire sample with the relatively low Sn content (6 at. %) exhibited a main peak which corresponds to the direct energy gap emission, at a wavelength of around 2200 nm, with a broad line-width (232 nm) of the emission spectrum. The direct peak is due to the strong radiative recombination of the direct bandgap transition. At this Sn content, separate peaks due to direct and indirect transitions cannot be clearly identified due to the reduced energy difference between the direct and indirect bandgap, resulting in only a single peak with broad line-width (232 nm) and tailing. A large amount of Sn in the  $\text{Ge}_{1-x}\text{Sn}_x$  alloy nanowires resulted in the reduction of the bandgap energy difference between the direct and indirect transition, which was approximately 0.14 eV in bulk Ge. Nanowire samples containing a high Sn content (9.2 at. %) exhibited a single PL emission peak centred at 2233 nm (band gap ( $E_g$ ) around 0.55 eV), with a relatively narrow line width (202 nm) compared to the PL plot from the low Sn content  $\text{Ge}_{1-x}\text{Sn}_x$  nanowire sample. The relatively narrower line width of the PL emission confirms the single energy emission at the  $\Gamma$  point.<sup>40</sup> Typically, a PL emission with a broad line width is observed in indirect bandgap alloys with a high Sn content due to the amalgamation of the indirect valley and the direct peak into a single broad emission. However, for our  $\text{Ge}_{1-x}\text{Sn}_x$  nanowires, with 9.2 at. % Sn incorporation, the direct band-to-band transition

resulted in relatively narrow PL emission, compared to the broad emission from  $\text{Ge}_{1-x}\text{Sn}_x$  alloy nanowires incorporating 6 at. % Sn. A single peak with a relatively narrow line width could signify emission from only the direct bandgap transition rather than unification of both direct and indirect transitions. The low PL emission intensity observed from the nanowire samples could be due to the luminescence quenching from metallic Sn impurities, which are present in the catalysts at the tip of the nanowires and also in negligible amounts as spherical particles in samples. Also the high surface-to-volume ratio of nanowires compared to thin films can account for the lower luminescence intensity. Relatively broad PL spectra for both nanowire samples, compared to previous reports, could result from the random distribution of Sn in the alloys. Sn incorporation in the nanowire samples also showed a standard deviation (around 1 %) which may also account for the broadness of the PL spectra obtained.

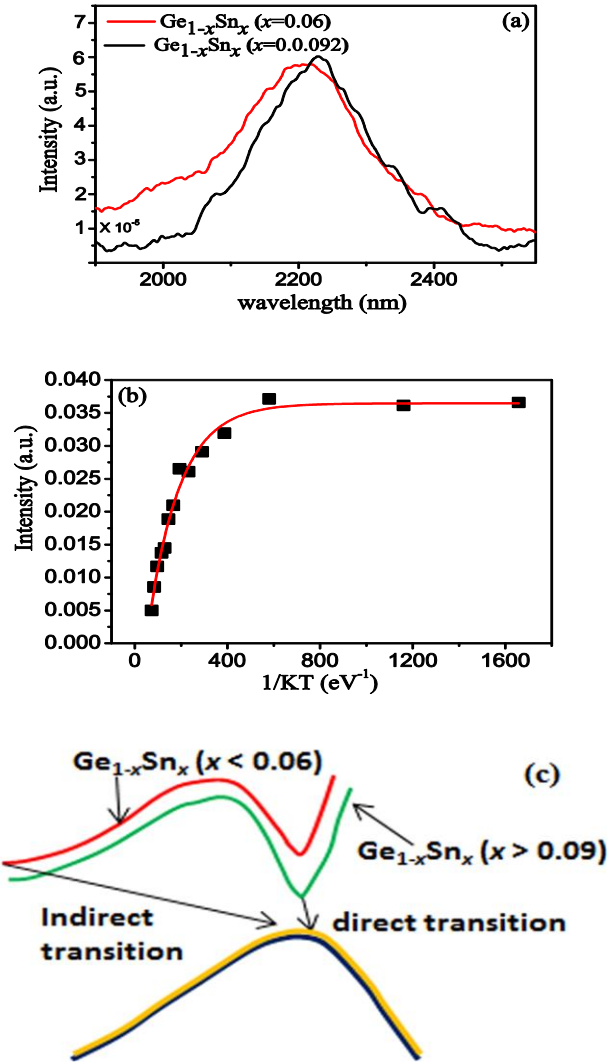


**Figure 2.6: Optical emission characteristics of alloy nanowires.** (a) PL spectra of  $\text{Ge}_{1-x}\text{Sn}_x$  nanowires ( $x = 0.06$  and  $0.092$ ) recorded at 7 K. Broadened PL peak is observed for alloy nanowires with  $x = 0.06$ . Single emission with narrow line width is observed for  $\text{Ge}_{1-x}\text{Sn}_x$  nanowires with  $x = 0.092$ . Inset in the center shows a projection (lines are only guide to eyes) of possible direct and indirect transition pathway for different Sn compositions. Part (b) shows the Arrhenius plot from 9.2%  $\text{Ge}_{1-x}\text{Sn}_x$  nanowires in agreement with single exponential decay of photoluminescence intensity with temperature. Part (b) shows the Arrhenius plot from 9.2%  $\text{Ge}_{1-x}\text{Sn}_x$  nanowires in agreement with single exponential decay of photoluminescence intensity with temperature with the coefficient of determination close to unity ( $R^2 = 0.986$ ). Part (c) shows a projection (lines are only guide to eyes) of possible direct and indirect transition pathway for different Sn compositions.

The position of the maximum in the direct energy emission from the  $\text{Ge}_{1-x}\text{Sn}_x$  nanowires matched well with the reported emission from alloy thin films and disks with similar Sn incorporation (8-10 at. %).<sup>11, 21, 40, 41</sup> Specifically, the emission energy matched very well with reported data for unstrained  $\text{Ge}_{1-x}\text{Sn}_x$  disks.<sup>21</sup> Emission from the  $\text{Ge}_{1-x}\text{Sn}_x$  nanowires at low temperature also complements the low temperature PL observation from  $\text{Ge}_{1-x}\text{Sn}_x$  thin films.<sup>40</sup> Thin film samples with 8 and 9 at. % Sn showed similar broad peaks at 10 K, which transformed to a single emission narrow peak with 10 at. % Sn in the film samples.<sup>40</sup> A shift (around 0.01 eV) in the PL maximum to a lower energy was also observed in the PL plots of our nanowire samples with an increase in the average Sn concentration from 6 to 9.2 at. %. The shift in the PL peak energy we observed for nanowire samples incorporating 6 and 9.2 at. % Sn was lower than has been reported for thin film samples.<sup>11,41</sup> However, the change in the bandgap of the nanowire alloys with different compositions and morphologies will depend on hole splitting, changes in effective mass, alloy broadening, band-tail states, carrier lifetime and steady state carrier occupation. Also, the different degrees of randomness in the alloys, which may be present between the 9.2 and 6 at. % samples (9.2 at. % samples had an additional step cooling, leading to high degree of randomness as observed in the EELS maps) can affect the band structure and bandgap tuning. A comparison in PL spectra at 77 K between pure Ge and  $\text{Ge}_{1-x}\text{Sn}_x$  nanowires (9.2 at. % Sn) show a massive red shift in the emission wavelength with the inclusion of Sn (2.8. Appendix Figure A2.12(a)). In order to achieve similar emission intensity the excitation power in the case of Ge nanowires was 700 mW in comparison to 30 mW for  $\text{Ge}_{1-x}\text{Sn}_x$  nanowire samples. The peak position for the Ge nanowire samples was around 1750 nm, which matches well with the indirect bandgap of Ge, while for  $\text{Ge}_{1-x}\text{Sn}_x$  samples emission was at 2150 nm.

To predict the direct-band transition, a temperature-dependent photoluminescence study between 7 and 160 K was performed. An Arrhenius plot, depicting integrated photoluminescence intensity as a function of inverted temperature is shown in Figure 2.6(b) (for 9.2 at. %) and in 2.8. Appendix Figure A2.13 (for 6 at. %). The PL of direct-bandgap semiconductors generally decreases in intensity with increasing temperature, which can be attributed to a reduced transfer of electrons from the  $\Gamma$  to L valleys by thermal activation.<sup>4, 42</sup> Thus the increase in the intensity of the PL peak with decreasing temperature for  $\text{Ge}_{1-x}\text{Sn}_x$  nanowires samples is attributed to the higher population of the  $\Gamma$  valley. With increasing temperature the fast diffusion of photocarriers toward surfaces and interfaces leads to non-radiative surface and interface recombination respectively, reducing the radiative transition rate.<sup>42</sup> Furthermore, we also observed broadening of the PL peak (2.8. Appendix Figure A2.12(b)) with increasing temperature for  $\text{Ge}_{1-x}\text{Sn}_x$  nanowires, which can be ascribed to the temperature dependent broadening of the Fermi distribution of carriers within electron bands.<sup>42</sup> A methodology to discriminate a direct from an indirect fundamental bandgap using temperature-dependent PL measurements has been presented recently.<sup>4</sup> On the basis of the same arguments, nanowire samples with 6 and 9.2 at. % Sn, manifested by monotonically increasing PL intensity with decreasing temperature, is similar to PL observed from direct bandgap III–V alloys or dichalcogenides.<sup>43, 44</sup> A power-dependent PL measurement of  $\text{Ge}_{1-x}\text{Sn}_x$  nanowires (9.2 at. % Sn) (2.8. Appendix Figure A2.12(c)) depicts the evolution of PL spectra from the GeSn nanowires under different excitation power densities at 77 K. For the lowest power ( $P_0 = 30$  mW, enhanced in figure by a factor of 300 for clarity) the PL peak position was around 2150 nm. With increasing excitation (up to  $16 P_0$ ) spectral broadening was observed, coupled with a blue-shift of the PL peak position. We attribute this change to carrier filling of closely-spaced  $\Gamma$  and L energy bands. This shift was not observed in the case of Ge nanowires within the scope of available



excitation powers between 350 and 700 mW. Additionally, in order to achieve similar PL intensity from both Ge and  $\text{Ge}_{1-x}\text{Sn}_x$  nanostructures (2.8. Appendix Figure A2.12(a)), Ge nanowires had to be excited with a laser power of 700 mW, while for  $\text{Ge}_{1-x}\text{Sn}_x$  nanowires 30 mW excitation power was sufficient. This enhancement of a factor greater than 20 yields provides further evidence to support the transition from indirect to direct bandgap nanowires with increasing Sn incorporation.

We have calculated the activation energies for non-radiative processes from Arrhenius plots. The activation energy was found to increase with increasing ‘directness’ of the bandgap.<sup>42</sup> The decrease in the PL intensity at high temperatures is due to an increase of the non-radiative recombination affects, *i.e.* the activation (deactivation) energy values.<sup>42</sup> Experimental activation energy for 9.2 at. % nanowire samples, calculated from Arrhenius plots, was 7 meV and for 6 at. % nanowire samples was 3 meV. The activation energy value for the 9.2 at. % nanowire samples matches well with the reported value for 12 at. % Sn incorporated thin film samples<sup>42</sup>, which have been designated in previous reports as “direct” transitions. Furthermore, Arrhenius plots have been fitted with a single exponential function. A coefficient of determination ( $R^2$ ) close to unity, *i.e.* for a good fit, indicates a single channel of recombination, while poor fit indicates competitive transition channels. For 6 at. % Sn containing nanowire samples the value of  $R^2$  was calculated to be 0.935 (2.8. Appendix Figure A2.13), while for the 9.2 at. % Sn incorporated nanowire samples  $R^2$  values of 0.986 were obtained (Figure 2.6(b)). This result indicates that a single charge carrier transition mechanism dominates only for samples with a high Sn content (Figure 2.6(c)). Although the current PL measurements indicate a direct bandgap, further confirmation regarding the nature of the emission is required, *e.g.* including radiative rates and quantum efficiencies. Spatial

orientation, quantum confinement effects and the internal strain in nanowires can strongly impact the electronic band structure and bandgap bowing<sup>43</sup> of alloys at the nanoscale.

## 2.5. Discussion

$\text{Ge}_{1-x}\text{Sn}_x$  nanowires fabricated with Au and AuAg catalysts at 440 °C showed considerable incorporation of Sn in the range around 6-9 at. %, much beyond the bulk equilibrium solubility (around 1%). The incorporation of Sn in the Ge nanowires through nanowire sidewalls due to homoepitaxy and vapour-solid growth is negligible, as the nanowires were not tapered and demonstrated a uniform radial Sn distribution, as determined by EDX line-profiles (2.8. Appendix Figure A2.4). A U-shape line profile with a larger Sn concentration at the edge of the nanowires would have been observed for sidewall Sn incorporation. Size dependent corrections to the bulk phase diagram due to the influence of capillary forces and stress at the nanoscale<sup>28,46,47</sup> results in significant undercooling of the liquid droplet and can in principle alter the equilibrium content of Sn in Ge. Calculations of the nanoscale equilibrium content of a solid impurity in a 1-D lattice, taking account of surface anisotropy and elastic stress, do not support a large dissolution of impurity atoms much beyond equilibrium solubility.<sup>25</sup> Careful analysis of the Sn-rich portion of the ternary Au-Ge-Sn phase diagram<sup>48</sup> shows that for our growth conditions, at equilibrium the Sn-rich (more than 90 %) droplet has a Ge:Sn ratio of close to unity and the growth should occur *via* the invariant reaction U4:  $\text{L} + \text{AuSn}_2 \leftrightarrow \text{diamond A4} + \text{AuSn}_4$  mediated by the formation of AuSn intermetallic phases. We did not observe the presence of these intermetallic phases within the nanowire (EDX analysis in 2.8. Appendix Figure A2.14 shows no traceable amount of Au or Ag in nanowires) or at the hetero-interface through EDX and EELS observations, effectively ruling out equilibrium growth. The droplet morphology/volume also did not change significantly upon varying the amount of Sn in the injecting solutions, as would have been expected for near-

equilibrium growth.<sup>49</sup> Also, the amount of Sn incorporated in the nanowires increased upon using AuAg catalysts which promotes faster Ge nanowire growth kinetics than Au seeds,<sup>27</sup> thus underscoring the role of kinetic factors in the non-equilibrium incorporation of Sn in Ge.

Non-equilibrium induction of Sn impurity in the Ge host is justified through diffusionless solute trapping at a finite growth velocity of the crystals. ‘Solute trapping’ is a process of solute redistribution at the interface resulting in an increase of chemical potential and deviation of partition coefficient.<sup>50</sup> Local chemical equilibrium at the alloy solidification front at the liquid (seed)-solid (nanowire) interface is relaxed due to a large interface velocity resulting in kinetic interface undercooling. At a high solidification rate at the catalyst-nanowire interface impurity adatoms can be trapped on the high energy sites of the crystal lattice, leading to the formation of metastable solids; for example  $\text{Ge}_{1-x}\text{Sn}_x$  with non-equilibrium Sn content, at the nanowire growth front. The kinetic incorporation of Sn is aided by the following factors: (i) Sn diffusion in Ge at the growth conditions is negligible, (ii) the epitaxial mismatch between Sn and Ge results in elastic strains at and near the catalyst-nanowire interface and (iii) the lack of truncating side facets at the catalyst-particle interface. Assuming that growth of the nanowire is layer by layer, the step flow kinetics can result in solute trapping of Sn from the Sn-rich droplet. The deviation of chemical equilibrium at the interface is influenced by the kinetic parameter, *i.e.* interfacial diffusion speed in this case. For bulk metal-semiconductor systems impurity trapping at the liquid-solid interface is highly probable at a very high interface velocity in the order of  $\text{m sec}^{-1}$ .<sup>51</sup> However, in the one-dimensional  $\text{Ge}_{1-x}\text{Sn}_x$  nanoscale systems the growth rate at the liquid-solid interface is only of the order of  $\text{nm sec}^{-1}$ . The growth velocity of  $\text{Ge}_{1-x}\text{Sn}_x$  nanowires is much lower ( $\sim 0.5\text{-}1 \text{ nm sec}^{-1}$ ) than the growth velocity required for kinetic driven solute trapping. However, for our particular

system a much higher Sn concentration in the catalyst seed (greater than 90 at. %) than the impurity concentration in a typical bulk solidification process and a continuous Sn flux throughout nanowire growth could account for the high Sn incorporation.<sup>52</sup> In the nanoscale system, where the crystal growth proceeds with the formation of steps at the interface, impurity atoms remains frozen at the step edges upon the formation of new row of atoms.<sup>25</sup> Hence, impurity incorporation during nanowire growth depends on the step velocity rather than on the interface velocity. With a high step velocity, the time required for local impurity exchange at the catalyst-nanowire interface decreases thus the rate of solute trapping increases in the nanowire. We delegate a detailed model to a later study, but it is important to note that solute trapping has been implicated in the catalyst incorporation of Al-catalyzed growth of Si nanowires.<sup>25</sup> A key difference, though, is that the equilibrium Al-solubility in the Al-Si droplet is much smaller (less than 5 %), unlike the Sn-rich droplet that catalyzes the growth of  $\text{Ge}_{1-x}\text{Sn}_x$  nanowires. The high Sn concentration around the growing steps is further aided by low Sn diffusivity within the nanowire and along its sidewalls, and the kinetic pathway favors Sn incorporation into the newly forming layer at the expense of elastic strains relative to the pristine Ge crystal. The elastic strains can be effectively accommodated by the Sn-rich droplet. Finally, at equilibrium the catalyst-nanowire interface also involves truncating side facets.<sup>53</sup> These truncating facets are absent in  $\text{Ge}_{1-x}\text{Sn}_x$  nanowires and the interface is fully faceted which is indirect confirmation of the elastic strains due to non-equilibrium Sn incorporation. As a result, the Sn incorporation is uniform through the nanowire, as opposed to being localized at the core or within a surface shell.

Induction of Sn in the alloy nanowires is further encouraged with a 2 hr annealing at 230 °C, during the cooling down of nanowires (2.8. Appendix Figure A2.6). The choice of the step cool down

process and temperature was driven by the existence of a small Sn precipitation window at the lowest eutectic, near the Sn rich side of the binary bulk Au-Sn phase diagram<sup>32</sup>, at around 215-230 °C. The position and width of the Sn precipitating window in the AuAg-Sn pseudo binary phase diagram was assumed from the Au-Sn and Ag-Sn phase diagrams. This small window encourages further precipitation of Sn from non-equilibrium Sn rich eutectic Au-Sn and AuAg-Sn catalysts during the annealing process. A deposition and dissolution based process could be responsible for the increase in the Sn amount in the alloy nanowire, where a Sn precipitation from the supersaturated catalyst drop is encouraged at 230 °C. Precipitated tin from the supersaturated catalyst gets further dissolved into the Ge nanowire host lattice at 230 °C due to the eutectic solubility. Metastability and continuous dissolution of Sn in the Ge host is expected at the eutectic temperature. A very large amount of Sn could be dissolved in the Ge lattice in the metastable state as projected in the Ge-Sn phase diagram. So the coincidence of the Sn precipitation from the seed droplet at 230 °C and dissolution of this Sn in the Ge nanowires at the eutectic temperature (at 230 °C) encourages large homogeneous Sn influx into the nanowire. Sn diffusion in Ge at 230 °C is negligible. So a diffusion mediated incorporation process would have a large concentration of Sn near the seed-nanowire interface, with a continuous drop in Sn concentration along the nanowire length. Compositional analysis of 9.2 at. % sample (grown following the step cool-down process) does not demonstrate this trend but shows similar distribution of Sn along the length of nanowires (2.8. Appendix Figure A2.8). To confirm the participation of the particular step down temperature of 230 °C in large Sn incorporation, nanowires were annealed during cool-down at four different temperatures of 210, 220, 230 and 250 °C. However, only those subsequently annealed at 230 °C displayed an increased Sn incorporation whereas no or negligible increase was observed for other temperatures (2.8. Appendix Figure A2.15). So in the step cool-down process, the coincidence of

the lowest eutectic in AuAg-Sn system and Ge-Sn system assists to increase the amount of Sn (~ 2.5 at. %) further beyond the capability of kinetic trapping. Undercooling and the shift in the liquidus from their bulk counterpart for nanoscale Ge-Sn systems may also be expected for Au-Sn and Ge-Sn binary phase diagram.

## 2.6. Conclusion

Varying the growth parameters to influence the kinetics of the  $\text{Ge}_{1-x}\text{Sn}_x$  system can dramatically impact Sn uptake in the nanowires. By exploring the effects of temperature, precursor and catalyst an optimal growth regime was explored to obtain high growth kinetics of  $\text{Ge}_{1-x}\text{Sn}_x$  nanowires. By using tetraethyltin as the Sn source and varying the composition of the AuAg alloy catalyst, morphologically uniform and crystalline nanowires with homogeneous Sn incorporation of > 9 at. % were obtained with an  $\text{Au}_{0.80}\text{Ag}_{0.20}$  catalyst. Longer  $\text{Ge}_{1-x}\text{Sn}_x$  nanowires were more Sn rich than the shorter  $\text{Ge}_{1-x}\text{Sn}_x$  nanowires, establishing a relationship between growth kinetics and Sn incorporation. Faster growth rates resulted in nanowires with higher Sn incorporation, confirming the participation of a kinetic dependence of the solute trapping for Sn incorporation. The understanding of the role of the growth constraint and growth kinetics in the VLS process in Sn impurity incorporation in  $\text{Ge}_{1-x}\text{Sn}_x$  nanowires could contribute towards the development of group IV alloys with different stoichiometry and also other new functional alloy materials. For example, a further manipulation in Sn content in  $\text{Ge}_{1-x}\text{Sn}_x$  nanowires can be expected with the introduction and variation of new parameters such as catalyst concentration or pressure.

The  $\text{Ge}_{1-x}\text{Sn}_x$  nanowires with  $x = 0.09$  were determined to be direct bandgap from both PL and EELS analysis. An indirect to direct transition point was identified for the nanowires between 7

and 9 at. % of Sn incorporation. Enhanced spontaneous ordering of Sn impurities, as detected *via* Raman spectroscopy, resulted in a sharp direct band gap emission from the  $\text{Ge}_{1-x}\text{Sn}_x$  nanowires with  $x = 0.09$ . More knowledge on the effect of qualitative distribution of the foreign atoms in the host semiconductor lattice *via* complemented atomic scale mapping (e.g. atom probe tomography) and advance optical analysis will allow exploration of novel properties such as nanoscale strain engineering, controlled defect formation, band structure modulation in the existing nanoscale group IV alloy semiconductor architecture. The fabrication of direct bandgap  $\text{Ge}_{1-x}\text{Sn}_x$  nanowires with high Sn content ( $> 9$  at. %) demonstrates a low cost, silicon compatible solution to the ongoing demand for nanoscale group IV photonics *via* a conventional catalytic approach. These direct bandgap  $\text{Ge}_{1-x}\text{Sn}_x$  nanowires, with narrow emission widths, a uniform morphology, high crystallinity and homogeneous Sn distribution, demonstrate themselves to be suitable candidates for implementation in photonic and optoelectronic devices.

To explore the limits of the solute trapping model, and to investigate a simpler growth method, the next step was to vary the growth parameters to induce a faster nanowire growth rate. According to the solute trapping model, this faster growth rate should result in higher impurity incorporation in the nanowires. Additionally, the elimination of the step-anneal may result in an improvement in impurity distribution, which in turn could improve light emission and bandgap narrowing.

## 2.7. References

1. Hu, C. Green Transistor as a Solution to the IC Power Crisis. *Proc. 9th Int. Conf. Solid-State Integrated-Circuit Technol.* 16–20 (IEEE, 2008).
2. Brubaker, M.D. et al. On-Chip Optical Interconnects Made with Gallium Nitride Nanowires. *Nano Lett.* **13**, 374-377 (2013).
3. Soref, R. Mid-infrared photonics in silicon and germanium. *Nature Photonics* **4**, 495-497 (2010).
4. Wirths, S. et al. Lasing in direct-bandgap GeSn alloy grown on Si. *Nature Photonics* **9**, 88-92 (2015).
5. Zhang, P.H., Crespi, V.H., Chang, E., Louie, S.G. & Cohen, M.L. Computational design of direct-bandgap semiconductors that lattice-match silicon. *Nature* **409**, 69-71 (2001).
6. Moontragoon, P., Soref, R.A. & Ikonik, Z. The direct and indirect bandgaps of unstrained  $\text{Si}_x\text{Ge}_{1-x-y}\text{Sn}_y$  and their photonic device applications. *Journal of Applied Physics* **112**, 073106 (2012).
7. Sau, J.D. & Cohen, M.L. Possibility of increased mobility in Ge-Sn alloy system. *Physical Review B* **75**, 045208 (2007).
8. Jenkins, D.W. & Dow, J.D. ELECTRONIC-PROPERTIES OF METASTABLE  $\text{Ge}_x\text{Sn}_{1-x}$  alloys. *Physical Review B* **36**, 7994-8000 (1987).
9. He, G. & Atwater, H.A. Interband transitions in  $\text{Sn}_x\text{Ge}_{1-x}$  alloys. *Physical review letters* **79**, 1937-1940 (1997).



10. Yin, W.-J., Gong, X.-G. & Wei, S.-H. Origin of the unusually large band-gap bowing and the breakdown of the band-edge distribution rule in the  $\text{Sn}_x\text{Ge}_{1-x}$  alloys. *Physical Review B* **78**, 161203 (2008).
11. Chen, R. et al. Increased photoluminescence of strain-reduced, high-Sn composition  $\text{Ge}_{1-x}\text{Sn}_x$  alloys grown by molecular beam epitaxy. *Applied Physics Letters* **99**, 181125 (2011).
12. Moontragoon, P., Ikonic, Z. & Harrison, P. Band structure calculations of Si-Ge-Sn alloys: achieving direct band gap materials. *Semiconductor Science and Technology* **22**, 742-748 (2007).
13. Gupta, S., Magyari-Koepe, B., Nishi, Y. & Saraswat, K.C. Achieving direct band gap in germanium through integration of Sn alloying and external strain. *Journal of Applied Physics* **113**, 073707 (2013).
14. Kouvetakis, J., Menendez, J. & Chizmeshya, A.V.G. in Annual Review of Materials Research, **36**, 497-554 (2006).
15. Johnson, K.A. & Ashcroft, N.W. Electronic structure of ordered silicon alloys: Direct-gap systems. *Physical Review B* **54**, 14480-14486 (1996).
16. Bauer, M.R. et al. Tunable band structure in diamond-cubic tin-germanium alloys grown on silicon substrates. *Solid State Communications* **127**, 355-359 (2003).
17. Bauer, M. et al. Ge-Sn semiconductors for band-gap and lattice engineering. *Applied Physics Letters* **81**, 2992-2994 (2002).
18. Bauer, M.R. et al. SnGe superstructure materials for Si-based infrared optoelectronics. *Applied Physics Letters* **83**, 3489-3491 (2003).
19. Bauer, M. et al. Synthesis of ternary SiGeSn semiconductors on Si(100) via  $\text{Sn}_x\text{Ge}_{1-x}$  buffer layers. *Applied Physics Letters* **83**, 2163-2165 (2003).

20. Ragan, R., Ahn, C.C. & Atwater, H.A. Nonlithographic epitaxial  $\text{Sn}_x\text{Ge}_{1-x}$  dense nanowire arrays grown on Ge(001). *Applied Physics Letters* **82**, 3439-3441 (2003).
21. Gupta, S. et al. Highly Selective Dry Etching of Germanium over Germanium-Tin ( $\text{Ge}_{1-x}\text{Sn}_x$ ): A Novel Route for  $\text{Ge}_{1-x}\text{Sn}_x$  Nanostructure Fabrication. *Nano Lett.* **13**, 3783-3790 (2013).
22. Mullane, E., Kennedy, T., Geaney, H., Dickinson, C. & Ryan, K.M. Synthesis of Tin Catalyzed Silicon and Germanium Nanowires in a Solvent-Vapor System and Optimization of the Seed/Nanowire Interface for Dual Lithium Cycling. *Chem. Mat.* **25**, 1816-1822 (2013).
23. Barth, S., Seifner, M.S. & Bernardi, J. Microwave-assisted solution–liquid–solid growth of  $\text{Ge}_{1-x}\text{Sn}_x$  nanowires with high tin content. *Chemical Communications* **51**, 12282-12285 (2015).
24. Chen, W. et al. Incorporation and redistribution of impurities into silicon nanowires during metal-particle-assisted growth. *Nature communications* **5**, 4134 (2014).
25. Moutanabbir, O. et al. Colossal injection of catalyst atoms into silicon nanowires. *Nature* **496**, 78-82 (2013).
26. Biswas, S., Singha, A., Morris, M.A. & Holmes, J.D. Inherent Control of Growth, Morphology, and Defect Formation in Germanium Nanowires. *Nano Lett.* **12**, 5654-5663 (2012).
27. Biswas, S., O'Regan, C., Petkov, N., Morris, M.A. & Holmes, J.D. Manipulating the growth kinetics of vapor-liquid-solid propagated ge nanowires. *Nano Lett.* **13**, 4044-4052 (2013).

28. Biswas, S., O'Regan, C., Morris, M.A. & Holmes, J.D. In-situ Observations of Nanoscale Effects in Germanium Nanowire Growth with Ternary Eutectic Alloys. *Small* **11**, 103-111 (2015).
29. He, S.T., Xie, S.S., Yao, J.N., Gao, H.J. & Pang, S.J. Self-assembled two-dimensional superlattice of Au-Ag alloy nanocrystals. *Applied Physics Letters* **81**, 150-152 (2002).
30. A Prince, P.L., O Fabrichnaya Springer Materials The Landolt-Bornstein New Series IV/IIB. (Springer, 2012).
31. E. Kasper, M.K., M. Oehme and T. Arguirov Germanium tin: silicon photonics toward the mid-infrared. *Photon. Res.* **1**, 69 (2013).
32. Ciulik, J. & Notis, M.R. The Au-Sn phase-diagram. *Journal of Alloys and Compounds* **191**, 71-78 (1993).
33. Hemesath, E.R. et al. Catalyst Incorporation at Defects during Nanowire Growth. *Nano Lett.* **12**, 167-171 (2012).
34. Allen, J.E. et al. High-resolution detection of Au catalyst atoms in Si nanowires. *Nature Nanotechnology* **3**, 168-173 (2008).
35. Caroff, P. et al. Controlled polytypic and twin-plane superlattices in III-V nanowires. *Nature Nanotechnology* **4**, 50-55 (2009).
36. Bell, D.C. et al. Imaging and analysis of nanowires. *Microscopy Research and Technique* **64**, 373-389 (2004).
37. Jiang, X. et al. Rational growth of branched nanowire heterostructures with synthetically encoded properties and function. *Proceedings of the National Academy of Sciences of the United States of America* **108**, 12212-12216 (2011).

38. Li, S.F., Bauer, M.R., Menendez, J. & Kouvetakis, J. Scaling law for the compositional dependence of Raman frequencies in SnGe and GeSi alloys. *Applied Physics Letters* **84**, 867-869 (2004).
39. Lin, H., Chen, R., Huo, Y., Kamins, T.I. & Harris, J.S. Raman study of strained Ge<sub>1-x</sub>Sn<sub>x</sub> alloys. *Applied Physics Letters* **98**, 261917 (2011).
40. Ghetmiri, S.A. et al. Direct-bandgap GeSn grown on silicon with 2230 nm photoluminescence. *Applied Physics Letters* **105**, 151109 (2014).
41. Senaratne, C.L., Gallagher, J.D., Aoki, T., Kouvetakis, J. & Menendez, J. Advances in Light Emission from Group-IV Alloys via Lattice Engineering and n-Type Doping Based on Custom-Designed Chemistries. *Chem. Mat.* **26**, 6033-6041 (2014).
42. Stange, D., Wirths, S., von den Driesch, N., Mussler, G., Stoica, T., Ikonik, Z., Hartmann, J. M., Mantl, S., Grützmacher, D., and Buca, D. Optical Transitions in Direct-Bandgap Ge<sub>1-x</sub>Sn<sub>x</sub> Alloys. *ACS Photonics* **2**, 1539-1545 (2015).
43. Lezama, I.G., Arora, A., Ubaldini, A., Barreateau, C., Giannini, E., Potemski, M., Morpurgo, A.F. Indirect-to-Direct Band Gap Crossover in Few-Layer MoTe<sub>2</sub>. *Nano letters* **15**, 2336-2342 (2015).
44. Peng, X., Wei, Q. and Copple, A. Strain-engineered direct-indirect band gap transition and its mechanism in two-dimensional phosphorene, *Phys. Rev. B* **90**, 085402 (2015).
45. Harris, C. & O'Reilly, E.P. Nature of the band gap of silicon and germanium nanowires. *Physica E-Low-Dimensional Systems & Nanostructures* **32**, 341-345 (2006).
46. Sutter, E.A. & Sutter, P.W. Size-Dependent Phase Diagram of Nanoscale Alloy Drops Used in Vapor-Liquid-Solid Growth of Semiconductor Nanowires. *ACS Nano* **4**, 4943-4947 (2010).

47. E. J. Schwalbach & Voorhees, P.W. Phase equilibrium and nucleation in VLS-grown nanowires. *Nano Lett.* **8**, 3739-3745 (2008).
48. Jin, S., Valenza, F., Novakovic, R. & Leinenbach, C. Wetting Behavior of Ternary Au-Ge-X (X= Sb, Sn) Alloys on Cu and Ni. *Journal of electronic materials* **42**, 1024-1032 (2013).
49. Lim, S.K., Crawford, S., Habermann, G. & Gradečak, S. Controlled modulation of diameter and composition along individual III–V nitride nanowires. *Nano Lett.* **13**, 331-336 (2012).
50. Galenko, P. Solute trapping and diffusionless solidification in a binary system. *Physical Review E* **76**, 031606 (2007).
51. Baker, J. & Gahn, J. Solute trapping by rapid solidification. *Acta Metallurgica* **17**, 575-578 (1969).
52. Allen, J.E. et al. High-resolution detection of Au catalyst atoms in Si nanowires. *Nature Nanotechnology* **3**, 168-173 (2008).
53. Wang, H., Zepeda-Ruiz, L.A., Gilmer, G.H. & Upmanyu, M. Atomistics of vapour-liquid-solid nanowire growth. *Nature communications* **4**, 1956-1956 (2013).

## 2.8. Appendix

The appendix section of this chapter contains supplementary information relating to Chapter 2 (e.g. surplus SEM, EDX, TEM, *etc.*).

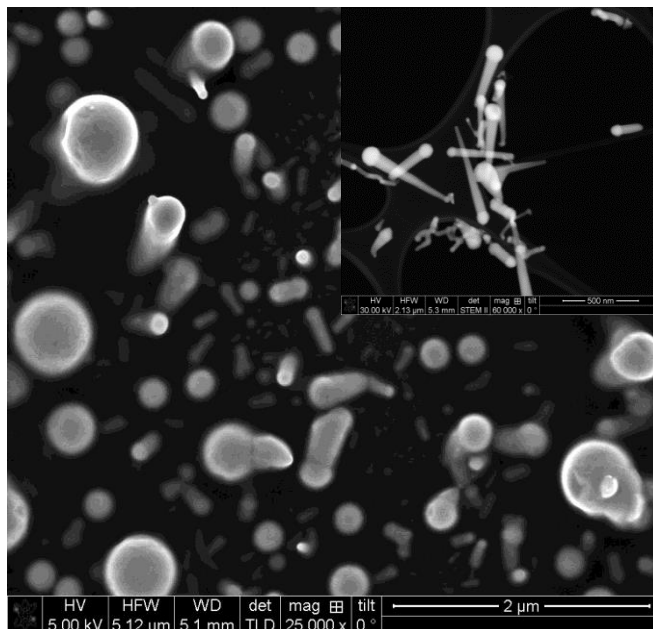


**Figure A2.1:** SEM image of the nanowire grown without any foreign metal catalysts (Au or AuAg) shows tapered nanowire with thicker top and thinner bottom with 7.5  $\mu\text{L}$  (15 at. %) of Sn precursor in the injecting solution. Nanowires are much shorter than the Au or AuAg seeded growth after 2 hrs growth time with lower Sn incorporation ( $\sim 3.5$  at. %). Dark-field STEM image in inset shows tapered nature of nanowire. Self-seeded growth of  $\text{Ge}_{1-x}\text{Sn}_x$  occurs near equilibrium. The droplet volume expands during nanowire growth as the expansion of Sn catalyst droplet is much faster than the Sn incorporation rate from seed to nanowire. Expansion in the volume of Sn catalyst droplet during growth drives the tapering of nanowires. The combined effect of slow growth kinetics of Ge nanowires from self-catalytic Sn seeds and continuous expansion of the triple-phase interface due to a constant Sn flux encourage prominent tapering in the nanowires without any Au and AuAg growth promoter.

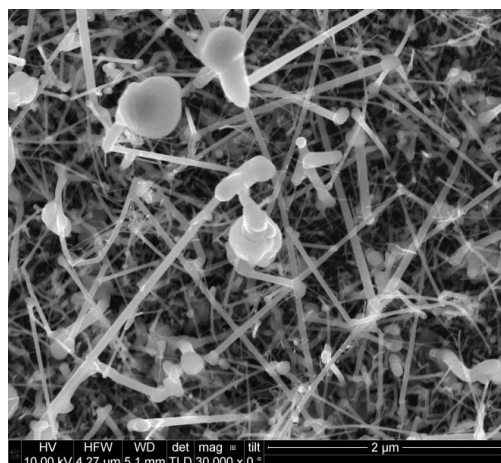


**Figure A2.2:** SEM image of the nanowire grown with Au catalyst shows and with 20 at. % Sn in the injecting solution shows spherical clusters due to homogeneous nucleation of Ge and Sn. Also bimodal distribution in diameter is observed with high Sn in precursor solution.

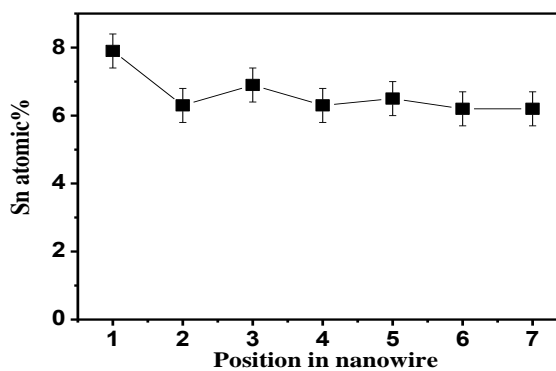
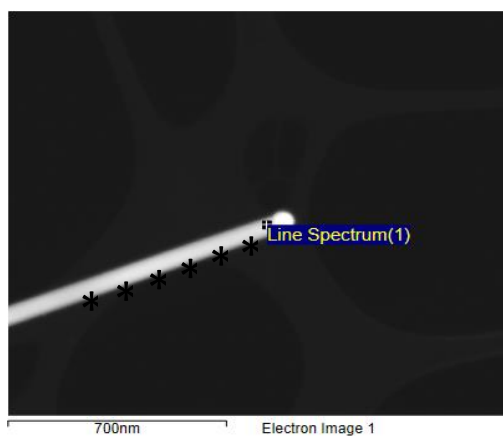


**Figure A2.3:** EDX scan along the length of a nanowire grown with AuAg seed shows uniformity in Sn distribution throughout the nanowire length. Error bar represent typical error of 0.5 at. % in EDX measurement.

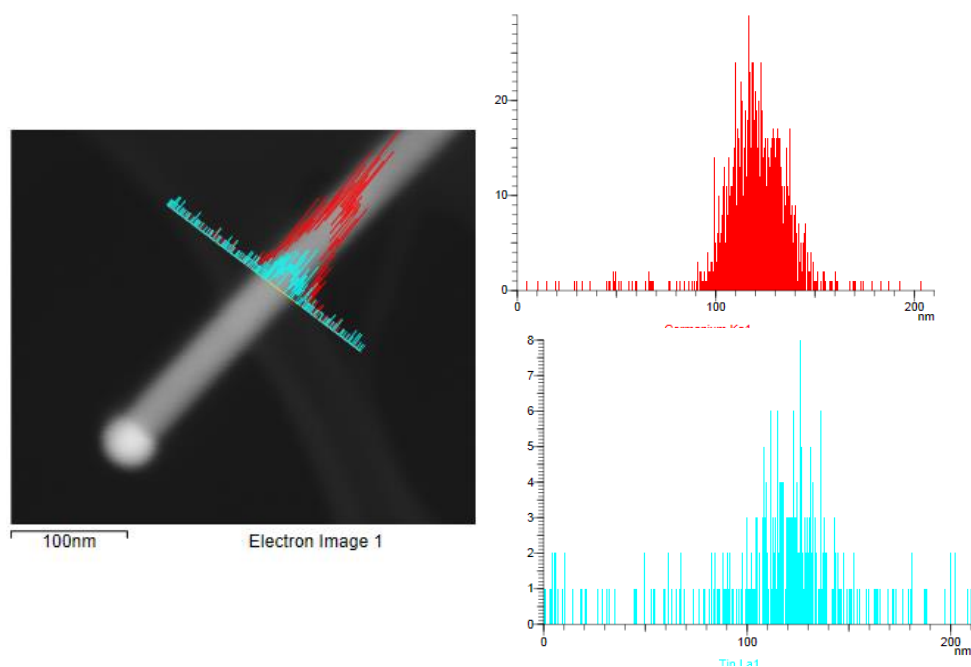


**Figure A2.4:** EDX radial concentration profile of Ge and Sn from a nanowire with 6.3 at. % of Sn grown with AuAg catalyst. EDX profile shows no segregation of Sn at or near nanowire surface.

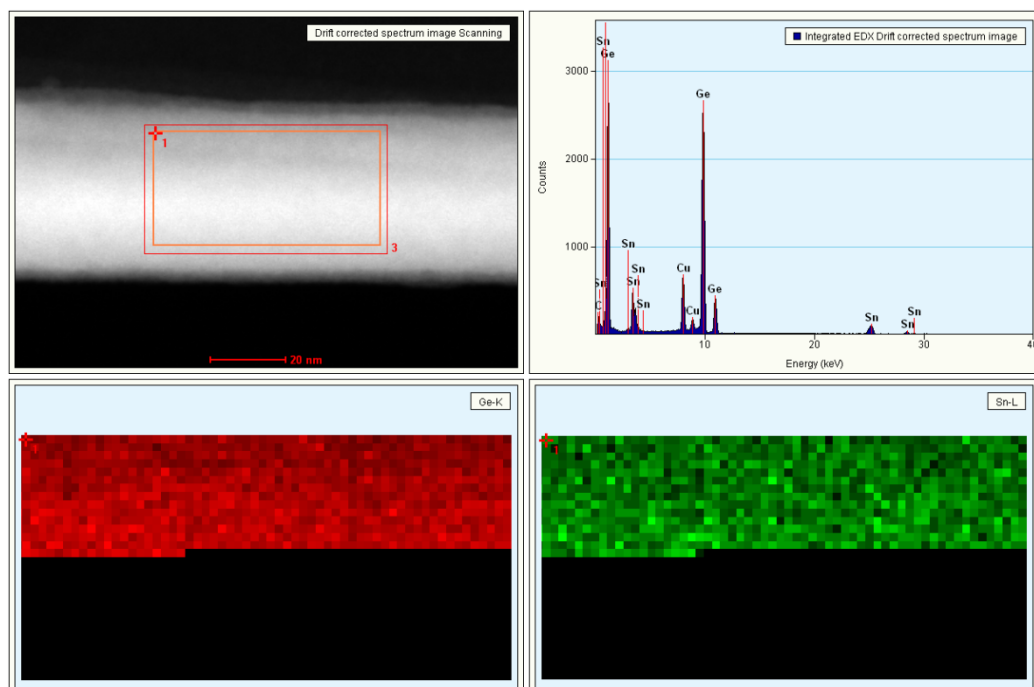


**Figure A2.5:** EDX mapping from an AuAg seeded  $\text{Ge}_{1-x}\text{Sn}_x$  nanowire body.



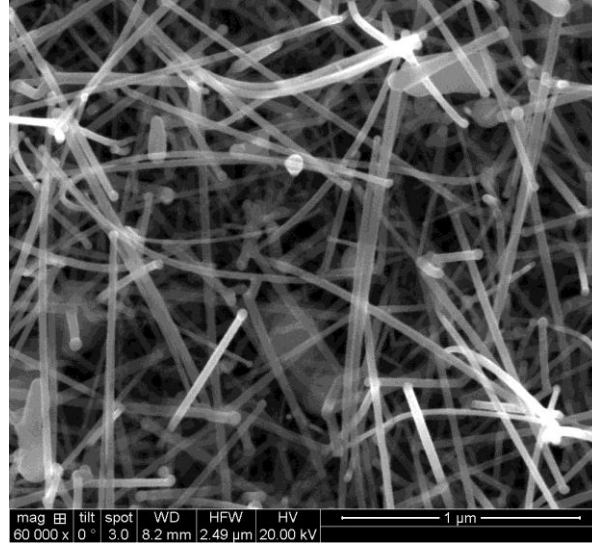


**Figure A2.6:** SEM image of the nanowire grown with AuAg catalyst with 15 at. % Sn in the injecting solution. Nanowires morphology remains intact after a step cool down process at 230 °C.

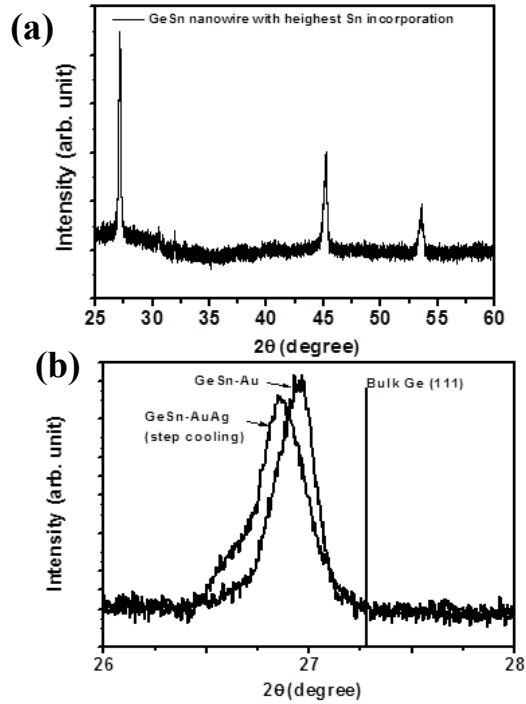


**Figure A2.7:** (a) X-ray diffraction spectrum from the  $\text{Ge}_{1-x}\text{Sn}_x$  nanowire sample grown with AuAg seed and with an additional step cooling. Lattice constant calculated for this nanowire is 5.739 Å with Sn concentration of 9.8 % according to Vegard's law. (b) X-ray diffraction shows relative shift in the (111) Ge reflection for  $\text{Ge}_{1-x}\text{Sn}_x$  nanowire with AuAg seed (with an additional step cooling) and  $\text{Ge}_{1-x}\text{Sn}_x$  nanowire with Au seed (measured Sn~ 6.8%).

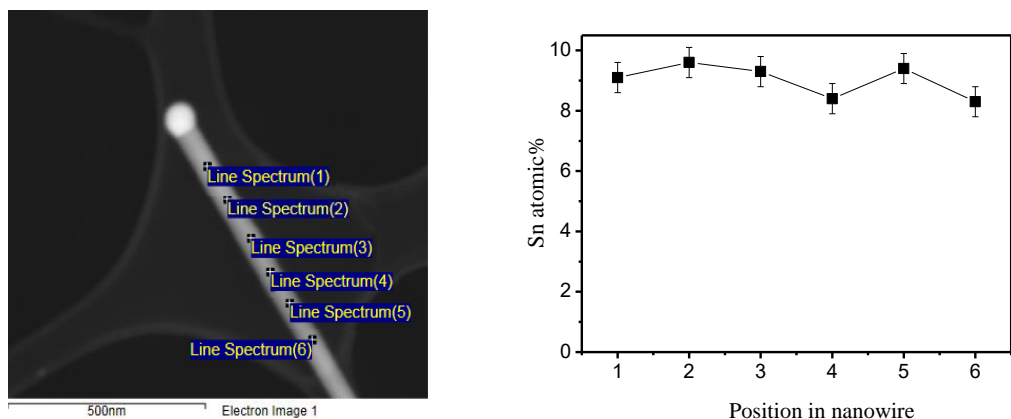


**Figure A2.8:** EDX scan along the length of a nanowire grown with AuAg seed and with an additional step cooling shows uniformity in Sn distribution throughout the nanowire length. Additional annealing step have no ill effect in depositing more Sn near the metallic tip. Error bar represent typical error of 0.5 at. % in EDX measurement.

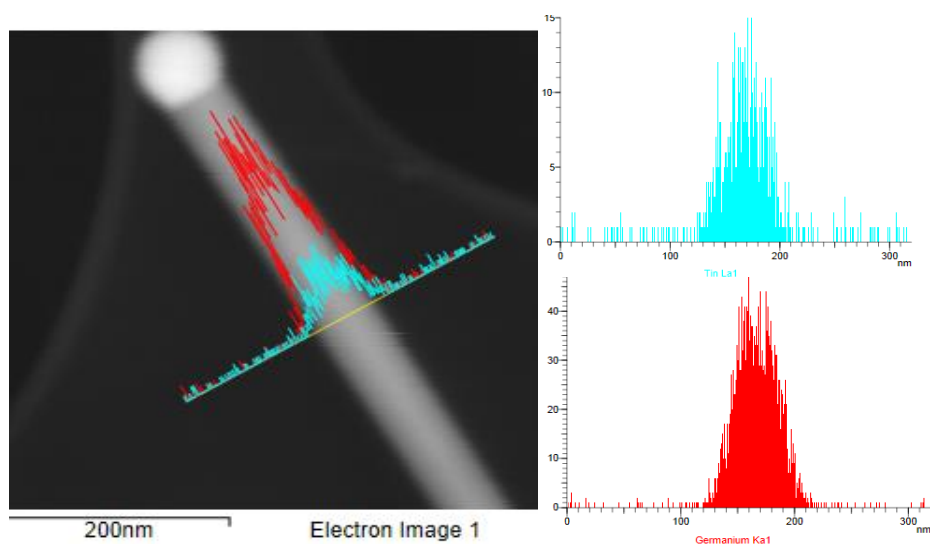


**Figure A2.9:** EDX radial concentration profile of Ge and Sn from a nanowire (~ 9 at. % Sn) grown with AuAg catalyst with an additional step cooling. EDX profile shows no segregation of Sn at or near nanowire surface.

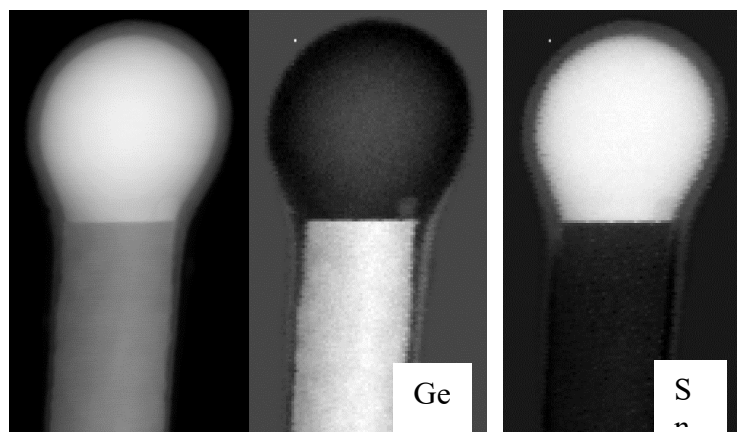


**Figure A2.10:** Low resolution EELS mapping of  $\text{Ge}_{1-x}\text{Sn}_x$  nanowire showing sparse distribution of Sn in the nanowire and high Sn rich catalyst seed.

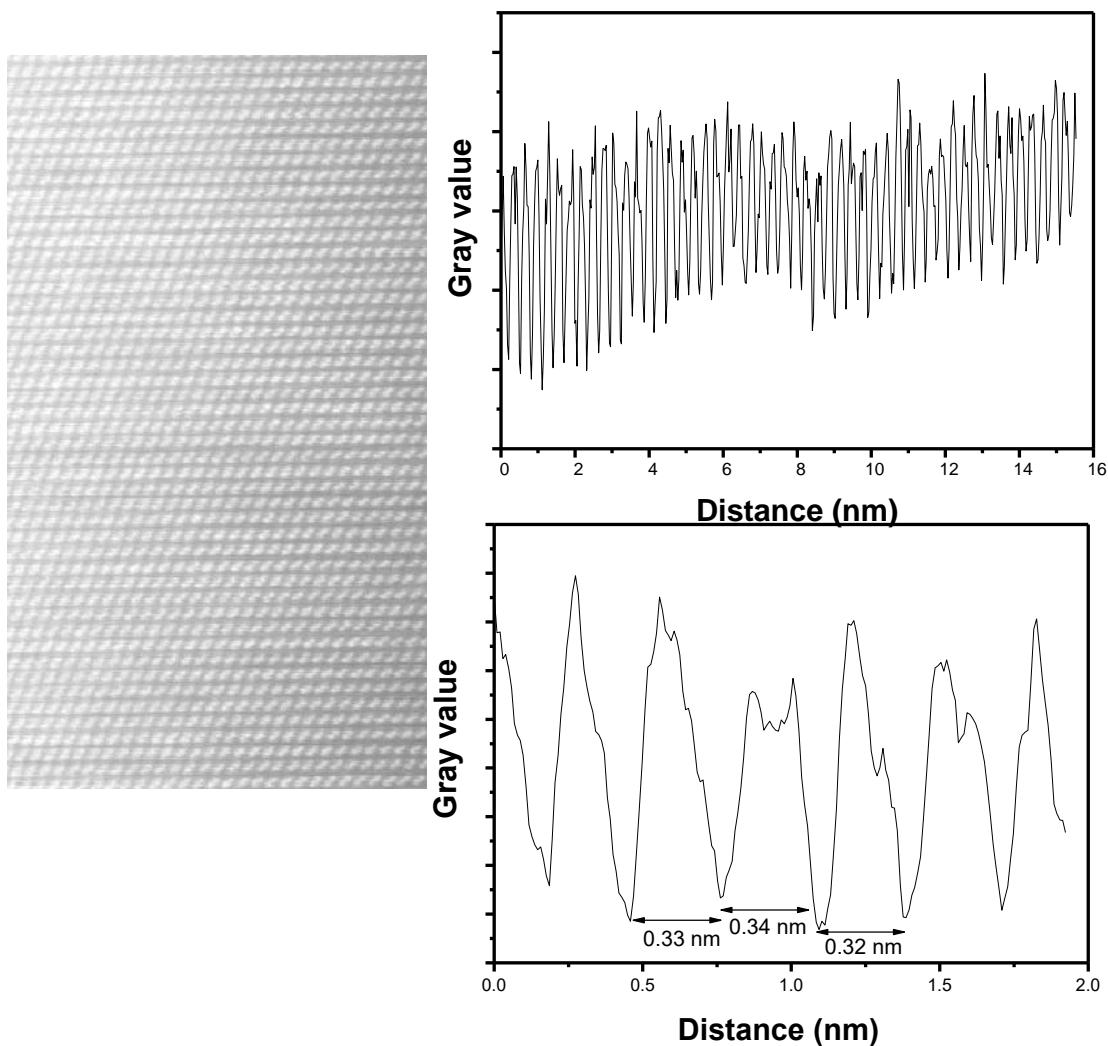


**Figure A2.11:** Calculation of average interplanar spacing from brightness-contrast plot profile from the STEM image in part (a). Average interplanar spacing was calculated to be 3.31 Å from the profile of 50 successive planes (b). Local randomness in the interplanar spacing is evident from the plot (c) with different interplanar spacing (d value) for subsequent planes.

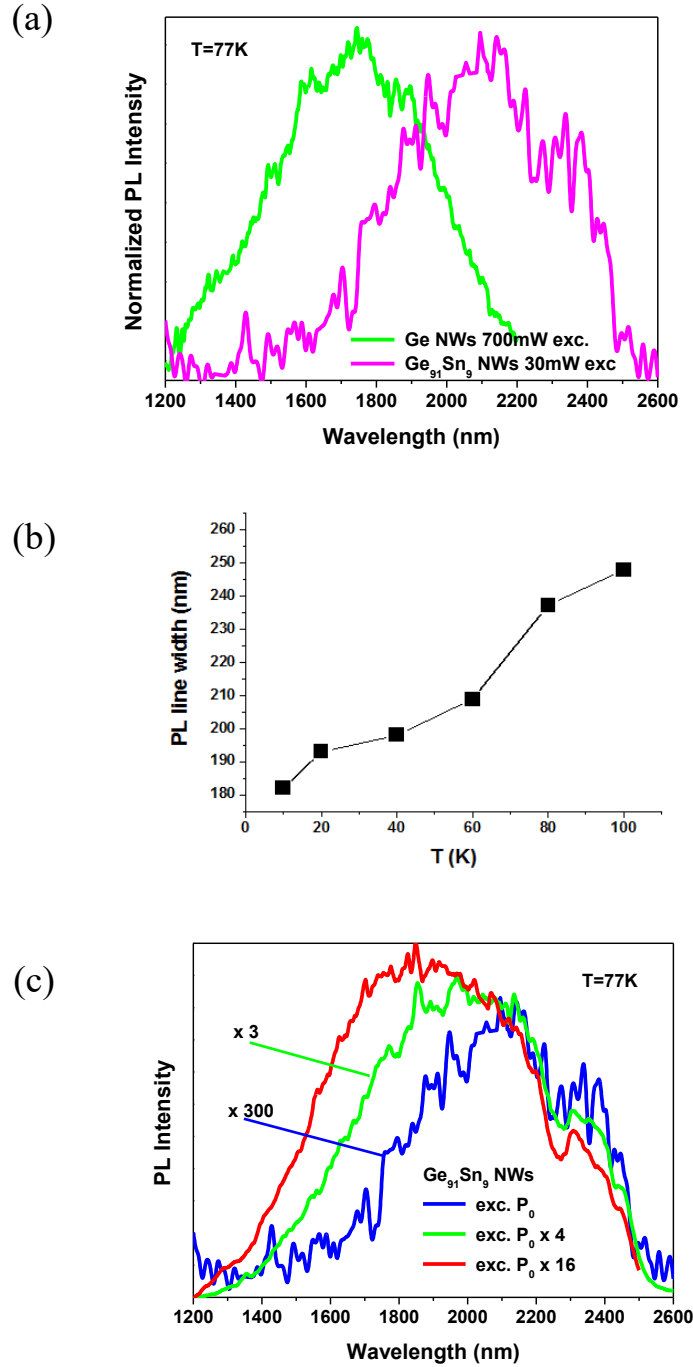


**Figure A2.12:** (a) Comparison between Ge and GeSn nanowires at 77 K. In order to achieve similar emission intensity the excitation power in the case of Ge nanowires was 700 mW in comparison with 30 mW for GeSn nanowires. (b) PL Line width as a function of temperature for 9.2 at. % Sn incorporated GeSn nanowire. (c) Power-dependent photoluminescence of GeSn nanowires at 77 K. Spectrum for low power ( $P_0 = 30$  mW) enhanced by a factor of 300 for clarity

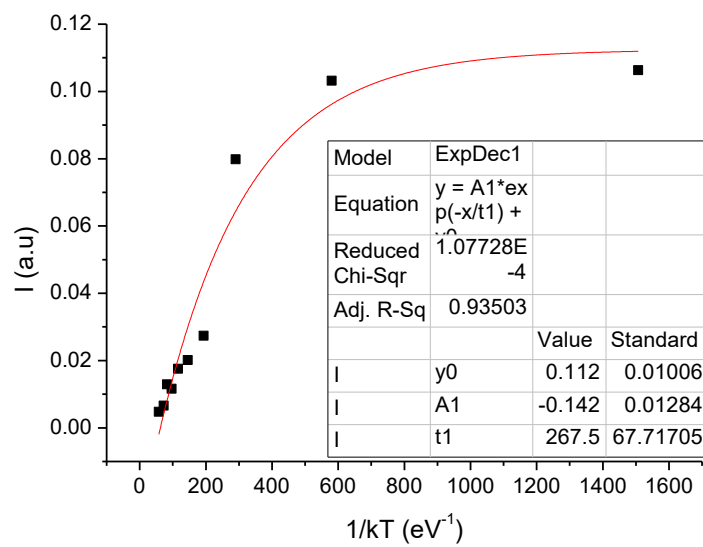


**Figure A2.13:** Arrhenius plot for GeSn nanowires with 6 at. % Sn shows poor agreement with single exponential decay model.

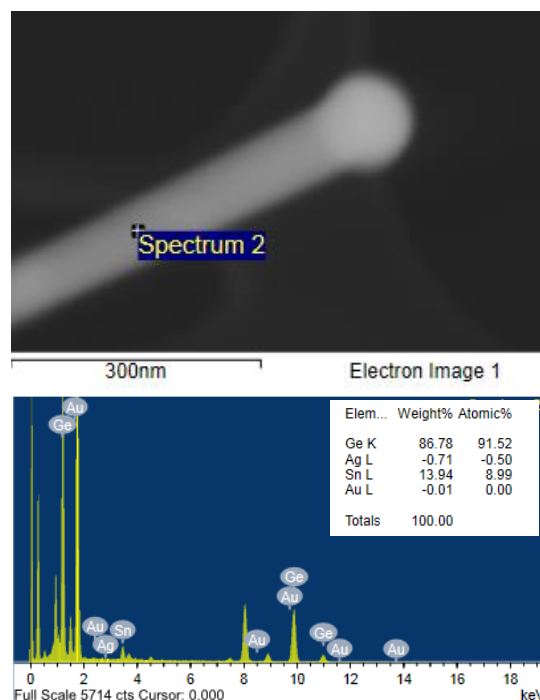


**Figure A2.14:** Point EDX from  $\text{Ge}_{1-x}\text{Sn}_x$  nanowire grown with step cooling confirms presence of any traceable amount of Au or Ag in the nanowire.

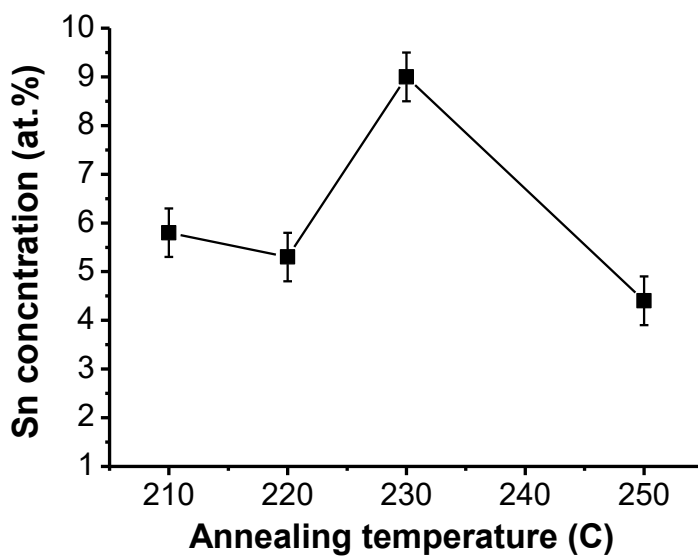


**Figure A2.15:** EDX concentration profile of Sn for different nanowires samples with different step cool-down temperature. Highest Sn is observed for 230 °C. Error bar represent typical error of 0.5 at. % in EDX measurement.

# Chapter 3

## Influence of Growth Kinetics on Sn Incorporation in Direct Band gap $\text{Ge}_{1-x}\text{Sn}_x$ Nanowires

This chapter has been published as a peer-reviewed article in RSC Journal of Materials Chemistry C. Consequently, sections of the chapter such as the abstract and introduction may contain repeating concepts and paragraphs. I co-wrote this paper with SB and JDH, and performed the nanowire synthesis. I carried out the elemental analysis and analysed the structural (QR), Raman (TB and AS) and optical data (DS and TO).

Doherty, J.; Biswas, S.; Saladukha, D.; Ramasse, Q.; Bhattacharya, T. S.; Singha, A.; Ochalski, T. J.; Holmes, J. D. Influence of Growth Kinetics on Sn Incorporation in Direct Band gap  $\text{Ge}_{1-x}\text{Sn}_x$  Nanowires *Mater. Chem. C*, **2018**, 6, 8738-8750.



### 3. Influence of Growth Kinetics on Sn Incorporation in Direct Bandgap $\text{Ge}_{1-x}\text{Sn}_x$ Nanowires

---

#### 3.1. Abstract

$\text{Ge}_{1-x}\text{Sn}_x$  alloys with substantial incorporation of Sn show promise as direct bandgap group IV semiconductors. This article reports the influence of growth kinetics on Sn inclusion in  $\text{Ge}_{1-x}\text{Sn}_x$  alloy nanowires through manipulation of the growth constraints, i.e. temperature, precursor type and catalyst.  $\text{Ge}_{1-x}\text{Sn}_x$  nanowire growth kinetics were manipulated in a vapour-liquid-solid (VLS) growth process by varying the growth temperature between 425 and 470 °C, using Au and Ag alloys as growth catalysts and different tin precursors such as allyltributyltin, tertaethyltin and tetraallyltin. The profound impact of growth kinetics on the incorporation of Sn; from 7 to 9 at. %; in  $\text{Ge}_{1-x}\text{Sn}_x$  nanowires was clearly apparent, with the fastest growing nanowires (of comparable diameter) containing a higher amount of Sn. A kinetically dependent “solute trapping” process was assigned as the primary inclusion mechanism for Sn incorporation in the  $\text{Ge}_{1-x}\text{Sn}_x$  nanowires. The participation of a kinetic dependent, continuous Sn incorporation process in the single-step VLS nanowire growth resulted in improved ordering of the  $\text{Ge}_{1-x}\text{Sn}_x$  alloy lattice; as opposed to a randomly ordered alloy. The amount of Sn inclusion and the Sn impurity ordering in  $\text{Ge}_{1-x}\text{Sn}_x$  nanowires has a profound effect on the quality of the light emission and on the directness of the band gap as confirmed by temperature dependent photoluminescence study and electron energy loss spectroscopy.

### 3.2. Introduction

A major hindrance to the integration of group IV materials in optoelectronic devices is the lack of a direct bandgap in both Si and Ge.<sup>1</sup> A direct bandgap group IV semiconductor would be beneficial for efficient band-to-band tunnelling devices, such as a tunnelling field effect transistor (TFET),<sup>2,3</sup> for lasing platforms<sup>4,5</sup> and for the development of mid-IR photonic devices such as waveguide amplifiers and multi-wavelength light sources.<sup>6</sup> A number of researchers have reported both theoretically and experimentally that a direct bandgap can be achieved in Ge by alloying the semiconductor with Sn,<sup>7,8</sup> lowering the separation between indirect (L) and direct ( $\Gamma$ ) valleys (140 meV in bulk Ge) in the conduction band of Ge.<sup>9</sup>

The fabrication of direct bandgap  $\text{Ge}_{1-x}\text{Sn}_x$  alloys in 1D nanoforms is imperative for the manufacturing of nanoelectronic devices, such as TFETs and gate-all-around FETs<sup>2,3,10</sup> as the 1D morphology provides excellent electrostatic control over the channel. Unlike Si and SiGe nanosystems, where an external perturbation such as strain is necessary to obtain a direct bandgap transition,<sup>10</sup> a direct bandgap transition in  $\text{Ge}_{1-x}\text{Sn}_x$  nanowires can be obtained through band mixing and deformation.<sup>11,12</sup> The generation of  $\text{Ge}_{1-x}\text{Sn}_x$  nanowires have been previously reported *via* both top-down fabrication<sup>13,14</sup> and bottom-up growth.<sup>15–17</sup> However, the etch chemistry required to fabricate highly crystalline, uniform top-down  $\text{Ge}_{1-x}\text{Sn}_x$  nanowires is, as of yet, still in its infancy, and bottom-up grown nanowires often exhibit low aspect ratios and non-uniform morphologies, with bending and kinking, thus restricting efficient light emission from these materials.<sup>15</sup> Taking account of the lack of optically efficient group IV alloy nanomaterials, we have recently reported the fabrication of direct bandgap  $\text{Ge}_{1-x}\text{Sn}_x$  nanowires with up to 9.2 at. % Sn *via* a two-step catalytic bottom up growth.<sup>12</sup> In this approach, Sn was incorporated into the Ge nanowire at the growth

temperature during VLS growth<sup>18,19</sup> and an additional after-growth dissolution process at the Ge-Sn eutectic temperature, resulting in high incorporation of Sn in Ge where Sn atoms are randomly ordered in the  $\text{Ge}_{1-x}\text{Sn}_x$  lattice. Impurity ordering in semiconductor alloys provide an additional engineering of freedom as the ordering is associated with the electronic band structure such as reduction of band gap, degeneracy at the valence band, emission width and lifetime.<sup>20,21</sup> In the case of  $\text{Ge}_{1-x}\text{Sn}_x$  nanowire, a randomly ordered alloy resulted in luminescence with broad linewidths which are not ideal for photonic devices.<sup>12</sup>

Therefore, incorporation of a substantial amount ( $x > 0.09$  is desired for direct band gap) of Sn into a 1D Ge host lattice during VLS growth process, where the impurity atoms are assimilated directly and in a more ordered way during the three phase growth *via* solute-trapping, is imperative for further engineering of the band structure and emission characteristics of  $\text{Ge}_{1-x}\text{Sn}_x$  nanowires. A perfectly binary/ternary alloy would produce a completely random distribution in terms of atomic ordering of impurities. A deviation from this random distribution can generate “short-range ordering”<sup>20</sup> of at least one of the atomic constituents of the alloy with an impact on the basic properties of the alloyed semiconductors.<sup>22,23</sup> The uniform and relatively ordered distribution of Sn impurities in a 1-D alloy lattice during the VLS nanowire growth can be achieved *via* the “solute trapping” process, where the impurities are incorporated by solute redistribution at the catalyst-nanowire interface *via* an increase of chemical potential and deviation of the partition coefficient.<sup>12,18,19,24</sup> As a kinetic dependent incorporation model, solute trapping of foreign adatoms, *i.e.* the incorporation of Sn impurities, can be altered/controlled by influencing the kinetics of the growth system. Manipulation of the rate determining steps in VLS growth allows the velocity at which nanowires grow to be controlled thus giving an opportunity to engineer

impurity incorporation, as according to the solute trapping mechanism, an increase in the growth rate of a nanowire will increase the impurity incorporation in the nanowire body. Growth kinetics of semiconductor nanowires can be modified by influencing the concentration of the growth species in the vapour phase, by using high temperatures to induce faster cracking of precursors or by using precursors with higher catalytic decomposition rates. These growth parameters directly influence supersaturation;  $\Delta\mu$ ; to manipulate the growth rate of nanowires by altering the partial pressure of the vapour source. Increased supersaturation and hence the nanowire growth rate can also be achieved by lowering the equilibrium concentration ( $C_e$ ) of the growth species in the liquid seeds in the VLS growth, with the use of bi-metallic growth catalysts.<sup>24</sup>

This article describes how growth parameters such as temperature, precursor and catalyst composition influence  $\text{Ge}_{1-x}\text{Sn}_x$  nanowire growth kinetics. We demonstrate the influence of nanowire growth kinetics on the subsequent solute trapping and incorporation of Sn in the  $\text{Ge}_{1-x}\text{Sn}_x$  nanowires. The quantitative (amount of Sn) and qualitative (homogeneity and ordering of Sn) characteristics of Sn incorporation in  $\text{Ge}_{1-x}\text{Sn}_x$  is verified through elemental microscopic analysis, high resolution microscopy and Raman spectroscopy. Influence of Sn concentration and ordering on the nature of the light emission (band gap transition, emission widths, band gap *etc.*) from the  $\text{Ge}_{1-x}\text{Sn}_x$  alloy nanowires are also explored *via* temperature dependent photoluminescence and electron energy loss spectroscopy.

### 3.3. Experimental

#### 3.3.1. Method

For the growth of  $\text{Ge}_{1-x}\text{Sn}_x$  nanowires dodecanethiol-stabilised, phase pure, Au and AuAg alloy nanoparticles were used as growth seeds. Colloidal nanoparticles were synthesised by co-reducing a mixture of chloroauric acid ( $\text{HAuCl}_4$ ) and silver nitrate ( $\text{AgNO}_3$ ) in a chloroform/water biphasic solution.<sup>12,25–27</sup> These metal nanoparticles were spin-coated onto a Si (001) substrate with native oxide. The substrate was loaded into a metal reaction vessel which was then left under vacuum at 180 °C overnight to ensure a moisture free growth atmosphere and the desorption of the surfactant molecules.

Solutions of diphenylgermane (DPG) and Sn precursors in anhydrous toluene were prepared in an  $\text{N}_2$  filled glove box with a typical Ge and Sn precursor concentration of 0.025 mL and 0.0075 mL respectively in 10 mL toluene. A solution containing both Ge and Sn precursors was loaded into a Hamilton sample-lock syringe inside the nitrogen-filled glovebox. Prior to injection, the coated Si substrate was further annealed for 15 min at 440 °C under a flowing  $\text{H}_2/\text{Ar}$  atmosphere inside a tube furnace to heat the Si substrate to 440 °C. The precursor solution was then injected into the metal reaction vessel using a high-pressure syringe pump at a rate of 0.025 mL  $\text{min}^{-1}$ . A  $\text{H}_2/\text{Ar}$  flow rate of 0.6 sccm was maintained during the entire growth period. A typical nanowire growth time was 2 h.

To explore the limits of kinetic dependent solute trapping of Sn impurities in Ge nanowires, the following parameters of the system were varied; temperature, catalyst and precursor. The growth

temperature was varied in 15 °C increments from 425 °C to 470 °C. Three different precursors, allyltributylstannane (ATBS), tetraallyltin (TAT) and tetraethyltin (TET), were used as the Sn source. Also, phase pure Au and AuAg alloy nanoparticles ( $\text{Au}_{0.90}\text{Ag}_{0.10}$  and  $\text{Au}_{0.80}\text{Ag}_{0.20}$  nanoparticles) of 4-5 nm diameter were explored as catalysts (see 3.7. Appendix Figure A3.1).

### 3.3.2. Characterisation

Bottom-up grown  $\text{Ge}_{1-x}\text{Sn}_x$  nanowires were imaged on a FEI Helios NanoLab 600i scanning electron microscope (SEM). All energy-dispersive X-ray (EDX) measurements were recorded in high-angle annular dark-field mode in the FEI Helios NanoLab 600i operating at 30 kV and 0.69 nA with an attached Oxford X-Max 80 detector. Error in the EDX measurements indicates a standard error of 0.5 at. %. Nanowire length and diameter measurements were determined using SEM images on ImageJ, in which the nanowires were clearly visible from end to end. Mean values for the length and diameter of the nanowires were determined from a minimum of 50 nanowires. Helium Ion Microscope (HIM) images were obtained using a Zeiss ORION Nanofab. TEM analysis was performed on a JEOL JEM-2100 operating at 200 kV in bright-field condition for imaging. High-resolution STEM imaging and EELS mapping was performed using a Nion UltraSTEM100 microscope, operated at 100 kV. Probe-forming optics were adjusted to deliver a 0.9 Å probe, with 120 pA beam current and 31 mrad convergence semi-angle. EELS data were acquired on a Gatan Enfina spectrometer, at 1 eV per channel to capture both the Sn and Ge edges simultaneously. As a result, the effective energy resolution was limited to 2.5 eV by the detector point spread function (B3 pixels), even though the cold field emission gun of the instrument had a native energy width of 0.35 eV in the operating conditions. Raman scattering measurements were performed in a backscattering geometry using a micro-Raman setup consisting of a spectrometer

(model LabRAM HR, Jobin Yvon) and a Peltier-cooled charge-coupled device detector. An air cooled He-Ne laser of wavelength 488 nm with intensity of  $1.77 \times 10^7 \text{ W/m}^2$  was used as an excitation source, with a spot size of 700 nm. PL data was obtained using a Ti:Sa pulsed laser as the excitation source, tuned to 950 nm with 80 MHz repetition rate, 300 fs pulse width and 0.2 W average power. The laser spot was focused to a 9  $\mu\text{m}$  spot, providing  $200 \text{ kW/cm}^2$  of pump power density. Samples were chilled in liquid nitrogen cryostat down to 80 K. PL was detected by a liquid nitrogen chilled InAs detector with a sensitivity range from 0.9  $\mu\text{m}$  to 3  $\mu\text{m}$  ( $\sim 0.41\text{-}1.338 \text{ eV}$ ). Thermogravimetric Analysis (TGA) was carried out on a Mettler Toledo TGA/DSC 1 Star System using a  $20 \text{ }^\circ\text{C/min}$  ramp rate from 25 to  $600 \text{ }^\circ\text{C}$  under a flow of nitrogen gas.

### 3.4. Results and Discussion

The growth kinetics of the  $\text{Ge}_{1-x}\text{Sn}_x$  nanowires can be influenced through the manipulation of the growth parameters of the system. Increased growth kinetics should result in a faster growth rate, and therefore longer nanowires. Solute trapping, a kinetically dependent trapping model,<sup>18,19</sup> directly links nanowire growth rate to impurity incorporation. Any impurity, such as Sn, incorporation through solute trapping should increase with increasing nanowire growth kinetics. Therefore, controlling the  $\text{Ge}_{1-x}\text{Sn}_x$  nanowire growth parameters should allow optimisation of Sn incorporation into the nanostructures. The growth kinetics of nanowires fabricated *via* VLS growth are dependent on the following: (i) the incorporation of the growth species from the vapour phase to the liquid growth promoter, (ii) the diffusion of the growth species inside the liquid melt and (iii) crystallisation of the growth material at the liquid-solid interface.<sup>28</sup> In a supersaturation limited process, the rate determining steps for VLS growth are believed to be steps (i)<sup>29,30</sup> and (iii).<sup>28</sup> The supersaturation,  $\Delta\mu$ , is the chemical potential difference between adatoms of the growth species in the vapour phase and the solid crystal phase<sup>26</sup> with  $v \propto \left[\frac{\Delta\mu}{kT}\right]^2$ , where  $v$  is the growth velocity of a crystal. Supersaturation directly influences nanowire growth kinetics and can be manipulated *via* the use of catalysts with different equilibrium concentration of growth species<sup>31</sup> (3.7. Appendix, Equation A3.1). Incorporation of the growth species into the liquid seed can also be manipulated to promote faster growth kinetics by employing higher temperatures<sup>32</sup> and precursors with high catalytic decomposition rates.

To understand the influence temperature had on the growth kinetics and on Sn incorporation in the nanowires, and to determine the optimum growth temperature, the temperature was varied from



425 to 470 °C in increments of 15 °C. Growth kinetics have previously been shown to heavily influence the Sn incorporation in GeSn films<sup>33,34</sup> where the Sn incorporation decreases with increasing temperature, while growth rate increases. However as of yet there has been no such verification on the influences of temperature on Sn incorporation in GeSn nanowires. We have limited the temperature range deliberately between 425 and 470 °C as; (i) below 425 °C the nanowire yield becomes poor due to poor decomposition of Ge precursor (DPG) and (ii) above 470 °C due to fast decomposition of low boiling point Sn precursors, homogenous nucleation of Sn dominates resulting in spherical Sn clusters and a possible decrease in Sn content in the nanowires. The other experimental parameters ( $\text{Au}_{0.90}\text{Ag}_{0.10}$  nanoparticle catalyst and Ge:Sn initial molar ratio of 85:15) were kept constant, based on prior  $\text{Ge}_{1-x}\text{Sn}_x$  nanowire growth experience<sup>12</sup> using DPG and ATBS as Ge and Sn precursors respectively. Figure 3.1 shows SEM images of  $\text{Ge}_{1-x}\text{Sn}_x$  nanowires grown at temperatures ranging from 425 to 455 °C. Distribution of nanowire lengths for each temperature is depicted in Figure 3.1(d) and shows the growth of the longest nanowires at 440 °C. The mean Sn content in the nanowires grown at different temperature is provided in Figure 3.1(e). The nanowires grown at 440 °C, with a mean length of  $2.21 \pm 1.35 \mu\text{m}$ , contained the highest Sn content (6.5 at. %). Also, the formation of spherical Sn clusters was minimal for nanowires grown at 440 °C, as shown in Figure 3.1(b).

High growth temperatures can influence the precursor decomposition and partial precursor pressure and hence the incorporation of growth species into the catalyst during VLS growth, thus increasing the nanowire growth velocity. Also, in contrary, considering the nanowire growth as a crystallisation limited process, longer nanowires at lower growth temperatures could be justified from classical crystal growth theory,<sup>26,28</sup> as growth velocity ( $v$ ) is proportional to  $\left(\frac{\Delta\mu}{kT}\right)^2$ , where  $T$

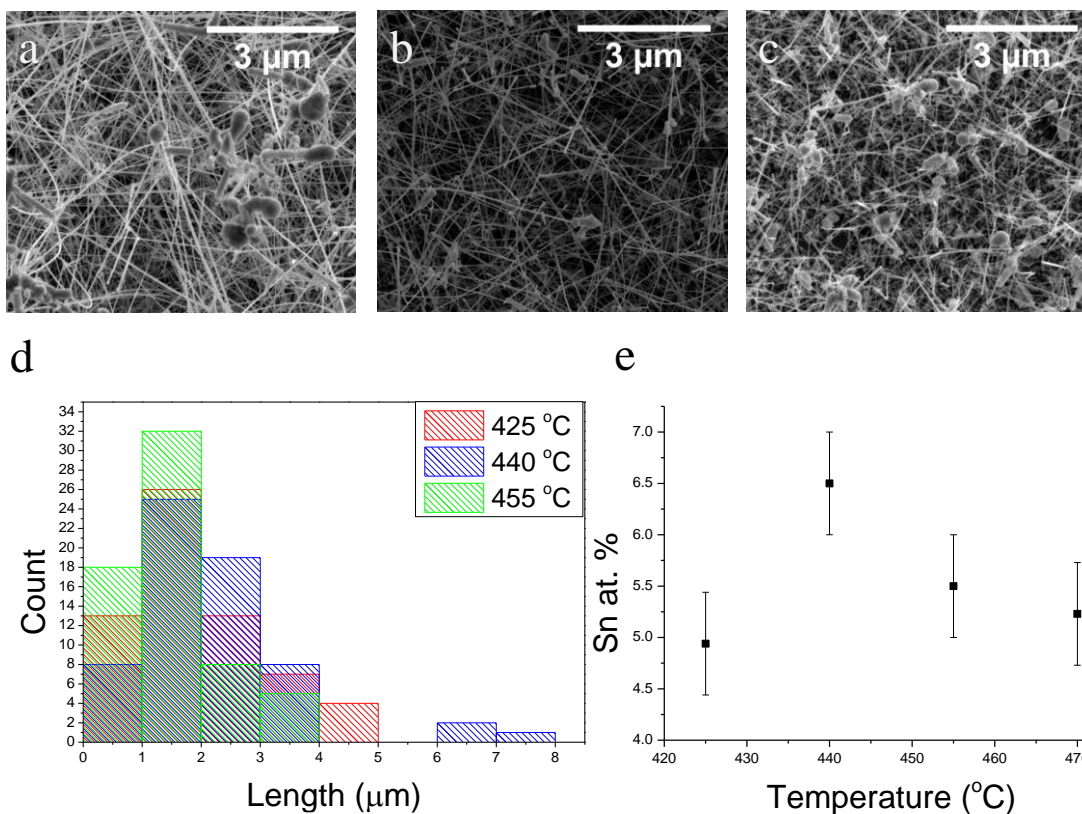


**Figure 3.1.** SEM images of Ge<sub>1-x</sub>Sn<sub>x</sub> nanowires grown using ATBS as the Sn source, catalysed by Au<sub>0.90</sub>Ag<sub>0.10</sub> nanoparticles at (a) 425 °C, (b) 440 °C and (c) 455 °C. (d) Nanowire length distributions for each sample. Plot in part (e) displays the varying Sn incorporation with temperature. Error bars represent the typical error of 0.5 at. % in EDX elemental measurements.

is the synthesis temperature and  $\Delta\mu$  is supersaturation. However, in our atmospheric pressure VLS experiments the effect of temperature on the growth kinetics is influenced by both the kinetic driven precursor decomposition at elevated temperature and crystallisation at the triple-phase interface. The change in the growth temperature was minimal (between 425 to 470 °C) to negate heavily influencing the decomposition of DPG and ATBS to affect the partial precursor pressure and incorporation of Ge and Sn in the catalysts, with both catalysts decomposing below 425 °C. Whereas the crystallisation at the triple phase interface at different temperatures can play a defining role in determining the overall rate of nanowire growth and thus the extent of Sn incorporation.

Competitive kinetics between these two temperature dependent processes determine the nanowire growth kinetics. At high growth temperatures (455 and 470 °C), the lower Sn content in the nanowires compared to the nanowires grown at 440 °C (Figure 3.1(e)) could be a direct result of the slower growth kinetics (mean nanowire length of 2.21  $\mu\text{m}$  at 440 °C compared to 1.55  $\mu\text{m}$  at 455 °C) resulting from slow crystallisation at triple phase boundary at elevated temperature.

To further investigate suitable Sn impurity precursors for improving Sn incorporation in the  $\text{Ge}_{1-x}\text{Sn}_x$  nanowires, alternative Sn sources to ATBS were utilised, *i.e.* tetraallyltin (TAT, boiling point of 269 °C) and tetraethyltin (TET, boiling point of 181 °C). Precursors whose boiling points were much lower than ATBS (353 °C) were chosen in an effort to promote faster decomposition and higher Sn incorporation. The optimal growth temperature was held at 440 °C with other precursors, as higher growth temperature would result in rather fast precursor decomposition and homogenous Sn nucleation. In each of these compounds, the Sn molecule is bonded to four carbon atoms by single bonds. ATBS, as previously shown in Figure 3.1, is a suitable precursor for incorporating large amounts (6.5 at. %) of Sn into the Ge lattice while keeping the structural and morphological quality intact. High Sn incorporation and controlled nanowire morphology with ATBS as a Sn precursor is due to the similar decomposition kinetics and boiling points of ATBS and diphenyl germane (DPG), 353 and 325 °C respectively at atmospheric pressure. Using TAT as a Sn source resulted in  $\text{Ge}_{1-x}\text{Sn}_x$  nanowires with an overall lower Sn content of < 2 at. % with an  $\text{Au}_{0.90}\text{Ag}_{0.10}$  catalyst (3.7. Appendix, Figure A3.2). Significant Sn segregation and spherical clustering was apparent when TAT was used as the Sn source (3.7. Appendix, Figure A3.2), compared with ATBS or TET. This clustering, and low Sn incorporation, may be due to the instability of TAT under the reaction conditions due to the presence of four carbon-carbon double

bonds<sup>35</sup>. Thermogravimetric analysis (TGA) of the Sn precursors revealed that their decomposition temperatures related directly to their boiling points (3.7. Appendix, Figure A3.3).

The third Sn precursor of choice, TET, produced long  $\text{Ge}_{1-x}\text{Sn}_x$  nanowires with a high Sn content, negligible Sn clustering and uniform diameter ( $57.4 \pm 15.2$  nm) with the  $\text{Au}_{0.90}\text{Ag}_{0.10}$  nanoparticle catalyst (Figure 3.2). An initial Ge:Sn molar ratio of 77:23 was determined as optimal for the growth of  $\text{Ge}_{1-x}\text{Sn}_x$  nanowires; a Ge:Sn molar ratio of 85:15, which was used with ATBS as the Sn source, resulted in ‘branched’ nanowires consisting of a large nanowire “trunk” with smaller nanowire “branches” (3.7. Appendix, Figure A3.4). An SEM image of the nanowires grown at 440 °C using TET with an  $\text{Au}_{0.90}\text{Ag}_{0.10}$  catalyst is shown in Figure 3.2(a). A mean Sn concentration of

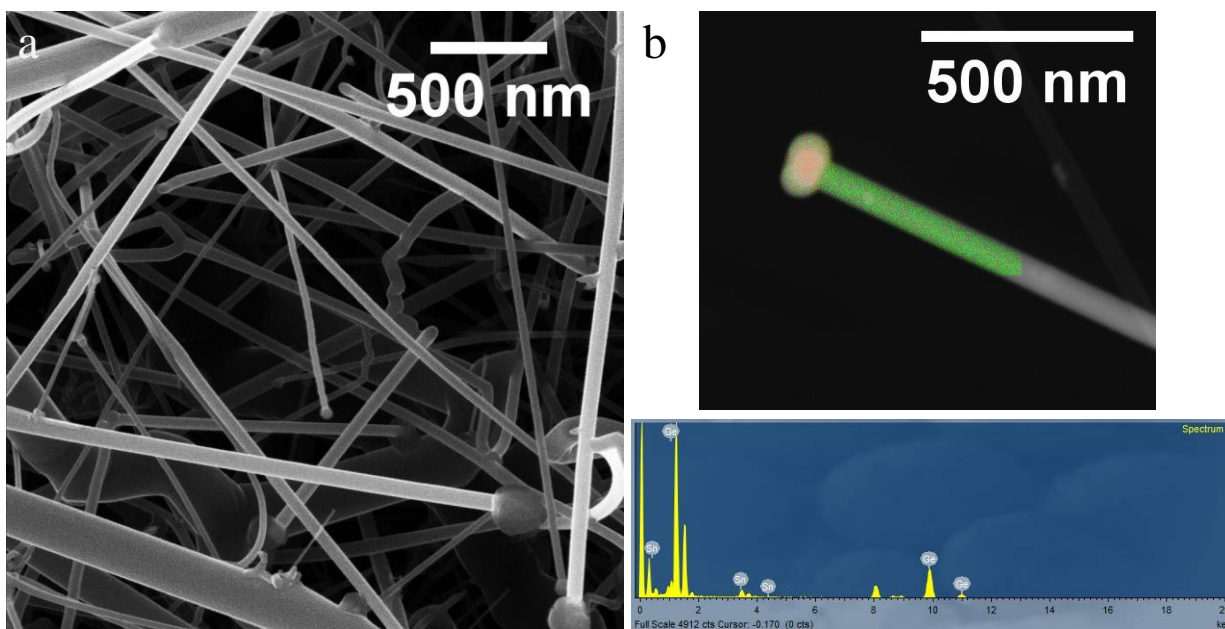


**Figure 3.2:** (a) Helium ion microscope (HIM) image of  $\text{Ge}_{1-x}\text{Sn}_x$  nanowires with average Sn content of 8.7 at. %, synthesised with TET with  $\text{Au}_{0.90}\text{Ag}_{0.10}$  nanoparticles as growth promoters. Part (b) shows a single nanowire EDX elemental map with corresponding spectra: Sn is denoted by red and Ge by green, demonstrating the homogeneous distribution of Sn in the nanowire.

8.7 %  $\pm$  0.7 % was determined *via* EDX analysis of the nanowires grown with TET as a precursor, an increase of 2.2 at. % when compared to nanowires grown under the same conditions using ATBS (6.5 at. % Sn). To ensure that the Sn in these  $\text{Ge}_{1-x}\text{Sn}_x$  nanowires was homogeneously distributed in the nanowire, *i.e.* without Sn segregation in the bulk or surface of the nanowire or a gradual decrease in the Sn content from the seed to the end of a nanowire, EDX maps (Figure 3.2(b)) and linescans (3.7. Appendix, Figure A3.5) were obtained for individual nanowires. The lack of Sn segregation is verified by the absence of bright red spots (corresponding to Sn) in the elemental map shown in Figure 3.2(b). Precursor choice had a clear impact on the Sn incorporation of the  $\text{Ge}_{1-x}\text{Sn}_x$  nanowires, with TET producing nanowires with the highest Sn content while maintaining uniform diameter and negligible tapering. As encouraging results in terms of morphology and Sn content was obtained with TET at 440 °C, an experiment was carried out at 470 °C using TET as the Sn source to verify the influence of temperature with TET as Sn precursor. This elevated temperature resulted in a lower yield of nanowires, numerous spherical Sn clusters and erratic Sn content (between 4 – 8 at. %) in the nanowires (3.7. Appendix, Figure A3.6). Though decreasing the temperature may have positive influence on triple phase crystallisation (independent of precursor characteristics) we did not observe an increase in growth rate at 425 °C with ATBS. Thus we have restricted experiments with TET between 440 and 470 °C.

An alternative method to increase the growth rate and thus potentially the Sn incorporation in  $\text{Ge}_{1-x}\text{Sn}_x$  nanowires is to increase the supersaturation  $\Delta\mu$ ; chemical potential difference between adatoms of growth species in the vapour phase and the solid crystal phase; as per classical crystal growth theory.<sup>28</sup> A higher  $\Delta\mu$  promotes a faster crystallisation rate, thus increasing the growth velocity of the nanowire. In our previous work, we demonstrated an effective way to increase the

supersaturation for the group IV nanowires by lowering the equilibrium concentration ( $C_e$ ) of the growth material in a liquid metastable alloy, *e.g.* Au-Ge, as  $\Delta\mu = kT \ln\left(\frac{C}{C_e}\right)$  where  $C$  is the concentration of the growth species. To lower the  $C_e$  of a growth species, a foreign species can be added to the metal seed particle which will shift the liquidus phase boundary of the growth species towards a lower solute concentration. For a nanoscopic system having high surface-to-volume ratio, the contribution of the surface energy to the thermodynamics is prominent, resulting in a diameter dependent growth rate. Nanowire growth and the expression ( $\Delta\mu = \Delta\mu_0 - \frac{4\Omega\alpha}{d}$ , where  $\Omega$  is atomic volume of Ge and  $\alpha$  represents specific free energy of the wire surface) for radial dependent chemical potential and hence supersaturation clearly indicate a growth rate increment with a decrease in equilibrium concentration of Ge in the metastable phase, as  $\Delta\mu \propto \ln\left(\frac{C}{C_e}\right)$  for a certain diameter range. For Ge nanowires, alloying Au catalyst seeds with Ag (up to a certain limit of Au<sub>0.80</sub>Ag<sub>0.20</sub>) promotes growth rates of up to 5 times as fast when compared to the growth with pure Au.<sup>26</sup> AuAg metal alloy catalysts trigger faster growth rates for the same diameter ( $d$ ) nanowires when compared to those grown from a pure Au catalyst, due to the change in equilibrium concentration of Ge and thus supersaturation in the metastable liquid alloy. Taking account of this influence of alloy seeds on the nanowire growth, phase pure Au and three AuAg alloy nanoparticles (Au<sub>0.90</sub>Ag<sub>0.10</sub>, Au<sub>0.80</sub>Ag<sub>0.20</sub> and Au<sub>0.70</sub>Ag<sub>0.30</sub>) were explored as catalysts for Ge<sub>1-x</sub>Sn<sub>x</sub> growth. All of the nanoparticle catalysts had diameters between 4-5 nm (3.7. Appendix, Figure A3.1). TET, which was determined as an ideal Sn precursor for large Sn incorporation, was used as the precursor with all three catalysts. An increase in the length, as well as Sn content, of the nanowires was observed in correspondence with increasing Ag in the nanoparticle alloys (Figure 3.3). Au seeded nanowires grown at 440 °C with TET as a tin source contained 7.4 at. % Sn, whereas those seeded with Au<sub>0.90</sub>Ag<sub>0.10</sub> and Au<sub>0.80</sub>Ag<sub>0.20</sub> seed under the same growth conditions

contained 8.7 at. % and 9.1 at. % respectively. With a further increase in the amount of Ag in the AuAg seed, the nanowires catalysed by  $\text{Au}_{0.70}\text{Ag}_{0.30}$  contained large amounts of Sn ( $\sim 10.9$  at. % Sn) however the resulting nanowires were low in yield, had irregular morphologies and were highly tapered (3.7. Appendix, Figure A3.7). The tin distribution in  $\text{Au}_{0.70}\text{Ag}_{0.30}$  catalysed  $\text{Ge}_{1-x}\text{Sn}_x$  nanowires was also not uniform as depicted by EDX analysis (see EDX linescan in 3.7. Appendix, Figure A3.7(b)). As such,  $\text{Au}_{0.80}\text{Ag}_{0.20}$  nanoparticles were found to be the optimal catalyst for  $\text{Ge}_{1-x}\text{Sn}_x$  nanowire growth with TET as the Sn precursor, giving a high Sn content, uniform diameter nanowires ( $\sim 60$  nm), with no apparent evidence of nanowire tapering. An SEM image of  $\text{Ge}_{1-x}\text{Sn}_x$  nanowires grown with an  $\text{Au}_{0.80}\text{Ag}_{0.20}$  catalyst and TET as the precursor at  $440^\circ\text{C}$  can be seen in Figure 3.3(a). EDX point analysis on 50 nanowires provided an average Sn content of  $9.1 \pm 1.3$  at. % Sn in these  $\text{Ge}_{1-x}\text{Sn}_x$  nanowires. EDX maps and linescans were generated to confirm the homogenous distribution of Sn in the nanowires (3.7. Appendix, Figure A3.8). The lack of bright red spots in the body of the nanowires in the elemental map (3.7. Appendix, Figure A3.8(b)) further suggests the lack of Sn clustering and segregation in the bulk or on the surface of the nanowires. Figure 3.3(c) summarises the variation in the amount of Sn in the  $\text{Ge}_{1-x}\text{Sn}_x$  nanowires with increasing Ag in the nanoparticle catalyst. To verify the increased growth rate of these  $\text{Ge}_{1-x}\text{Sn}_x$  nanowires with increasing Ag content in the nanoparticle, the lengths of these nanowires were compared for similar diameters across the samples. As the nanowires catalysed

by  $\text{Au}_{0.70}\text{Ag}_{0.30}$  were irregular in both diameter and length and highly tapered, they were not included in the length comparison. The mean diameter of the nanowires catalysed with Au,  $\text{Au}_{0.90}\text{Ag}_{0.10}$  and  $\text{Au}_{0.80}\text{Ag}_{0.20}$  were in a similar size range;  $63.5 \pm 17.4$  nm,  $57.4 \pm 15.2$  nm and  $65.5 \pm 16.8$  nm respectively. This similarity in diameter excludes the influence of diameter on the growth kinetics (Gibbs-Thompson effect) which allows a direct comparison between the mean lengths of the  $\text{Ge}_{1-x}\text{Sn}_x$  nanowires grown from different seeds. The histogram shown in Figure

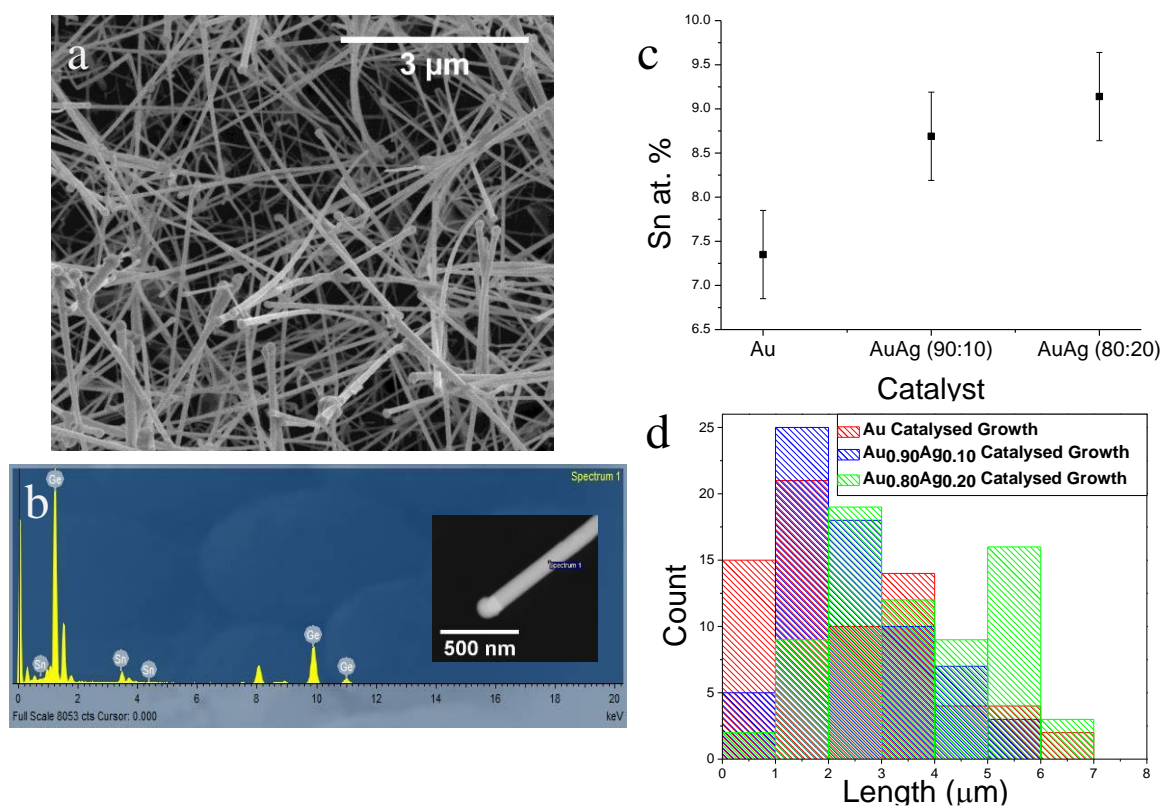


**Figure 3.3:** (a) SEM image of  $\text{Ge}_{1-x}\text{Sn}_x$  nanowires grown using TET as a Sn source, catalysed by  $\text{Au}_{0.80}\text{Ag}_{0.20}$  nanoparticles. EDX analysis in (b) confirms the high Sn incorporation ( $x = 0.091$ ). A graph demonstrating the increase in the amount of Sn incorporated into the nanowires with increasing Ag in the nanoparticle catalyst can be seen in (c). Error bars represent the typical error of 0.5 at. %. The length distributions of these samples in (d) show the increase in the mean nanowire length with increasing Ag content in the nanoparticle catalyst.



3.3(d) depicts the increasing mean nanowire length ( $2.44 \pm 1.54 \mu\text{m}$ ,  $2.63 \pm 1.63 \mu\text{m}$  and  $3.6 \pm 1.51 \mu\text{m}$  with Au,  $\text{Au}_{0.90}\text{Ag}_{0.10}$  and  $\text{Au}_{0.80}\text{Ag}_{0.20}$  catalysts respectively) with increasing Ag content in the nanoparticle catalyst. Thus the growth kinetics of  $\text{Ge}_{1-x}\text{Sn}_x$  nanowires have been increased by increasing the Ag content of the  $\text{Au}_x\text{Ag}_{1-x}$  catalysts. This increase in the growth kinetics manifests itself in increased Sn incorporation in the Ge nanowires with the  $\text{Au}_{0.80}\text{Ag}_{0.20}$  growth promoter (Figure 3.3(c)). During the nanowire growth process, with uptake of Sn from the vapour phase, the nanoparticle catalyst becomes largely Sn rich (3.7. Appendix, Figure A3.8). However, the initial composition of the AuAg nanoparticle catalyst influences the supersaturation of the system, which in turn impacts the nucleation and growth rate,<sup>36</sup> which is apparent from Figure 3.3(d).

Through the manipulation of the growth limiting factors of the  $\text{Ge}_{1-x}\text{Sn}_x$  nanowire system the growth kinetics have been influenced. This influence manifests itself in the increased growth rates and thus increased lengths of the nanowires. A distribution of the lengths of  $\text{Ge}_{1-x}\text{Sn}_x$  nanowires with 6.5, 7.4, 8.7 and 9.1 at. % Sn (3.7. Appendix, Figure A3.9(a)) details the relationship between the length and the Sn content. By influencing the growth kinetics to increase the growth rate of the  $\text{Ge}_{1-x}\text{Sn}_x$  nanowires, the Sn incorporation of the nanowires has been positively impacted. A comparison of the mean Sn content relative to the mean nanowire length of the  $\text{Ge}_{1-x}\text{Sn}_x$  nanowires (3.7. Appendix, Figure A3.9(b)) confirms the correlation between the growth kinetics of the system and the incorporation of Sn impurities. The increased growth kinetics of the  $\text{Ge}_{1-x}\text{Sn}_x$  nanowires, obtained by manipulating the growth limiting factors of the system, has resulted in nanowires with 9.1 at. % Sn through conventional VLS growth.

In the case of  $\text{Ge}_{1-x}\text{Sn}_x$  nanowires, due to the dependence of the Sn incorporation on the nanowire growth kinetics, we assert that Sn is incorporated *via* the solute trapping mechanism, a kinetically driven process,<sup>12,37</sup> as indicated by the increasing Sn inclusion with increasing length (Figure 3.3(d)). In the case of nanowires, solute trapping has already been suggested as the method of incorporation of Al, from the catalyst, into Si nanowires<sup>24</sup> where increased temperature resulted in faster growth kinetics of nanowire and higher Sn incorporation. Assuming layer by layer growth of the nanowires,<sup>38,39</sup> the step flow kinetics can result in solute trapping of Sn by each succeeding layer of the nanowire. Solute trapping describes the incorporation of impurities by solute redistribution at the catalyst-nanowire interface; there is an increase of chemical potential and deviation of the partition coefficient.<sup>18,19,40</sup> At this liquid-solid (catalyst-nanowire) interface, the difference in atomic concentration in the different phases is characterised by the equilibrium coefficient of the atomic distribution between phases,  $k_e$ . This equilibrium partition coefficient is related to the chemical potential difference, *i.e.* supersaturation  $\Delta\mu$ ; by  $k_e \propto \exp\left(-\frac{\Delta\mu}{RT}\right)$ . During nanowire growth, the large interface velocity at the liquid-solid interface relaxes the local chemical equilibrium which results in kinetic interface undercooling.<sup>41</sup> Impurity adatoms can be trapped on the high energy sites of the crystal lattice at a high solidification rate which can lead to the formation of metastable solids ( $\text{Ge}_{1-x}\text{Sn}_x$  with  $x > 0.01$ ) at the growth front.<sup>12</sup> This deviation of the chemical equilibrium at the interface is influenced by the interfacial diffusion speed,  $V_{DI}$ , a kinetic parameter where  $V_{DI} = -\frac{D_I}{\lambda}$ .  $V_{DI}$  is a ratio of the diffusion coefficient at the interface ( $D_I$ ) and the characteristic distance for the diffusion jump ( $\lambda$ ) which is equal to the width of the solid-liquid interface.<sup>18</sup>

For a given system with an equilibrium partition coefficient  $k_e$  and an interfacial diffusion  $V_{DI}$ , the amount of impurity trapped in the nanowire is governed by equation 1<sup>18</sup>:

$$k(V) = \frac{\left(1 - V^2/V_D^2\right) k_e + \frac{V}{V_{DI}}}{1 - V^2/V_D^2 + \frac{V}{V_{DI}}} \dots (Eq. 3.1)$$

Hence, as  $V$ , the interface velocity approaches infinity,  $k(V)$ , the solute partitioning function, approaches 1. Therefore, when the interfacial velocity is much greater than the diffusion speed ( $V_D$ , the characteristic bulk speed) solute trapping will increase with complete solute trapping at  $k(V) = 1, V \geq V_D$ . As such, impurity incorporation is primarily dependent on the interfacial velocity. In the case of  $\text{Ge}_{1-x}\text{Sn}_x$  nanowire, very slow bulk diffusion velocity of Sn in Ge<sup>42</sup> allows for the solute trapping of Sn to occur at the relatively slow interfacial growth velocity of the  $\text{Ge}_{1-x}\text{Sn}_x$  nanowires.

Hence, a variation in the interfacial velocity and nanowire growth kinetics during bottom-up VLS growth will influence the solute partitioning function and thus the “solute trapping” of an impurity into a nanowire. Also, by manipulating the supersaturation of the growth system, the equilibrium coefficient  $k_e$  and thus the solute partitioning function is affected to further influence the solute trapping as per  $k_e \propto \exp\left(-\frac{\Delta\mu}{RT}\right)$  seen above. Thus, the solute trapping of Sn in GeSn can be readily influenced by altering the kinetics of the growth system with the varied catalysts and precursors (as seen from the variation in Sn incorporation in Figure 3.3(c)). Other than the kinetic factors such as interfacial velocity and supersaturation, particularly for the Ge-Sn system, the incorporation of Sn is also aided by Sn’s negligible diffusion in Ge at the growth conditions, the epitaxial mismatch between Sn and Ge, the resulting elastic strain at the interface and the lack of

truncating side facets at the seed-nanowire interface (which can act as attractive sites for Sn aggregation).<sup>12</sup>

Raman Spectroscopy, a powerful and non-destructive tool, was used for the quantitative and qualitative assessment of the alloy nanowires. Figure 3.4(a) shows the Raman spectra of bulk Ge, pure Ge nanowire and the  $\text{Ge}_{1-x}\text{Sn}_x$  nanowires incorporated with different concentrations of Sn. By

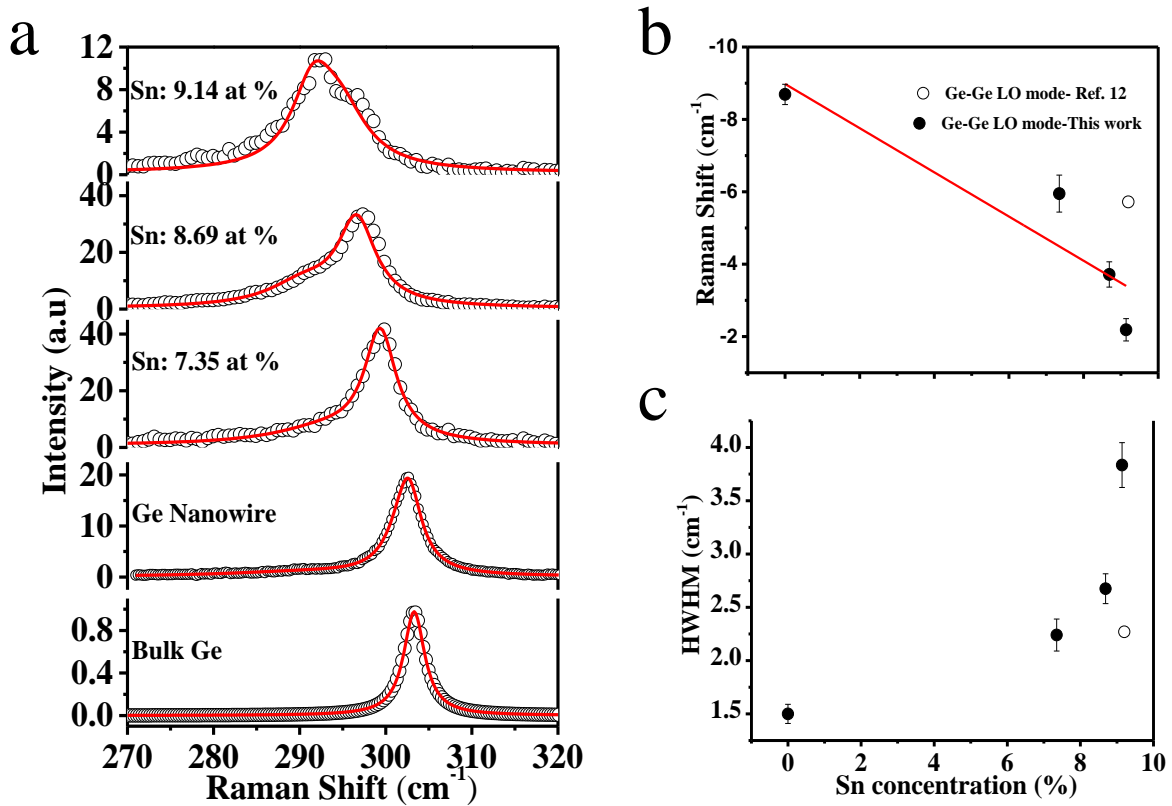


**Figure 3.4:** (a) Room temperature Raman spectrum for the Ge–Ge mode in  $\text{Ge}_{1-x}\text{Sn}_x$  alloy nanowires (where  $x$  varies from 0.07 to 0.09). (b) The downshift of Ge–Ge LO mode and (c) the HWHM of the Raman peak for the Ge–Ge mode of Ge–Sn alloy nanowires with Sn percentage variation. Experimental data are represented with dots which fits (straight line) well with the linear expression,  $\Delta\omega = ax$ . Black dots represent the characteristics of Ge–Ge LO mode of present study; white dots represent the Ge–Ge mode of  $\text{Ge}_{1-x}\text{Sn}_x$  nanowire grown with a two step process<sup>12</sup>. Error bars indicate the error associated with the instrumental resolution and fitting. The excitation wavelength is 488 nm.

dispersing the nanowires on a Cu grid and utilising a small spot size (700 nm), the measurements have been done on single nanowires. A very low laser power was used to avoid laser induced heating. For all of the samples the diameter of each measured nanowire is the same. The spectra are fitted with Lorentzian functions. In bulk, the Ge-Ge LO vibration is observed at  $303.3 \text{ cm}^{-1}$  whereas for the Ge NW this vibration shifts to  $302.7 \text{ cm}^{-1}$ , which is due to the phonon confinement effect. In  $\text{Ge}_{1-x}\text{Sn}_x$  alloys the Ge-Ge mode monotonically moves towards lower frequency (see Figure 3.4(b)) and shows asymmetry in the lower energy side of the spectrum due to the development of a Ge-Sn coupled vibrational mode<sup>43</sup> with increasing Sn concentration (as determined by EDX measurements). With Sn incorporation in the Ge lattice, both compositional variations and strain cause a shift of the Ge-Ge LO mode compared to bulk Ge as well as from phase pure Ge nanowire. The shift coefficient of the Ge-Ge mode can be written as  $\Delta\omega = \omega(\text{SnGe}) - \omega(\text{Ge}) = \Delta\omega_{\text{composition}} + \Delta\omega_{\text{strain}}$ .<sup>44</sup> The compositional dependence of Ge-Ge Raman modes can be understood by the combined effect of mass disorder and bond distortion. Participation of compressive and tensile strain towards the Raman shift is not justified for nanowire samples, as due to the large surface area, strain can be effectively released for these nanostructures. Compressive strain may originate from the surface oxides in nanowires. But this strain shifts the Ge-Ge Raman mode of the Ge nanowire towards higher frequency compared to unstrained Ge, whereas in our Ge nanowire, we have observed only red shift in phase pure as well as Sn incorporated Ge nanowire with respect to the highly pure bulk Ge. This result exhibits that the oxide layer induced strain effect is non-significant for our Ge nanowire samples. Therefore, the total shift of Ge-Ge frequency is mainly attributed to the alloy disorder. We have fitted the Raman peak shift ( $\Delta\omega$ ) against Sn composition ( $x$ ), as determined through EDX analysis, with a linear expression ( $\Delta\omega$ ) =  $ax$ , where  $a$  is a constant termed the alloy disorder coefficient.<sup>44</sup> For a fully

relaxed  $\text{Ge}_{1-x}\text{Sn}_x$  alloy the theoretical value for the alloy disorder coefficient is calculated as  $95 \text{ cm}^{-1}$ .<sup>145</sup> From the linear shift of experimental data presented in Figure 3.4(b) the value obtained for the alloy disorder coefficient was  $75.63 \text{ cm}^{-1}$  for the relaxed alloy nanowires. This is higher than the earlier report for  $\text{Ge}_{1-x}\text{Sn}_x$  nanowires,<sup>12</sup> where a smaller value ( $64.3 \text{ cm}^{-1}$ ) is attributed to a random alloying effect primarily in the nanowire sample with  $> 9 \text{ at. \% Sn}$  content. Apart from the Raman shift of the Ge-Ge mode a distinct increase in the half width at half maximum (HWHM) of the Ge-Ge LO mode on the low energy side was observed with increasing Sn concentration as shown in Figure 3.4(c).

To further evaluate impurity ordering in the  $\text{Ge}_{1-x}\text{Sn}_x$  ( $x > 0.09$ ) alloy nanowires, we compared the Raman signal from  $9.14 \text{ at. \% Sn}$  incorporated alloy nanowires with  $\text{Ge}_{1-x}\text{Sn}_x$  nanowires where Sn is incorporated *via* a “two step” solute trapping and precipitation dissolution process.<sup>12</sup> As all of the nanowire samples are similar in diameter and exhibit a standard deviation of approximately  $\pm 1 \text{ at. \% Sn}$  from their mean Sn contents, the  $\text{Ge}_{1-x}\text{Sn}_x$  nanowires presented in this work can be compared to those in ref. 12. Both the Raman shift and the HWHM of the Ge-Ge phonon mode from the alloy nanowire in ref. 12 are included in Figure 3.4 (b) and (c) respectively. A clear downshift in the Raman frequency was observed for the alloy nanowire grown in this work compared with the nanowire grown *via* two-step process. The calculated alloy disorder coefficient for the particular nanowire ( $x = 0.091$ ) sample grown in this work is also much larger ( $93.2 \pm 4.1 \text{ cm}^{-1}$ ) than the alloy nanowire ( $x = 0.092$ ) grown in ref. 12 ( $62.4 \text{ cm}^{-1}$ ). In fact, the alloy disorder coefficient for the nanowire with  $9.1 \text{ at. \% Sn}$ ; grown in this work is very near to the theoretical value for a perfectly relaxed  $\text{Ge}_{1-x}\text{Sn}_x$  alloy. Another interesting observation (Figure 3.4 (c)) is the much smaller low energy HWHM in case of alloy nanowires ( $9.2 \text{ at. \% Sn}$ ) grown in ref. 12. A

nanowire sample consisting of a mixture of partially ordered phase can lead to an apparent broadening of the low-energy half width of the Raman spectrum due to the appearance of additional Raman intensity at lower energies. The observation of large composition dependent Raman shift, high alloy disorder coefficient and a broad low-energy half width for the  $\text{Ge}_{1-x}\text{Sn}_x$  ( $x = 0.091$ ) nanowire implies an improvement in ordering of Sn *via* a single step inclusion process through trapping mechanism<sup>43,45</sup> when compared to previous work<sup>12</sup> where a two-step process was availed to encourage around 9 at. % Sn incorporation. Deviation from a perfectly random distribution and observation of short range ordering was previously observed through atom probe tomography in SiGeSn ternary alloy with > 4 at. % Sn content.<sup>20</sup>

The induction of impurity atoms into the nanowire lattice can induce defects at which impurities subsequently accumulate.<sup>46</sup> As such, it is imperative to determine the structural quality of the  $\text{Ge}_{1-x}\text{Sn}_x$  nanowires with large (> 9 at. %) Sn content. The dark field STEM images shown in Figure 3.5(a) display the single crystalline nature of the  $\text{Ge}_{1-x}\text{Sn}_x$  nanowires with the highest Sn incorporation (9.1 at. %).  $\text{Ge}_{1-x}\text{Sn}_x$  nanowires typically displayed a 1-2 nm oxide on the nanowire surface. A high resolution STEM image recorded in HAADF mode from a particular area of the nanowire, highlighted with the blue coloured box, depicts the high crystallinity of the nanowire. Generally, the crystal structure of the  $\text{Ge}_{1-x}\text{Sn}_x$  alloy nanowires, with various Sn incorporations, exhibited a 3C lattice arrangement without any stacking faults and twin boundaries. Measuring the spacing between 50 successive layers of the nanowire, recorded with <110> zone axis alignment, confirmed small fluctuation in the interplanar distance (3.7. Appendix Figure A3.10). This observation is in contrast with the large fluctuation in the interplanar spacing observed (3.7. Appendix, Figure A3.10) for the  $\text{Ge}_{1-x}\text{Sn}_x$  nanowires; grown with two step process; with 9.2 at. %

Sn incorporation, where a post-growth eutectic dissolution aided large Sn incorporation.<sup>12</sup> Relative order of atomic-scale randomness in  $\text{Ge}_{1-x}\text{Sn}_x$  alloy can generate varied local lattice distortion and spacing at an Ångström-level scale. Thus, small fluctuation of the interplanar spacing in the line profiles of the nanowires (3.7. Appendix, Figure A3.10) suggests an improvement over the atomic ordering of Sn impurities in  $\text{Ge}_{1-x}\text{Sn}_x$  alloy lattice where Sn is incorporated *via* a single solute trapping mechanism rather than *via* a eutectic diffusion and solubility process. The mean interplanar spacing of 0.34 nm between  $\{111\}$  planes is observed from Fast Fourier Transform (FFT) analysis of the HR STEM, which agrees well with the  $d$  value for bulk diamond Ge crystal of 0.326 nm (JCPDS 04-0545). This slight increase in the  $d$  spacing is to be expected upon the incorporation of Sn into the Ge host lattice due to the difference in the lattice constants of Ge and Sn which can instigate a lattice expansion. The nanowires predominantly displayed  $\langle 111 \rangle$  as the



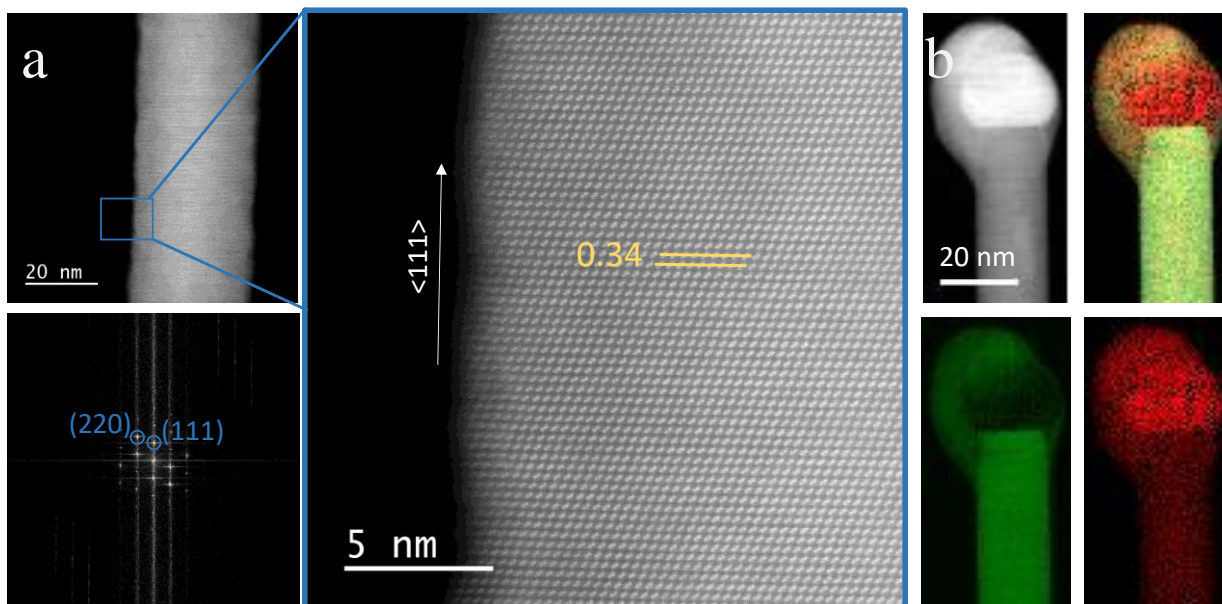


**Figure 3.5:** (a) High resolution STEM image of a  $\text{Ge}_{1-x}\text{Sn}_x$  nanowire with an average 9.1 at. % Sn. FFT confirms the formation for Ge-like diamond cubic  $\text{Ge}_{1-x}\text{Sn}_x$  crystal. This is also verified by lattice spacing measured for 50 successive planes. The nanowires are single crystalline with no apparent defects. EELS mapping in (b) displays the sharp interface between the catalyst seed and the nanowire body. Sn is denoted by red and Ge by green. Also a Sn rich GeSn phase segregated extension with “bulb” shape is observed around the seed.

growth direction which is the most common growth orientation for Ge nanowires with mean diameter above 50 nm.<sup>12,26</sup> Further TEM (3.7. Appendix, Figure A3.11) studies on  $\text{Ge}_{1-x}\text{Sn}_x$  verified that the nanowires were defect free with  $\langle 111 \rangle$  as the dominant growth direction.

To confirm the sparse and uniform distribution of Sn in the Ge lattice of the nanowires, we probed the spatial arrangement of Sn through electron energy loss spectroscopy (EELS). EELS mapping was carried out in low resolution HAADF STEM mode. HAADF and the corresponding EELS chemical profile recorded from the rectangular box region are depicted in Figure 3.5(b). EELS spectral images are recorded for Sn  $M_{4,5}$  (red) and Ge  $L_{2,3}$  (green) edges and highlight the incorporation of Sn in the Ge nanowire core. The sharp contrast between the Sn rich seed and the

nanowire body is visible in the HAADF image and in the EELS spectral images for Ge and Sn. No Sn clustering and segregation in the bulk of the nanowire, or sidewall precipitation of metallic Sn, was observed from the EELS spectral images. A deformed catalyst, a phase segregated largely amorphous “bulb” around a highly contrasted metallic seed, at the tip of the nanowire was also observed *via* TEM (see 3.7. Appendix, Figure A3.11) and HADDF STEM analysis (Figure 3.5(b)). EDX elemental mapping on this “bulb” region revealed that the composition of this amorphous region was less Sn rich than the seed it surrounded (40-50 at. % Sn in the amorphous region compared to ~80 at. % in the actual hemispherical catalyst). The EELS spectral image corresponding to Sn also confirmed the phase segregated amorphous region to be less Sn rich than the actual growth seed (Figure 3.5(b)). Although EELS, EDX and Raman analysis verify the quality (uniformity, ordering etc.) of Sn distribution in the Ge lattice, atomic scale study such as atom probe tomography<sup>20</sup> is required to provide deeper insights into the distribution of Sn in non-equilibrium  $\text{Ge}_{1-x}\text{Sn}_x$ .

Ge is a good candidate for achieving a direct bandgap by alloying with Sn as there is only a small energy separation of 140 meV between the indirect (L) and direct ( $\Gamma$ ) valleys in the conduction band. Photoluminescence (PL) is a primary technique to determine the nature of the bandgap in nanoscale alloy systems.<sup>11,47–50</sup> The linewidths of the PL spectra, as well as peak position, give invaluable insight into the nature of the electronic transition. To examine the nature of the band transition of  $\text{Ge}_{1-x}\text{Sn}_x$  nanowires, low temperature PL studies were carried out using a liquid nitrogen cryostat. A PL spectrum taken at 80 K using a Ti:Sa laser with 950 nm wavelength was obtained for the nanowires with 9.1 at. % Sn (Figure 3.6(a) black line). The PL spectrum for the 9.1 at. % Sn incorporated alloy nanowire shows a single peak centred at 2046 nm, which equates

to a band gap energy of 0.61 eV, which energy value is higher than theoretically predicted values ( $< 0.6$  eV).<sup>51</sup> By fitting the spectra to a GaussAmp function, the full width half maximum (FWHM) was obtained. The emission has a relatively narrow linewidth of 220 nm. A PL spectrum recorded at 80 K for the  $\text{Ge}_{1-x}\text{Sn}_x$  nanowire with  $x = 0.07$  also displayed a red-shifted single peak which was centred at 1875 nm, or 0.66 eV (Figure 3.6(a) red line). Comparatively, this peak had a notably broad linewidth of 617 nm. This broad linewidth could be due to the indirect nature of the band

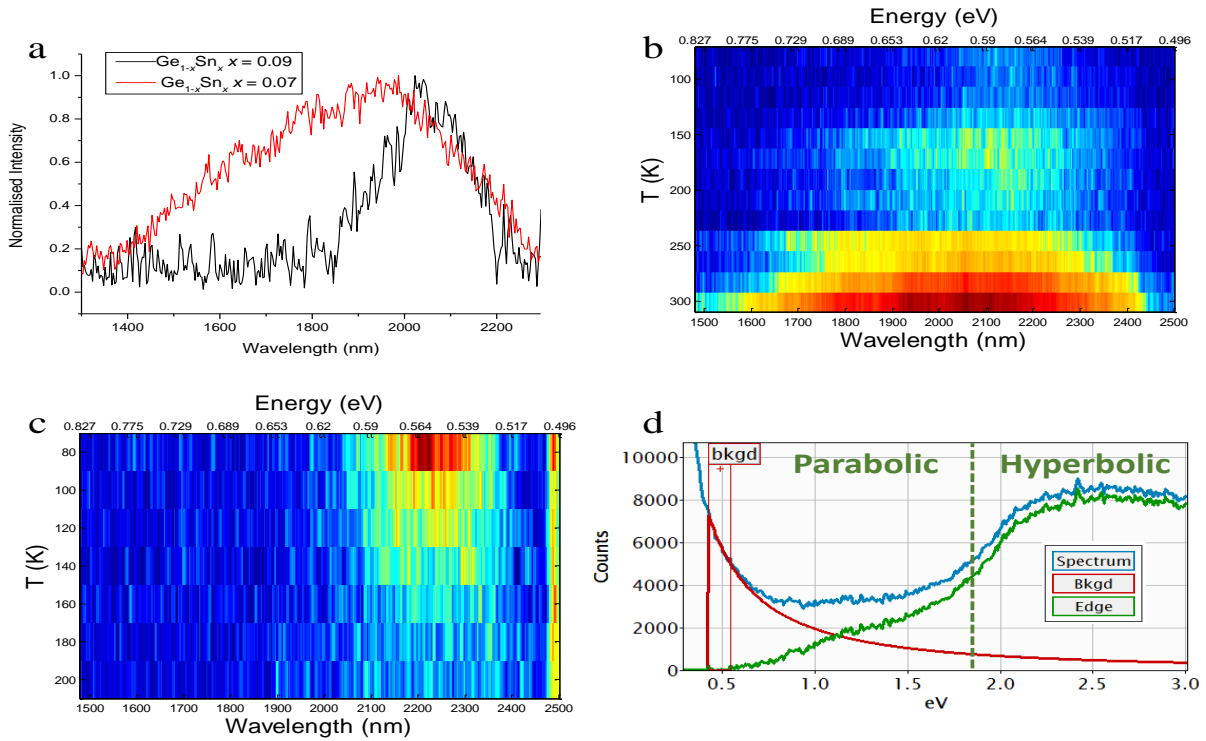


**Figure 3.6:** (a) Photoluminescence spectra for  $\text{Ge}_{1-x}\text{Sn}_x$  nanowires with 9.1 at. % Sn showing a narrow emission at 2046 nm (0.61 eV) at 80 K (black line) and  $\text{Ge}_{1-x}\text{Sn}_x$  nanowires with 7.4 at. % Sn showing much broader emission at 1875 nm (0.66 eV). Temperature dependent studies in part (b) and (c) confirm the bandgap transition for the indirect ( $x = 0.074$ ) nanowires and direct bandgap transition of the  $\text{Ge}_{1-x}\text{Sn}_x$  nanowires with  $x = 0.091$ . The contour plot in (b) shows a direct relationship between temperature and intensity, characteristic of an indirect bandgap material. Contrarily, (c) displays a decreasing intensity with increasing temperature, indicative of a direct bandgap material. (d) EEL spectra of a  $\text{Ge}_{1-x}\text{Sn}_x$  nanowire with 9.1 at. % Sn. The green line begins to rise at approx. 0.6 eV, indicating a bandgap at that energy. The parabolic nature of the green curve to the green dashed line is indicative of a direct transition.

transition. At this Sn content separate peaks due to direct and indirect transition cannot be identified due to the reduced energy difference between direct and indirect bandgap, resulting in a single peak with a broad linewidth. The energy of this peak (0.66 eV) matches well with the direct peak of pure Ge, but there has been a significant redshift from the indirect pure Ge peak (0.80 eV).<sup>52</sup>

Additionally, temperature dependent PL studies are also an invaluable data set in proving the nature of a bandgap<sup>4,53</sup>. Temperature dependent PL studies have previously been used to prove the direct nature of  $\text{Ge}_{1-x}\text{Sn}_x$  materials<sup>4,12,54,55</sup>. The nature of the bandgap was verified by the temperature dependent studies from 80 K – 300 K. PL temperature mapping contour plot of  $\text{Ge}_{1-x}\text{Sn}_x$  ( $x = 0.074$ ) nanowires showed a decrease in PL intensity with decreasing the temperature up to 80K (Figure 3.6(b), further spectral plots in 3.7. Appendix, Figure A3.12). The peak position of the contour plot differs (Figure 3.6(c)) slightly from the single spectra at 80 K (black line, Figure 3.6(a)). This may be due to the variation in Sn concentration ( $\pm 1.2$  at. %) across the growth substrate, combined with the considerable spot size of the laser, resulting in varying PL spectra dependent on the region of the substrate. The room-temperature PL originating from electron–hole recombination at the centre of the Brillouin zone ( $\Gamma$ -point) should decrease in intensity with decreasing temperature for a typical indirect bandgap semiconductor.<sup>56,57</sup> The increase in the PL intensity with increasing temperature is due to the thermally activated electrons located in the L-valley populating the  $\Gamma$  valley leading to increase in the PL intensity.<sup>57</sup> An uncommon small blue shift of the PL emission with increasing temperature (Figure 3.6(b)), which is untypical of semiconductors, was observed for 7.4 at. % Sn incorporated  $\text{Ge}_{1-x}\text{Sn}_x$  nanowires. Ionization of deep impurity levels into the band gap could result in a blue shift in the PL peak with increasing

temperature.<sup>58</sup> However blue-shift originating from this effect usually occurs at low temperatures (<100 K), as after the activation of deep impurity levels at higher temperature the PL peak starts to red-shift as is the case with typical semiconductors. In  $\text{Ge}_{1-x}\text{Sn}_x$  ( $x = 0.074$ ) nanowires, due to the very small difference between the direct and indirect bandgap, the direct transition becomes very close to the indirect and becomes dominant with increasing temperature due to shorter charge carrier lifetimes. In indirect materials close to the indirect-to-direct crossover point, with the rise of temperatures, transitions from both the L &  $\Gamma$  valley can be observed.<sup>53</sup> This explains the uncommon blue shift of emission with increasing temperature (Figure 3.6(b) and 3.7. Appendix, Figure A3.12).<sup>55</sup> The observation of broad PL emission at low temperature and an uncommon increase in the bandgap energy with increasing temperature indicates that the  $\text{Ge}_{1-x}\text{Sn}_x$  nanowires with 7.4 at. % Sn incorporation are very close to the transition point where  $\text{Ge}_{1-x}\text{Sn}_x$  becomes a direct bandgap material. The transition from indirect to direct bandgap could be gradual, due to a degree of band overlap resulting from the narrow energy difference between the direct and indirect bands. Similar behaviour is reported for  $\text{Ge}_{1-x}\text{Sn}_x$  thin films,<sup>59</sup> as well as pure Ge films and nanowires.<sup>60–62</sup>

Temperature dependent PL studies were also carried out from 80 to 200 K on the  $\text{Ge}_{1-x}\text{Sn}_x$  nanowires with 9.1 at. % Sn. The variation in the PL intensity with temperature is depicted in the temperature map in Figure 3.6(c). PL spectra recorded at different temperatures can also be found in 3.7. Appendix (Figure A3.12). A comparison of integrated intensity and band energy as a function of temperature is depicted in Figure A3.13 in 3.7. Appendix for further clarity. The PL intensity decreases with increasing temperature, which can be attributed to a reduced transfer of electrons from the  $\Gamma$  to L valleys by thermal activation.<sup>55</sup> Thus the increase in the intensity of the

PL peak with decreasing temperature for  $\text{Ge}_{1-x}\text{Sn}_x$  ( $x = 0.091$ ) nanowire samples is attributed to the higher population of the  $\Gamma$  valley. With increasing temperature the fast diffusion of photocarriers toward surfaces and interfaces leads to non-radiative surface and interface recombination respectively, reducing the radiative transition rate with activation energy  $E_A$ . Non-radiative surface recombination generates a number of phonons and can occur in both 7.4 and 9.1 at. % Sn content  $\text{Ge}_{1-x}\text{Sn}_x$  nanowires. However, it has different effects on indirect and direct band-gap materials. In the case of 7.4 at. % Sn incorporated nanowires, phonons are required for recombination and its high concentration makes PL from phonon-assisted L-valley brighter at higher temperatures. Whereas for  $\text{Ge}_{1-x}\text{Sn}_x$  ( $x = 0.091$ ) nanowires phonons do not participate in the radiative recombination process and thus non-radiative channels result in the loss of electron-hole pairs on the surface. The activation energy  $E_A$  of non-radiative process at higher temperature was obtained as 16 meV from an Arrhenius plot (3.7. Appendix, Figure A3.14) for the  $\text{Ge}_{1-x}\text{Sn}_x$  nanowires with 9.1 at. % Sn. Decrease in the PL intensity with increase in temperature; which is typical behaviour of a direct bandgap III-V, dichalcogenides and IV-VI semiconductor,<sup>4,12,53,54,56</sup> and the activation energy value comparable to the direct bandgap compressively strained GeSn alloys<sup>47</sup> confirms the direct bandgap for  $\text{Ge}_{1-x}\text{Sn}_x$  nanowires with 9.1 at. % Sn incorporation. It is apparent that the nature of the bandgap in the  $\text{Ge}_{1-x}\text{Sn}_x$  nanowires has changed significantly, from near direct to direct, with the increase in amount of Sn in the alloy by merely 1.6 at. %. Though the steady state PL measurements gave an indication on the nature of the bandgap for  $\text{Ge}_{1-x}\text{Sn}_x$  alloy, direct measurements of the carrier lifetime are required in order to precisely resolve the directness of the electronic band structure.

In order to explore the effect of alloy ordering on the band structure of  $\text{Ge}_{1-x}\text{Sn}_x$  nanowires, it is important to iterate the dependence of the photoluminescence on the alloy disorder. Optically, this change in the fundamental bandgap and band structure can be observed through the photoluminescence line width.<sup>63,64</sup> The electronic states near to the conduction band edge and the valence band edges could be strongly affected by the alloy ordering which translates into an intrinsically higher inhomogeneous broadening of PL emission.<sup>65,66</sup> The consequence of short-range alloy ordering on the PL is apparent from the observation of the narrow line-width for the emission (Figure 3.6 (a)) from spontaneously, comparatively ordered  $\text{Ge}_{1-x}\text{Sn}_x$  ( $x = 0.091$ ) nanowires, as determined from Raman analysis. The emission from the alloy nanowires synthesised in this work with  $> 9$  at. % Sn is significantly narrower than that from the randomly ordered  $\text{Ge}_{1-x}\text{Sn}_x$  nanowires.<sup>12</sup> PL spectrum recorded at 80 K from the randomly ordered  $\text{Ge}_{1-x}\text{Sn}_x$  nanowires fabricated by a two-step process (3.7. Appendix, Figure A3.15) has a line-width of 761 nm. This is significantly (3.5 times) broader than the PL emission from the more spontaneously ordered alloy nanowire synthesized in this work; with a similar Sn incorporation grown *via* single step VLS process. Apart from the PL line width, a significant increase in the activation energy ( $E_A$ ) for non-radiative process is observed for the ordered  $\text{Ge}_{1-x}\text{Sn}_x$  ( $x = 0.091$ ) nanowires (16 meV) compared to  $\text{Ge}_{1-x}\text{Sn}_x$  ( $x = 0.092$ ) nanowire (7 meV) with random Sn distribution.<sup>12</sup> An increase in the activation energy with increasing degree of ordering was also observed for III-V semiconductors.<sup>21,67</sup> It has been suggested that as  $E_A$  for the non-radiative process represents the barrier between the ordered domains and disordered domain containing the non-radiative centres, an increase in  $E_A$  signifies higher degree of ordering in the semiconductor.<sup>67,68</sup> Although the current PL measurements indicate improved emission in terms of line width from the alloy nanowire with enhanced short-range ordering of impurity, further confirmation regarding the effect of alloy

ordering on the bandgap and light emission is required, *e.g.* including radiative rates and quantum efficiencies.

Furthermore, to confirm the nature of the bandgap in the alloy nanowires, EELS analysis was carried out on  $\text{Ge}_{1-x}\text{Sn}_x$  nanowires with 9 at. % Sn using a Nion UltraSTEM at high resolution. Background subtraction (red line) of the EELS spectrum (blue line) was achieved by taking the zero loss peak, resulting in a spectrum denoted by the green line seen shown in Figure 3.6(d).<sup>69,70</sup> The onset (an enlarged view of the sub 1.0 eV region can be found in 3.7. Appendix (Figure A3.16)) of the spectrum (green line) was used to determine the value of the bandgap energy ( $E_g$ ). The EELS spectrum shows a transition at 0.61 – 0.62 eV, which agrees well with the bandgap energy determined from the PL study shown in Figure 3.6(a). The shape of the EELS curve also provides information about the nature of the transition. For a direct transition, an  $(E - E_g)^{1/2}$  term is observed in the spectrum, an  $(E - E_g)^{3/2}$  term determines the shape of the spectrum for an indirect transition.<sup>71,72</sup> Therefore, the nature of the transition can be easily determined from the shape of the spectrum which is produced. The parabolic shape of the curve between ~0.58 eV and ~1.8 eV indicates a direct transition, while the hyperbolic curve which succeeds this is typical of an indirect transition. These curves are indicated in Figure 3.6(d) with the turning point of the curve denoted by the dark green dashed line.

### 3.5. Conclusion

Varying the growth parameters to influence the kinetics of the  $\text{Ge}_{1-x}\text{Sn}_x$  system can dramatically impact Sn uptake in the nanowires. By exploring the effects of temperature, precursor and catalyst an optimal growth regime was explored to obtain high growth kinetics of  $\text{Ge}_{1-x}\text{Sn}_x$  nanowires. By



using tetraethyltin as the Sn source and varying the composition of the AuAg alloy catalyst, morphologically uniform and crystalline nanowires with homogeneous Sn incorporation of  $> 9$  at. % were obtained with an  $\text{Au}_{0.80}\text{Ag}_{0.20}$  catalyst. Longer  $\text{Ge}_{1-x}\text{Sn}_x$  nanowires were more Sn rich than the shorter  $\text{Ge}_{1-x}\text{Sn}_x$  nanowires, establishing a relationship between growth kinetics and Sn incorporation. Faster growth rates resulted in nanowires with higher Sn incorporation, confirming the participation of a kinetic dependence of the solute trapping for Sn incorporation. The understanding of the role of the growth constraint and growth kinetics in the VLS process in Sn impurity incorporation in GeSn nanowires could contribute towards the development of group IV alloys with different stoichiometry and also other new functional alloy materials. For example, a further manipulation in Sn content in  $\text{Ge}_{1-x}\text{Sn}_x$  nanowires can be expected with the introduction and variation of new parameters such as catalyst concentration or pressure.

The  $\text{Ge}_{1-x}\text{Sn}_x$  nanowires with  $x = 0.09$  were determined to be direct bandgap from both PL and EELS analysis. An indirect to direct transition point was identified for the nanowires between 7 and 9 at. % of Sn incorporation. Enhanced spontaneous ordering of Sn impurities, as detected *via* Raman spectroscopy, resulted in a sharp direct band gap emission from the  $\text{Ge}_{1-x}\text{Sn}_x$  nanowires with  $x = 0.09$ . More knowledge on the effect of qualitative distribution of the foreign atoms in the host semiconductor lattice *via* complemented atomic scale mapping (e.g. atom probe tomography) and advance optical analysis will allow exploration of novel properties such as nanoscale strain engineering, controlled defect formation, band structure modulation in the existing nanoscale group IV alloy semiconductor architecture. The fabrication of direct bandgap  $\text{Ge}_{1-x}\text{Sn}_x$  nanowires with high Sn content ( $> 9$  at. %) demonstrates a low cost, silicon compatible solution to the ongoing demand for nanoscale group IV photonics *via* a conventional catalytic approach. These direct

bandgap  $\text{Ge}_{1-x}\text{Sn}_x$  nanowires, with narrow emission widths, a uniform morphology, high crystallinity and homogeneous Sn distribution, demonstrate themselves to be suitable candidates for implementation in photonic and optoelectronic devices.

To demonstrate the functionality of these direct bandgap  $\text{Ge}_{1-x}\text{Sn}_x$  nanowires with high Sn incorporation ( $x > 0.09$ ),  $\text{Ge}_{1-x}\text{Sn}_x$  nanowires with 10.5 at. % Sn were used as photodetectors in Chapter 4.

### 3.6. References

- 1 a. T. Fiory and N. M. Ravindra, *J. Electron. Mater.*, 2003, **32**, 1043–1051.
- 2 A. M. Ionescu and H. Riel, *Nature*, 2011, **479**, 329–337.
- 3 C. Schulte-Braucks, S. Glass, E. Hofmann, D. Stange, N. von den Driesch, J. M. Hartmann, Z. Ikonic, Q. T. Zhao, D. Buca and S. Mantl, *Solid. State. Electron.*, 2017, **128**, 54–59.
- 4 S. Wirths, R. Geiger, N. V. Den Driesch, G. Mussler, T. Stoica, S. Mantl, Z. Ikonic, M. Luysberg, S. Chiussi, J. M. Hartmann, H. Sigg, J. Faist, D. Buca and D. Grützmacher, 2015, 1–5.
- 5 S. Al-Kabi, S. A. Ghetmiri, J. Margetis, T. Pham, Y. Zhou, W. Dou, B. Collier, R. Quinde, W. Du, A. Mosleh, J. Liu, G. Sun, R. A. Soref, J. Tolle, B. Li, M. Mortazavi, H. A. Naseem and S. Q. Yu, *Appl. Phys. Lett.*, , DOI:10.1063/1.4966141.
- 6 R. Soref, *Nat. Photonics*, 2010, **4**, 495–497.
- 7 J. D. Sau and M. L. Cohen, *Phys. Rev. B - Condens. Matter Mater. Phys.*, 2007, **75**, 1–7.
- 8 D. W. Jenkins and J. D. Dow, *Phys. Rev. B*, 1987, **36**, 7994–8000.
- 9 V. Richard D’Costa, W. Wang, Q. Zhou, E. Soon Tok and Y. C. Yeo, *Appl. Phys. Lett.*, , DOI:10.1063/1.4862659.
- 10 Q. T. Zhao, S. Richter, C. Schulte-Braucks, L. Knoll, S. Blaeser, G. V. Luong, S. Trellenkamp, A. Schafer, A. Tiedemann, J. M. Hartmann, K. Bourdelle and S. Mantl, *IEEE J. Electron Devices Soc.*, 2015, **3**, 103–114.
- 11 S. Assali, A. Dijkstra, A. Li, S. Koelling, M. A. Verheijen, L. Gagliano, N. von den Driesch,

- D. Buca, P. M. Koenraad, J. E. M. Haverkort and E. P. A. M. Bakkers, *Nano Lett.*, 2017, **17**, 1538–1544.
- 12 S. Biswas, J. Doherty, D. Saladukha, Q. Ramasse, D. Majumdar, M. Upmanyu, A. Singha, T. Ochalski, M. A. Morris and J. D. Holmes, *Nat. Commun.*, 2016, **7**, 11405.
  - 13 R. Ragan, C. C. Ahn and H. a. Atwater, *Appl. Phys. Lett.*, 2003, **82**, 3439–3441.
  - 14 S. Gupta, R. Chen, Y. C. Huang, Y. Kim, E. Sanchez, J. S. Harris and K. C. Saraswat, *Nano Lett.*, 2013, **13**, 3783–3790.
  - 15 M. S. Seifner, F. Biegger, A. Lugstein, J. Bernardi and S. Barth, *Chem. Mater.*, 2015, **27**, 6125–6130.
  - 16 E. Mullane, T. Kennedy, H. Geaney, C. Dickinson and K. M. Ryan, *Chem. Mater.*, 2013, **25**, 1816–1822.
  - 17 M. S. Seifner, S. Hernandez, J. Bernardi, A. Romano-Rodriguez and S. Barth, *Chem. Mater.*, 2017, **29**, 9802–9813.
  - 18 P. Galenko, *Phys. Rev. E - Stat. Nonlinear, Soft Matter Phys.*, 2007, **76**, 1–9.
  - 19 K. Glasner, *Phys. D Nonlinear Phenom.*, 2001, **151**, 253–270.
  - 20 S. Mukherjee, N. Kodali, D. Isheim, S. Wirths, J. M. Hartmann, D. Buca, D. N. Seidman and O. Moutanabbir, *Phys. Rev. B*, 2017, **95**, 1–5.
  - 21 J. D. Lambkin, L. Considine, S. Walsh, G. M. O'Connor, C. J. McDonagh and T. J. Glynn, *Appl. Phys. Lett.*, 1994, **65**, 73–75.

- 22 G. Wagner, K. Richter and P. Paufler, *Phys. Rev. B - Condens. Matter Mater. Phys.*, 1999, **59**, 15253–15260.
- 23 A. Mascarenhas, S. Kurtz, A. Kibbler and J. M. Olson, *Phys. Rev. Lett.*, 1989, **63**, 2108–2111.
- 24 O. Moutanabbir, D. Isheim, H. Blumtritt, S. Senz, E. Pippel and D. N. Seidman, *Nature*, 2013, **496**, 78–82.
- 25 S. Biswas, C. O'Regan, M. a. Morris and J. D. Holmes, *Small*, 2015, **11**, 103–111.
- 26 S. Biswas, C. O'Regan, N. Petkov, M. a. Morris and J. D. Holmes, *Nano Lett.*, 2013, **13**, 4044–4052.
- 27 S. T. He, S. S. Xie, J. N. Yao, H. J. Gao and S. J. Pang, *Appl. Phys. Lett.*, 2002, **81**, 150–152.
- 28 E. I. Givargizov, *J. Cryst. Growth*, 1975, **31**, 20–30.
- 29 S. A. Dayeh and S. T. Picraux, *Nano Lett.*, 2010, **10**, 4032–4039.
- 30 V. Schmidt, S. Senz and U. Gösele, *Phys. Rev. B - Condens. Matter Mater. Phys.*, 2007, **75**, 1–6.
- 31 S. Biswas, A. Singha, M. a. Morris and J. D. Holmes, *Nano Lett.*, 2012, **12**, 5654–5663.
- 32 H.-J. Yang and H.-Y. Tuan, *J. Mater. Chem.*, 2012, **22**, 2215.
- 33 J. Aubin and J. M. Hartmann, *J. Cryst. Growth*, 2018, **482**, 30–35.
- 34 T. S. S. Wirths, D. Buca, A.T. Tiedemann, B. Holländer, P. Bernardy and S. M. D.

- Grützmacher, *ECS Trans.*, 2012, **50**, 885–893.
- 35 D. C. Lee, T. Hanrath and B. A. Korgel, *Angew. Chemie - Int. Ed.*, 2005, **44**, 3573–3577.
  - 36 C. O'Regan, S. Biswas, C. O'Kelly, S. J. Jung, J. J. Boland, N. Petkov and J. D. Holmes, *Chem. Mater.*, 2013, **25**, 3096–3104.
  - 37 R. Reitano, P. M. Smith and M. J. Aziz, *J. Appl. Phys.*, 1994, **76**, 1518–1529.
  - 38 S. Huang, Y. Wu, X. Zhu, L. Li, Z. Wang, L. Wang and G. Lu, *J. Appl. Phys.*, 2011, **109**, 1–6.
  - 39 S. Rackauskas, H. Jiang, J. B. Wagner, S. D. Shandakov, T. W. Hansen, E. I. Kauppinen and A. G. Nasibulin, .
  - 40 D. Zentrum, 2011, 457–466.
  - 41 H. Assadi and a. L. Greer, *J. Cryst. Growth*, 1997, **172**, 249–258.
  - 42 P. Kringhoj and R. G. Elliman, *Appl. Phys. Lett.*, 1994, **65**, 324–326.
  - 43 S. F. Li, M. R. Bauer, J. Menéndez and J. Kouvetakis, *Appl. Phys. Lett.*, 2004, **84**, 867–869.
  - 44 S. Su, W. Wang, B. Cheng, W. Hu, G. Zhang, C. Xue, Y. Zuo and Q. Wang, *Solid State Commun.*, 2011, **151**, 647–650.
  - 45 R. Cheng, W. Wang, X. Gong, L. Sun, P. Guo, H. Hu, Z. Shen, G. Han and Y.-C. Yeo, *ECS J. Solid State Sci. Technol.*, 2013, **2**, P138–P145.
  - 46 E. R. Hemesath, D. K. Schreiber, E. B. Gulsoy, C. F. Kisielowski, A. K. Petford-Long, P. W. Voorhees and L. J. Lauhon, *Nano Lett.*, 2012, **12**, 167–171.

- 47 S. A. Ghetmiri, W. Du, J. Margetis, A. Mosleh, L. Cousar, B. R. Conley, A. Nazzal, G. Sun, R. a Soref, J. Tolle, B. Li, H. a Naseem, S. A. Ghetmiri, W. Du, J. Margetis, A. Mosleh, L. Cousar, J. Tolle, B. Li, H. a Naseem and S. Yu, , DOI:10.1063/1.4898597.
- 48 J. Mathews, R. T. Beeler, J. Tolle, C. Xu, R. Roucka, J. Kouvetakis and J. Meéndez, *Appl. Phys. Lett.*, 2010, **97**, 2–5.
- 49 A. Mosleh, S. A. Ghetmiri, B. R. Conley, M. Hawkridge, M. Benamara, A. Nazzal, J. Tolle, S.-Q. Yu and H. A. Naseem, *J. Electron. Mater.*, 2014, **43**, 938–946.
- 50 H. Dumont, L. Auvray and Y. Monteil, *Opt. Mater. (Amst)*., 2003, **24**, 309–314.
- 51 Q. Zhang, Y. Liu, J. Yan, C. Zhang and Y. Hao, *Opt. Express*, 2015, **23**, 7924–7932.
- 52 G. He and H. A. Atwater, *Phys. Rev. Lett.*, 1997, **79**, 1937–1940.
- 53 D. Stange, S. Wirths, N. Von Den Driesch, G. Mussler, T. Stoica, Z. Ikonc, J. M. Hartmann, S. Mantl, D. Grützmacher and D. Buca, *ACS Photonics*, 2015, **2**, 1539–1545.
- 54 F. Pezzoli, A. Giorgioni, D. Patchett and M. Myronov, *ACS Photonics*, 2016, **3**, 2004–2009.
- 55 D. Saladukha, J. Doherty, S. Biswas, T. J. Ochalski and J. D. Holmes, *Silicon Photonics Xii*, 2017, **10108**, 101081C.
- 56 M. Y. Ryu, T. R. Harris, Y. K. Yeo, R. T. Beeler and J. Kouvetakis, *Appl. Phys. Lett.*, 2013, **102**, 1–5.
- 57 D. Stange, S. Wirths, N. Von Den Driesch, G. Mussler, T. Stoica, Z. Ikonc, J. M. Hartmann, S. Mantl, D. Grützmacher and D. Buca, *ACS Photonics*, 2015, **2**, 1539–1545.

- 58 M. Leroux, N. Grandjean, B. Beaumont, G. Nataf, F. Semond, J. Massies, P. Gibart, M. Leroux, N. Grandjean, B. Beaumont, G. Nataf, F. Semond, J. Massies and P. Gibart, , DOI:10.1063/1.371242.
- 59 S. Al-Kabi, S. A. Ghetmiri, J. Margetis, W. Du, A. Mosleh, M. Alher, W. Dou, J. M. Grant, G. Sun, R. A. Soref, J. Tolle, B. Li, M. Mortazavi, H. A. Naseem and S. Q. Yu, *J. Electron. Mater.*, 2016, **45**, 2133–2141.
- 60 T. H. Cheng, C. Y. Ko, C. Y. Chen, K. L. Peng, G. L. Luo, C. W. Liu and H. H. Tseng, *Appl. Phys. Lett.*, 2010, **96**, 1–4.
- 61 G. Grzybowski, R. Roucka, J. Mathews, L. Jiang, R. T. Beeler, J. Kouvetakakis and J. Menéndez, *Phys. Rev. B*, 2011, **84**, 205307.
- 62 S. Manna, A. Katiyar, R. Aluguri and S. K. Ray, *J. Phys. D. Appl. Phys.*, 2015, **48**, 215103.
- 63 H. Taleb and K. Abedi, *Front. Optoelectron.*, 2012, **5**, 445–456.
- 64 E. F. Schubert, E. O. Göbel, Y. Horikoshi, K. Ploog and H. J. Queisser, *Phys. Rev. B*, 1984, **30**, 813–820.
- 65 C. Pashartis and O. Rubel, *Phys. Rev. Appl.*, 2017, **7**, 1–12.
- 66 M. M. Nakata, T. M. Mazzo, G. P. Casali, F. A. La Porta and E. Longo, *Chem. Phys. Lett.*, 2015, **622**, 9–14.
- 67 K. L. Teo, J. S. Colton, P. Y. Yu, E. R. Weber and M. F. Li, 1998, **1697**, 10–13.
- 68 G. E. Yu, *Acta Mater.*, 1997, **45**, 2297–2305.



- 69 J. A. Aguiar, B. W. Reed, Q. M. Ramasse, R. Erni and N. D. Browning, *Ultramicroscopy*, 2013, **124**, 130–138.
- 70 B. . Reed and M. Sarikaya, *Ultramicroscopy*, 2002, **93**, 25–37.
- 71 B. Rafferty and L. Brown, *Phys. Rev. B*, 1998, **58**, 10326–10337.
- 72 D. Keller, S. Buecheler, P. Reinhard, F. Pianezzi, D. Pohl, A. Surrey, B. Rellinghaus, R. Erni and A. N. Tiwari, *Microsc. Microanal.*, 2014, **20**, 1246–1253.

### 3.7. Appendix

The appendix section of this chapter contains supplementary information relating to Chapter 3 (*e.g.* surplus SEM, EDX, TEM, *etc.*).

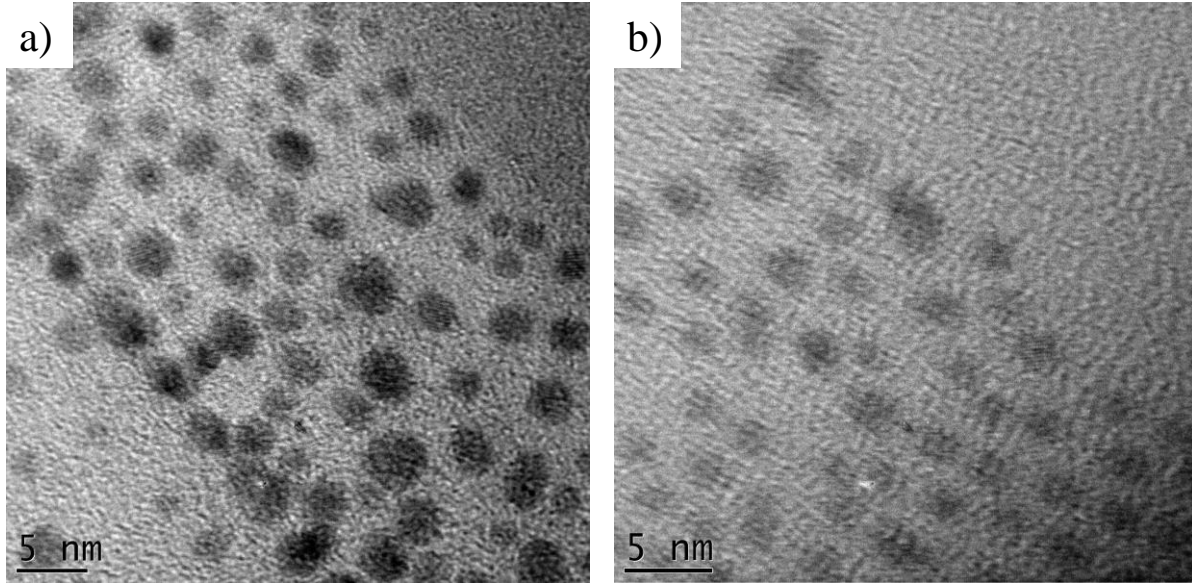


**Figure A3.1:** Au<sub>1-x</sub>Ag<sub>x</sub> nanoparticles used to catalyse the growth of the Ge<sub>1-x</sub>Sn<sub>x</sub> nanowires. The nanoparticles have increasing Ag content from (a) Au<sub>0.90</sub>Ag<sub>0.10</sub> to (b) Au<sub>0.80</sub>Ag<sub>0.20</sub> and both have a mean diameter of  $\sim 4$ -5 nm.

$$\Delta\mu = kT \ln\left(\frac{C}{C_e}\right) \dots (Eq. S1)$$

**Equation A3.1:** where  $C$  is the concentration of the growth species. To lower the  $C_e$  of a growth species, a foreign species can be added to the metal seed particle which will shift the liquidus phase boundary towards a lower solute concentration.

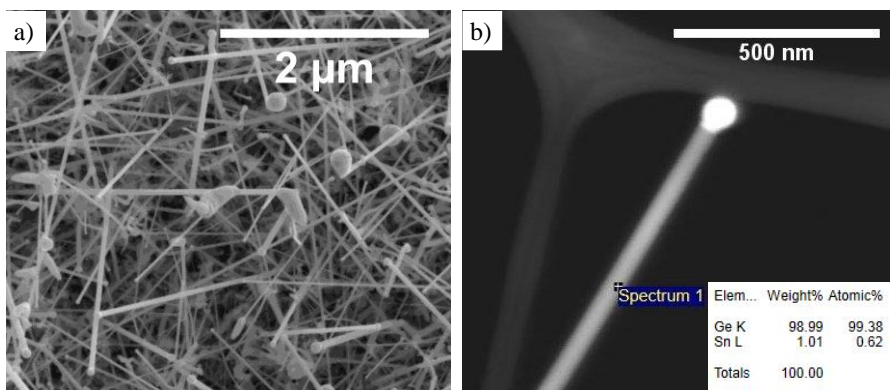


**Figure A3.2:**  $\text{Ge}_{1-x}\text{Sn}_x$  nanowires grown using tetraallyltin (TAT) as a Sn source. (a) depicts Sn segregation and clustering using TAT as the Sn precursor. The  $\text{Ge}_{1-x}\text{Sn}_x$  nanowires grown from TAT also have a very low amount of Sn incorporation (b), with the mean Sn content of approximately 2 at. %.

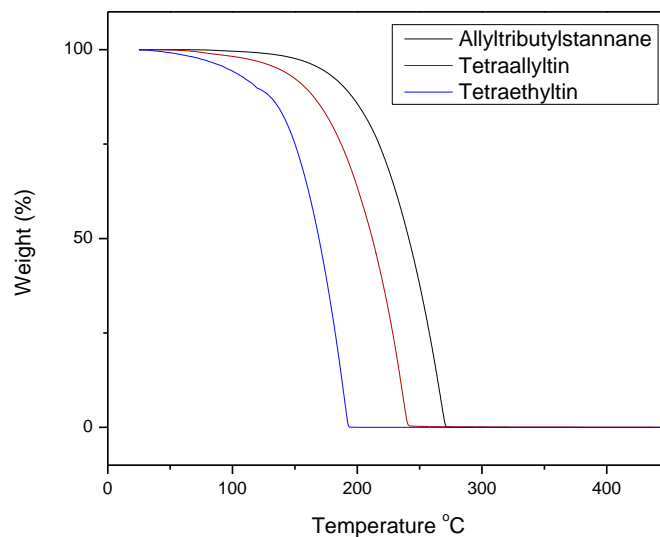


**Figure A3.3:** Thermogravimetric Analysis (TGA) of the three Sn precursors; allyltributylstannane, tetraallyltin and tetraethyltin. The decomposition temperatures of these Sn molecules follows the general trend of their boiling points; ranging from TET with the lowest boiling point (181 °C at atmospheric pressure) to ATBS with the highest (353 °C at atmospheric pressure).

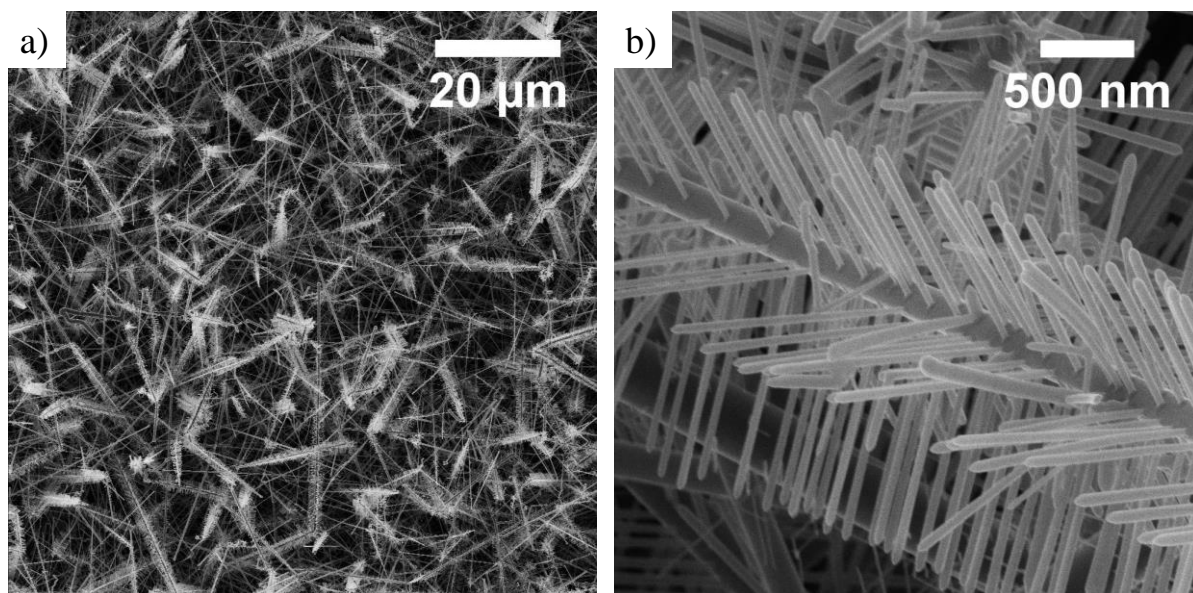


**Figure A3.4:** SEM images of the branched  $\text{Ge}_{1-x}\text{Sn}_x$  nanowires grown using a specific TET concentration. The density of these branched nanowires across the substrate can be seen in (a), these branched nanowires are relatively high yield compared to the non-branched nanowires. (b) Displays the highly ordered nature of these branches, with the branch nanowires seemingly aligned along the trunk.

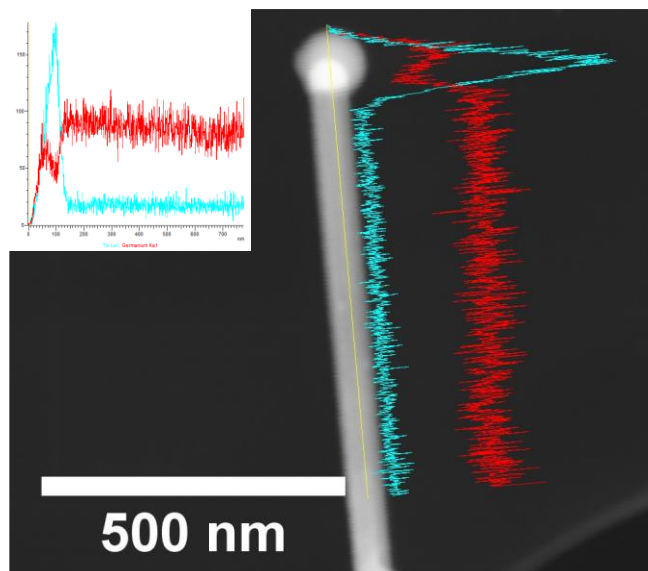


**Figure A3.5:** Linescan of EDX analysis of  $\text{Ge}_{1-x}\text{Sn}_x$  nanowires with mean Sn content 8.7 at. %. In the linescan Ge is denoted by red and Sn by blue. The Sn rich nature of the seed is clearly apparent.

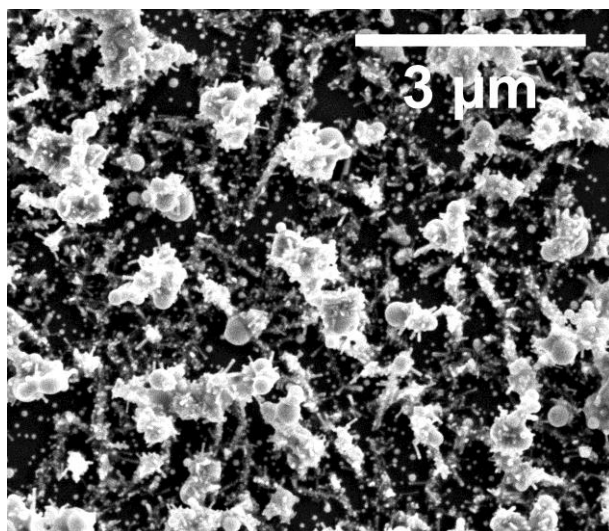


**Figure A3.6:** SEM (a) of  $\text{Ge}_{1-x}\text{Sn}_x$  nanowires grown with TET as the Sn source at 470 °C. EDX analysis revealed an erratic amount of Sn incorporation from one nanowire to another (*i.e.* 4 – 8 at. % Sn).

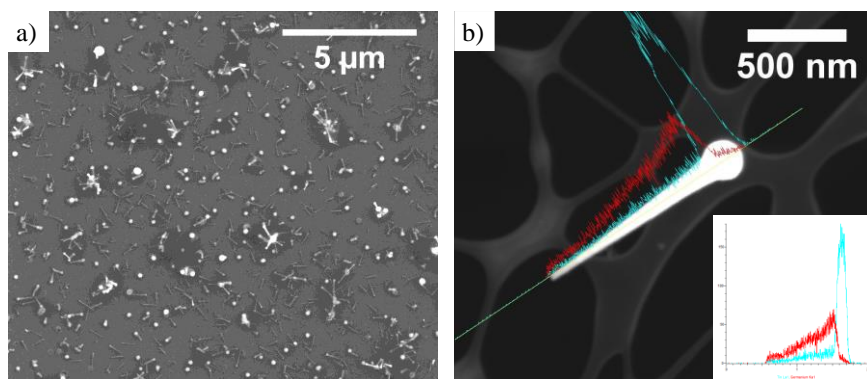


**Figure A3.7:**  $\text{Ge}_{1-x}\text{Sn}_x$  nanowires catalysed by  $\text{Au}_{0.70}\text{Ag}_{0.30}$  nanoparticles with ~11 at. % Sn. The low yield of these nanowires is apparent from (a), the  $\text{Ge}_{1-x}\text{Sn}_x$  nanowires are sporadic clusters across the substrate. A STEM image (b) shows the severe tapering of these nanowires from tip to end. The linescan in (b) reveals that the Sn content of the nanowire is also inconsistent along the bulk of the nanowire, with more Sn incorporation in the wider diameter area of the nanowire, closer to the seed. The EDX point measurements were taken approximately 200 nm from the seed to compensate for this inconsistency.

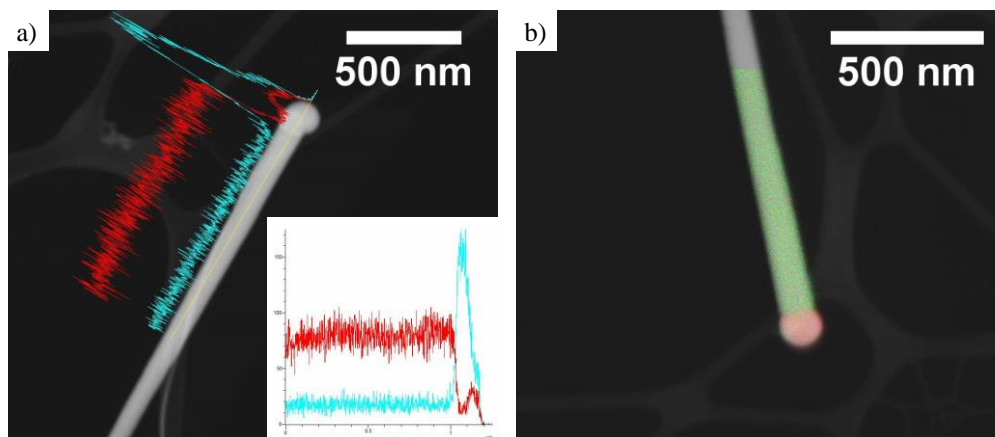


**Figure A3.8:** EDX analysis of  $\text{Ge}_{1-x}\text{Sn}_x$  nanowires catalysed by  $\text{Au}_{0.80}\text{Ag}_{0.20}$  nanoparticles with 9.14 at. % Sn. In the linescan (a) Ge is denoted by red and Sn by blue. In the elemental map (b) Ge is denoted by Green and Sn by red. The Sn rich nature of the seed and lack of Sn clustering and segregation is apparent from the linescan in (a) and the elemental map in (b). Ge is denoted by Green and Sn by red. The Sn rich nature of the seed and lack of Sn clustering and segregation is apparent from the linescan in (a) and the elemental map in (b).

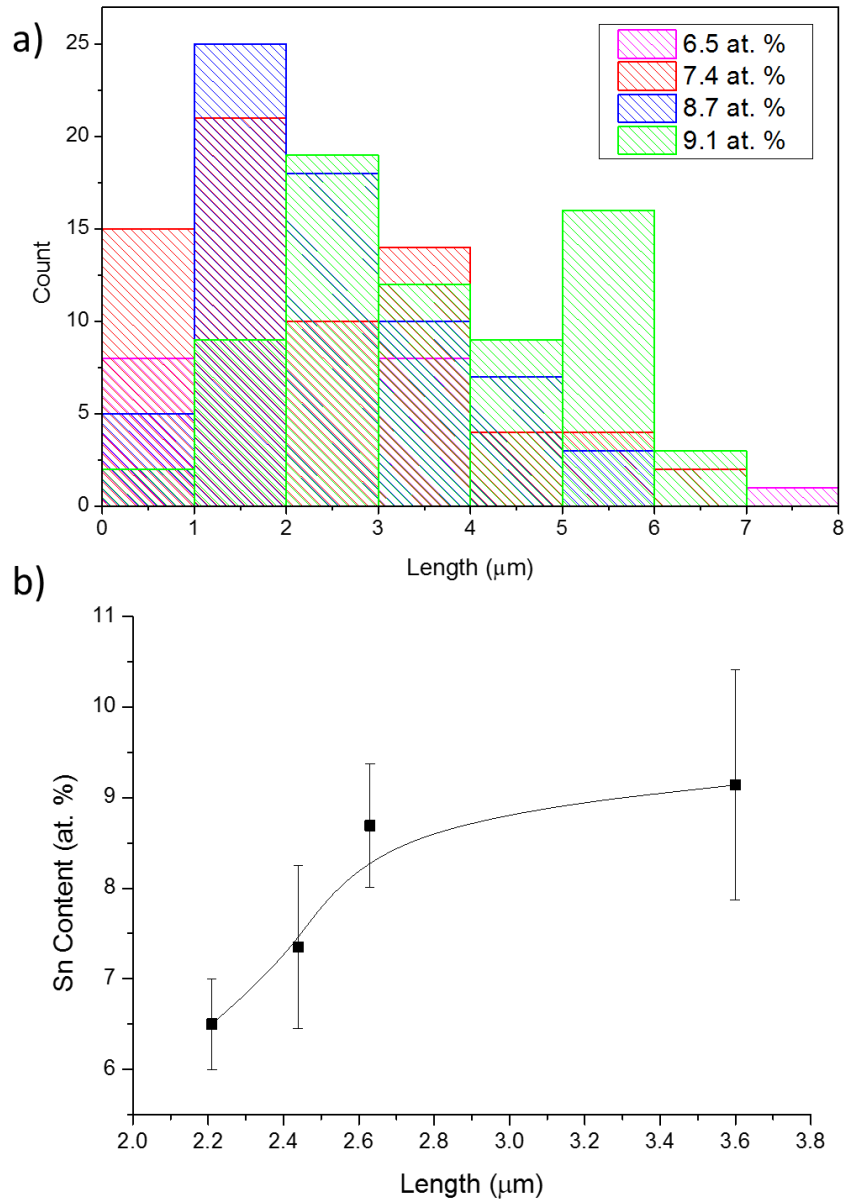


**Figure A3.9:** The length distributions (a) of  $\text{Ge}_{1-x}\text{Sn}_x$  nanowires with varying Sn content, ranging from 6.5 at. % Sn, fabricated with ATBS as Sn source and  $\text{Au}_{0.90}\text{Ag}_{0.10}$  nanoparticles as catalyst, to 9.1 at. % Sn, obtained using TET as Sn source and  $\text{Au}_{0.80}\text{Ag}_{0.20}$  nanoparticles as catalyst. (b) Displays the relationship between mean Sn content and mean length, the error bars here represent the standard deviation from the mean Sn content.



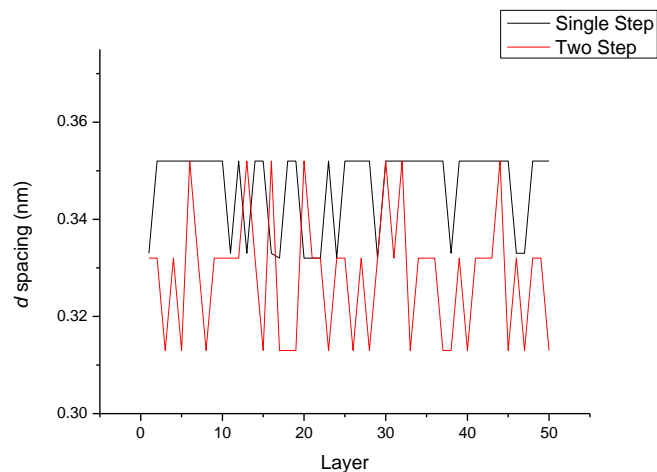


**Figure A3.10:** Comparison of the interplanar ( $d$ ) spacing of 50 successive layers of  $\text{Ge}_{1-x}\text{Sn}_x$  nanowires. The black line denotes the nanowires fabricated through increased growth kinetics with 9.1 at. % Sn, while the red line represents nanowires grown using a two-step method with 9.2 at. % Sn.

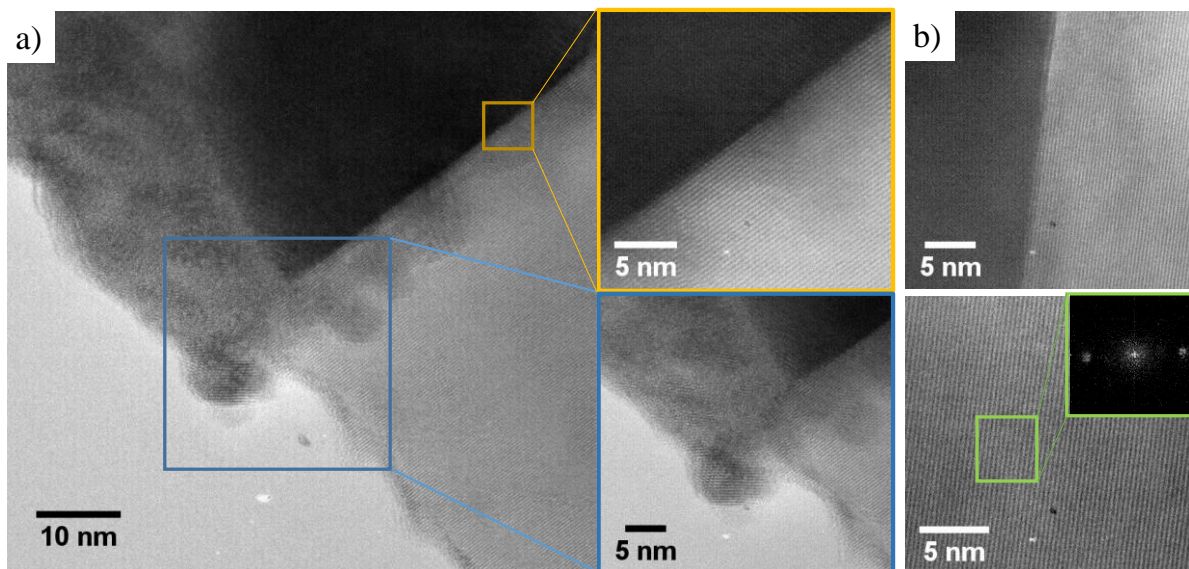


**Figure A3.11:** TEM analysis of  $\text{Ge}_{1-x}\text{Sn}_x$  nanowires with 9.1 at. % Sn. The sharp interface between the nanowire seed and body is clearly seen in (a), in the orange coloured box, and (b). There is no segregation of metallic Sn apparent at the interface. Also visible is the less Sn rich “bulb” surrounding the Sn rich seed (blue coloured box). These nanowires were defect free with no apparent stacking faults of twin boundaries and display  $\langle 111 \rangle$  as the dominant growth direction.



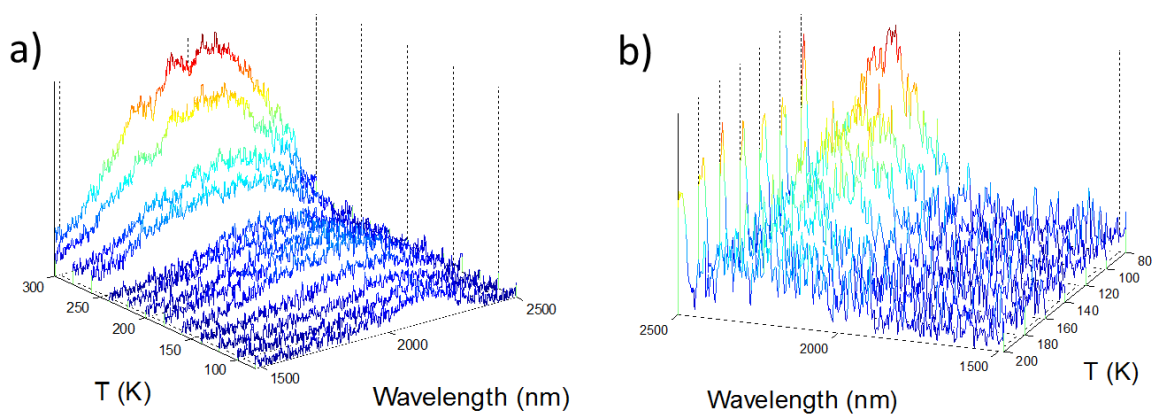


**Figure A3.12:** Temperature dependent photoluminescence studies in part (a) and (b) convey the different behaviours of the  $\text{Ge}_{1-x}\text{Sn}_x$  nanowires with 7.4 and 9.1 at. % Sn respectively. In (a), the dominance of indirect transitions at low temperature with this Sn content is observed. The temperature dependent PL displays an increase of intensity with increasing temperature; indicative of an indirect bandgap material. In (b), the contrary is observed – due to dominance of indirect transitions at low temperature with this Sn content ( $x = 0.09$ ) an inverse relationship exists between temperature and PL intensity. In terms of absolute intensity,  $\text{Ge}_{1-x}\text{Sn}_x$  nanowires with 7.4 at. % Sn have a maximum intensity of  $1.29 \text{ E-}4$ , while the 9.1 at. % Sn sample has a maximum intensity of  $3.83 \text{ E-}5$ .

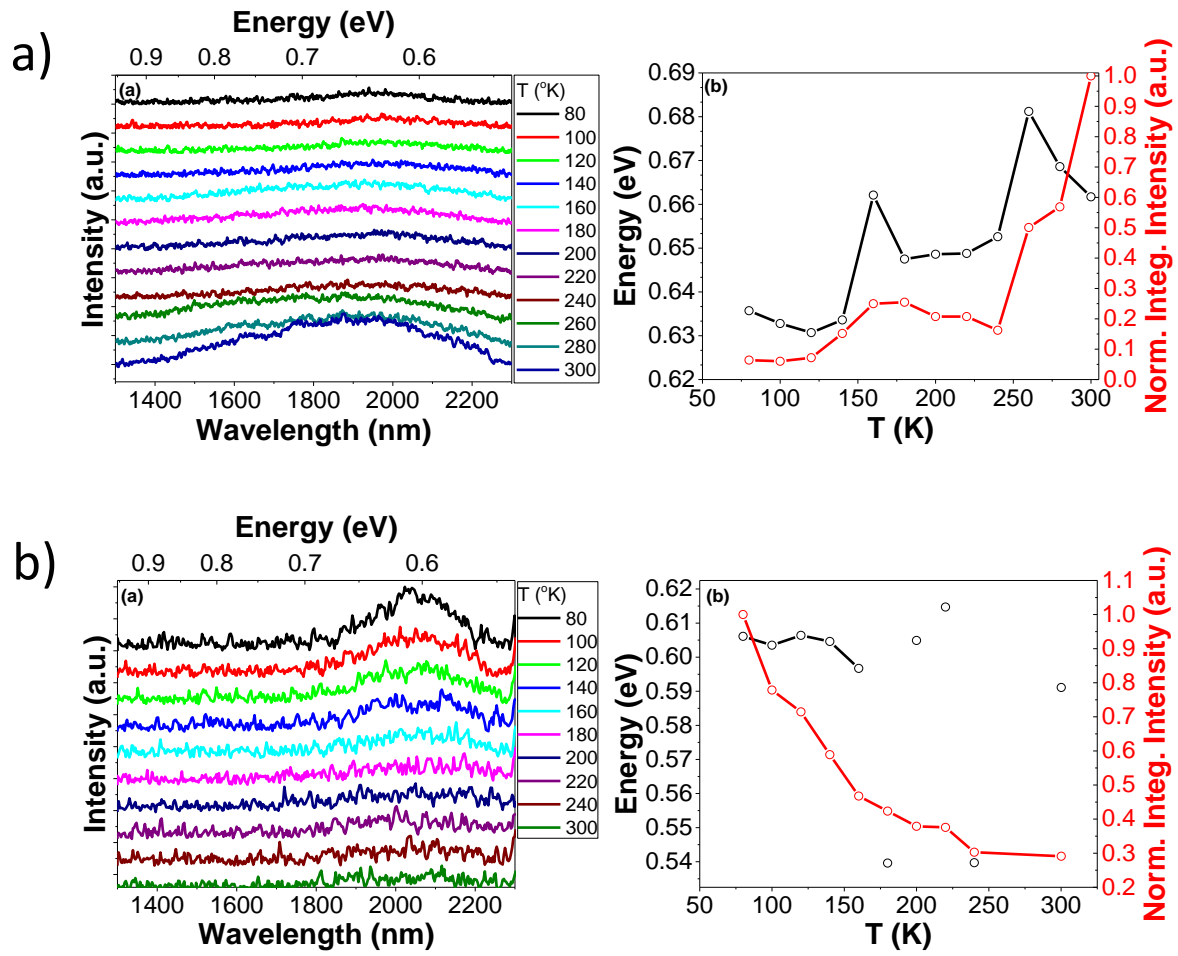


**Figure A3.13:** Temperature dependent photoluminescence studies in part (a) and (b) convey the different behaviours of the  $\text{Ge}_{1-x}\text{Sn}_x$  nanowires with 7.4 and 9.1 at. % Sn respectively. They also display the shift in energy and integrated intensity as a function of temperature.

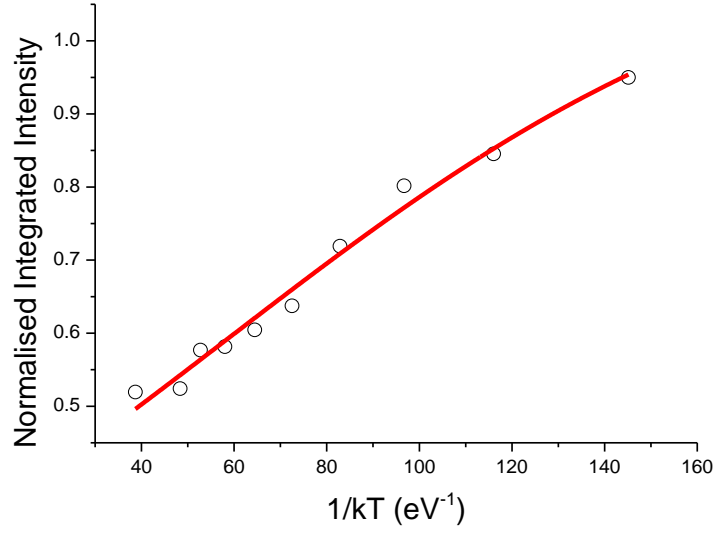


**Figure A3.14:** Arrhenius plot for the  $\text{Ge}_{1-x}\text{Sn}_x$  nanowires with  $x = 0.09$  at low temperature. The red line represents the Arrhenius fit, which gave an activation energy of  $E_A = 16$  meV.

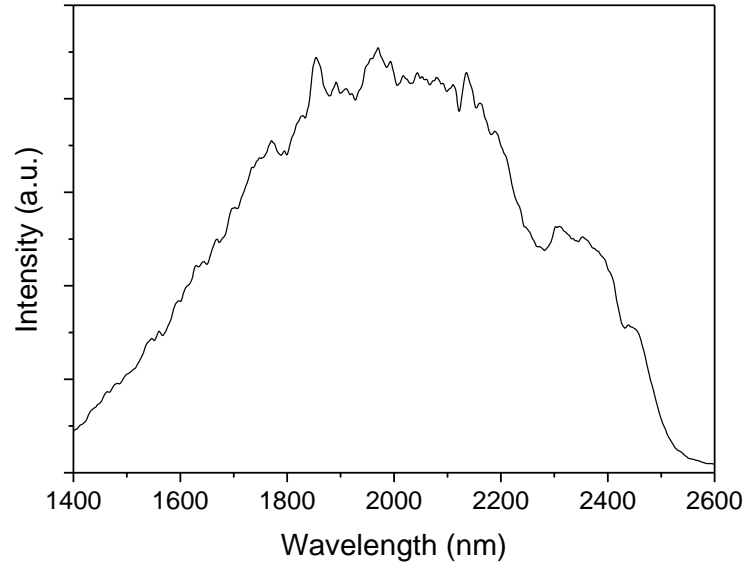


**Figure A3.15:** Photoluminescence spectra of 9.2 at. % Sn sample fabricated through a two-step process. The peak has a broad FWHM of 761 nm, centred at 1988 nm (0.62 eV).

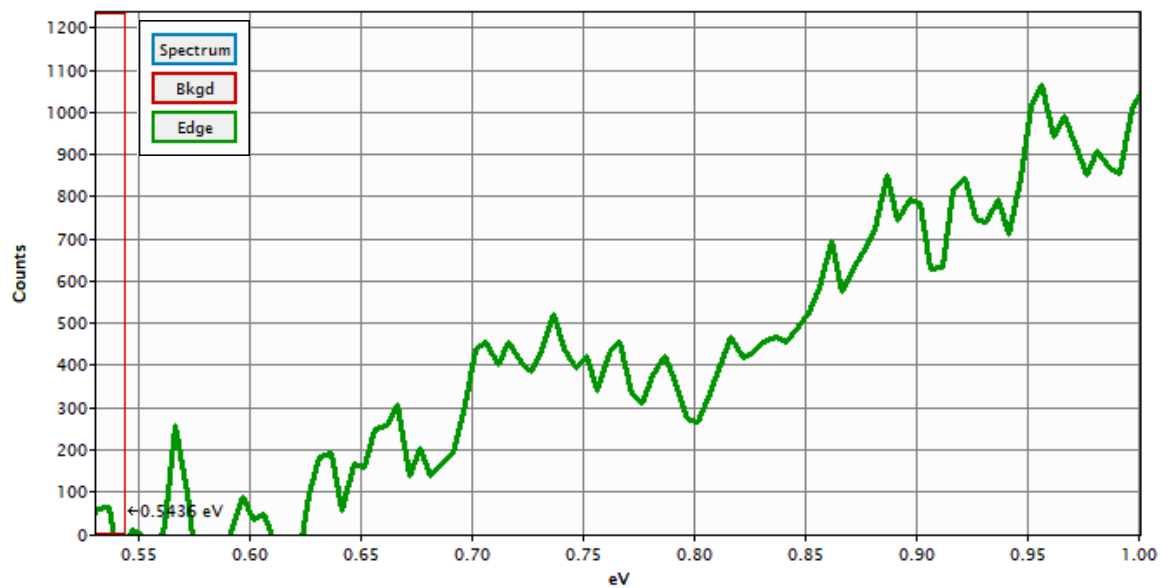


**Figure A3.16:** Enlarged view of the sub 1.0 eV region of the EELS Spectra. The bandedge can be clearly seen at approx. 0.61 – 0.62 eV.

# Chapter 4

## Direct Bandgap $\text{Ge}_{1-x}\text{Sn}_x$ ( $x = 0.10$ ) Nanowires in Photodetection

This chapter is intended for submission in early 2019. Consequently, sections of the chapter such as the abstract and introduction may contain repeating concepts and paragraphs. I co-wrote this paper with SB and JDH, and performed the nanowire synthesis. I carried out the elemental analysis and preliminary structural analysis. I analysed the structural (MC, KM and UB), Raman (AS) and optical data (DS and TO). HM fabricated the nanowire devices while MR carried out the photoresponse measurements.

Doherty, J.; Rao, M.; Saladukha, D.; Manning, H.; Conroy, M.; Moore, K.; Bangert, U.; Singha, A.; Ochalski, T. J.; Biswas, S.; Holmes, J. D Direct Bandgap  $\text{Ge}_{1-x}\text{Sn}_x$  ( $x = 0.10$ ) Nanowires in Photodetection (in preparation).

## 4. Direct Bandgap $\text{Ge}_{1-x}\text{Sn}_x$ ( $x = 0.10$ ) Nanowires in Photodetection

---

### 4.1. Abstract

$\text{Ge}_{1-x}\text{Sn}_x$  is a promising material for optoelectronics due to its compatibility with Si and its direct bandgap at a Sn content above 7 at. %. In this article, we report for the first time the implementation of  $\text{Ge}_{1-x}\text{Sn}_x$  nanowires as efficient photodetectors. Bottom-up grown  $\text{Ge}_{1-x}\text{Sn}_x$  nanowires have the advantage of large surface areas with no or negligible compressive strain, resulting in efficient light absorption and a reduction in the energy required for direct band transition. Liquid-injection chemical vapour deposition technique has been by utilized for the growth of  $\text{Ge}_x\text{Sn}_{1-x}$  ( $x = 0.105$ ) nanowires from  $\text{Au}_{0.90}\text{Ag}_{0.10}$  nanoparticles catalysts, *via* a vapour-liquid-solid (VLS) growth paradigm. The structural and optical quality of these high Sn content  $\text{Ge}_x\text{Sn}_{1-x}$  nanowires was investigated to determine their applicability and functionality in photodetector devices. The as-grown  $\text{Ge}_{1-x}\text{Sn}_x$  nanowires were single crystalline with a direct bandgap of 0.59 eV, as determined from photoluminescence spectroscopy. These highly crystallinity direct bandgap  $\text{Ge}_{1-x}\text{Sn}_x$  nanowires, with narrow emission widths, uniform morphologies and chemical homogeneity were found to be to be ideal candidates for photodetectors due to their high responsivity, increased photosensitivity and broad range photoresponse.

## 4.2. Introduction

$\text{Ge}_{1-x}\text{Sn}_x$  alloy semiconductor thin films and nanomaterials are promising materials for optoelectronic devices.<sup>1-3</sup> In particular,  $\text{Ge}_{1-x}\text{Sn}_x$  thin films are predicted to have increased photoconductivity over a broader wavelength range compared and higher carrier mobilities compared to their pure Ge counterparts.<sup>4,5,6</sup> Furthermore, with a Sn concentration  $> 6.5$  at. % Sn,  $\text{Ge}_{1-x}\text{Sn}_x$  can transition to a direct bandgap material.<sup>7-9</sup> However, since Ge has a relatively "weak" indirect band gap, in the sense that the direct band gap is only 140 meV larger than the indirect band gap, band mixing effects could be prominent and can have a marked effect on the nature of the states at the conduction band edge, particularly for Sn compositions  $< 10\%$ . The evolution of a direct band gap could be continuous with increasing Sn composition, with Ge  $\Gamma$  character transferring continuously to the  $\text{Ge}_{1-x}\text{Sn}_x$  conduction band edge states between  $x = 0$  and 10 %.<sup>10,11</sup> Thus  $\text{Ge}_{1-x}\text{Sn}_x$  alloys with above 10 at.% Sn could have high potential for incorporation in optoelectronic devices such as photodiodes, lasers,<sup>2,12</sup> LEDs<sup>13,14</sup> and waveguide amplifiers<sup>15</sup>.

The optical properties of an alloy can be influenced by composition, as demonstrated both theoretically<sup>16</sup> and experimentally.<sup>17-19</sup>  $\text{Ge}_{1-x}\text{Sn}_x$  photodetectors have been demonstrated using thin films with varying Sn amounts, exhibiting a red shift to lower energies with the increasing addition of Sn, as well as increasing dark conductivity.<sup>20-24</sup> However, due to the lattice mismatch between Ge and Sn, thin films often experience a large amount of strain. Compressive strain shifts the energy gap to lower wavelengths, which results in the need for higher Sn incorporation to achieve a direct bandgap.<sup>9,25</sup>

Some solutions to reduce the strain induced in  $\text{Ge}_{1-x}\text{Sn}_x$  films have been proposed, including introducing a Ge buffer layer<sup>12</sup> or increasing the  $\text{Ge}_{1-x}\text{Sn}_x$  layer thickness.<sup>26,27</sup> A promising solution to achieve high Sn incorporation in Ge without any compressive strain is to move towards a one dimensional (1-D) morphology, which facilitates strain relaxation through free sidewall facets.<sup>28</sup> The large surface to volume ratio and Debye length compared to small size results superior light sensitivity; shape and size dependent optical and electronic properties make  $\text{Ge}_{1-x}\text{Sn}_x$  nanowires a great potential candidate for efficient photodetector. Although there has been significant progress in fabricating and characterizing  $\text{Ge}_{1-x}\text{Sn}_x$  thin film photodetectors,<sup>22,29,30</sup> to the best of our knowledge, there are no reports on photodetection from  $\text{Ge}_{1-x}\text{Sn}_x$  nanowires.

Recently, the growth of  $\text{Ge}_{1-x}\text{Sn}_x$  nanowires has been achieved by both top-down<sup>31</sup> and bottom-up approaches,<sup>7,32,33</sup> including the bottom-up growth of Ge/ $\text{Ge}_{1-x}\text{Sn}_x$  core/shell nanowires.<sup>28,34,35</sup>  $\text{Ge}_{1-x}\text{Sn}_x$  nanowires (with > 6.5 at. % Sn) have been reported to display a direct bandgap,<sup>7,34,36</sup> with the direct bandgap light emission verified by photoluminescence studies in some cases. We have previously reported the growth of optically active  $\text{Ge}_{1-x}\text{Sn}_x$  nanowires through a three phase vapour-liquid-solid (VLS) process, which resulted in uniform nanowires with large Sn ( $\approx 9$  at. %) incorporation and good crystal quality. In this article, we report the fabrication of  $\text{Ge}_{1-x}\text{Sn}_x$  nanowire with greater than 10 at. % Sn incorporation *via* conventional VLS growth. We detail the morphological, structural, chemical and optical characterisation of these nanowires and consider their potential application as efficient nanowire photodetectors. A significant improvement in the peak width was observed for the  $\text{Ge}_{1-x}\text{Sn}_x$  nanowires with > 10 at. % Sn, compared to  $\text{Ge}_{1-x}\text{Sn}_x$  nanowires with low Sn concentrations. These nanowires are integrated in photodetector devices and shows promising



results with high photosensitivity better than previously reported  $\text{Ge}_{1-x}\text{Sn}_x$  thin film photodiodes, as well as detection into the visible range.

### 4.3. Results and Discussion

The incorporation of large amounts of Sn ( $> 6.5$  at. %  $\text{Sn}^{37}$ ) impurity into the  $\text{Ge}_{1-x}\text{Sn}_x$  nanowire result in a transition from indirect to direct bandgap through a gradual process<sup>10,11</sup>. This transition to a direct bandgap is required if  $\text{Ge}_{1-x}\text{Sn}_x$  nanowires are to be used as efficient as optoelectronic materials in photodetectors and photodiodes. Direct band gap  $\text{Ge}_{1-x}\text{Sn}_x$  nanowires can be achieved in a feasible bottom-up approach, without the need for any additional epitaxial engineering. By utilising allyltributylstannane (ATBS) as the Sn precursor,  $\text{Au}_{0.90}\text{Ag}_{0.10}$  nanoparticles as the growth catalyst and a step anneal during the cool-down process, at the Ge-Sn eutectic window ( $230^\circ\text{C}$ ) to promote excess Sn dissolution,<sup>38</sup>  $\text{Ge}_{1-x}\text{Sn}_x$  ( $x = 0.105$ ) were produced (see 4.6. Appendix for detailed method). The catalyst nanoparticles were diluted to 50 % of their original concentration (from 40 to  $20\ \mu\text{M cm}^{-3}$ ), in order to generate fewer nucleation sites and promote a greater uptake of precursor in the individual nanowires, resulting in the growth of  $\text{Ge}_{1-x}\text{Sn}_x$  nanowires with a high Sn incorporation. The scanning electron microscopy (SEM) image shown in Figure 4.1(a) displays  $\text{Ge}_{1-x}\text{Sn}_x$  nanowires with a mean diameter of  $65.3 \pm 21.0$  nm, with fairly good coverage across the growth substrate. The SEM image also shows the absence of any agglomerates and a negligible amount of metallic Sn clusters. The SEM image (Figure 4.1(a)) also confirms that the nanowires are  $> 2\ \mu\text{m}$  in length, which is ideal for convenient metal electrode deposition and surface manipulation during device fabrication. Energy dispersive X-ray (EDX) analysis on single nanowires (approximately 50 nanowires were analysed) confirmed a mean Sn incorporation of  $10.5 \pm 0.5$  at. % in the  $\text{Ge}_{1-x}\text{Sn}_x$  nanowires (Figure 4.1(b)). The small variation in Sn content from one nanowire to another can be clearly seen in the histogram in the inset of

Figure 4.1(b), and is essential for the uniformity, reproducibly and scalability of the fabricated device from these nanowires. The dark field scanning transmission electron microscopy

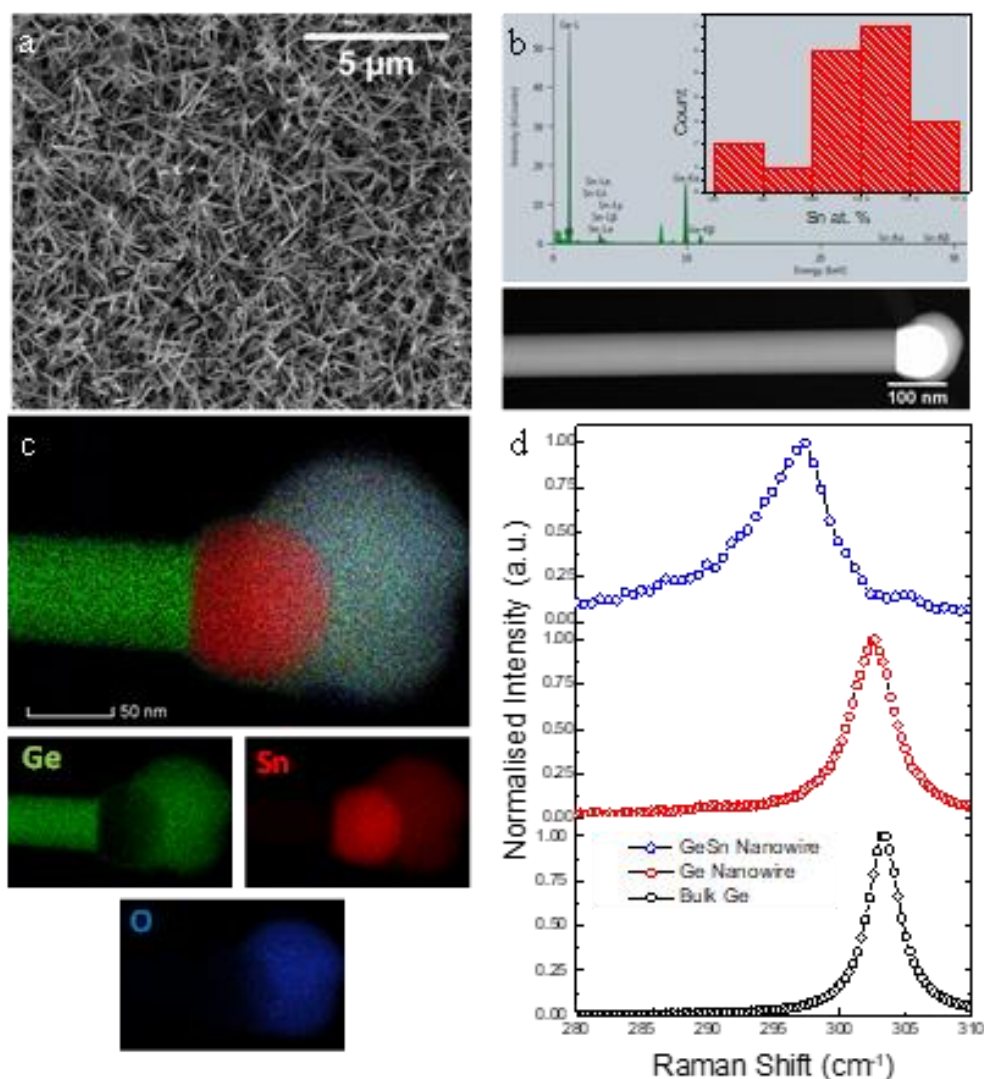


**Figure 4.1:** (a) SEM image of uniform  $\text{Ge}_{1-x}\text{Sn}_x$  nanowires with 10.5 at. % Sn. (b) EDX spectra from the body of a  $\text{Ge}_{1-x}\text{Sn}_x$  nanowire confirms Sn inclusion and no additional impurity induction in the nanowire, *i.e.* from the  $\text{Au}_{0.90}\text{Ag}_{0.10}$  nanoparticle catalyst. A histogram showing the narrow Sn distribution of these  $\text{Ge}_{1-x}\text{Sn}_x$  is provided in the inset of (b). STEM image in part (b) confirms the uniform diameter of the nanowire with a metal particle at the tip confirming VLS growth. (c) The EDX element map in dark field STEM mode shows the elemental distribution in the catalyst seed and nanowire body. The individual elemental maps show the sharp interface between the seed and the body of the nanowire, as well as the pronounced oxidation on the “bulb” surrounding the seed. Raman spectrum in (d) obtained from the  $\text{Ge}_{1-x}\text{Sn}_x$  nanowires with  $x = 0.105$  shows a red shift in the Ge-Ge peak from bulk Ge and Ge nanowire.

(STEM) image of a typical  $\text{Ge}_{1-x}\text{Sn}_x$  nanowire is also shown in Figure 4.1(b), displaying decent length ( $> 3 \mu\text{m}$ ), and negligible tapering.

Reproducibility of nanowires in terms of diameter, length and Sn composition are important factors to consider for the implementation of these  $\text{Ge}_{1-x}\text{Sn}_x$  nanowires in devices. The presence of a spherical seed is also apparent at the tip of the nanowire, confirming the participation of a VLS growth paradigm. Sn has a propensity to cluster or agglomerate at the high temperatures ( $\approx 440^\circ\text{C}$ ) used for the growth of  $\text{Ge}_{1-x}\text{Sn}_x$  nanowires<sup>26,39</sup>. Therefore, to ensure that the Sn in these  $\text{Ge}_{1-x}\text{Sn}_x$  nanowires is homogeneously distributed throughout the body of the nanowire, *i.e.* without Sn segregation in the bulk or surface of the nanowires or a gradual decrease in the Sn content from the nanowire tips to their bodies, EDX elemental maps (Figure 4.1(c)) were obtained for individual nanowires. The lack of Sn segregation or clustering was verified by the absence of bright red spots (corresponding to Sn) in the EDX elemental map (Sn denoted in red, Ge in green, O in blue) as shown in in Figure 4.1(c). The bulk of the seed is comprised of Sn (approx. 80 at. %) with a negligible amount of Ag or Au (4.6. Appendix, A4.1), which has been typical of  $\text{Ge}_{1-x}\text{Sn}_x$  nanowire growth at temperature around  $400^\circ\text{C}$ .<sup>7</sup> A “bulb” like feature can also be seen around a spherical seed, surrounded by a thick oxide layer it (Figure 4.1(c), O elemental map). This bulb is less Sn rich than the seed which it surrounds, containing approx. 50 at. % Sn.

Raman scattering is an effective tool to estimate the structural and chemical environment in the core of a nanowire. Measurements were performed on individual  $\text{Ge}_{1-x}\text{Sn}_x$  nanowires at a very low laser power to avoid laser induced heating. In bulk Ge, the Ge-Ge LO vibration is observed at  $303.3 \text{ cm}^{-1}$  whereas for Ge nanowires this vibration shifts to  $302.7 \text{ cm}^{-1}$ , which is due to a phonon confinement effect (Figure 4.1 (d)). Figure 4.1(d) also shows the Raman spectrum of a single  $\text{Ge}_{1-x}\text{Sn}_x$  alloy nanowire with 10.5 at. % Sn incorporation. In  $\text{Ge}_{1-x}\text{Sn}_x$  alloys the Ge-

Ge mode moves towards a lower frequency (peak centred at  $296.8 \text{ cm}^{-1}$ ) and shows asymmetry in the lower energy side of the spectrum due to the development of a Ge-Sn coupled vibrational mode with a high Sn concentration. A red shift of  $6.5 \text{ cm}^{-1}$  of the Ge-Ge LO mode was observed for the  $\text{Ge}_{1-x}\text{Sn}_x$  nanowires with 10.5 at. % Sn, from bulk Ge. The shift of the Ge-Ge frequency in the Raman spectra of the  $\text{Ge}_{1-x}\text{Sn}_x$  alloys could be due to both a compositional variations and strain effects. As the participation of compressive and tensile strain towards the Raman shift is not justified for nanowire samples, due to the large surface area of the nanowires, the total shift of Ge-Ge frequency to lower values for the grown  $\text{Ge}_{1-x}\text{Sn}_x$  nanowires is mainly attributed to alloy disorder.<sup>40</sup> The Ge-Ge LO mode in  $\text{Ge}_{1-x}\text{Sn}_x$  has previously been shown to progressively shift towards a lower frequency with an increasing Sn concentration, due to the incorporation of Sn in the Ge lattice, altering the bond energy of the lattice.<sup>7,25,41,42</sup> By using the expression  $\omega(x) - \omega_0 = ax$ , where  $a$  is a constant termed as the alloy disorder coefficient and  $x$  is Sn composition, a value of  $a$  was found to be  $65 \text{ cm}^{-1}$ . This value of alloy disorder coefficient is smaller than previous reports of strain-free  $\text{Ge}_{1-x}\text{Sn}_x$ , nanowires and thin films, with similar Sn incorporation.<sup>40,43-45</sup> This discrepancy in the  $a$  value and a relatively smaller Raman shift in the Ge-Ge LO peak for the 10.5 at. % Sn incorporated  $\text{Ge}_{1-x}\text{Sn}_x$  nanowire may arise from the random alloying affect.<sup>7,44</sup> Notably, the alloy disorder coefficient is very similar to the  $\text{Ge}_{1-x}\text{Sn}_x$  nanowire with 9.1 at.% Sn grown with a similar two-step technique,<sup>7</sup> where a lower  $a$  value is assigned to the random nature of the alloy.

Determining the structural quality in nanowires is imperative for device implementation as defects can act as sites where impurities can agglomerate (in this case Sn, Au and Ag), resulting in metallic hotspots of inefficient light absorption and emission. Crystal defects in the nanowire can affect the device performance due to the formation of carrier recombination

centres as well as current leakage paths.<sup>46</sup> The structural quality of the  $\text{Ge}_{1-x}\text{Sn}_x$  nanowires was determined by bright field STEM imaging. The interface between the catalyst seed and nanowire body was examined by high resolution STEM and is depicted in Figure 4.2 (a). A bright contrasted seed region is clearly evident in the image with no apparent tailing or segregation of Sn from the Sn rich seed. This further confirms the formation of sharp junction at the interface as indicated from the EDX elemental maps in Figure 4.1(c). Figure 4.2(b) depicts the defect free, single crystalline nature of the  $\text{Ge}_{1-x}\text{Sn}_x$  ( $x = 0.105$ ) nanowires. Fast Fourier Transform (FFT) analysis of the nanowire aligned to the  $\langle 110 \rangle$  zone axis (Figure 2(b) inset) revealed an interplanar spacing ( $d$ ) of 0.36 nm (3.56 Å), which is significantly larger than the  $d$  value for bulk diamond Ge crystal of 0.326 nm (JCPDS 04–0545). The large  $d$  value was

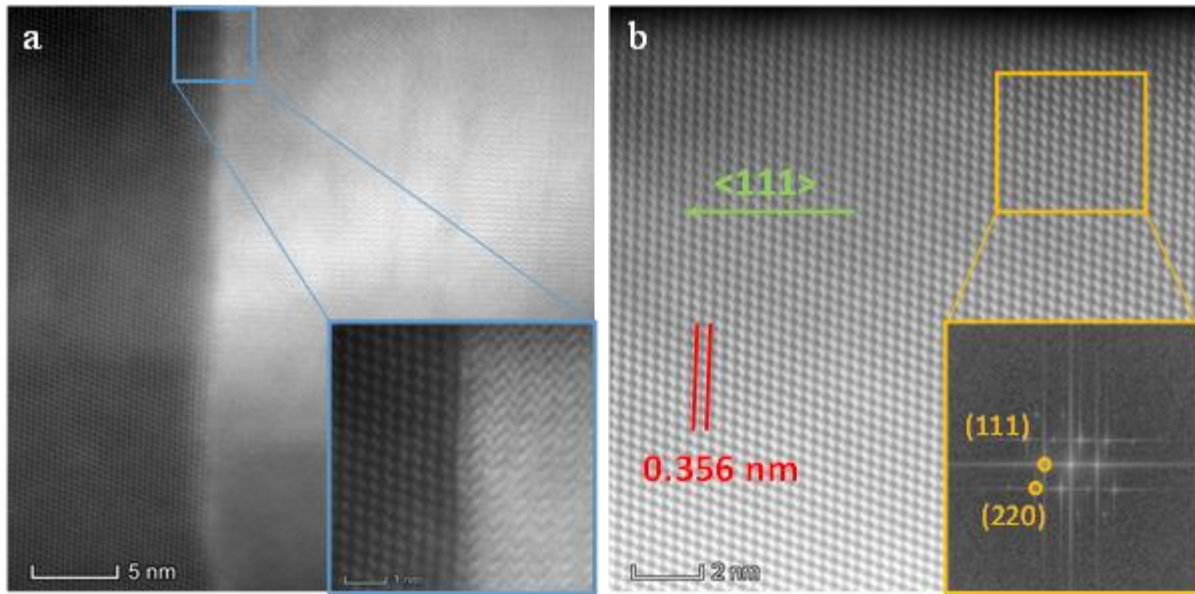


**Figure 4.2:** (a) High resolution BF STEM image displaying the seed-nanowire interface. Magnified image in the inset confirms the sharp interface with no apparent tailing effect or segregation of Sn. (b) High resolution STEM image of a  $\text{Ge}_{1-x}\text{Sn}_x$  ( $x = 0.105$ ) nanowire aligned to the  $\langle 110 \rangle$  zone axis and FFT (in the inset) confirms the formation for Ge-like diamond cubic  $\text{Ge}_{1-x}\text{Sn}_x$  crystal with  $\langle 111 \rangle$  dominant growth direction. The nanowires are single crystalline with no apparent crystal defects.

confirmed by measuring the lattice spacing between 50 layers. This increase in the  $d$  spacing is to be expected upon the incorporation of Sn into the Ge host lattice due to the difference in the lattice constants of Ge and Sn which can instigate a lattice expansion.<sup>7</sup> Furthermore, according to the Raman spectroscopy analysis (Figure 4.1(d)), random ordering in the impurity in these  $\text{Ge}_{1-x}\text{Sn}_x$  nanowires may results in random  $d$  spacing.<sup>7</sup> The formation of a random alloy would not be identifiable through high resolution STEM or EDX mapping due to 2-dimensional (2D) representation of the 3D nanowire materials and would require high resolution probing (*e.g.* atomic probe tomography) of the atomic fluctuation deep inside the lattice for further investigation. The nanowires predominantly displayed a  $\langle 111 \rangle$  growth direction, the most common growth orientation for Ge nanowires with a mean diameter above 50 nm<sup>7,47</sup>. Generally, the crystal structure of the  $\text{Ge}_{1-x}\text{Sn}_x$  alloy nanowires, with various Sn incorporations, exhibited a 3C lattice arrangement without any stacking faults and twin boundaries.

In an indirect bandgap semiconductor, a photon cannot be emitted due to the excess use of energy in transferring momentum to the crystal lattice. Hence, for an efficient optical device, a strong, direct bandgap is preferred. Photoluminescence (PL) is a primary technique to determining the nature of the bandgap in nanoscale alloy systems.<sup>9,34,48–50</sup> PL peak positions and linewidths can be used to determine the nature of an electronic band transition. To examine the nature of the band transition of  $\text{Ge}_{1-x}\text{Sn}_x$  nanowires, low temperature PL studies were carried out using a liquid helium cryostat. A PL spectrum recorded from  $\text{Ge}_{1-x}\text{Sn}_x$  nanowires ( $x = 10.5$  at. % Sn) at 80 K using a Ti:Sa laser with an excitation wavelength of 950 nm is depicted in Figure 4.3(a). The PL spectrum shows a single peak centred at 2087 nm, which equates to a band gap energy of 0.59 eV. By fitting the spectra to the Gauss function, the full width half maximum (FWHM) of the peak was obtained. The emission peak has a relatively

narrow linewidth of 184 nm compared to the  $\text{Ge}_{1-x}\text{Sn}_x$  nanowires with  $\sim 9$  at.% Sn incorporation.<sup>7,40</sup> The PL peak position of the  $\text{Ge}_{1-x}\text{Sn}_x$  (0.59 eV) reported here is slightly lower than previously reported (0.58 eV) for  $\text{Ge}_{1-x}\text{Sn}_x$  nanowires ( $x = 0.092$ ) grown using the same step anneal,<sup>7</sup> however the PL shown in Reference 7 was recorded at a lower power; inducing a red shift in bandgap energy towards lower energy. Comparatively,  $\text{Ge}_{1-x}\text{Sn}_x$  nanowires ( $x = 0.092$ ) grown without the use of a step anneal displayed a PL peak centred at 0.61 eV.<sup>40</sup> This reduction in peak energy could be due to decreased band mixing in the  $\text{Ge}_{1-x}\text{Sn}_x$  nanowires ( $x$

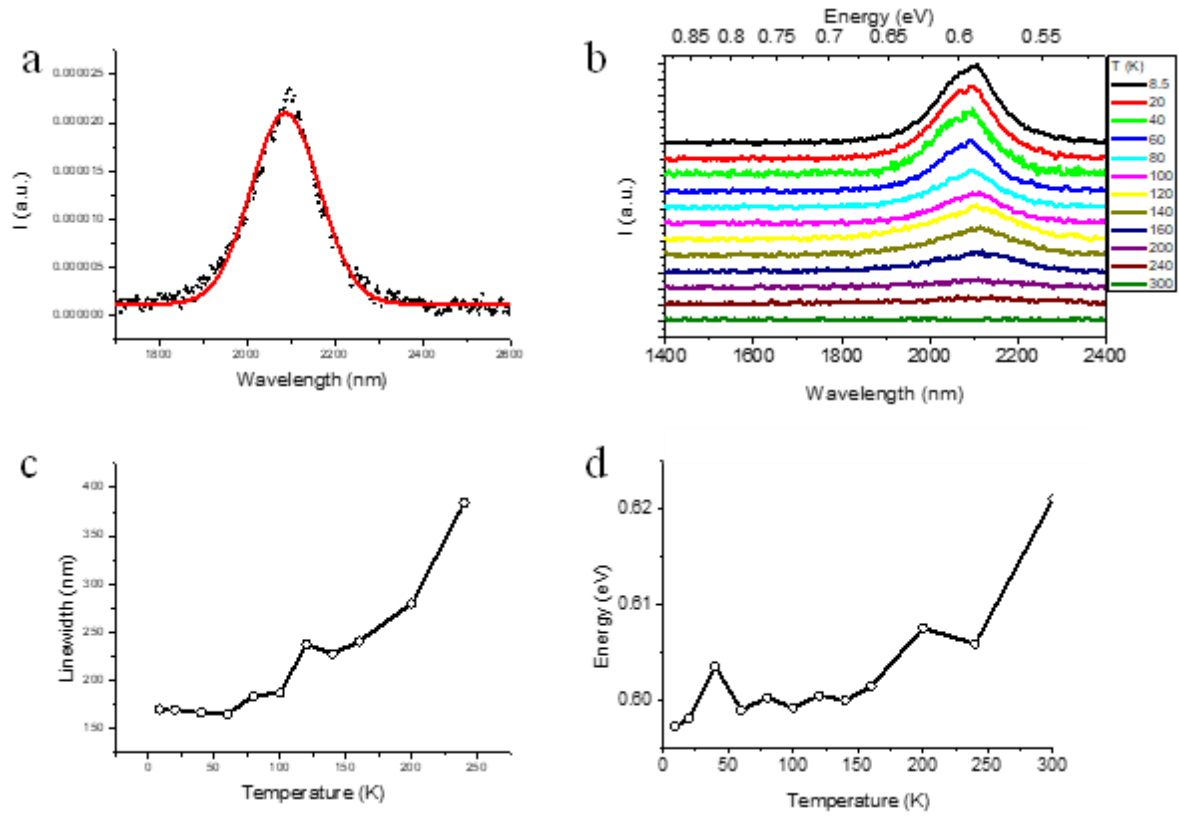


**Figure 4.3:** (a) Photoluminescence spectra for  $\text{Ge}_{1-x}\text{Sn}_x$  ( $x = 0.105$ ) nanowires showing single narrow emission at 2087 nm (0.59 eV) at 80 K. (b) Temperature dependent photoluminescence of the  $\text{Ge}_{1-x}\text{Sn}_x$  nanowires with  $x = 0.105$ . The temperature dependent PL displays a decrease of intensity with increasing temperature; indicative of a direct bandgap material. (c) and (d) Display the temperature dependence of the linewidth and peak centre of the  $\text{Ge}_{1-x}\text{Sn}_x$  nanowires with  $x = 0.105$  respectively. The blue shift to higher energies with temperature can be seen in (d).

= 0.105) reported here, resulting in a direct band transition at lower energies. Band mixing effects are prominent and have a marked effect on the nature of the states at the conduction band edge, particularly for Sn compositions < 10%. A single peak with a relatively narrow line-width could signify direct bandgap transition with significantly less band mixing.

Additionally, temperature dependent PL studies are also invaluable for probing the nature of a bandgap.<sup>12,51</sup> Temperature dependent PL studies have previously been used to probe the direct nature of  $\text{Ge}_{1-x}\text{Sn}_x$  materials.<sup>7,12,52,53</sup> The nature of the bandgap for  $\text{Ge}_{1-x}\text{Sn}_x$  ( $x= 0.105$ ) alloy nanowires was verified by the temperature dependent studies from 8.5 – 300 K. PL spectra recorded as a function of temperatures are plotted in Figure 4.3(b). The effect of temperature on the PL linewidth and peak position are displayed in Figures 4.3(c) and (d) respectively. The linewidth (determined by the FWHM when fitted with a Gaussian function) decreases with decreasing temperature until it reaches < 80 K, after which it plateaus. This narrow linewidth deviation at low temperature is indicative of a single channel of recombination and thus indicates a direct bandgap.<sup>9</sup> The temperature dependence of the PL peak position shows an increase in bandgap energy from 300 to 40 K, but at temperatures below 40 K the peak shifts to lower energies. A similar red shift in the bandgap energy at low temperatures has previously been observed in  $\text{Ge}_{1-x}\text{Sn}_x$  alloys and has been attributed to electron localisation in a fluctuating potential resulting from disorder in the alloy on an atomic scale.<sup>8</sup> This observation for the grown  $\text{Ge}_{1-x}\text{Sn}_x$  ( $x = 0.105$ ) nanowires correlates with the formation of the randomly ordered alloy as also indicated by Raman spectroscopy (Figure 4.1(d)). PL emission from the  $\text{Ge}_{1-x}\text{Sn}_x$  ( $x = 0.105$ ) nanowires decreases in intensity with increasing temperature (Figure 4.3 (b)), which can be attributed to a reduced transfer of electrons from the  $\Gamma$  to L valleys by thermal activation.<sup>53</sup> Thus the increase in the intensity of the PL peak with decreasing temperature for  $\text{Ge}_{1-x}\text{Sn}_x$  ( $x = 0.105$ ) nanowires samples is attributed to the higher population of the  $\Gamma$  valley.



A monotonical decrease in the PL intensity with increase in temperature; which is typical behaviour of a direct bandgap semiconductor,<sup>7,12,51,52,54</sup> confirms the direct bandgap nature of the  $\text{Ge}_{1-x}\text{Sn}_x$  ( $x = 0.105$ ) nanowires. With increasing temperature the fast diffusion of photocarriers toward surfaces and interfaces leads to non-radiative surface and interface recombination respectively, reducing the radiative transition rate, along with the activation energy  $E_A$ . The activation energy  $E_A$  of 12.5 meV was obtained for the  $\text{Ge}_{1-x}\text{Sn}_x$  ( $x = 0.105$ ) nanowires for non-radiative process at temperatures between 7 – 300 K (4.6. Appendix, Figure A4.2). This activation energy value, while somewhat low, is comparable to values obtained previously for the direct bandgap  $\text{Ge}_{1-x}\text{Sn}_x$  alloy thin films<sup>12</sup> and nanowires.<sup>40</sup> The slightly low activation energy can be attributed to the apparent random ordering of the  $\text{Ge}_{1-x}\text{Sn}_x$  alloy,<sup>7</sup> as inferred from the Raman spectroscopy and PL peak shift at low temperature (below 40 K).

The photoresponse of a single  $\text{Ge}_{1-x}\text{Sn}_x$  nanowire was studied by depositing 0.8  $\mu\text{m}$  Au gap electrodes using electron beam lithography (Figure 4.4 (a)). The photoresponse characteristics of the device were measured with UV light and visible light of three different wavelengths 450 nm, 600 nm, and 750 nm. The I-V characteristics demonstrated in Figure 4.4 (b) and (c) indicate a pronounced photoresponse with UV light and a steady increase of photocurrent for wavelengths of 450 nm to 750 nm. The photosensitivity, defined as  $(I_{\text{light}} - I_{\text{dark}})/I_{\text{dark}}$ , under a white UV illumination is approximately  $4 \times 10^4 \%$ . This could be due to the very low dark current of the  $\text{Ge}_{1-x}\text{Sn}_x$  nanowire – a desirable trait in any photodetection device. The photosensitivity value of the  $\text{Ge}_{1-x}\text{Sn}_x$  nanowire is very high when compared with Si nanowires<sup>55,56</sup> and other nanowires,<sup>57</sup> which is attributed to the direct band gap and high crystallinity of  $\text{Ge}_{1-x}\text{Sn}_x$  nanowire. Compared to  $\text{Ge}_{1-x}\text{Sn}_x$  thin film devices,  $\text{Ge}_{1-x}\text{Sn}_x$  nanowire also show increased photosensitivity.<sup>58,59</sup> More importantly,  $\text{Ge}_{1-x}\text{Sn}_x$  nanowire demonstrated

to photoresponse even in the visible light range, displaying a broad responsivity range from IR to visible light.

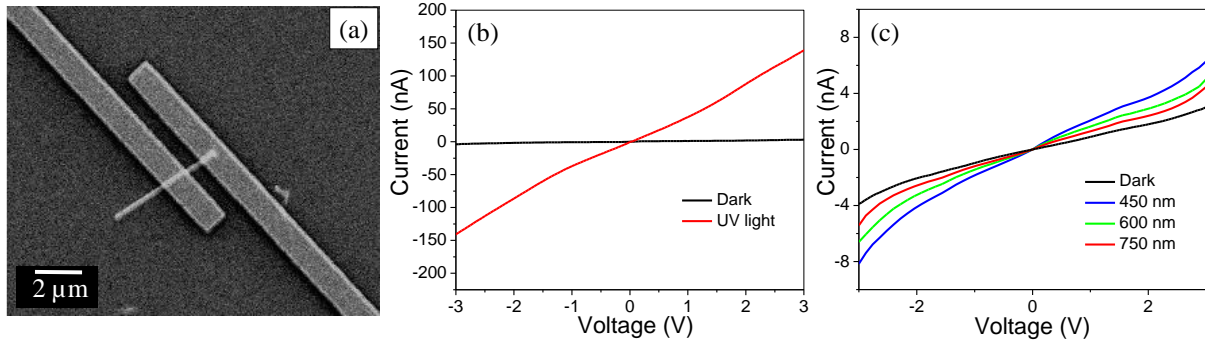


**Figure 4.4:** (a) SEM image of GeSn nanowire after depositing Au electrodes. Current versus voltage characteristics of GeSn nanowire illuminated with (b) UV light, (b) monochromatic light of wavelengths 450 nm, 600 nm and 750 nm and in dark.

It is important to note that these preliminary photoemission results may be arising as the result of a contact Schottky barrier. With short channel lengths, the Schottky barrier can dominate over the small energy bandgap of these nanowires. Therefore, it is essential, as a future study, to explore the photosensitivity and response of nanowires over different channel lengths.

#### 4.4. Conclusion

$\text{Ge}_{1-x}\text{Sn}_x$  ( $x > 0.10$  at.%) nanowires show improved optical quality, with direct band gap and narrow light emission width, compared to previously reported  $\text{Ge}_{1-x}\text{Sn}_x$  nanowires. These single crystalline, defect free  $\text{Ge}_x\text{Sn}_{1-x}$  nanowires with uniform diameter and Sn content show a certain degree of randomness in Sn distribution on the atomic scale, which possibly influence the optical quality of the nanowires. The bottom-up grown, direct bandgap  $\text{Ge}_{1-x}\text{Sn}_x$  nanowires with high Sn content ( $> 10$  at. %) represents a low cost, silicon compatible solution to the ongoing demand for nanoscale group IV optoelectronics/photronics material. The large number of variables available in the alloy nanowire systems, including diameter, length and alloy

distribution will allow greater scope in future for the manipulation of optical and electronic properties. The photosensitivity of  $\text{Ge}_x\text{Sn}_{1-x}$  nanowires ( $x = 0.105$ ) was determined to be very high when compared with other nanowire based devices, and with  $\text{Ge}_x\text{Sn}_{1-x}$  thin film devices, with a photocurrent to dark ratio of 40,000.

To explore the range of functionalities of  $\text{Ge}_x\text{Sn}_{1-x}$  nanowires with a predicted indirect bandgap ( $x = 0.048$ ) were investigated as anode materials for Li-ion batteries. This work is presented in Chapter 5.

#### 4.5. References

1. Zaima, S. *et al.* Growth and applications of GeSn-related group-IV semiconductor materials. *2016 IEEE Photonics Soc. Summer Top. Meet. Ser. SUM 2016* **16**, 37–38 (2016).
2. Homewood, K. P. & Lourenço, M. A. Optoelectronics: The rise of the GeSn laser. *Nat. Photonics* **9**, 78–79 (2015).
3. Kasper, E., Kittler, M., Oehme, M. & Arguirov, T. Germanium tin: silicon photonics toward the mid-infrared [Invited]. *Photonics Res.* **1**, 69 (2013).
4. Soref, R. A. & Friedman, L. Direct-gap Ge/GeSn/Si and GeSn/Ge/Si heterostructures. *Superlattices and Microstructures* **14**, 189–193 (1993).
5. D’Costa, V. R., Tolle, J., Xie, J., Menéndez, J. & Kouvetakis, J. Transport properties of doped GeSn alloys. *AIP Conf. Proc.* **1199**, 57–58 (2009).
6. Zaumseil, P., Nakatsuka, O., Zaima, S. & Schroeder, T. Electrical and optical properties improvement of GeSn layers formed at high temperatures under well-controlled Sn migration. *Mater. Sci. Semicond. Process.* **57**, 48–53 (2017).
7. Biswas, S. *et al.* Non-equilibrium induction of tin in germanium: Towards direct bandgap Ge<sub>1-x</sub>Sn<sub>x</sub>nanowires. *Nat. Commun.* **7**, 11405 (2016).
8. Stange, D. *et al.* Optical Transitions in Direct-Bandgap Ge<sub>1-x</sub>Sn<sub>x</sub>Alloys. *ACS Photonics* **2**, 1539–1545 (2015).
9. Ghetmiri, S. A. *et al.* Direct-bandgap GeSn grown on silicon with 2230nm photoluminescence Direct-bandgap GeSn grown on silicon with 2230 nm photoluminescence. **151109**, (2014).

10. Dutt, B. *et al.* Theoretical analysis of GeSn alloys as a gain medium for a Si-compatible laser. *IEEE J. Sel. Top. Quantum Electron.* **19**, (2013).
11. Polak, M. P., Scharoch, P. & Kudrawiec, R. The electronic band structure of Ge<sub>1-x</sub>Sn<sub>x</sub> in the full composition range: indirect, direct, and inverted gaps regimes, band offsets, and the Burstein–Moss effect. *J. Phys. D. Appl. Phys.* **50**, 195103 (2017).
12. Wirths, S. *et al.* Lasing in direct-bandgap GeSn alloy grown on Si. *Nat. Photonics* **9**, 88–92 (2015).
13. Schwartz, B. *et al.* Electroluminescence of GeSn/Ge MQW LEDs on Si substrate. *Opt. Lett.* **40**, 3209–3212 (2015).
14. Zhou, Y. *et al.* Systematic study of GeSn heterostructure-based light-emitting diodes towards mid-infrared applications. *J. Appl. Phys.* **120**, 1–8 (2016).
15. Peng, Y.-H., Cheng, H. H., Mashanov, V. I. & Chang, G.-E. GeSn p-i-n waveguide photodetectors on silicon substrates. *Appl. Phys. Lett.* **105**, 231109 (2014).
16. You, X. & Zhou, R. Electronic Structure and Optical Properties of GaAs<sub>1-x</sub>Bi<sub>x</sub> Alloy. **2014**, (2014).
17. Nabetani, Y. *et al.* Structure and optical properties of ZnSeO alloys with O composition up to 6.4%. *Mater. Sci. Semicond. Process.* **6**, 343–346 (2003).
18. Abdel-Rahim, M. A., Hafiz, M. M. & Alwany, A. E. B. The effect of composition on structural and optical properties of ZnSe alloys. *Opt. Laser Technol.* **47**, 88–94 (2013).
19. Shiraishi, T., Hisatsune, K., Tanaka, Y., Miura, E. & Takuma, Y. Optical properties of Au-Pt and Au-Pt-In alloys. *Gold Bull.* **34**, 129–133 (2001).

20. Zheng, J. *et al.* GeSn p-i-n photodetectors with GeSn layer grown by magnetron sputtering epitaxy. *Appl. Phys. Lett.* **108**, 1–5 (2016).
21. Pham, T. *et al.* Systematic study of Si-based GeSn photodiodes with 26  $\mu\text{m}$  detector cutoff for short-wave infrared detection. *Opt. Express* **24**, 4519 (2016).
22. Xu, S. *et al.* GeSn lateral p-i-n photodetector on insulating substrate. *Opt. Express* **26**, 17312–17320 (2018).
23. Oehme, M. *et al.* GeSn p-i-n detectors integrated on Si with up to 4% Sn. *Appl. Phys. Lett.* **101**, (2012).
24. Su, S. J. *et al.* GeSn on Si photodetectors grown by molecular beam epitaxy. *IEEE Int. Conf. Gr. IV Photonics GFP* 33–35 (2011). doi:10.1109/GROUP4.2011.6053706
25. Al-Kabi, S. *et al.* Optical Characterization of Si-Based  $\text{Ge}_{1-x}\text{Sn}_x$  Alloys with Sn Compositions up to 12%. *J. Electron. Mater.* **45**, 2133–2141 (2016).
26. Yu, I. S. *et al.* Investigation of  $\text{Ge}_{1-x}\text{Sn}_x/\text{Ge}$  with high Sn composition grown at low-temperature. *AIP Adv.* **1**, (2011).
27. Wang, W., Zhou, Q., Dong, Y., Tok, E. S. & Yeo, Y.-C. Critical thickness for strain relaxation of  $\text{Ge}_{1-x}\text{Sn}_x$  ( $x \leq 0.17$ ) grown by molecular beam epitaxy on Ge(001). *Appl. Phys. Lett.* **106**, 232106 (2015).
28. Albani, M. *et al.* Critical strain for Sn incorporation into spontaneously graded Ge/GeSn core/shell nanowires. *Nanoscale* **10**, 7250–7256 (2018).
29. Werner, J., Oehme, M., Schirmer, A., Kasper, E. & Schulze, J. Molecular beam epitaxy grown GeSn p-i-n photodetectors integrated on Si. *Thin Solid Films* **520**, 3361–3364 (2012).

30. Su, S. *et al.* GeSn p-i-n photodetector for all telecommunication bands detection. *Opt. Express* **19**, 6400 (2011).
31. Gong, X. *et al.* Uniaxially Strained Germanium-Tin (GeSn) Gate-All-Around Nanowire PFETs Enabled by a Novel Top-Down Nanowire Formation Technology. *2013 Symp. VLSI Circuits* 34–35 (2013).
32. Seifner, M. S., Biegger, F., Lugstein, A., Bernardi, J. & Barth, S. Microwave-Assisted Ge<sub>1-x</sub>Sn<sub>x</sub> Nanowire Synthesis: Precursor Species and Growth Regimes. *Chem. Mater.* **27**, 6125–6130 (2015).
33. Haffner, T. *et al.* Growth of Ge<sub>1-x</sub>Sn<sub>x</sub> Nanowires by Chemical Vapor Deposition via Vapor-Liquid-Solid Mechanism Using GeH<sub>4</sub> and SnCl<sub>4</sub>. *Phys. Status Solidi* **215**, 1700743 (2017).
34. Assali, S. *et al.* Growth and Optical Properties of Direct Band Gap Ge/Ge<sub>0.87</sub>Sn<sub>0.13</sub> Core/Shell Nanowire Arrays. *Nano Lett.* **17**, 1538–1544 (2017).
35. Zhu, Z. *et al.* GeSn/Ge dual-nanowire heterostructure. *Summer Top. Meet. Ser. SUM 2017* 71–72 (2017). doi:10.1109/PHOSST.2017.8012655
36. Seifner, M. S., Hernandez, S., Bernardi, J., Romano-Rodriguez, A. & Barth, S. Pushing the composition limit of anisotropic Ge<sub>1-x</sub>Sn<sub>x</sub> nanostructures and determination of their thermal stability. *Chem. Mater.* **29**, 9802–9813 (2017).
37. Yin, W. J., Gong, X. G. & Wei, S. H. Origin of the unusually large band-gap bowing and the breakdown of the band-edge distribution rule in the Sn<sub>x</sub>Ge<sub>1-x</sub> alloys. *Phys. Rev. B - Condens. Matter Mater. Phys.* **78**, 1–4 (2008).
38. Biswas, S. *et al.* Non-equilibrium induction of tin in germanium: Towards direct

- bandgap Ge  $1-x$ Sn $x$ nanowires. *Nat. Commun.* **7**, (2016).
39. Li, H. *et al.* Characteristics of Sn segregation in Ge/GeSn heterostructures. *Appl. Phys. Lett.* **105**, 1–4 (2014).
  40. Doherty, J. *et al.* Influence of growth kinetics on Sn incorporation in direct band gap Ge  $1-x$  Sn  $x$  nanowires. *J. Mater. Chem. C* 8738–8750 (2018). doi:10.1039/C8TC02423E
  41. Conley, B. R. *et al.* CVD growth of Ge $1-x$ Sn $x$  using large scale Si process for higher efficient multi-junction solar cells. *2013 IEEE 39th Photovolt. Spec. Conf.* 1346–1349 (2013). doi:10.1109/PVSC.2013.6744392
  42. Lieten, R. R. *et al.* Structural and Optical Properties of Amorphous and Crystalline GeSn Layers on Si. *ECS J. Solid State Sci. Technol.* **3**, P403–P408 (2014).
  43. Lin, H., Chen, R., Huo, Y., Kamins, T. I. & Harris, J. S. Raman study of strained Ge  $1-x$  Sn  $x$  alloys. *Appl. Phys. Lett.* **98**, 261917 (2011).
  44. Li, S. F., Bauer, M. R., Menéndez, J. & Kouvetakis, J. Scaling law for the compositional dependence of Raman frequencies in SnGe and GeSi alloys. *Appl. Phys. Lett.* **84**, 867–869 (2004).
  45. Gupta, S. *et al.* Highly selective dry etching of germanium over germanium-tin (Ge $1-x$ Sn $x$ ): A novel route for Ge $1-x$ Sn $x$ nanostucture fabrication. *Nano Lett.* **13**, 3783–3790 (2013).
  46. Zhang, Y. G. *et al.* Evaluation of the performance correlated defects of metamorphic InGaAs photodetector structures through plane-view EBIC. *Semicond. Sci. Technol.* **29**, (2014).
  47. Biswas, S., O'Regan, C., Petkov, N., Morris, M. a. & Holmes, J. D. Manipulating the



- growth kinetics of vapor-liquid-solid propagated ge nanowires. *Nano Lett.* **13**, 4044–4052 (2013).
48. Mathews, J. *et al.* Direct-gap photoluminescence with tunable emission wavelength in Ge<sub>1-y</sub>Sn<sub>y</sub> alloys on silicon. *Appl. Phys. Lett.* **97**, 2–5 (2010).
  49. Mosleh, A. *et al.* Material Characterization of Ge<sub>1-x</sub>Sn<sub>x</sub> Alloys Grown by a Commercial CVD System for Optoelectronic Device Applications. *J. Electron. Mater.* **43**, 938–946 (2014).
  50. Dumont, H., Auvray, L. & Monteil, Y. Optical signature of atomic ordering in In<sub>0.53</sub>Ga<sub>0.47</sub>As/InP: Photoluminescence properties and IR response. *Opt. Mater. (Amst)*. **24**, 309–314 (2003).
  51. Stange, D. *et al.* Optical Transitions in Direct-Bandgap Ge<sub>1-x</sub>Sn<sub>x</sub>Alloys. *ACS Photonics* **2**, 1539–1545 (2015).
  52. Pezzoli, F., Giorgioni, A., Patchett, D. & Myronov, M. Temperature-Dependent Photoluminescence Characteristics of GeSn Epitaxial Layers. *ACS Photonics* **3**, 2004–2009 (2016).
  53. Saladukha, D., Doherty, J., Biswas, S., Ochalski, T. J. & Holmes, J. D. Optical study of strain-free GeSn nanowires. *Silicon Photonics Xii* **10108**, 101081C (2017).
  54. Ryu, M. Y., Harris, T. R., Yeo, Y. K., Beeler, R. T. & Kouvetakis, J. Temperature-dependent photoluminescence of Ge/Si and Ge<sub>1-y</sub>Sn<sub>y</sub>/Si, indicating possible indirect-to-direct bandgap transition at lower Sn content. *Appl. Phys. Lett.* **102**, 1–5 (2013).
  55. Hwang, J. D., Chen, Y. H., Kung, C. Y. & Liu, J. C. High photo-to-dark-current ratio in SiGe/Si Schottky-barrier photodetectors by using an a-Si:H cap layer. *IEEE Trans.*

- Electron Devices* **54**, 2386–2391 (2007).
56. Jiang, Y., Zhai, H., Cao, W., Yang, H. & Liu, H. Visible-light self-driven photodetector with enhanced performance based on CdS /Si nanowire heterojunction. *Electron. Mater. Lett.* **12**, 841–845 (2016).
  57. Ali, H. *et al.* High-Responsivity Photodetection by a Self-Catalyzed Phase-Pure p-GaAs Nanowire. *Small* **14**, 1–9 (2018).
  58. Yasar, F., Fan, W. & Ma, Z. Flexible Amorphous GeSn MSM Photodetectors. *IEEE Photonics J.* **10**, 1–9 (2018).
  59. Mahmodi, H. & Hashim, M. R. Effect of substrate temperature on the morphological, structural, and optical properties of RF sputtered Ge<sub>1-x</sub>Sn<sub>x</sub> films on Si substrate. *Chinese Phys. B* **26**, 56801 (2017).

## 4.6. Appendix

The appendix section of this chapter contains supplementary information relating to Chapter 4 (*e.g.* experimental method and characterisation).

### 4.6.1. Experimental

For the growth of  $\text{Ge}_{1-x}\text{Sn}_x$  nanowires dodecanethiol-stabilized  $\text{Au}_{0.90}\text{Ag}_{0.10}$  alloy nanoparticles<sup>1-5</sup> were used as growth seeds. Colloidal nanoparticles were synthesized by co-reducing a mixture of chloroauric acid ( $\text{HAuCl}_4$ ) and silver nitrate ( $\text{AgNO}_3$ ) in a chloroform/water biphasic solution. These nanoparticles were suspended in 10 ml of toluene as standard, but subsequently diluted to 50 % of their original concentration. Si (001) wafers with a native oxide were used as growth substrates following spin coating with the diluted nanoparticles. The substrates were loaded into a metal reaction vessel which was then left under vacuum at 180 °C overnight to ensure desorption of the surfactant molecules.

We have previously reported<sup>6,7</sup> the use of diphenylgermane (DPG) and allyltributylstannane (ATBS) as growth precursors. Solutions of 0.025 ml of DPG and 0.0075 ml of ATBS in 10 ml anhydrous toluene were prepared in an  $\text{N}_2$  filled glove box. A solution containing both Ge and Sn precursors were loaded into a Hamilton sample-lock syringe inside the nitrogen-filled glovebox.

Prior to injection, the coated Si substrates were annealed for 15 min at 440 °C inside a tube furnace under a flowing  $\text{H}_2/\text{Ar}$  atmosphere. The precursor solution was then injected into the metal reaction vessel using a syringe pump at a rate of  $0.025 \text{ ml min}^{-1}$ . A  $\text{H}_2/\text{Ar}$  flow rate of 0.6 sccm was maintained during the entire growth period. A typical nanowire growth time was 2 h. An additional annealing step was also introduced during the cool-down process where the substrate was kept at 230 °C for 2 h under a  $\text{H}_2/\text{Ar}$  flowing atmosphere.

#### 4.6.2. Characterisation

Bottom-up grown  $\text{Ge}_{1-x}\text{Sn}_x$  nanowires were imaged on an FEI Helios NanoLab 600i scanning electron microscope. All EDX measurements were recorded in high-angle annular dark-field mode in the FEI Helios NanoLab 600i operating at 30 kV and 0.69 nA with an attached Oxford X-Max 80 detector. Error in the EDX measurements indicates a standard error of the EDX of 0.5 at. %. Nanowire length and diameter measurements were determined using SEM images on ImageJ, in which the nanowires were clearly visible from end to end. Length measurements were not carried out in STEM or TEM mode in case of breakages during sonication. Mean values for the length and diameter were determined from a minimum of 50 nanowires. EDX mapping was performed on a Titan Themis double-corrected and monochromated Transmission Electron Microscope at 300kV with a Bruker Super X detector. Software for imaging and EDS mapping is FEI Velox. Raman scattering measurements were performed in a backscattering geometry using a micro-Raman setup consisting of a spectrometer (model LabRAM HR, Jobin Yvon) and a Peltier-cooled charge-coupled device detector. An air cooled He-Ne laser of wavelength 488 nm, with an intensity of  $1.77 \times 10^7 \text{ W/m}^2$ , was used as an excitation source. Photoluminescence (PL) data was obtained using a Ti:Sa pulsed laser as the excitation source, tuned to 950 nm with 80 MHz repetition rate, 300 fs pulse width and 0.2 W average power. The laser spot was focused to a 9  $\mu\text{m}$  spot, providing  $200 \text{ kW/cm}^2$  of pump power density. Samples were chilled in liquid nitrogen cryostat down to 7 K. PL was detected by a liquid helium chilled InAs detector with a sensitivity range from 0.9  $\mu\text{m}$  to 3  $\mu\text{m}$  ( $\sim 0.41$ -1.338 eV).

### 4.6.3. Figures

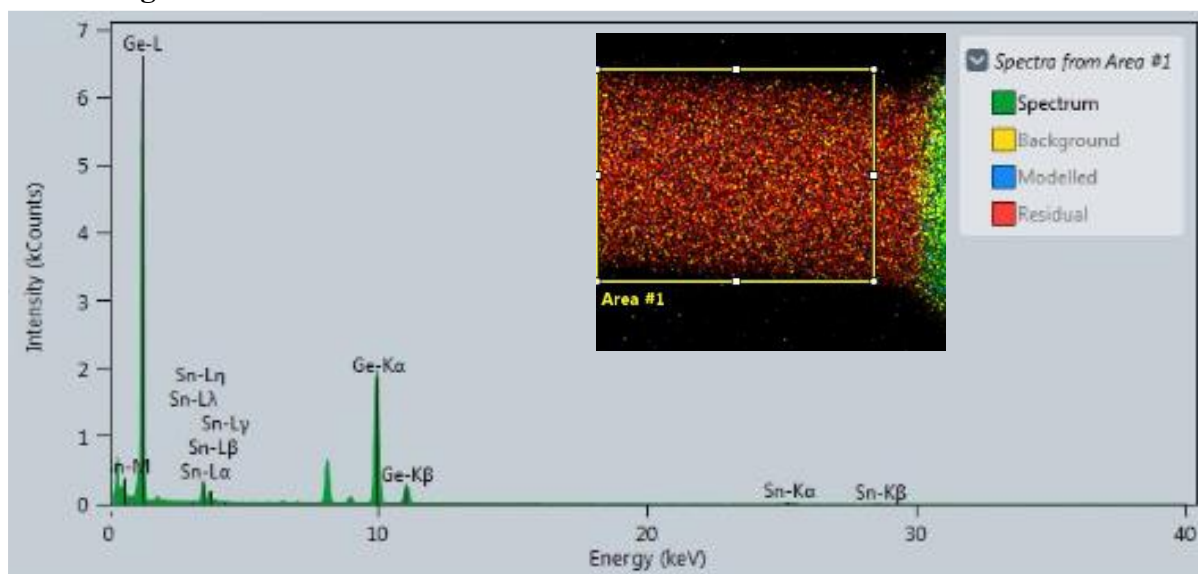


**Figure A3.1:** EDX Spectra of a  $\text{Ge}_{1-x}\text{Sn}_x$  nanowire body ( $x = 0.105$ ) displaying negligible incorporation of Au or Ag from the nanowire seed into the bulk of the nanowire.

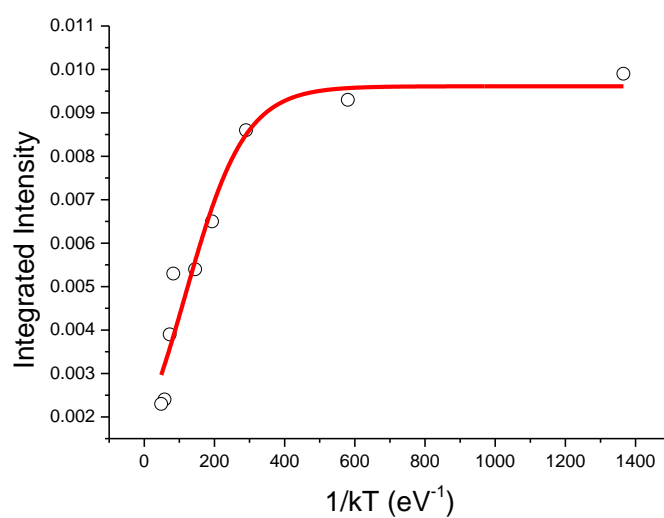


**Figure A3.2:** An Arrhenius plot ( $f$ ) from 10.5 at. %  $\text{Ge}_x\text{Sn}_{1-x}$  nanowires showing good agreement with the theoretical fit denoted by the red line ( $R^2 = 0.92$ ) and an activation energy of  $E_A = 12.5$  meV.

#### 4.6.4. References

1. Biswas, S. *et al.* Non-equilibrium induction of tin in germanium: Towards direct bandgap Ge  $1-x$ Sn $x$ nanowires. *Nat. Commun.* **7**, 11405 (2016).
2. Biswas, S., O'Regan, C., Morris, M. a. & Holmes, J. D. In-situ Observations of Nanoscale Effects in Germanium Nanowire Growth with Ternary Eutectic Alloys. *Small* **11**, 103–111 (2015).
3. Biswas, S., O'Regan, C., Petkov, N., Morris, M. a. & Holmes, J. D. Manipulating the growth kinetics of vapor-liquid-solid propagated ge nanowires. *Nano Lett.* **13**, 4044–4052 (2013).
4. Biswas, S., Singha, A., Morris, M. a. & Holmes, J. D. Inherent control of growth, morphology, and defect formation in germanium nanowires. *Nano Lett.* **12**, 5654–5663 (2012).
5. He, S. T., Xie, S. S., Yao, J. N., Gao, H. J. & Pang, S. J. Self-assembled two-dimensional superlattice of Au-Ag alloy nanocrystals. *Appl. Phys. Lett.* **81**, 150–152 (2002).
6. Biswas, S. *et al.* Non-equilibrium induction of tin in germanium: Towards direct bandgap Ge  $1-x$ Sn $x$ nanowires. *Nat. Commun.* **7**, (2016).
7. Doherty, J. *et al.* Influence of growth kinetics on Sn incorporation in direct band gap Ge  $1-x$  Sn  $x$  nanowires. *J. Mater. Chem. C* 8738–8750 (2018).

# **Chapter 5**

## **Germanium Tin Nanowires as Anode Materials for High Performance Li-Ion Batteries**

This chapter is intended for submission in early 2019. Consequently, sections of the chapter such as the abstract and introduction may contain repeating concepts and paragraphs. I co-wrote this paper with SB and JDH, and performed the nanowire synthesis. I carried out the elemental analysis and analysed the structural (MC, KM and UB) data, while DMcN carried out the electrochemical tests.

Doherty, J.; McNulty, D.; Conroy, M.; Moore, K.; Bangert, U.; Biswas, S.; O'Dwyer, C.; Holmes, J. D Germanium Tin Nanowires as Anode Materials for High Performance Li-Ion Batteries (in preparation).

## 5. Germanium Tin Nanowires as Anode Materials for High Performance Li-Ion Batteries

---

### 5.1. Abstract

The combination of two active Li-ion materials (Ge and Sn) can result in improved conduction paths and higher capacity retention. Here we report the implementation of  $\text{Ge}_{1-x}\text{Sn}_x$  nanowires as anode materials for Li-ion batteries.  $\text{Ge}_{1-x}\text{Sn}_x$  alloy nanowires have been successfully grown *via* a vapour-liquid-solid (VLS) technique on stainless steel current collectors from AuAg alloy nanoparticle catalysts.  $\text{Ge}_{1-x}\text{Sn}_x$  nanowires ( $x = 0.048$ ) were predominantly seeded from the  $\text{Au}_{0.80}\text{Ag}_{0.20}$  catalysts with negligible amount of growth also catalysed from stainless steel substrate. The  $\text{Ge}_{1-x}\text{Sn}_x$  nanowires were determined to be single crystalline and defect free, with a predominant  $\langle 111 \rangle$  growth direction. The electrochemical performance of the  $\text{Ge}_{1-x}\text{Sn}_x$  nanowires as an anode material for Li-ion batteries was investigated *via* galvanostatic cycling and detailed analysis of differential capacity plots. The nanowire electrodes demonstrated an exceptional capacity retention of 93.4 % from the 2<sup>nd</sup> to the 100<sup>th</sup> charge at a C/5 rate, while maintaining a specific capacity value of ~921 mAh/g after 100 cycles. Voltage profiles and differential capacity plots revealed that the  $\text{Ge}_{1-x}\text{Sn}_x$  nanowires behave as an alloying mode anode material, as reduction/oxidation peaks for both Ge and Sn were observed, however it is clear that the reversible lithiation of Ge is responsible for the majority of the charge stored, due to the relatively low amount of Sn present within the alloy nanowires (4.8 at. % Sn).



## 5.2. Introduction

Advancement in Li-ion batteries requires the availability of scalable, cost-effective materials with high energy density.<sup>1</sup> Despite its relatively low capacity (372 mAh/g), graphite remains to be the most commonly used anode material for Li-ion batteries.<sup>2</sup> Other group IV materials, such as Si, Ge and Sn, exhibit bulk capacities far in excess of those of graphite (1620 mAh/g, 3579 mAh/g, 991 mAh/g respectively),<sup>3</sup> however, due to the enormous expansion of bulk Ge and Si upon lithiation, leading to the pulverisation of the material, the cycle life, and thus retention of the material, is decreased. Nanowires offer a unique solution to this problem; the ability of nanowires to transition from crystalline to amorphous phase while retaining their structural integrity make them suitable structures for use in Li-ion batteries. Hence, the manufacturing of group IV nanowires for use as battery materials has been widely explored.<sup>3–6</sup> Ge nanowires in particular have been identified for their suitability as anode materials in Li-ion batteries.<sup>2,7–10</sup> Both Sn and Pb-catalysed Ge nanowires have previously been reported to demonstrate high capacities when used as an anode material for Li ion batteries.<sup>11</sup>

Ge shows enhanced battery performance over its group IV counterparts, Si and Sn, and increased carrier mobility.<sup>12</sup> However, Ge also demonstrates poor cycling life and capacity fading. With its high electronic conductivities and theoretical capacity, Sn is a good candidate for alloying with Ge for energy storage applications.<sup>13</sup> The combination of two active Li-ion materials can result in improved conduction paths with higher capacity retention.<sup>14</sup> The use of  $\text{Ge}_{1-x}\text{Sn}_x$  alloys has previously been shown to enhance the energy storage properties of Ge in nanocrystal and amorphous form.<sup>12–14</sup>  $\text{Ge}_{1-x}\text{Sn}_x$  nanocrystals with  $x = 0.05$  showed an improvement in capacitance and retention over Ge nanocrystals.<sup>12</sup> However, the surface area of these nanomaterials may be too high, leading to significant side reactions.<sup>14</sup> The open continuous channel along the axis of a nanowire, on the other hand, could result in an increase

in capacity and retention due to a decrease in sidewall reactions.<sup>15</sup> Therefore, we report the fabrication of  $\text{Ge}_{1-x}\text{Sn}_x$  ( $x = 0.048$ ) alloy nanowires, which are grown directly on stainless steel substrates for use as anode materials in Li-ion batteries. The growth of  $\text{Ge}_{1-x}\text{Sn}_x$  nanowires directly on the stainless steel current collector eliminates the requirement to prepare a conductive slurry of the active material with a binder. The high capacities ( $> 900 \text{ mAh/g}$  after 100 cycles) and impressive capacity retention verify the potential of our binder-free  $\text{Ge}_{1-x}\text{Sn}_x$  nanowire electrodes as promising anode materials.

### 5.3. Results and Discussion

The direct growth of  $\text{Ge}_{1-x}\text{Sn}_x$  nanostructures on a stainless steel substrate for use as anode material for Li-ion batteries presents a new venture in the growth of  $\text{Ge}_{1-x}\text{Sn}_x$  nanowires, and to our knowledge, this study represents the first reported instance of  $\text{Ge}_{1-x}\text{Sn}_x$  alloy nanowires for use in Li-ion batteries. Nanowire growth was carried out using a modified version of a previously reported<sup>16</sup> bottom-up method using diphenylgermane (DPG) and tetraethyltin (TET) as the Ge and Sn sources respectively, and  $\text{Au}_{0.80}\text{Ag}_{0.20}$  nanoparticles as the growth catalysts (for detailed experimental methods and characterisation, see 5.5. Appendix). This precursor and catalyst combination was previously reported to produce  $\text{Ge}_{1-x}\text{Sn}_x$  ( $x = 0.09$ ) nanowires on Si growth substrates.<sup>16</sup> A scanning electron microscopy (SEM) image of  $\text{Ge}_{1-x}\text{Sn}_x$  nanowires grown on stainless steel is presented in Figure 5.1(a). The nanowires have a mean diameter of  $75 \pm 30 \text{ nm}$ . Low resolution STEM imaging (Figure 5.1(b)) reveals metallic nanoparticles at the tips of the nanowires and negligible tapering along their lengths. Energy dispersive X-ray (EDX) analysis of the  $\text{Ge}_{1-x}\text{Sn}_x$  nanowires revealed an average Sn content of  $4.8 \pm 2.1 \text{ at. \%}$ . This Sn incorporation was consistent throughout the nanowires, both radially and axially, as

verified by EDX elemental mapping (Figure 5.1(c)). EDX mapping also revealed the formation of a Sn-rich alloy at the tips of the nanowires at a growth temperature of 440 °C (Figure 5.1(c)).

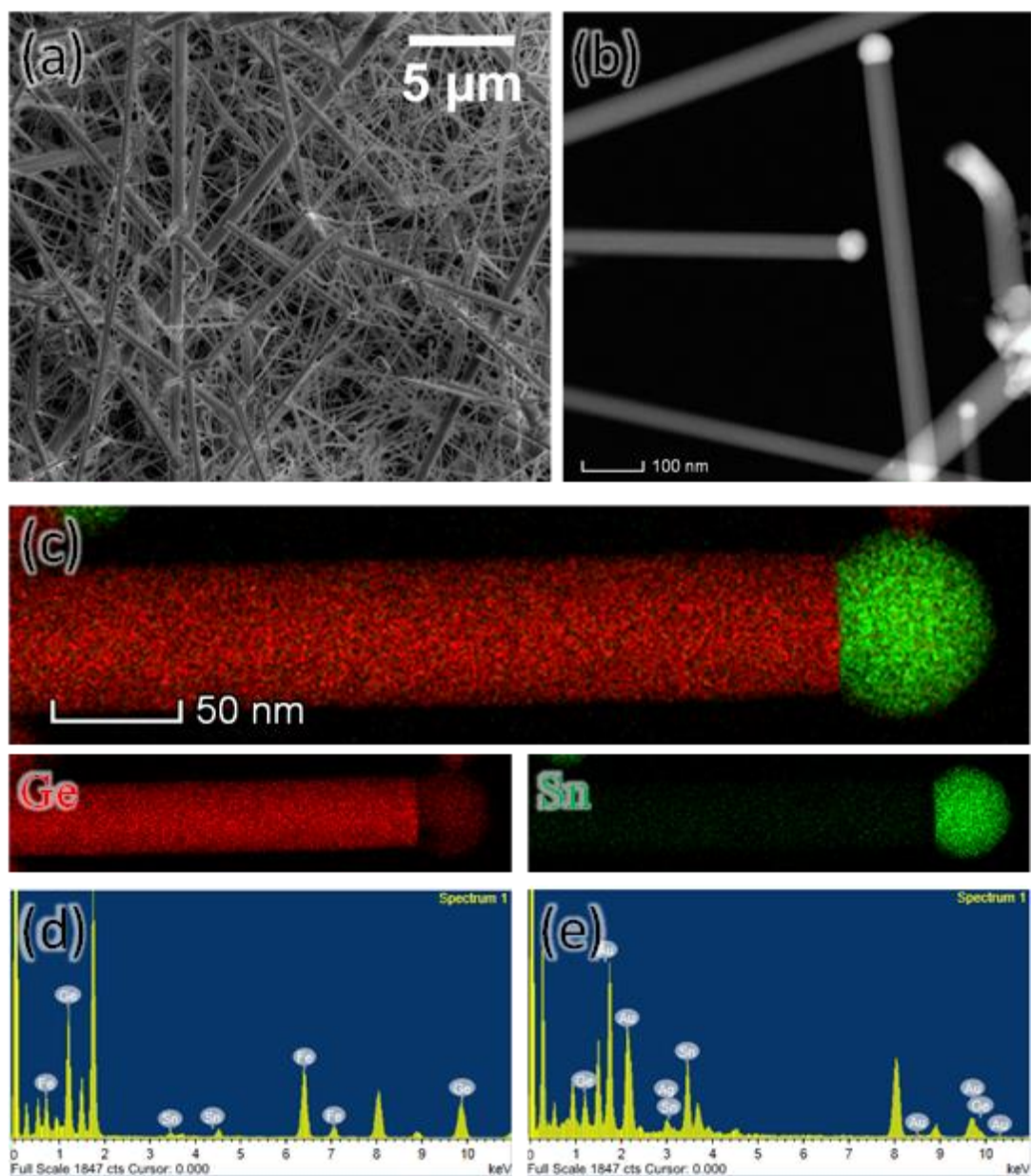


**Figure 5.1:** SEM and STEM images of the  $\text{Ge}_{1-x}\text{Sn}_x$  nanowires grown on stainless steel reveal a large variation in nanowire diameter (a) across the substrate, but a negligible change in diameter due to tapering of single nanowires (b) respectively. (c) EDX elemental mapping of  $\text{Ge}_{1-x}\text{Sn}_x$  nanowires with  $x = 0.048$ . Ge is denoted in red and Sn in green. The nanowire in (c) is AuAg-seeded, clearly apparent from the presence of a Sn rich nanowire seed in the elemental map and therefore may have a higher than average Sn content ( $x > 0.048$ ). Evidence of the two competing growth seeds is provided in (d) and (e), with EDX spectra displaying the presence of Fe, and Au and Ag respectively.

However, the use of a stainless steel substrate did alter the quality of the grown nanowires, in terms of morphology and Sn content, compared to  $\text{Ge}_{1-x}\text{Sn}_x$  nanowires previously grown on Si substrates.<sup>16,17</sup> These differences could possibly be due to the difference in the surface energies of the substrates which result in different wetting angles and surface curvatures of the intermediate eutectic liquid during VLS growth. Differences in the curvature of the liquid eutectic can readily influence the absorption of growth species and growth kinetics at different interfaces (vapour-liquid, liquid-solid *etc.*), thus resulting in  $\text{Ge}_{1-x}\text{Sn}_x$  nanowires with different morphologies and Sn incorporation. Additionally, the possible participation of iron-based catalysts as additional growth promoters<sup>18</sup> from the stainless steel substrate may also have resulted in a vapour-solid-solid (VSS)-like nanowire growth regime, thus resulting in wider diameter distribution (5.6. Appendix, Figure A5.1). The large variation in the Sn content ( $4.8 \pm 2.1$  at. %) in the  $\text{Ge}_{1-x}\text{Sn}_x$  nanowire sample can be attributed to the two competing growth regimes present with the participation of two different growth promoters. Analysis of the catalyst seed at the nanowire tips also revealed two distinct compositions, Fe rich Fe/Ge/Sn and Sn rich Au/Ag/Ge/Sn. The Ge/Fe rich nanowire tips had a composition of approximately 65 at. % Fe and 35 at. % Ge with minimal Sn incorporation ( $\sim 3$  at. %). These  $\text{FeGe}_2$  catalysts resulted in Sn deficient  $\text{Ge}_{1-x}\text{Sn}_x$  nanowires (5.6. Appendix, Figure A5.2). Alternatively,  $\text{Ge}_{1-x}\text{Sn}_x$  nanowires with Sn rich tips, containing Au and Ag, contained a higher Sn content (5.6. Appendix, Figure A5.2). By analysing the nanowire tips (approximately 40 nanowires), it was found that statistically  $\sim 75$  % of the nanowires were seeded by Au and Ag (Sn rich). Fe-seeded nanowires accounted for a minority of the  $\text{Ge}_{1-x}\text{Sn}_x$  nanowires grown. The lower Sn composition in these  $\text{Ge}_{1-x}\text{Sn}_x$  nanowires (5.6. Appendix, Figure A5.2) seeded directly by stainless steel substrate is expected due to the VSS nature of the Fe seeded  $\text{Ge}_{1-x}\text{Sn}_x$  growth; the eutectic temperatures of Fe-Ge<sup>19</sup> and Fe-Sn<sup>20</sup> are far above the temperature used to grow the  $\text{Ge}_{1-x}\text{Sn}_x$  nanowires. As Sn incorporation is likely aided by a solute trapping

mechanism,<sup>16,21</sup> participation and formation of a Fe-Ge-Sn based alloy solid growth seed in the VSS nanowire growth does not encourage trapping of foreign impurities. Interestingly, in the Fe-seeded  $\text{Ge}_{1-x}\text{Sn}_x$  nanowires, Sn was still present in non-trivial amounts in the majority of the nanowires (5.6. Appendix, Figure A5.2). However, as both of these nanowire types contribute as anode materials in Li-ion batteries to the overall capacitance and cycle life, both types of  $\text{Ge}_{1-x}\text{Sn}_x$  nanowire were included in the determination of the average Sn composition.

A high resolution scanning transmission electron microscopy (HRSTEM) of the  $\text{Au}_{0.80}\text{Ag}_{0.20}$ -seeded  $\text{Ge}_{1-x}\text{Sn}_x$  nanowires ( $x = 0.048$ ) revealed the highly crystalline nature of the nanowires with sharp seed/nanowire interfaces (Figure 5.2). Figure 5.2(a) depicts the bright field HRSTEM image of a defect free, single crystalline nature of a  $\text{Ge}_{1-x}\text{Sn}_x$  nanowires. As defect free materials allow for long life cycles, the structural uniformity of the  $\text{Ge}_{1-x}\text{Sn}_x$  nanowires is imperative for their use as Li ion anode materials.<sup>22</sup> Fast Fourier Transform (FFT) analysis of the nanowire, with  $\langle 110 \rangle$  zone axis alignment (Figure 5.2(a) inset), revealed an interplanar spacing ( $d$ ) of 0.33 nm, which is marginally larger than the  $d$  value for bulk diamond Ge crystals of 0.326 nm (JCPDS 04–0545). The  $d$  spacing is expected to increase upon the incorporation of Sn into the Ge host lattice due to the difference in the lattice constants of Ge and Sn, which can instigate a lattice expansion, and has been previously reported.<sup>21</sup> The nanowires predominantly displayed a  $\langle 111 \rangle$  growth direction, the most common growth orientation for Ge nanowires with a mean diameter above 50 nm.<sup>21,23</sup> Generally, the crystal structure of the  $\text{Ge}_{1-x}\text{Sn}_x$  alloy nanowires, with various Sn incorporations, exhibited a 3C lattice arrangement without any stacking faults and twin boundaries. The interface between the nanowire seed and body was examined and can be seen in Figure 5.2(b). No apparent tailing or segregation of Sn from the Sn rich seed was observed, confirming the sharp junction at the interface as indicated

from the EDX elemental maps in Figure 5.1(c). FFT of a nanowire seed (Figure 5.2(b), inset) matches well with tetragonal Sn (JCPDS 04–0673), confirming the Sn-rich nature of the nanowire seed. The interplanar spacing of the nanowire seed ( $d$ ) was 0.28 nm, confirmed by measurement of the lattice spacing for multiple layers.

The electrochemical performance of the  $\text{Ge}_{1-x}\text{Sn}_x$  nanowires as an anode material for Li-ion batteries was investigated *via* galvanostatic cycling in a half-cell configuration versus Li metal. A selection of the charge and discharge voltage profiles obtained from galvanostatic cycling using a C/5 rate are shown in Figure 5.3(a) and (b). The first charge curve consisted of a sloping region from an open circuit voltage (OCV) (3.20 V) to  $\sim 0.35$  V, followed by a long plateau from  $\sim 0.30$  V to the low potential limit of 0.01 V. The sloping region is associated

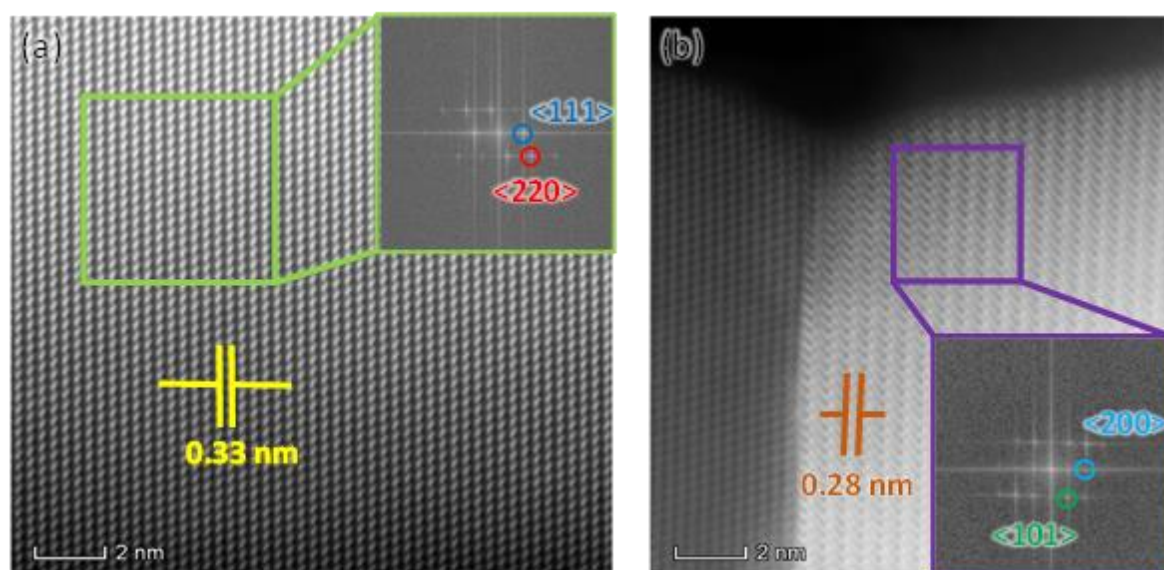


**Figure 5.2:** HRSTEM analysis of  $\text{Ge}_{1-x}\text{Sn}_x$  nanowires. (a) The  $\text{Ge}_{1-x}\text{Sn}_x$  nanowires are single crystalline with no apparent defects or twin boundaries. The lattice spacing of the nanowires is 0.33 nm, confirmed by FFT (inset). These nanowires are grown along the  $\langle 111 \rangle$  direction. The sharp interface between the nanowire seed and body is shown in (b); FFT provided in the inset. There is negligible apparent tailing of the Sn rich seed at the growth interface.

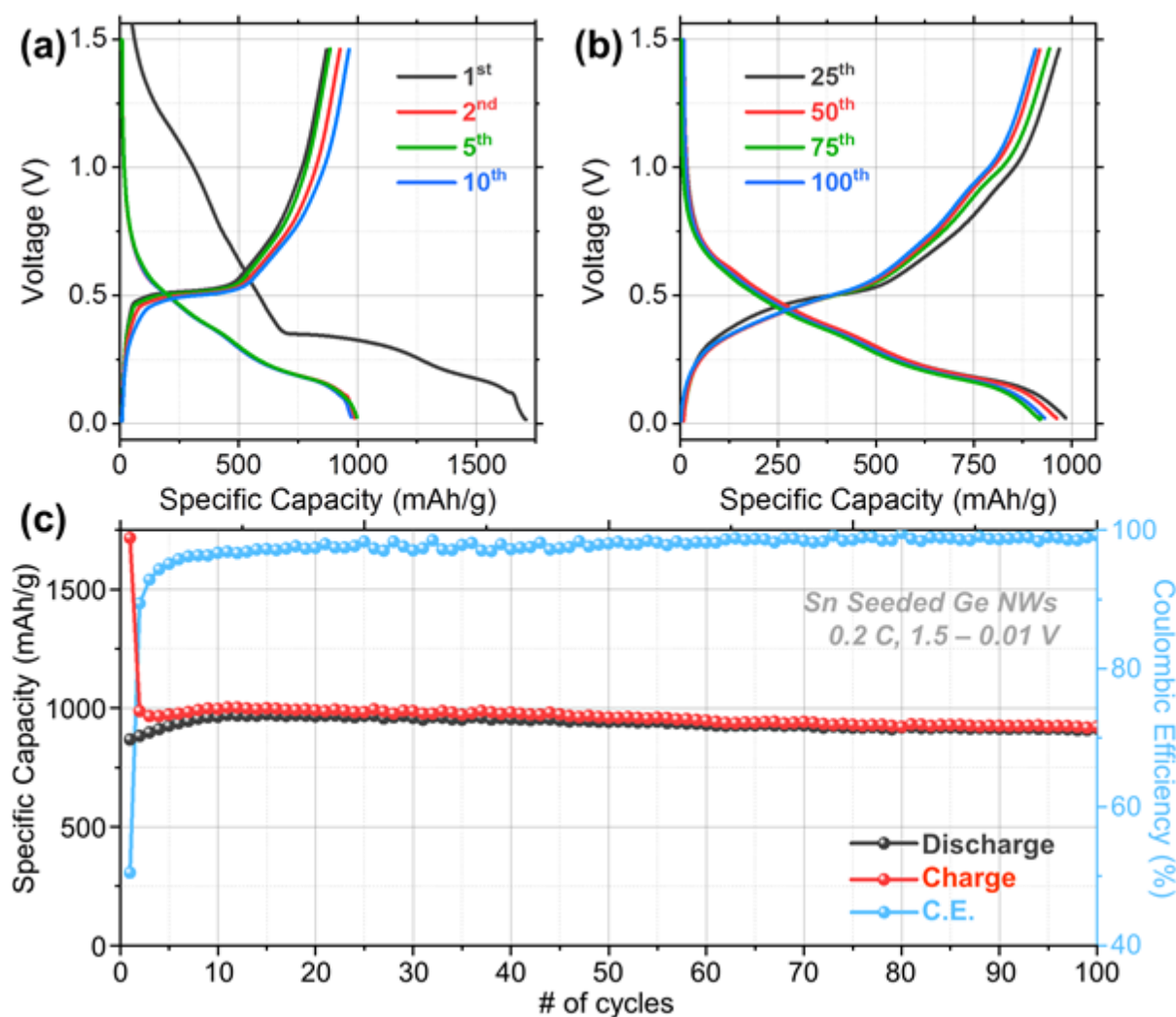


**Figure 5.3:** Charge and discharge voltage profiles for (a) the 1<sup>st</sup>, 2<sup>nd</sup>, 5<sup>th</sup> and 10<sup>th</sup> cycles (b) the 25<sup>th</sup>, 50<sup>th</sup>, 75<sup>th</sup> and 100<sup>th</sup> cycles for  $\text{Ge}_{1-x}\text{Sn}_x$  nanowires at  $C/5$  in a potential window of 1.5 – 0.01 V (vs Li/Li+). (c) Specific capacity and Coulombic efficiency values obtained for  $\text{Ge}_{1-x}\text{Sn}_x$  nanowires over 100 cycles.

with the formation of an SEI layer and the irreversible decomposition of the electrolyte on the surface of the  $\text{Ge}_{1-x}\text{Sn}_x$  nanowires. The plateau is attributed to the alloying of the nanowires with Li.<sup>24</sup> The first discharge curve consisted of a plateau at ~0.50 V, corresponding to the dealloying of the  $\text{Ge}_{1-x}\text{Sn}_x$  nanowires. The initial charge and discharge capacities were ~1716 and 867 mAh/g, respectively, corresponding to an initial Coulombic efficiency (ICE) of 50.5 %. The large initial charge capacity is likely due to the formation of an SEI layer on the surface of the nanowires as well as the formation of quasi reversible  $\text{Li}_2\text{O}$ .<sup>25</sup> The ICE value obtained

for  $\text{Ge}_{1-x}\text{Sn}_x$  nanowires is comparable to or greater than ICE values reported for other Ge nanowire anodes.<sup>7,26</sup> Low ICE is a persistent issue for alloying mode anode materials such as Ge and Si based negative electrode materials however, there are some reports demonstrating that the prelithiation of Si nanostructures can improve ICE values. Forney et al. prelithiated Si-CNT anodes *via* mechanical pressing of stabilized lithium metal powder onto the working electrode, and demonstrated a significant increase in ICE values.<sup>27</sup> The voltage profiles from the 2<sup>nd</sup> cycle to the 100<sup>th</sup> cycle are quite consistent, which is indicative of a highly reversible process.

The specific capacity values obtained over 100 cycles at a rate of C/5 and the corresponding coulombic efficiencies are shown in Figure 5.3(c). The specific capacity after the 2<sup>nd</sup> charge was ~986 mAh/g and after 100 cycles this decreased marginally to ~921 mAh/g, corresponding to an exceptional capacity retention of 93.4 %. The average Coulombic efficiency from the 2<sup>nd</sup> to the 100<sup>th</sup> cycle was also impressive, having a value of 97.8 %. Preserving such a high level of capacity after 100 cycles clearly validates the viability of  $\text{Ge}_{1-x}\text{Sn}_x$  nanowires for use as an anode material in practical commercial Li-ion cells. The specific capacity values achieved for the  $\text{Ge}_{1-x}\text{Sn}_x$  nanowires are comparable to<sup>11,28</sup> or greater than<sup>29–32</sup> previously reported values for other Ge based anode materials.

In order to better appreciate the charge storage mechanism of the  $\text{Ge}_{1-x}\text{Sn}_x$  nanowires, which results in their impressive capacity retention properties, differential capacity plots from galvanostatic charge and discharge curves were calculated. The initial charge curve consisted of a series of plateaus which can be seen more clearly in the differential capacity plot (DCP) presented in Figure A5.3(a). The DCP for the first charge consisted of 5 peaks in total. The



wide band centred at  $\sim 1.21$  V is associated with the formation of an SEI layer and is only observed during the first cycle.<sup>33</sup> The weak peak present at  $\sim 0.74$  V may be attributed to the alloying of Li with the low amount of Sn (4.8 at. %) which is present in the nanowires. A reduction peak at this potential has previously been reported for Sn-based anode materials.<sup>28</sup> The strong, sharp peak centred at 0.35 V is due to the lithiation of crystalline Ge (c-Ge) and is only observed during the first cycle, suggesting that after the initial lithiation of the nanowires, they do not return to a fully delithiated crystalline Ge phase. A similar observation for this reduction peak was made by Mullane et al. for Cu-catalysed Ge nanowires.<sup>2</sup> The strong peak at 0.19 V and the weaker shoulder at 0.15 V are due to the initial formation of Li-Ge alloys in the form of a-Li<sub>15</sub>Ge<sub>4</sub> and c-Li<sub>15</sub>Ge<sub>4</sub>, respectively.<sup>28</sup> A strong, wide, asymmetric oxidation peak was observed in the first cathodic scan from 0.35 to 0.55 V, which can be deconvoluted into two distinct peaks centred at 0.49 and 0.51 V, as shown in Figure A5.3(c), corresponding to the delithiation of the c-Li<sub>15</sub>Ge<sub>4</sub> and a-Li<sub>15</sub>Ge<sub>4</sub> phases, respectively.<sup>34,35</sup>

The DCP for the 2<sup>nd</sup> charge consisted of two wide peaks centred at 0.53 and 0.39 V and a sharp peak at 0.18 V, as shown in 5.6. Appendix, Figure A5.3. The two broad peaks are associated with the formation of amorphous Li-Ge alloys (a-Li<sub>x</sub>Ge  $\rightarrow$  a-Li<sub>15</sub>Ge<sub>4</sub>) and the sharp peak is due to the formation of c-Li<sub>15</sub>Ge<sub>4</sub>.<sup>10,36</sup> Contour plots, calculated from a series of DCPs from charge and discharge voltage profiles, ranging from the 2<sup>nd</sup> to the 100<sup>th</sup> cycle are shown in Figure 4. The reduction peaks associated with the formation of the a-Li<sub>15</sub>Ge<sub>4</sub> and c-Li<sub>15</sub>Ge<sub>4</sub> phases, centred at 0.39 and 0.18 V, remain present during the 100 cycles, as shown in Figure 5.4(a). This indicates how highly reversible the lithiation/delithiation of Ge<sub>1-x</sub>Sn<sub>x</sub> nanowires is. The presence of these reduction peaks and the consistency of the potentials at which they occur is a major contributing factor to the impressive capacity retention of the nanowires from

the 2<sup>nd</sup> cycle onwards. Initially the majority of the charge stored by the  $\text{Ge}_{1-x}\text{Sn}_x$  nanowires is due to the formation of the  $\text{c-Li}_{15}\text{Ge}_4$  phase, as indicated by the red area in Figure 4(a), however as cycling continues the intensity of this reduction peak decreases slightly while the intensity of the reduction peak associated with the formation of the  $\text{a-Li}_{15}\text{Ge}_4$  phase remains consistent. This suggests that with increased cycling more of the charge stored is due to the transition from  $\text{a-Li}_x\text{Ge} \rightarrow \text{a-Li}_{15}\text{Ge}_4$ .

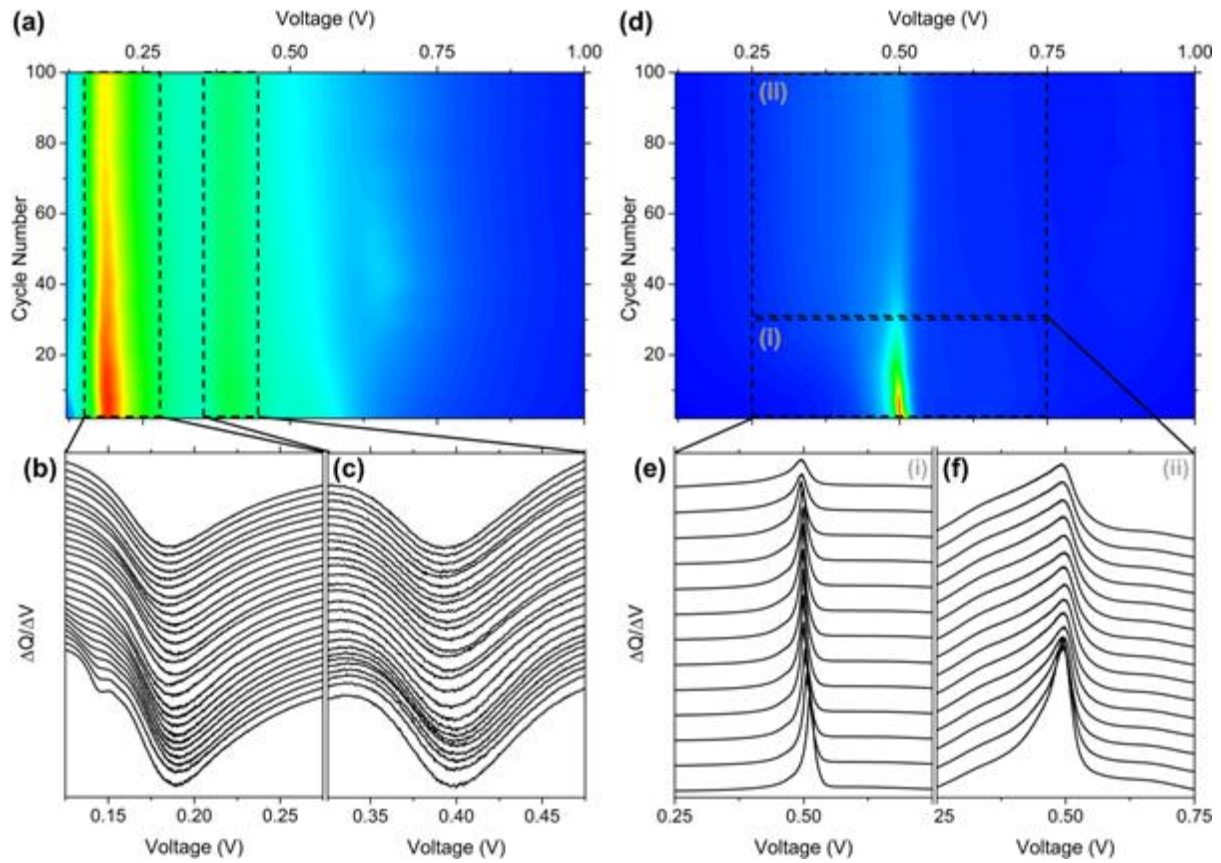


**Figure 4:** (a) Differential capacity contour plot calculated from differential charge curves. Stacked differential capacity curves demonstrating the reduction peak associated with the formation of (b) the  $\text{c-Li}_{15}\text{Ge}_4$  phase and (c) the  $\text{a-Li}_{15}\text{Ge}_4$  phase. (d) Differential capacity contour plot calculated from differential discharge curves. Stacked differential capacity curves demonstrating the oxidation peak associated with the delithiation of for  $\text{Ge}_{1-x}\text{Sn}_x$  nanowires (e) from the 1<sup>st</sup> to the 30<sup>th</sup> cycle and (f) from the 31<sup>th</sup> to the 100<sup>th</sup> cycle.

The contour plot calculated from the DCPs for discharge curves is shown in Figure 5.4(d). The asymmetric oxidation peak associated with the delithiation of the c-Li<sub>15</sub>Ge<sub>4</sub> and a-Li<sub>15</sub>Ge<sub>4</sub> phases remains after 100 cycles, however there is a significant decrease in the intensity after the first 30 cycles. The stacked DCPs in Figures 4e and f indicate that the width of the peak increases with increased cycling, which may be associated with decreased charge storage due to the formation of the c-Li<sub>15</sub>Ge<sub>4</sub> phase. Of note, the discharge capacity values presented in Figure 5.4(c) do not significantly decrease after 30 cycles, hence the widening of this oxidation peak with increased cycling does not have a substantial negative influence on the overall charge stored. Initially the majority charge storage mechanism for the Ge<sub>1-x</sub>Sn<sub>x</sub> nanowires is the formation of the c-Li<sub>15</sub>Ge<sub>4</sub> phase, however as cycling continues, less charge is being stored *via* the formation of this phase and more of the overall charge stored is due to the formation of the a-Li<sub>15</sub>Ge<sub>4</sub> phase. We have previously observed a similar trend for GeO<sub>2</sub> inverse opal structured anodes, whereby after a number of cycles the preferred charge storage mechanism was the formation of the a-Li<sub>15</sub>Ge<sub>4</sub> phase rather than the c-Li<sub>15</sub>Ge<sub>4</sub> phase.<sup>37</sup>

#### 5.4. Conclusion

Ge<sub>1-x</sub>Sn<sub>x</sub> alloy nanowires were successfully grown directly on stainless steel substrates, current collectors, thus eliminating the requirement to prepare a conductive slurry of the active material with a binder. Ge<sub>1-x</sub>Sn<sub>x</sub> nanowires with  $x = 0.048$  were determined to be seeded both from the Au<sub>0.80</sub>Ag<sub>0.20</sub> nanoparticle catalyst and from the substrate itself (Fe). The Ge<sub>1-x</sub>Sn<sub>x</sub> nanowires were single crystalline and defect free prior to lithiation. The electrochemical performance of the the Ge<sub>1-x</sub>Sn<sub>x</sub> nanowires as an anode material for Li-ion batteries was investigated *via* galvanostatic cycling. The nanowire electrodes demonstrated an exceptional capacity retention of 93.4 % from the 2<sup>nd</sup> to the 100<sup>th</sup> charge at a C/5 rate, while maintaining a specific capacity

value of ~921 mAh/g after 100 cycles. Voltage profiles and differential capacity plots revealed that the  $\text{Ge}_{1-x}\text{Sn}_x$  nanowires behaved as a dual alloying mode anode material as reduction/oxidation peaks for both Ge and Sn were observed. However, it was clear that the reversible lithiation of Ge was responsible for the majority of the charge stored due to the relatively low amount of Sn present within the alloy nanowires (4.8 at. % Sn).

To increase the potential capacitance of these  $\text{Ge}_x\text{Sn}_{1-x}$  nanowires, Chapter 6 looks at a move towards  $\text{Ge}_x\text{Sn}_{1-x}$  nanowires branched nanostructures. The growth mechanism of  $\text{Ge}_x\text{Sn}_{1-x}$  nanostructures with a low-Sn nanowire trunk (4.4 at. %) and high-Sn nanowire branches (8.0 at. %) is also investigated and detailed in Chapter 6.

## 5.5. References

1. Osiak, M., Geaney, H., Armstrong, E. & O'Dwyer, C. Structuring materials for lithium-ion batteries: Advancements in nanomaterial structure, composition, and defined assembly on cell performance. *J. Mater. Chem. A* **2**, 9433–9460 (2014).
2. Mullane, E., Kennedy, T., Geaney, H. & Ryan, K. M. A rapid, solvent-free protocol for the synthesis of germanium nanowire lithium-ion anodes with a long cycle life and high rate capability. *ACS Appl. Mater. Interfaces* **6**, 18800–18807 (2014).
3. Tian, H., Xin, F., Wang, X., He, W. & Han, W. High capacity group-IV elements (Si, Ge, Sn) based anodes for lithium-ion batteries. *J. Mater.* **1**, 153–169 (2015).
4. Bogart, T. D., Chockla, A. M. & Korgel, B. A. High capacity lithium ion battery anodes of silicon and germanium. *Curr. Opin. Chem. Eng.* **2**, 286–293 (2013).
5. Stokes, K. *et al.* Direct Synthesis of Alloyed Si  $1-x$  Ge  $x$  Nanowires for Performance-Tunable Lithium Ion Battery Anodes. *ACS Nano* **11**, 10088–10096 (2017).
6. Kennedy, T., Brandon, M. & Ryan, K. M. Advances in the Application of Silicon and Germanium Nanowires for High-Performance Lithium-Ion Batteries. *Adv. Mater.* **28**, 27 (2016).
7. Chockla, A. M., Klavetter, K. C., Mullins, C. B. & Korgel, B. A. Solution-grown germanium nanowire anodes for lithium-ion batteries. *ACS Appl. Mater. Interfaces* **4**, 4658–4664 (2012).
8. Flynn, G., Palaniappan, K., Sheehan, M., Kennedy, T. & Ryan, K. M. Solution synthesis of lead seeded germanium nanowires and branched nanowire networks and their application as Li-ion battery anodes. *Nanotechnology* **28**, (2017).

9. Li, X. *et al.* Germanium anode with excellent lithium storage performance in a germanium/lithium-cobalt oxide lithium-ion battery. *ACS Nano* **9**, 1858–1867 (2015).
10. Liu, X. H. *et al.* Reversible nanopore formation in Ge nanowires during lithiation-delithiation cycling: An in situ transmission electron microscopy study. *Nano Lett.* **11**, 3991–3997 (2011).
11. Mullane, E., Kennedy, T., Geaney, H., Dickinson, C. & Ryan, K. M. Synthesis of tin catalyzed silicon and germanium nanowires in a solvent-vapor system and optimization of the seed/nanowire interface for dual lithium cycling. *Chem. Mater.* **25**, 1816–1822 (2013).
12. Cho, Y. J. *et al.* Germanium-tin alloy nanocrystals for high-performance lithium ion batteries. *Phys. Chem. Chem. Phys.* **15**, 11691–11695 (2013).
13. Lee, H. & Cho, J. Sn<sub>78</sub>Ge<sub>22</sub>@carbon core-shell nanowires as fast and high-capacity lithium storage media. *Nano Lett.* **7**, 2638–2641 (2007).
14. Kim, M. G. & Cho, J. Nanocomposite of Amorphous Ge and Sn Nanoparticles as an Anode Material for Li Secondary Battery. *J. Electrochem. Soc.* **156**, A277 (2009).
15. Yang, Z. *et al.* Dispersion of SnO<sub>2</sub> nanocrystals on TiO<sub>2</sub>(B) nanowires as anode material for lithium ion battery applications. *RSC Adv.* **1**, 1834 (2011).
16. Doherty, J. *et al.* Influence of growth kinetics on Sn incorporation in direct band gap Ge<sub>1-x</sub>Sn<sub>x</sub> nanowires. *J. Mater. Chem. C* 8738–8750 (2018).
17. Biswas, S. *et al.* Non-equilibrium induction of tin in germanium: Towards direct bandgap Ge<sub>1-x</sub>Sn<sub>x</sub> nanowires. *Nat. Commun.* **7**, (2016).
18. Biswas, S. *et al.* Diameter-controlled germanium nanowires with lamellar twinning and

- polytypes. *Chem. Mater.* **27**, (2015).
19. Okamoto, H. Fe-Ge (Iron-Germanium). *J. Phase Equilibria Diffus.* **29**, 1 (2008).
  20. Hari Kumar, K.C., P. Wollants, L. D. Thermodynamic evaluation of Fe-Sn phase. (1994).
  21. Biswas, S. *et al.* Non-equilibrium induction of tin in germanium: Towards direct bandgap Ge  $1-x$ Sn $x$ nanowires. *Nat. Commun.* **7**, 11405 (2016).
  22. Park, K. H. *et al.* Defect-free, size-tunable graphene for high-performance lithium ion battery. *Nano Lett.* **14**, 4306–4313 (2014).
  23. Biswas, S., O'Regan, C., Petkov, N., Morris, M. a. & Holmes, J. D. Manipulating the growth kinetics of vapor-liquid-solid propagated ge nanowires. *Nano Lett.* **13**, 4044–4052 (2013).
  24. Chan, C. K., Zhang, X. F. & Cui, Y. High capacity Li ion battery anodes using Ge nanowires. *Nano Lett.* **8**, 307–309 (2008).
  25. Ngo, D. T., Kalubarme, R. S., Le, H. T. T., Park, C. N. & Park, C. J. Conducting additive-free amorphous GeO<sub>2</sub>/C composite as a high capacity and long-term stability anode for lithium ion batteries. *Nanoscale* **7**, 2552–2560 (2015).
  26. Kim, G. T. *et al.* Behavior of Germanium and Silicon Nanowire Anodes with Ionic Liquid Electrolytes. *ACS Nano* **11**, 5933–5943 (2017).
  27. Forney, M. W., Ganter, M. J., Staub, J. W., Ridgley, R. D. & Landi, B. J. Prelithiation of silicon-carbon nanotube anodes for lithium ion batteries by stabilized lithium metal powder (SLMP). *Nano Lett.* **13**, 4158–4163 (2013).

28. Kennedy, T. *et al.* High-performance germanium nanowire-based lithium-ion battery anodes extending over 1000 cycles through in situ formation of a continuous porous network. *Nano Lett.* **14**, 716–723 (2014).
29. Qiang, T. *et al.* Ge@C core-shell nanostructures for improved anode rate performance in lithium-ion batteries. *RSC Adv.* **5**, 17070–17075 (2015).
30. Guo, W., Mei, L., Feng, Q. & Ma, J. Facile synthesis of Ge/C nanocomposite as superior battery anode material. *Mater. Chem. Phys.* **168**, 6–9 (2015).
31. Choe, H. S. *et al.* Synthesis of Ge/C composites as anodes using glucose as a reductant and carbon source for lithium-ion batteries. *RSC Adv.* **6**, 72926–72932 (2016).
32. Li, W. *et al.* Germanium nanoparticles encapsulated in flexible carbon nanofibers as self-supported electrodes for high performance lithium-ion batteries. *Nanoscale* **6**, 4532–4537 (2014).
33. Fang, S., Shen, L., Zheng, H. & Zhang, X. Ge-graphene-carbon nanotube composite anode for high performance lithium-ion batteries. *J. Mater. Chem. A* **3**, 1498–1503 (2015).
34. Lim, L. Y., Fan, S., Hng, H. H. & Toney, M. F. Storage Capacity and Cycling Stability in Ge Anodes: Relationship of Anode Structure and Cycling Rate. *Adv. Energy Mater.* **5**, (2015).
35. Yoon, S., Park, C.-M. & Sohn, H.-J. Electrochemical Characterizations of Germanium and Carbon-Coated Germanium Composite Anode for Lithium-Ion Batteries. *Electrochem. Solid-State Lett.* **11**, A42 (2008).
36. Baggetto, L. & Notten, P. H. L. Lithium-Ion (De)Insertion Reaction of Germanium



Thin-Film Electrodes: An Electrochemical and In Situ XRD Study. *J. Electrochem. Soc.* **156**, A169 (2009).

37. McNulty, D., Geaney, H., Buckley, D. & O'Dwyer, C. High capacity binder-free nanocrystalline GeO<sub>2</sub> inverse opal anodes for Li-ion batteries with long cycle life and stable cell voltage. *Nano Energy* **43**, 11–21 (2018).

## 5.6. Appendix

The appendix section of this chapter contains supplementary information relating to Chapter 5 (e.g. Experimental method and characterisation).

### 5.6.1. Experimental

For the catalysation of  $\text{Ge}_{1-x}\text{Sn}_x$  nanowires in a three phase bottom-up growth dodecanethiol-stabilized, phase pure,  $\text{Au}_{0.80}\text{Ag}_{0.20}$  alloy nanoparticles were used. Colloidal nanoparticles were synthesized by co-reducing a mixture of chloroauric acid ( $\text{HAuCl}_4$ ) and silver nitrate ( $\text{AgNO}_3$ ) in a chloroform/water biphasic solution.<sup>1-4</sup> These metal nanoparticles were deposited onto a stainless steel substrate *via* spin coating. A metal reaction vessel containing the nanoparticle-coated substrate was then left under vacuum at 180 °C for 12 hr to ensure a moisture-free growth atmosphere and the desorption of the surfactant molecules from the nanoparticle catalysts.

The Ge and Sn sources used were diphenylgermane (DPG) and tetraethyltin (TET) respectively. These precursors were dissolved in anhydrous toluene (10 ml) in an  $\text{N}_2$  filled glove box with typical Ge and Sn precursor volumes of 0.025 ml and 0.0045 ml respectively. A solution containing both Ge and Sn precursors was loaded into a Hamilton sample-lock syringe inside the nitrogen-filled glovebox.

A  $\text{Au}_{0.80}\text{Ag}_{0.20}$ -coated Si substrate was further annealed for 15 min at 440 °C under a flowing  $\text{H}_2/\text{Ar}$  atmosphere inside a tube furnace prior to the injection of precursors. The precursor solution was then injected into the metal reaction vessel using a syringe pump at a rate of 0.025  $\text{ml min}^{-1}$ . A  $\text{H}_2/\text{Ar}$  flow rate of 0.6 sccm was maintained during the entire growth period. Various growth times were employed to determine the growth rate, ranging from 15 – 120 min.

### 5.6.2. Characterisation

Bottom-up grown  $\text{Ge}_{1-x}\text{Sn}_x$  nanowires were imaged on a FEI Helios NanoLab 600i scanning electron microscope (SEM). All energy-dispersive X-ray (EDX) measurements were recorded in high-angle annular dark-field mode in the FEI Helios NanoLab 600i operating at 30 kV and 0.69 nA with an attached Oxford X-Max 80 detector. Error in the EDX measurements indicates a standard error of 0.5 at. %. EDX mapping was performed on a Titan Themis double-corrected and monochromated Transmission Electron Microscope at 300kV with a Bruker Super X detector. Software for imaging and EDS mapping is FEI Velox. Electrochemical measurements were performed using a BioLogic VSP Potentiostat/Galvanostat. The electrochemical properties of  $\text{Ge}_{1-x}\text{Sn}_x$  nanowire samples were investigated in a half cell configuration against a pure Li counter electrode in a two electrode, stainless steel split cell (a coin cell assembly that can be disassembled for post-mortem analysis). The electrolyte used consisted of a  $1 \text{ mol dm}^{-3}$  solution of lithium hexafluorophosphate salt in a 1:1 (v/v) mixture of ethylene carbonate in dimethyl carbonate with 3 wt% vinylene carbonate. The separator used was a glass fiber separator (EI-Cell ECC1-01-0012-A/L, 18 mm diameter, 0.65 mm thickness). The mass loading for anode samples was  $\sim 0.3 \text{ mg}$  and no additional conductive additives or binders were added. A Mettler Toledo XP2U ultra micro balance was used to determine the mass of  $\text{Ge}_{1-x}\text{Sn}_x$  nanowire material on the stainless steel substrates. Galvanostatic cycling was performed at 0.2 C in a potential window of 1.5 – 0.01 V (vs Li/Li<sup>+</sup>).

### 5.6.3. Figures

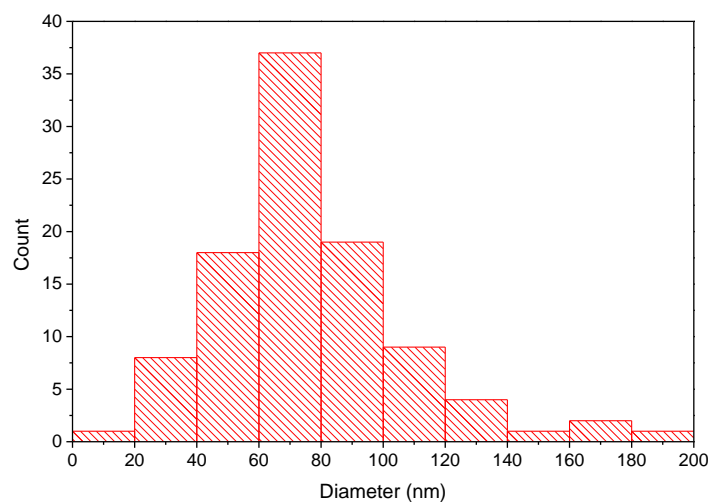


**Figure A5.1:** Diameter distribution of  $\text{Ge}_{1-x}\text{Sn}_x$  nanowires ( $x = 0.048$ ). The mean diameter of the  $\text{Ge}_{1-x}\text{Sn}_x$  nanowires was  $75 \pm 30$  nm.

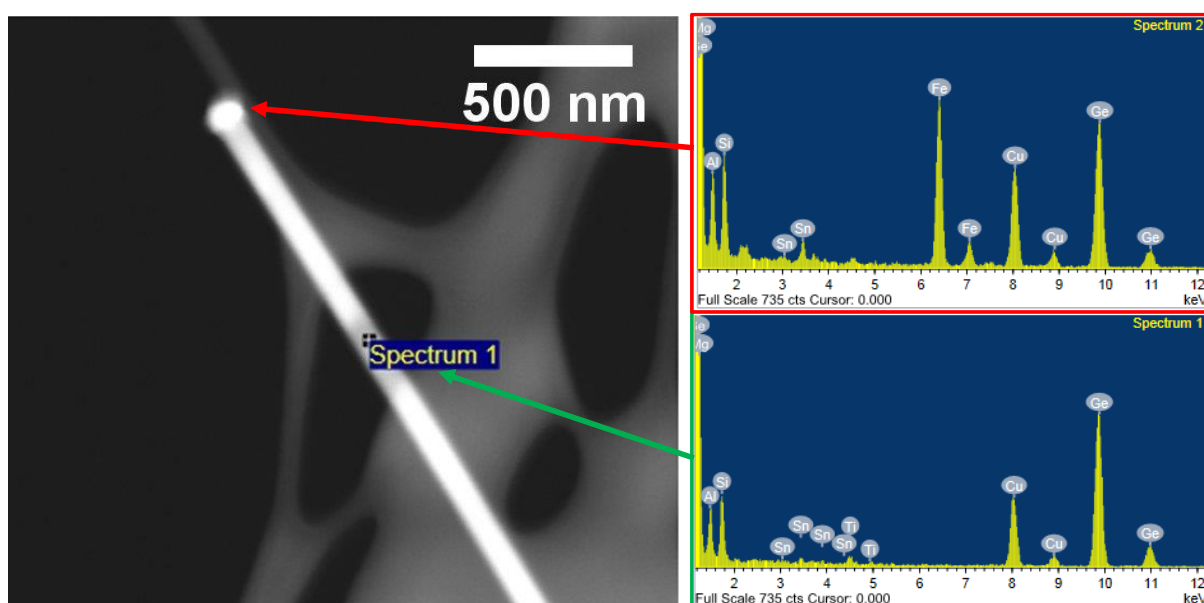


**Figure A5.2:** EDX analysis of an Fe-seeded  $\text{Ge}_{1-x}\text{Sn}_x$  nanowire. EDX analysis of the tip (red box) and the nanowire body (green box) displaying an Fe-rich seed and Sn incorporation of 1.31 at. % respectively.

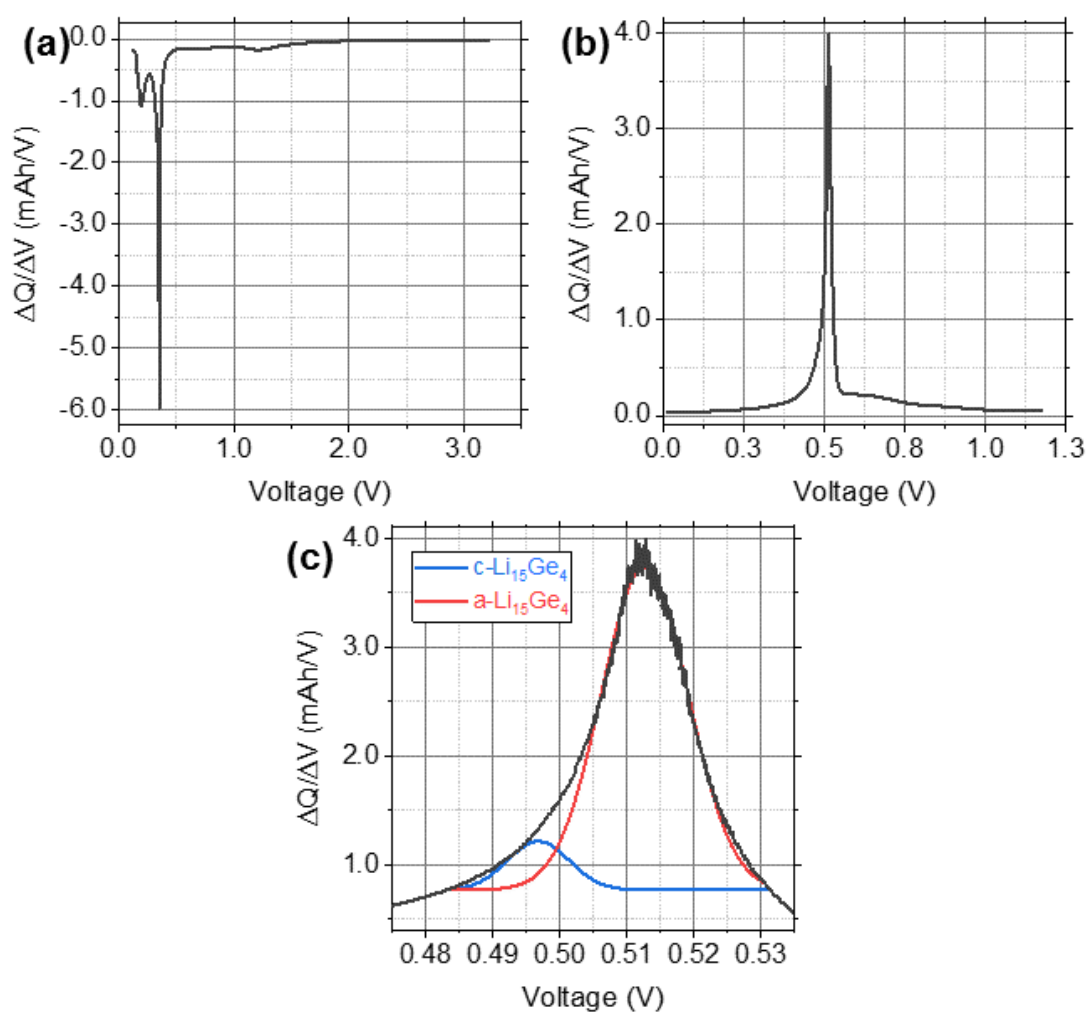


**Figure A5.3:** Differential charge curve from (a) the 1<sup>st</sup> charge and (b) the 1<sup>st</sup> discharge of a  $\text{Ge}_{1-x}\text{Sn}_x$  nanowire sample cycled at C/5 in a potential window of 1.5 – 0.01 V (vs  $\text{Li}/\text{Li}^+$ ). (c) Deconvolution of the oxidation peak observed during the first discharge which demonstrates the dealloying of the  $c\text{-Li}_{15}\text{Ge}_4$  and  $a\text{-Li}_{15}\text{Ge}_4$  phases.

#### 5.6.4. References

1. Biswas, S. *et al.* Non-equilibrium induction of tin in germanium: Towards direct bandgap Ge  $1-x$ Sn nanowires. *Nat. Commun.* **7**, 11405 (2016).
2. Biswas, S., O'Regan, C., Morris, M. a. & Holmes, J. D. In-situ Observations of Nanoscale Effects in Germanium Nanowire Growth with Ternary Eutectic Alloys. *Small* **11**, 103–111 (2015).
3. Biswas, S., O'Regan, C., Petkov, N., Morris, M. a. & Holmes, J. D. Manipulating the growth kinetics of vapor-liquid-solid propagated ge nanowires. *Nano Lett.* **13**, 4044–4052 (2013).
4. He, S. T., Xie, S. S., Yao, J. N., Gao, H. J. & Pang, S. J. Self-assembled two-dimensional superlattice of Au-Ag alloy nanocrystals. *Appl. Phys. Lett.* **81**, 150–152 (2002).

# **Chapter 6**

## **One-Step Fabrication of GeSn Branched Nanowires**

This chapter is intended for submission in early 2019. Consequently, sections of the chapter such as the abstract and introduction may contain repeating concepts and paragraphs. I co-wrote this paper with SB and JDH, and performed the nanowire synthesis. I carried out the elemental analysis with COR and analysed the structural (CD) and Raman (SR and AS) data, while DMcN carried out the electrochemical tests.

Doherty, J.; Biswas, S.; McNulty, D.; O'Regan, C.; Downing, C.; Raha, S.; Singha, A.; O'Dwyer, C.; Holmes, J. D One-Step Fabrication of GeSn Branched Nanowires (in preparation).

## 6. One-Step Fabrication of GeSn Branched Nanowires

---

### 6.1. Abstract

We report for the first time the self-catalysed, single step growth of branched GeSn nanowires by a catalytic vapour-liquid-solid (VLS) mechanism. These typical GeSn nanostructures consist of  $\langle 111 \rangle$  oriented Sn rich ( $\sim 8$  at. %) GeSn “branches” grown epitaxially on GeSn “trunks”, with a Sn content  $\sim 4$  at. %. The trunks are seeded from  $\text{Au}_{0.80}\text{Ag}_{0.20}$  nanoparticles followed by the catalytic growth of secondary branches (diameter  $\sim 50$  nm) from the excess of Sn on the sidewalls of the trunks, as determined by high resolution electron microscopy and energy dispersive X-ray (EDX) analysis. The nanowires, with  $\langle 111 \rangle$  directed GeSn branches oriented at  $\sim 70^\circ$  to the trunks, have no apparent defects or change in crystal structure at the trunk-branch interface; structural quality is retained at the interface with epitaxial crystallographic relation. Electrochemical performance of these highly ordered GeSn nanostructures were explored as a potential anode material for Li-ion batteries, due to their high surface to volume ratio and increased charge carrier pathways. The unique structure of branched nanowires led to high specific capacities comparable to, or greater than, conventional Ge nanowire anode materials and  $\text{Ge}_{1-x}\text{Sn}_x$  nanocrystals with the same Sn inclusion ( $x = 0.05$ ).



## 6.2. Introduction

The high surface-to-volume ratios of branched nanowires makes them ideal candidates for a number of applications, such as photovoltaics,<sup>1–3</sup> water splitting<sup>4,5</sup> and as electrode materials in batteries.<sup>6–8</sup> The radial growth of nanowire “branches” from the primary nanowire “trunk” represents a route to form higher faceted structures, with capabilities beyond the remit of one dimensional nanowires.<sup>9,10</sup> The formation of branched nanowires traditionally involves the preliminary growth of the main trunk nanowire, with the growth of the branches taking place in a secondary growth reaction, *e.g.* sputtering with a growth catalyst on the main trunk and subsequent growth of the secondary branches.<sup>6,11–13</sup> A single step<sup>1,3,14</sup> growth protocol for any homo- or heterostructure formation has the advantage of simplicity, cost-effectiveness, phase purity and improved crystal quality over the heterostructure grown in a multi-step process.

Branched nanostructures can be engineered from the same material (homostructures) or from different materials forming the trunk and branch segments (heterostructures).<sup>1,8,15</sup> These nanostructures can be highly ordered and the branches can be preferentially controlled<sup>16,17</sup> and could behave as a three-dimensional nanowire network.<sup>18</sup> Conventionally, branched nanowires, both heterostructured and homostructured, have been fabricated by two-step approaches. Typically, the trunks are grown first, followed by the generation of branches on the surface of the trunks using a secondary catalyst.<sup>8,10,11</sup> There have also been reports of branched nanowires grown in a single step through a “self-catalytic” process, either by segregation of a growth material towards the nanowire sidewall,<sup>3,14</sup> or by deposition of the initial catalyst onto the sidewalls.<sup>2</sup>

In recent years, there has been a surge in interest surrounding GeSn alloy nanosystems.<sup>19–22</sup>

Much of this interest has been due to reports, both theoretical and experimental, that a direct

bandgap can be achieved in Ge by alloying the semiconductor with Sn,<sup>23,24</sup> lowering the separation between the indirect (L) and direct ( $\Gamma$ ) valleys (140 meV in bulk Ge) in the conduction band of Ge.<sup>25</sup> While there have been numerous reports on the fabrication and characterisation of GeSn thin films,<sup>26–30</sup> researchers are still in the early stages of exploring GeSn nanostructures. The generation of  $\text{Ge}_{1-x}\text{Sn}_x$  ( $x \approx 0.06-0.20$ ) nanowires have previously been reported *via* both top-down fabrication<sup>31,32</sup> and bottom-up growth,<sup>33–35</sup> and GeSn nanocrystals have been reported with up to 40 at. % Sn incorporation.<sup>36–39</sup> Considering group IV branched nanostructures, there have been demonstrations of branched nanowires comprising of Si<sup>40</sup> and Si/Ge,<sup>8</sup> however, to the best of our knowledge, there are no reports of GeSn alloy branched nanowires. Particularly, branched GeSn nanostructures could have potential in many different optoelectronic and nanoelectronic applications, due to their unique material characteristics and novel morphology. GeSn branched nanostructures, with direct and narrow band gaps and high surface areas, have potential application as efficient light absorption and as high mobility materials in 3D nanowire networks. GeSn alloy branched nanostructures could potentially act as both type-I and type-II semiconductor heterojunctions,<sup>9</sup> where the bandgap of the branch and trunk segments could be controlled *via* the variation in Sn incorporation.

Branched GeSn alloy nanowires are also good candidates for energy storage applications due to the integration of different functional materials, greatly enhanced numbers of junctions, large surface areas and high carrier mobility.<sup>7,41</sup> For energy storage, Sn-catalysed Ge nanowires have been previously reported to demonstrate high capacities when used as an anode material for Li ion batteries,<sup>12</sup> and GeSn nanocrystals with 5 at. % Sn have shown improvement in capacitance and retention over Ge nanocrystals.<sup>36</sup> This, combined with the high surface area, increased charge carrier pathways and strong mechanical strength,<sup>41,42</sup> suggest that GeSn branched nanowires may exhibit high capacities when used as an anode material in Li ion batteries.<sup>6,8,11</sup>

This article reports for the first time the vapour-liquid-solid (VLS) growth of branched GeSn nanowires using  $\text{Au}_{0.80}\text{Ag}_{0.20}$  alloy nanoparticles as catalytic seeds. We exploited the conventional VLS growth paradigm to access the growth of branched GeSn heterostructures with epitaxially perfect interfaces. The 3D nanostructures exhibit heterogeneity in terms of Sn content variation between the trunks and the branches. The quality of the interface in the branched structures in terms of Sn distribution, crystal defects, epitaxy, *etc.* was analysed using high resolution scanning transmission electron microscopy (HRSTEM) and energy dispersive x-ray (EDX). A growth mechanism for the nanostructures is proposed taking account of growth constraints such as catalysts, precursors *etc.* The potential application of the branched GeSn nanowires as anode materials for Li ion batteries is also discussed.

### 6.3. Results and Discussion

For the growth of GeSn alloy branched nanostructures, a conventional, single step VLS growth mechanism was employed where a particular combination of catalyst, Sn precursor type and concentration resulted in the nucleation and epitaxial growth of small GeSn nanowires from the sidewalls of large GeSn nanowire trunks (see 6.6. Appendix for detailed experimental methods). Using previously reported<sup>43</sup> Ge and Sn precursor sources (diphenyl germane (DPG) and tetraethyl tin (TET) as Ge and Sn source respectively) and  $\text{Au}_{0.80}\text{Ag}_{0.20}$  nanoparticles as the catalyst, an extensive amount of branched GeSn alloy nanowires were produced, as shown in the scanning electron microscopy (SEM) image in Figure 6.1(a). Calculating an accurate yield of the branched structure was difficult, due to the depth of the deposited film and difference in the dimension of the branched and unbranched nanowires. The branches in the GeSn nanowires produced were highly uniform, in terms of diameter ( $57 \pm 14$  nm), and highly

ordered along the length of the nanowire trunks (Figure 6.1(b)). The mean diameter of trunks were found to be  $248 \pm 85$  nm. SEM analysis of the GeSn branches suggested that in some instances there was no apparent growth seed visible at the tip of the branches (Figure 6.1(b)), whereas in other nanostructures, metal seeds were visible at the tips (Figure 6.1(c), red arrows to indicate presence of seeds, TEM image is shown in inset for further clarification). Also visible in Figure 6.1(c) are small spherical seeds on a large nanowire trunk, and the growth of short branch nanowires on another trunk. Spherical metal tips are also clearly visible in many of the nanowire trunks shown in Figure 6.1(d). Figure 6.1(d) also depicts the increasing length of the branches along the length of the primary trunk, *i.e.* the branches closest to a nanowire seed are shorter in length than those further away from a seed (yellow lines are used as a guide for the eyes). The lengths of the nanowire branches along a single trunk ranged from a few tens of nanometres to almost a micron. Although there is no conclusive trend on the density of the branching on the size of the branched nanostructure, a comparatively higher density of branching with thicker trunk segment seems to be the common feature of these branched nanostructures (6.6. Appendix, Figure A6.1). Accurate estimation of the density of branching of the nanostructures is limited with the 2-D representation of the SEM image.

EDX point analysis of multiple branched nanowires revealed the mean Sn content in the trunks ( $4.4 \pm 0.7$  at. % Sn) to be significantly less than in the branches of the same nanostructure ( $8.0 \pm 1.2$  at. % Sn) (6.6. Appendix, Figure A6.2). An elemental map and the associated spectra for a nanowire trunk body at the seed/nanowire interface can be seen in Figure 6.2(a) (Au denoted

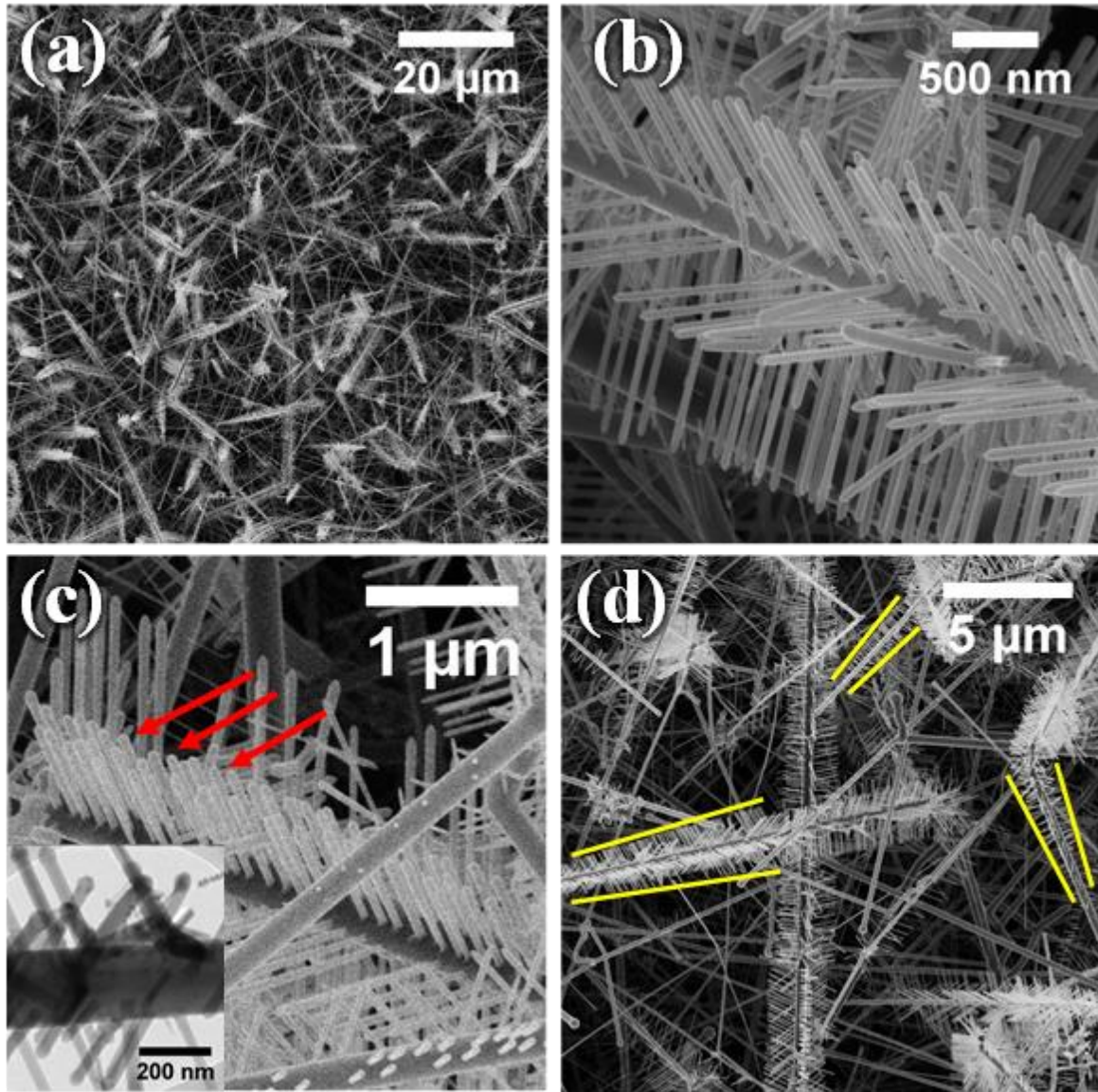


**Figure 6.1:** SEM images showing (a) the high yield of branched nanowires formed on an Si growth substrate. The branched nanowire shown in image (b) is typical of the those grown in this study, with highly oriented branches along the main trunk. The presence of spherical seeds on the branches, circled in red in (c), was not observed in all cases (*i.e.* no apparent seed in (b)). The yellow lines shown in image (d) indicate the increasing length of the branches along the length of the trunk (from tip to end).

by red, Sn by green and Ge by purple). The Au component in the metallic tip can be identified in the nanowire seed by presence of a bright red spot at the tip of the seed. The sharp interface typical of  $\text{Ge}_{1-x}\text{Sn}_x$  nanowires grown using our method is observable, with no obvious signs of

Sn segregation at the growth interface.<sup>43,44</sup> The Sn-rich nature of the catalytic seed post-growth has previously been reported for GeSn nanowire growth.<sup>43,44</sup> The accompanying spectra from the trunk nanowire body and seed confirms the lack of Au or Ag diffusion into the branched nanostructure, and the presence of Au and Ag in the catalyst seed. EDX elemental linescans of the GeSn branched nanostructures were used to investigate the elemental composition and

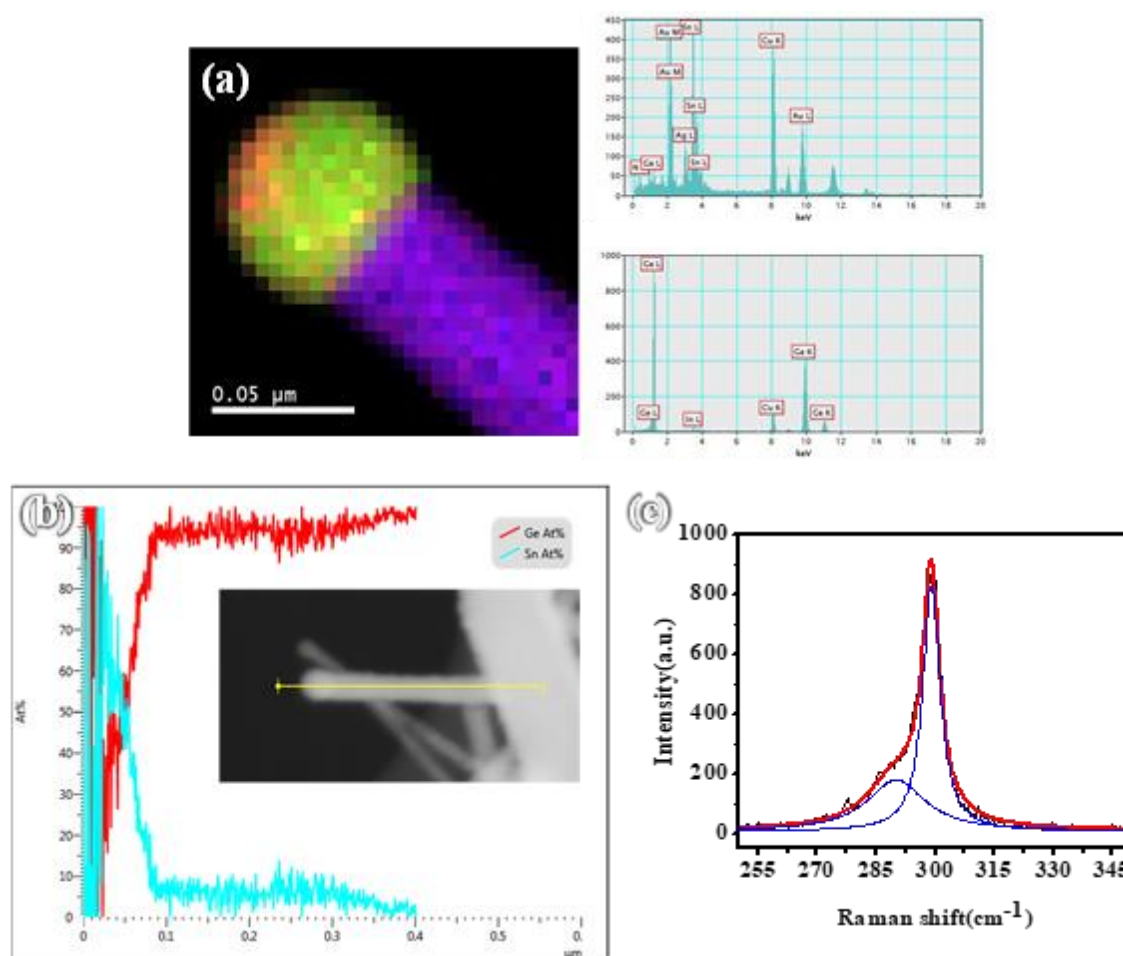


**Figure 6.2:** Elemental Analysis of the branched nanostructures. An elemental map (a) details the presence of Sn (green) and Au (red) in the tip of a nanowire trunk, with the trunk nanowire body mainly comprised of Ge (purple). EDX spectra from this nanowire trunk for both the seed and the body are also provided, displaying the presence of Au and Ag metal in the nanowire tip only. An elemental linescan at the junction between trunk and branch is provided (b) (Ge denoted in red, Sn in blue). Room temperature Raman spectrum for a branched nanostructure recorded with an excitation wavelength of 488 nm is shown in (c). Raman spectrum displays two distinct peaks, relating to the varying Sn content between nanowire trunk (4.4 at. % Sn) and branch (8.0 at. % Sn).

fluctuation at key junctions, *i.e.* from nanowire trunks into branched nanowires (Figure 6.2(b) – Sn denoted in blue, Ge in red). Due to the large discrepancy in the Sn content observed in the branches and trunks *via* point analysis, it is imperative to discover whether this increase in Sn was a gradual or abrupt transition. The linescan indicates a sharp shift in the Sn content on going from a trunk into a nanowire branch. In order to determine the contribution of the different catalyst seeds ( $\text{Au}_{0.80}\text{Ag}_{0.20}$  and Sn) in the growth of the trunk and branch elements of these nanowires, EDX analysis of the seeds were carried out on both trunk and branch components (6.6. Appendix, Figure A6.3). While the spectrum from a trunk nanowire seed clearly demonstrates the presence of the Au and Ag in the catalyst tip, the EDX spectrum from a branch nanowire seed contains no apparent Au or Ag signal, but is comprised solely of Ge and Sn.

Incorporation of Sn in the trunk and the branch segments of the GeSn nanostructures is further confirmed by Raman spectroscopy on individual nanostructures. Measurements were undertaken on three different branched nanostructures ((Figure 6.2(c)) and Figure A6.4 in 6.6. Appendix) where the nanostructures were transferred to a carbon coated Cu grid. A single Ge-Ge Raman peak from GeSn thin film alloys has been previously observed to progressively shift to a lower energy with increasing Sn concentration.<sup>44</sup> However, unlike conventional GeSn nanowires, Raman spectra from the GeSn branched nanostructures (Figure 2(c)) shows two distinct peaks (blue line denotes Lorentzian fitting) at higher (centred at  $298.7\text{ cm}^{-1}$  by averaging position of three different spectra) and lower (centred at  $289.2\text{ cm}^{-1}$  by averaging position of three different spectra) wavenumbers. These two peaks can be related to the variation in Sn content between the trunk and the branch components of the nanostructure. The relatively more intense Ge-Ge LO peak at lower frequency shows a red shift of approximately  $4.3\text{ cm}^{-1}$ , assuming a standard bulk Ge peak centred at  $303\text{ cm}^{-1}$  peak.<sup>43</sup> This Ge-Ge LO vibration can be assigned to the trunk

segment of the nanostructure, with a large volume and with low Sn content (4.4 at. % Sn), as the peak position matches well with previously reported GeSn alloys with similar Sn incorporation.<sup>45,46</sup> The second Ge-Ge LO peak at much lower frequency, approximately 13.8 cm<sup>-1</sup> red shifted from the bulk Ge-Ge vibration, can be attributed to the GeSn branches with a high Sn composition (8.0 at. % Sn). A Raman mode arising from a Ge-Sn bond, usually appearing around 260 cm<sup>-1</sup>, was not observed in the spectrum from the GeSn branched nanostructures. The red shift of Ge-Ge LO mode was larger than that observed previously in conventional GeSn nanowires with a similar Sn content.<sup>43,44</sup> However, apart from the Sn alloying effect, the shift of the Ge-Ge frequency in the Raman spectra can also occur from the strain effects and alloy disorder<sup>43,44</sup>, which may have had an effect on the observed Raman shift.

The structural quality of the GeSn nanowires was determined by high angle annular dark field (HAADF) STEM imaging (Figure 6.3). Representative HAADF STEM images of a branch-trunk interface and a nanowire branch containing a metal seed at the tip are shown in Figures 6.3(a) and (b) respectively. The interface between the nanowire trunk and branch is also depicted in the high resolution STEM image in Figure 6.3(c). The branches clearly stem from the main nanowire trunk, with no twin boundaries or other crystal defects, such as stacking faults, apparent at the interface. For the particular branch segment shown in Figure 6.3(a) the angle between the trunk and the branch was 71.6 °, in agreement with the minimum angle between two <111> directions in a cubic crystal arrangement and also previously observed for <111> nanowires grown from a (111) surface (70.53°),<sup>47</sup> as well as between nanofacets in twin boundaries in <111> Ge nanowires.<sup>48</sup> A similar crystallographic orientation between branch and trunk nanowire components is apparent in Figure 6.3(c), where an extension of {111}



stacking in the trunk segment is observed in the branch component, where the branches grow along  $\{111\}$  equivalent directions. The apparent continuity in the lattice from the trunk to the branch segments further confirms epitaxial orientation of the branch segments from the trunks.

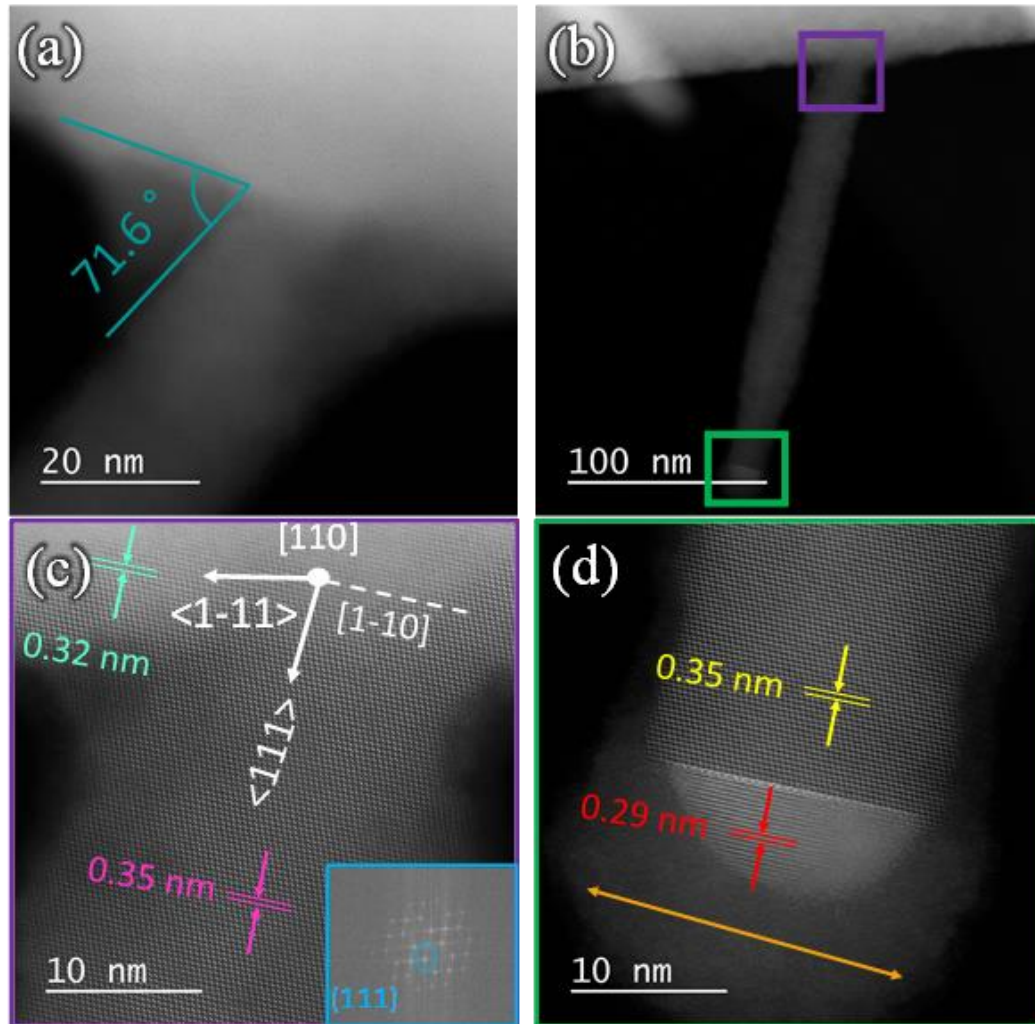


**Figure 6.3:** HRSTEM analysis of the branched nanowires. A branch protruding from a larger trunk can be seen in images (a) and (b). The angle between the  $\langle 111 \rangle$  oriented trunk and branch as measured is  $71.6^\circ$ . A high resolution image of the area near the branch-trunk interface (indicated by the purple box in (b)) can be seen in part (c), displaying the retention of the crystal growth direction between the trunk and the branch. The nanowires are  $\langle 111 \rangle$  oriented, as determined by FFT analysis (inset, blue box). The tip of this branch (green box) can be seen clearly in high resolution in image (d). There is a sharp interface between the small, hemispherical seed and the body of the nanowire.

The two-dimensional projection of the nanostructure during STEM imaging and the presence of a thin oxide layer, make the accurate determination of the angle between branch and trunk segments difficult. Fast Fourier Transform (FFT) analysis of a nanowire (Figure 6.3(c) inset) revealed the interplanar spacing ( $d$ ) close to the interface to be 0.32 nm, which is in agreement with the  $d$  value for bulk diamond Ge crystal of 0.326 nm (JCPDS 04–0545). The interplanar spacing for both a nanowire trunk (0.32 nm) and a nanowire branch (0.35 nm) revealed discrepancies resulting from differences (approx. 4 at. %) in the Sn contents in the different segments. The branch nanowires predominantly displayed a  $\langle 111 \rangle$  growth direction, the most common growth orientation for Ge nanowires with the mean diameter above 50 nm.<sup>44,49</sup> Generally the crystal structure of the  $\text{Ge}_{1-x}\text{Sn}_x$  alloy branched nanowires, with various Sn incorporations, exhibited a 3C lattice arrangement without any stacking faults and twin boundaries. This non-appearance of any crystal imperfections could be due to the minimal lattice mismatch between the branch and trunk segments and the accommodation of strain through sidewall facets due to the high surface-to-volume ratio of the thin GeSn branch components.

The small hemispherical seed of the branched nanowire, highlighted in the green box of Figure 6.3(b), is shown at higher resolution in Figure 6.3(d). There is a clearly observed, well-defined interface between the metal seed and the nanowire body. Also apparent is an amorphous bulb surrounding the small seed (indicated by the orange arrow, Figure 6.3(d)). This bulb has been previously observed in  $\text{Ge}_{1-x}\text{Sn}_x$  nanowire growth and is comprised of a GeSn oxide with high Sn content.<sup>43</sup> The relative size of this bulb compared to the crystalline seed which it encompasses makes precise EDX analysis of the branching seed difficult. However, measuring the lattice spacing of the hemispherical tip segment gives an interplanar spacing ( $d$ ) of 0.29

nm, which corresponds well with the {200} plane of metallic Sn (JCPDS cards #04–0673). This hemispherical seed at the tip of the branch elements was not apparent in all branched nanowires studied in this work (Figure 6.1(b), 6.6. Appendix, Figure A6.5(a)). In some cases, there was evidence of a small seed of reduced dimension, visible only due to the difference in the contrast between the branch nanowire body and the seed (6.6. Appendix, Figure A6.5(b)). Furthermore, a low resolution image (6.6. Appendix, Figure A6.6) of the branched nanowires displays metallic seeds at the tip of the shorter branches with longer branches along the length of the primary nanowire trunk having little to no observable metallic seeds. Metallic Sn seeds which are categorised as low-surface energy, type-B metallic seeds in VLS growth, can demonstrate prominent wetting at the liquid-solid interface.<sup>3,14</sup> This wetting leads to gradual reduction in the seed volume and disappearance from the nanowire tip during VLS growth. Similar observations on the appearance of metal seeds have previously been observed for single step branched nanowires,<sup>3</sup> grown from Pb seeds.

Precise control over the growth of branched nanowires, *e.g.* length, diameter, epitaxy, density, Sn content, *etc.*, is useful for future device (*e.g.* in photovoltaics) implementation. In order to engineer the extent of branching in the nanowires, and to determine the growth mechanism of these Sn-alloyed Ge nanostructures, time-dependent growth experiments were undertaken. Experiments were carried out under typical growth constraints with varying reaction times (15, 30, 45, 60, 80, 100 and 120 min). Information on the morphologies of the nanostructures through TEM imaging, EDX elemental mapping and schematics of typical nanowire growth scenario at 30, 80 and 120 min are provided in Figure 6.4. A build-up of Sn nanoparticles on the sidewalls of the nanowire trunk is apparent after 30 min of growth time, as determined from TEM analysis (Figure 6.4(a) and (b)) and EDX elemental mapping (Figure 6.4(c)). In Figure

6.4(a), nanoparticle-like clusters can be seen segregating/migrating from the nanowire seed toward the seed/nanowire interface and the nanowire sidewall (indicated by blue circles). This Sn diffusion from the seed triggers the secondary growth of branch nanowires. In Figure 6.4(b), a dark contrasted nanoparticle can be clearly seen (indicated by blue circle) on the sidewall of a primary nanowire trunk. The formation of large Sn rich cluster on the sidewall of the trunk nanowire (Figure 6.4(c) – with Sn denoted by red and Ge by green) is also apparent. Due to the limited growth time, the nanowire yield across the substrate after a 30 min reaction time was quite low (6.6. Appendix, Figure A6.7(a)). The growth of branched nanowire segments was initiated after a reaction time of approximately 80 min (Figure 6.4(d) and 6.6. Appendix, Figure A6.7(b)). TEM analysis confirmed the growth of short (< 100 nm) branched nanowires after 80 min growth, with the presence of a growth seed at the tip of the branches. Some nanowire trunks also showed the formation of a layer at the surface of the nanowire trunks after 80 min growth (Figure A6.8 in 6.6. Appendix). The lattice spacing of the crystalline edge of this shell (2.88 Å) is consistent with metallic Sn. This Sn rich surface of the nanowire trunk after 80 min growth indicates Sn wetting on the sidewall of the main trunk segment, either from the large metallic seed or through direct deposition of Sn from the precursor vapour phase. These Sn nanoparticles further act as the seeding location for the secondary growth of GeSn nanowire branches on primary trunk segments. Representative SEM images of GeSn nanostructures after 30 and 80 min growth times are provided in 6.6. Appendix, Figure A6.7. The schematic shown in Figure 6.4(e) represents a branched nanowire at 30, 80 and 120 min growth times (representative SEM image for 120 min growth is in Figure 6.1(a)). The branched nanowire lengths in the schematic have been emphasised for illustrative purposes. The schematic is presented as a visible representation for better understanding of branched nanowire growth only and is not a scientifically accurate drawing in terms of nanowire facets, shape of the metallic particles and interface geometry.

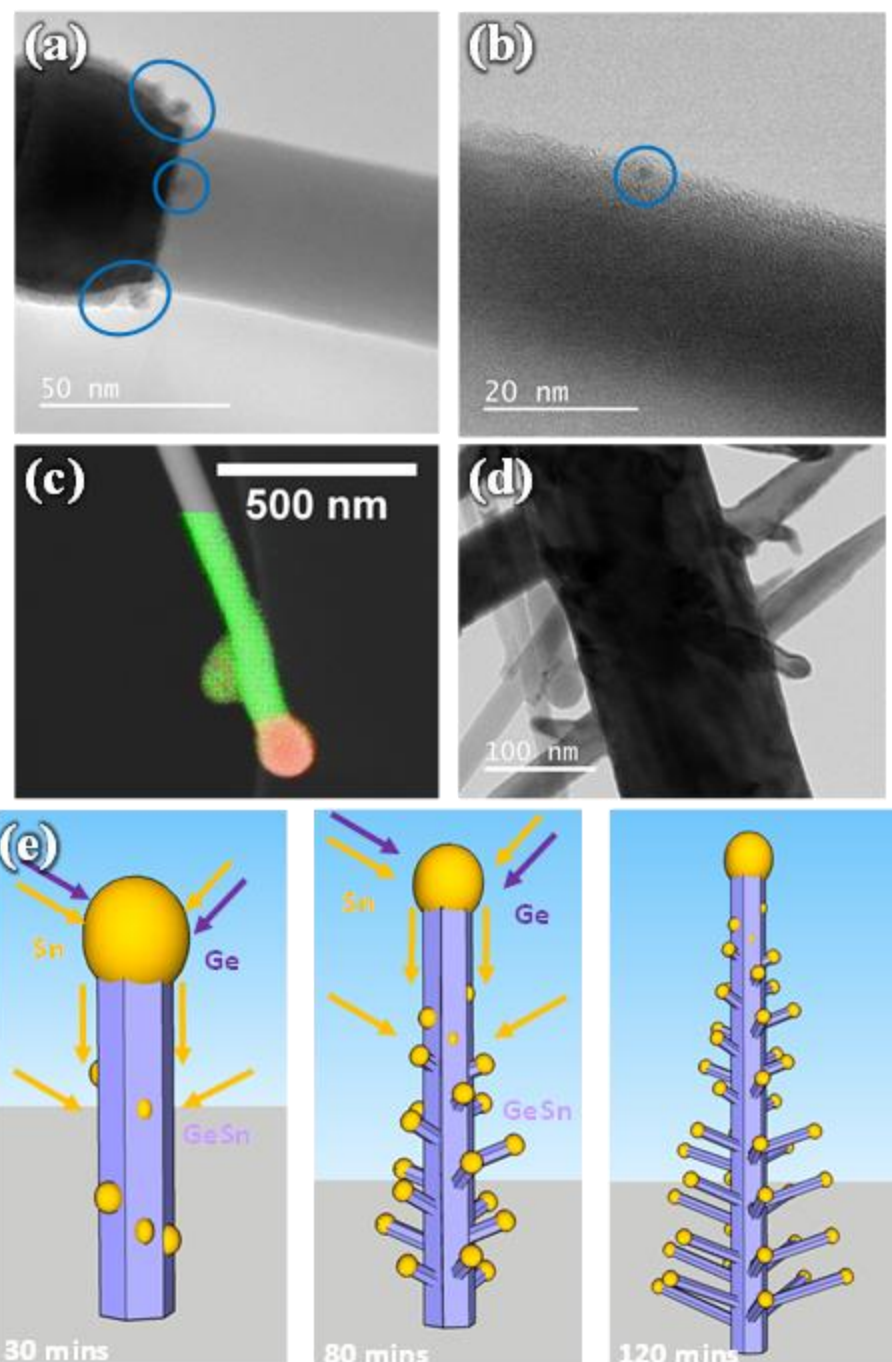


**Figure 6.4:** TEM and an EDX elemental map for the 30 min nanowire growth times are shown in images (a), (b) and (c) respectively. The TEM analysis reveals Sn particles and Sn segregation (marked with blue circles) on the surfaces of the trunk nanowires nanowires, as confirmed by EDX mapping. (d) shows a representative TEM image for 80 min nanowire growth time. Schematics of the nanowires at different growth times of 30, 80 and 120 mins are shown in (e).

As no intentional catalyst was added to break the isotropic GeSn crystal growth to fabricate branched nanostructures, an understanding of the mechanism responsible for this growth is imperative for the controlled fabrication of branched nanowires. There are three possible sources for the origin of the Sn rich outer layer (Figure 6.4 and Figure A6.8 in 6.6. Appendix) which acts as the seed for secondary growth of nanowire branches on the sidewalls of the GeSn trunks. The excess Sn on the nanowire sidewalls could originate from: (i) Sn segregation from the bulk of a nanowire trunk, (ii) Sn deposition and droplet formation on the sidewalls of nanowire trunks from the external continuous flux of Sn during growth and (iii) the wetting and migration of the Sn from the metallic tip of the nanowire trunk to the nanowire sidewalls. Among these mechanisms, Sn segregation from the nanowire bulk is not justified as uniform Sn distribution is observed in the nanowire body (Figure 6.2(c)), suggesting no migration of Sn from the nanowire bulk to the surface. Also stable  $\text{Ge}_{1-x}\text{Sn}_x$  alloy nanowires with higher Sn concentration ( $x = 0.09$ ) have been reported<sup>43</sup> using a similar growth technique without any apparent segregation of Sn to the nanowire sidewalls. As Sn segregation at the surface of a nanowire trunk from its bulk is unlikely at a Sn content of  $\approx 4$  at. %. Sn accumulation on the sidewalls of the GeSn nanowire trunks can occur *via* both the spontaneous deposition of Sn from Sn precursor and migration of smaller particles from the primary catalyst particle at the tip of the trunk. Although at the growth temperature employed (440 °C), the solubility of Sn in AuAg catalyst is limitless, but beyond a threshold volume of the catalyst, small Sn nanoparticle droplet can precipitate out from the liquid seed to wet the sidewalls of the nanowires (Figure 6.4 (a) and (b)). This is due to the formation of Sn-rich metastable catalyst particles (Figure 6.2(c)) with low surface energies at the growth temperature. In this study, the nanoparticle catalyst, Sn precursor and its concentration was found to have a real impact on the yield of branched nanostructures compared to the non-branched nanowires (See method in 6.6. Appendix). The  $\text{Au}_{0.80}\text{Ag}_{0.20}$  nanoparticle catalyst was found to be a crucial parameter in the

formation of the branched nanostructures (Figure 6.1(a) and Figure A6.9 in 6.6 Appendix). Ag-rich, AuAg seeds at a growth temperature of 440 °C require a larger Sn solubility to form the liquid Au, Ag and Sn alloy eutectic (according to the phase diagrams of Au-Sn<sup>50</sup> and Ag-Sn<sup>51</sup>). With high Sn solubility, it may be argued that the threshold volume (volume beyond which Sn precipitates from the seed) of the eutectic catalyst in the trunk nanowire is reached more readily for a Au<sub>0.80</sub>Ag<sub>0.20</sub> catalyst compared to pure Au, resulting in Sn nanoparticle droplet formation and the observation of a high yield of branched nanowires for Au<sub>0.80</sub>Ag<sub>0.20</sub> catalysts.

In another scenario, Sn can be directly adsorbed from the vapour phase, both at the spherical catalyst and at the faceted nanowire surface (a cross-sectional image of GeSn branched nanowire trunk can be seen in 6.6. Appendix, Figure A6.10). In VLS growth, adsorption of the growth species at the eutectic catalyst is typically influenced by the difference in the adatom concentration in the vapour and liquid phases. Thus, for a certain Sn precursor concentration in the vapour phase, the difference in the Sn adatom concentration between vapour and liquid phases is smaller for the Au<sub>0.80</sub>Ag<sub>0.20</sub> catalyst (due to larger Sn solubility) resulting in slow adsorption at the vapour-liquid interface. This slow adsorption rate may result in an excess Sn adatoms in the growth environment, which triggers Sn accumulation directly on the sidewalls of the nanowire trunks, or at the eutectic droplets. Accumulated Sn at the surface of the eutectic droplet (apart from the precipitated Sn from the catalyst) can also migrate to the nanowire sidewalls. This Sn at the nanowire sidewalls can act as growth catalyst, resulting in the continuous growth of the nanowire branches during the simultaneous growth of the nanowire trunks (Figure 1(d)). Though both mechanism (ii) and (iii) could be liable for the formation of branched nanowires, it can be argued that accumulation/precipitation and migration of Sn

droplets from the seed could be a more prominent mechanism. Observation of very regular and oriented branching and very little observation of uncontrolled hyper branches in fully grown branched structure (Figure 6.1) disprove the participation of uncontrolled and direct Sn deposition on the nanowire sidewalls from the vapour phase. These branched nanowires continue to grow until the Sn catalyst is consumed, leaving some branched nanowires with little to no evidence of a seed (Figure 6.1(b), 6.6. Appendix, Figure A6.5). A similar outcome has been observed for the growth of single step tin oxide nanowires, as reported by Schönherr et al.,<sup>14</sup> where small secondary seeds were also observed on the sidewalls of nanowire trunks where no external catalyst was provided.

A further increase in the Ag content in the in AuAg alloy seeds, *e.g.* Au<sub>0.70</sub>Ag<sub>0.30</sub>, resulted in very few branched nanostructures (6.6. Appendix, Figure A6.9). This may be due to the vastly altered growth kinetics with the increased Ag content of the catalytic seeds, ultimately leading to very little growth of Ge<sub>1-x</sub>Sn<sub>x</sub> nanowires.<sup>43</sup> The proposed growth mechanism for branched nanostructures is also supported by the, seemingly counter-intuitive, observation that an increase in the concentration of TET used as the Sn precursor (from 3 mmol/cc to 5 mmol/cc) resulted in a dramatic decrease in the yield of branched nanostructures.<sup>43</sup> The increased partial pressure of Sn with an increasing amount of the growth precursor would result in an increased Sn adsorption at the vapour-liquid interface during VLS growth, allowing for more Sn incorporation at the triple phase interface and in the nanowire *via* solute trapping,<sup>43</sup> rather than through accumulation on the surface of the nanowire or eutectic catalyst.



The integration of different functional materials, greatly enhanced junctions and high surface areas make branched nanostructures good candidates for energy storage devices.<sup>6,8,11</sup> Galvanostatic cycling at a rate of 0.2 C, over a voltage range of 1.50 to 0.01 V (vs Li/Li<sup>+</sup>) was performed in order to investigate the fundamental electrochemical performance of the branched GeSn nanowires, as shown in Figure 6.5. A selection of voltage profiles from the 1<sup>st</sup> to the 25<sup>th</sup> cycle are shown in Figure 6.5(a). The 1<sup>st</sup> charge curve consists of an initial sharp decrease from the open circuit voltage (OCV) of ~3.10 V down to ~0.33 V, which may be attributed to the formation of a solid-electrolyte interface (SEI) layer and the irreversible decomposition of the electrolyte on the surface of the electrode material,<sup>52</sup> followed by 3 long plateaus from ~0.33 to 0.25 V, 0.25 to 0.16 V and from 0.16 V to 0.01 V, corresponding to the progressive lithiation of the branched GeSn nanostructures.<sup>53</sup> A long plateau centred at ~0.5 V was observed in the first discharge curve, corresponding to the delithiation of the nanostructures.<sup>54</sup> The initial charge and discharge capacities were ~1298 and 1079 mAh/g, corresponding to an initial Coulombic efficiency (ICE) of 83 %. The exceptional capacity retention properties of the branched nanostructures are demonstrated in Figure 6.5(b). The charge capacities after the 2<sup>nd</sup> and 25<sup>th</sup> cycles were 1107 and 1040 mAh/g respectively, corresponding to an impressive capacity retention of 94 %.

Differential capacity plots (DCPs) were calculated for each charge and discharge curve in order to fully appreciate the electrochemical processes occurring during galvanostatic cycling. DCPs for the 1<sup>st</sup> charge and discharge are shown in Figure 6.5(c). The sharp peak in the DCP for the 1<sup>st</sup> charge at 0.31 V is due to the lithiation of crystalline Ge (c-Ge)<sup>55,56</sup> and is only observed during the first charge, indicating that the nanowires do not return to a fully delithiated crystalline Ge phase.<sup>55</sup> The other peaks at ~0.17 and 0.13 V are associated with the formation

of Li-Ge alloys in the form of a-Li<sub>15</sub>Ge<sub>4</sub> and c-Li<sub>15</sub>Ge<sub>4</sub>, respectively.<sup>57</sup> From the second charge onwards, reduction peaks were observed at  $\sim 0.52$ ,  $0.39$  and  $0.18$  V, corresponding to the progressive lithiation of the branched nanowires and the formation of a series of Li-Ge alloys (a-Li<sub>x</sub>Ge  $\rightarrow$  a-Li<sub>15</sub>Ge<sub>4</sub>  $\rightarrow$  c-Li<sub>15</sub>Ge<sub>4</sub>).<sup>58,59</sup> The consistency in the potential and intensity of these reduction peaks is illustrated in the contour plot showing the DCPs from the 2<sup>nd</sup> to the 25<sup>th</sup> charge in Figure 6.5(d). A sharp oxidation peak at  $\sim 0.51$  V was observed in the DCP for the first discharge, as shown in Figure 6.5(c), corresponding to the delithiation of the c-Li<sub>15</sub>Ge<sub>4</sub> phase.<sup>60</sup> The potential of this peak does not significantly vary with increased cycling as can be seen in the contour plot showing the DCPs from the 2<sup>nd</sup> to the 25<sup>th</sup> discharge (Figure 6.5(e)).

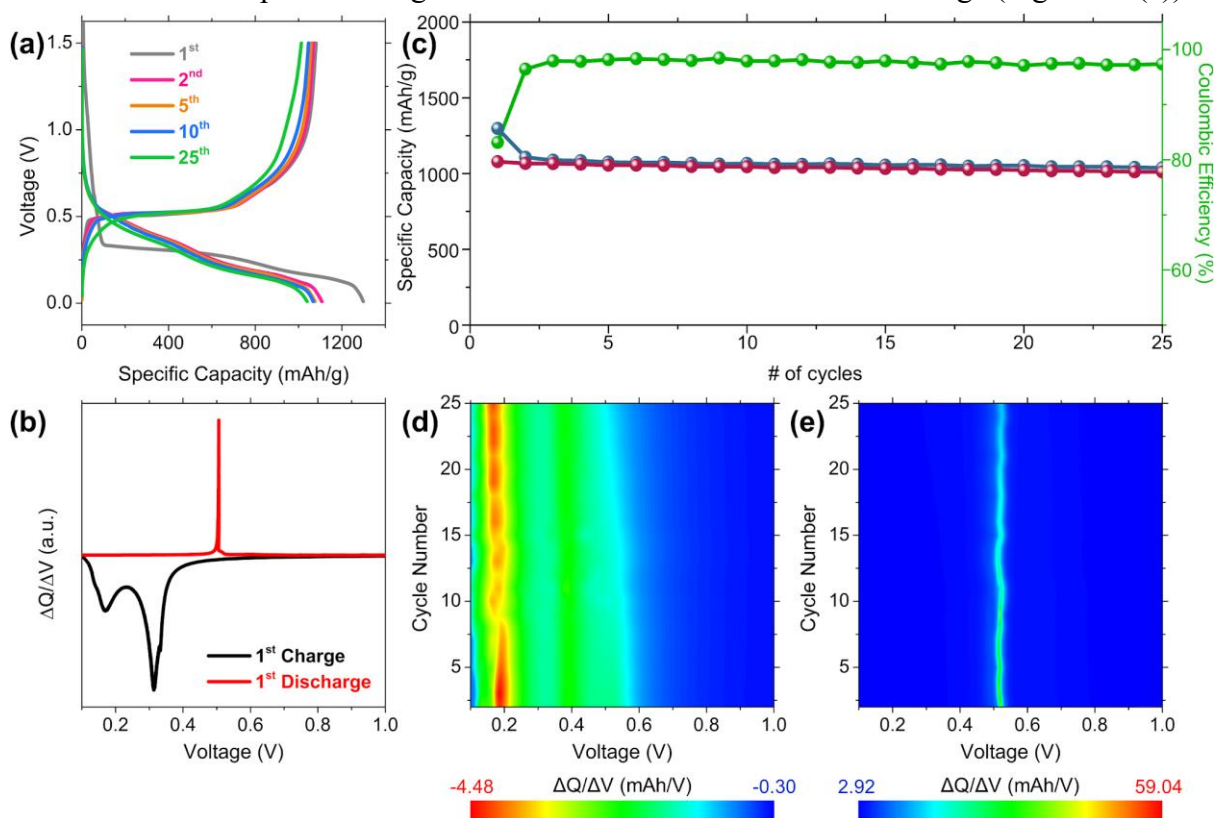


**Figure 6.5:** (a) Charge and discharge voltage profiles for the 1<sup>st</sup>, 2<sup>nd</sup>, 5<sup>th</sup>, 10<sup>th</sup> and 25<sup>th</sup> cycles for branched GeSn nanowires cycled at 0.2 C, in a potential window of 1.50 – 0.01 V (vs Li/Li+). (b) Charge and discharge capacity values and coulombic efficiencies obtained for branched GeSn nanowires IO over 25 cycles. Differential capacity contour plots calculated from (a) charge curves and (b) discharge curves for a branched GeSn nanowires cycled at 0.2 C, from the 2<sup>nd</sup> to the 25<sup>th</sup> cycle.

The specific capacity values achieved from the GeSn branched nanostructures are greater than<sup>61–67</sup> or comparable to<sup>68–71</sup> previously reported values for other Ge nanowire based anode materials. As there has been no report on the capacities of GeSn nanowires we are unable to make a comparison to GeSn nanowires, however these GeSn branched nanostructures show slight improvement over GeSn nanocrystals with similar Sn incorporation ( $x = 0.05$ ).<sup>36</sup> We propose that the remarkable specific capacities and the high ICE obtained with the GeSn branched nanostructures are due to the nanoscale branches which are protruding from large nanowire trunks. The nanoscale diameter ( $\sim 40$  nm) of the branches may allow for relatively short  $\text{Li}^+$  ion diffusion path lengths, compared to unbranched nanowires, which in turn may result in a high ICE and increased voltage stability, as shown in the DCPs. Additionally, GeSn based nanostructures offers cost-reduction in terms of anode materials production compared to pure Ge based material. The impressive electrochemical performance of the GeSn branched nanostructure in terms of voltage stability, capacity retention and high specific capacity values demonstrates that they are a very promising anode material for Li-ion batteries.

#### **6.4. Conclusion**

The fabrication of novel GeSn branched nanowires has been achieved through a single step VLS growth mechanism. This branching phenomenon of GeSn nanowires maintains epitaxy with the primary “trunk” crystal and retains its structural quality without any apparent crystal defects. A proposed growth mechanism has been described for the fabrication of these GeSn nanostructures, outlining the role of sidewall wetting by Sn in the self-catalysation of the nanowire branches. A particular set of catalyst, precursor and precursor concentration was required for sidewall wetting by Sn, as a result of deposition and precipitation from the vapour phase and liquid catalytic seeds at the tip of the nanowire trunks. The simple nature of the growth has the potential to lend itself to heightened control of branched nanowire structures if

more restrictions and parameters could be in place during growth, *e.g.* flux control. In-situ experiments may be required to conclude the specific source of sidewall Sn, which in turn could lead to precise engineering over the highly ordered 3D nanostructures. The branched GeSn nanowires, while chemically a homostructure, have the potential to act as electronic heterostructures due to the possibility of having different bandgaps resulting from the variation of Sn content in the different segments of the nanostructures. Furthermore, the GeSn branched nanowires exhibit suitability as an anode material in Li ion batteries, due to the short  $\text{Li}^+$  ion diffusion path lengths in the nanowire branches. Specific capacity for the branched nanowires were found to be either comparable to, or surpass, previously reported values for other Ge based anodes, demonstrating the capability of these materials for use in Li-ion batteries. We believe that further enhancement in Sn incorporation and a reduction in trunk dimension will improve the application of GeSn branched nanostructures in Li-ion batteries.

To push the limit of the Sn incorporation in  $\text{Ge}_x\text{Sn}_{1-x}$  nanowires, Chapter 7 presents the introduction of pressure as a variable in the growth process. The move from chemical vapour deposition toward supercritical fluid growth increases the precursor decomposition rate, potentially increasing the growth rate of the  $\text{Ge}_x\text{Sn}_{1-x}$  nanowires. As solute trapping has been previously theorised as the mechanism responsible for our above equilibrium Sn incorporation (Chapters 2 and 3), an increase in growth rate should correspond to an increase in Sn content.

## 6.5 References

1. Li, Z. *et al.* Single-crystalline self-branched anatase titania nanowires for dye-sensitized solar cells. *Electron. Mater. Lett.* **13**, 174–178 (2017).
2. Wu, H., Yang, Y., Oh, E., Lai, F. & Yu, D. Direct synthesis of high-density lead sulfide nanowires on metal thin films towards efficient infrared light conversion. *Nanotechnology* **23**, 265602 (2012).
3. Bierman, M. J., Lau, Y. K. A. & Jin, S. Hyperbranched PbS and PbSe nanowires and the effect of hydrogen gas on their synthesis. *Nano Lett.* **7**, 2907–2912 (2007).
4. Mor, G. K., Varghese, O. K., Paulose, M., Shankar, K. & Grimes, C. A. A review on highly ordered, vertically oriented TiO<sub>2</sub> nanotube arrays: Fabrication, material properties, and solar energy applications. *Sol. Energy Mater. Sol. Cells* **90**, 2011–2075 (2006).
5. Changdong Gu, Chun Cheng, Haiyou Huang, Tailun Wong, Ning Wang, and Tong-Yi Zhang. Growth and Photocatalytic Activity of Dendrite-like ZnO @ Ag & DESIGN 2009. *Cryst. Growth Des.* **9**, 3278–3285 (2009).
6. Flynn, G., Palaniappan, K., Sheehan, M., Kennedy, T. & Ryan, K. M. Solution synthesis of lead seeded germanium nanowires and branched nanowire networks and their application as Li-ion battery anodes. *Nanotechnology* **28**, (2017).
7. Cheng, C. & Fan, H. J. Branched nanowires: Synthesis and energy applications. *Nano Today* **7**, 327–343 (2012).
8. Kennedy, T. *et al.* Nanowire Heterostructures Comprising Germanium Stems and Silicon Branches as High-Capacity Li-Ion Anodes with Tunable Rate Capability. *ACS Nano* **9**, 7456–7465 (2015).

9. Jiang, X. *et al.* Rational growth of branched nanowire heterostructures with synthetically encoded properties and function. *Proc. Natl. Acad. Sci. U. S. A.* **108**, 12212–12216 (2011).
10. Dick, K. A. *et al.* Synthesis of branched ‘nanotrees’ by controlled seeding of multiple branching events. *Nat. Mater.* **3**, 380–384 (2004).
11. Lee, S. H., Jo, Y. R., Noh, Y., Kim, B. J. & Kim, W. B. Fabrication of hierarchically branched SnO<sub>2</sub> nanowires by two-step deposition method and their applications to electrocatalyst support and Li ion electrode. *J. Power Sources* **367**, 1–7 (2017).
12. Mullane, E., Kennedy, T., Geaney, H., Dickinson, C. & Ryan, K. M. Synthesis of tin catalyzed silicon and germanium nanowires in a solvent-vapor system and optimization of the seed/nanowire interface for dual lithium cycling. *Chem. Mater.* **25**, 1816–1822 (2013).
13. Geaney, H., Mullane, E. & Ryan, K. M. Solution phase synthesis of silicon and germanium nanowires. *J. Mater. Chem. C* **1**, 4996–5007 (2013).
14. Schönherr, P. & Hesjedal, T. One-Step SnO<sub>2</sub> Nanotree Growth. *Chem. - A Eur. J.* **22**, 13823–13825 (2016).
15. Hou, J. *et al.* One-step synthesis of CdTe branched nanowires and nanorod arrays. *Appl. Surf. Sci.* **257**, 7684–7688 (2011).
16. Beaudry, A. L. *et al.* Directed branch growth in aligned nanowire arrays. *Nano Lett.* **14**, 1797–1803 (2014).
17. Beaudry, A. L. *et al.* Flux engineering for indium tin oxide nanotree crystal alignment and height-dependent branch orientation. *Cryst. Growth Des.* **13**, 212–219 (2013).

18. Rauber, M. *et al.* Highly-ordered supportless three-dimensional nanowire networks with tunable complexity and interwire connectivity for device integration. *Nano Lett.* **11**, 2304–2310 (2011).
19. Soref, R. Mid-infrared photonics in silicon and germanium. *Nat. Photonics* **4**, 495–497 (2010).
20. Zaima, S. *et al.* Growth and applications of GeSn-related group-IV semiconductor materials. *2016 IEEE Photonics Soc. Summer Top. Meet. Ser. SUM 2016* **16**, 37–38 (2016).
21. Zheng, J. *et al.* Recent progress in GeSn growth and GeSn-based photonic devices. *J. Semicond.* **39**, 1–6 (2018).
22. Gupta, S. *et al.* New materials for post-Si computing: Ge and GeSn devices. *MRS Bull.* **39**, 678–686 (2014).
23. Sau, J. D. & Cohen, M. L. Possibility of increased mobility in Ge-Sn alloy system. *Phys. Rev. B - Condens. Matter Mater. Phys.* **75**, 1–7 (2007).
24. Jenkins, D. W. & Dow, J. D. Electronic properties of metastable  $\text{Ge}_x\text{Sn}_{1-x}$  alloys. *Phys. Rev. B* **36**, 7994–8000 (1987).
25. Richard D’Costa, V., Wang, W., Zhou, Q., Soon Tok, E. & Yeo, Y. C. Above-bandgap optical properties of biaxially strained GeSn alloys grown by molecular beam epitaxy. *Appl. Phys. Lett.* **104**, (2014).
26. Pezzoli, F., Giorgioni, A., Patchett, D. & Myronov, M. Temperature-Dependent Photoluminescence Characteristics of GeSn Epitaxial Layers. *ACS Photonics* **3**, 2004–2009 (2016).

27. Ghetmiri, S. A. *et al.* Direct-bandgap GeSn grown on silicon with 2230 nm photoluminescence. *Appl. Phys. Lett.* **105**, 6–11 (2014).
28. Mahmodi, H. *et al.* Low-temperature formation of GeSn nanocrystallite thin films by sputtering Ge on self- assembled Sn nanodots on SiO<sub>2</sub>/Si substrate. *Jpn. J. Appl. Phys* **56**, (2017).
29. Mosleh, A. *et al.* Material Characterization of Ge<sub>1-x</sub> Sn<sub>x</sub> Alloys Grown by a Commercial CVD System for Optoelectronic Device Applications. *J. Electron. Mater.* **43**, 938–946 (2014).
30. Bauer, M. R. *et al.* Tunable band structure in diamond-cubic tin-germanium alloys grown on silicon substrates. *Solid State Commun.* **127**, 355–359 (2003).
31. Ragan, R., Ahn, C. C. & Atwater, H. a. Nonlithographic epitaxial Sn<sub>x</sub>Ge<sub>1-x</sub> dense nanowire arrays grown on Ge(001). *Appl. Phys. Lett.* **82**, 3439–3441 (2003).
32. Gupta, S. *et al.* Highly selective dry etching of germanium over germanium-tin (Ge<sub>1-x</sub>Sn<sub>x</sub>): A novel route for Ge<sub>1-x</sub>Sn<sub>x</sub> nanostructure fabrication. *Nano Lett.* **13**, 3783–3790 (2013).
33. Seifner, M. S., Biegger, F., Lugstein, A., Bernardi, J. & Barth, S. Microwave-Assisted Ge<sub>1-x</sub>Sn<sub>x</sub> Nanowire Synthesis: Precursor Species and Growth Regimes. *Chem. Mater.* **27**, 6125–6130 (2015).
34. Seifner, M. S., Hernandez, S., Bernardi, J., Romano-Rodriguez, A. & Barth, S. Pushing the composition limit of anisotropic Ge<sub>1-x</sub>Sn<sub>x</sub> nanostructures and determination of their thermal stability. *Chem. Mater.* **29**, 9802–9813 (2017).
35. Haffner, T. *et al.* Growth of Ge<sub>1-x</sub> Sn<sub>x</sub> Nanowires by Chemical Vapor Deposition via



- Vapor-Liquid-Solid Mechanism Using  $\text{GeH}_4$  and  $\text{SnCl}_4$ . *Phys. Status Solidi* **215**, 1700743 (2017).
36. Cho, Y. J. *et al.* Germanium-tin alloy nanocrystals for high-performance lithium ion batteries. *Phys. Chem. Chem. Phys.* **15**, 11691–11695 (2013).
  37. Esteves, R. J. A., Ho, M. Q. & Arachchige, I. U. Nanocrystalline group IV alloy semiconductors: Synthesis and characterization of  $\text{Ge}_{1-x}\text{Sn}_x$  quantum dots for tunable bandgaps. *Chem. Mater.* **27**, 1559–1568 (2015).
  38. Ramasamy, K. *et al.*  $\text{Sn}_x\text{Ge}_{1-x}$  Alloy Nanocrystals: A First Step toward Solution-Processed Group IV Photovoltaics. *Chem. Mater.* **27**, 4640–4649 (2015).
  39. Tonkikh, A. A. *et al.* Cubic phase Sn-rich  $\text{GeSn}$  nanocrystals in a Ge matrix. *Cryst. Growth Des.* **14**, 1617–1622 (2014).
  40. Wang, D., Qian, F., Yang, C., Zhong, Z. & Lieber, C. M. Rational growth of branched and hyperbranched nanowire structures. *Nano Lett.* **4**, 871–874 (2004).
  41. Liu, X., Lin, Y., Zhou, S., Sheehan, S. & Wang, D. Complex nanostructures: Synthesis and energetic applications. *Energies* **3**, 285–300 (2010).
  42. Sorokin, P. B. *et al.* Theoretical study of atomic structure and elastic properties of branched silicon nanowires. *ACS Nano* **4**, 2784–2790 (2010).
  43. Doherty, J. *et al.* Influence of growth kinetics on Sn incorporation in direct band gap  $\text{Ge}_{1-x}\text{Sn}_x$  nanowires. *J. Mater. Chem. C* 8738–8750 (2018).
  44. Biswas, S. *et al.* Non-equilibrium induction of tin in germanium: Towards direct bandgap  $\text{Ge}_{1-x}\text{Sn}_x$  nanowires. *Nat. Commun.* **7**, 11405 (2016).

45. Lieten, R. R. *et al.* Structural and Optical Properties of Amorphous and Crystalline GeSn Layers on Si. *ECS J. Solid State Sci. Technol.* **3**, P403–P408 (2014).
46. Dou, W. *et al.* Crystalline GeSn growth by plasma enhanced chemical vapor deposition. **8**, 3220–3229 (2018).
47. Jagannathan, H. *et al.* Nature of germanium nanowire heteroepitaxy on silicon substrates. *J. Appl. Phys.* **100**, (2006).
48. Biswas, S. *et al.* Diameter-Controlled Germanium Nanowires with Lamellar Twinning and Polytypes. *Chem. Mater.* **27**, 3408–3416 (2015).
49. Biswas, S., O'Regan, C., Petkov, N., Morris, M. a. & Holmes, J. D. Manipulating the growth kinetics of vapor-liquid-solid propagated ge nanowires. *Nano Lett.* **13**, 4044–4052 (2013).
50. Li, J. F., Agyakwa, P. A. & Johnson, C. M. Suitable thicknesses of base metal and interlayer, and evolution of phases for Ag/Sn/Ag transient liquid-phase joints used for power die attachment. *J. Electron. Mater.* **43**, 983–995 (2014).
51. Baheti, V. A., Kashyap, S., Kumar, P., Chattopadhyay, K. & Paul, A. Solid–state diffusion–controlled growth of the phases in the Au–Sn system. *Philos. Mag.* **98**, 20–36 (2018).
52. Lv, D. *et al.* GeOx/reduced graphene oxide composite as an anode for li-ion batteries: Enhanced capacity via reversible utilization of Li<sub>2</sub>O along with improved rate performance. *Adv. Funct. Mater.* **24**, 1059–1066 (2014).
53. Liu, X. H. *et al.* Reversible nanopore formation in Ge nanowires during lithiation–delithiation cycling: An in situ transmission electron microscopy study. *Nano Lett.* **11**,

- 3991–3997 (2011).
54. Dileo, R. A. *et al.* Hybrid germanium nanoparticle-single-wall carbon nanotube free-standing anodes for lithium ion batteries. *J. Phys. Chem. C* **115**, 22609–22614 (2011).
  55. Mullane, E., Kennedy, T., Geaney, H. & Ryan, K. M. A rapid, solvent-free protocol for the synthesis of germanium nanowire lithium-ion anodes with a long cycle life and high rate capability. *ACS Appl. Mater. Interfaces* **6**, 18800–18807 (2014).
  56. McNulty, D., Geaney, H., Buckley, D. & O'Dwyer, C. High capacity binder-free nanocrystalline GeO<sub>2</sub> inverse opal anodes for Li-ion batteries with long cycle life and stable cell voltage. *Nano Energy* **43**, 11–21 (2018).
  57. Kennedy, T. *et al.* High-performance germanium nanowire-based lithium-ion battery anodes extending over 1000 cycles through in situ formation of a continuous porous network. *Nano Lett.* **14**, 716–723 (2014).
  58. Baggetto, L. & Notten, P. H. L. Lithium-Ion (De)Insertion Reaction of Germanium Thin-Film Electrodes: An Electrochemical and In Situ XRD Study. *J. Electrochem. Soc.* **156**, A169 (2009).
  59. Baggetto, L., Hensen, E. J. M. & Notten, P. H. L. In situ X-ray absorption spectroscopy of germanium evaporated thin film electrodes. *Electrochim. Acta* **55**, 7074–7079 (2010).
  60. Stokes, K. *et al.* Direct Synthesis of Alloyed Si<sub>1-x</sub>Ge<sub>x</sub> Nanowires for Performance-Tunable Lithium Ion Battery Anodes. *ACS Nano* **11**, 10088–10096 (2017).
  61. Qiang, T. *et al.* Ge@C core-shell nanostructures for improved anode rate performance in lithium-ion batteries. *RSC Adv.* **5**, 17070–17075 (2015).
  62. Guo, W., Mei, L., Feng, Q. & Ma, J. Facile synthesis of Ge/C nanocomposite as superior

- battery anode material. *Mater. Chem. Phys.* **168**, 6–9 (2015).
63. Choe, H. S. *et al.* Synthesis of Ge/C composites as anodes using glucose as a reductant and carbon source for lithium-ion batteries. *RSC Adv.* **6**, 72926–72932 (2016).
  64. Li, W. *et al.* Germanium nanoparticles encapsulated in flexible carbon nanofibers as self-supported electrodes for high performance lithium-ion batteries. *Nanoscale* **6**, 4532–4537 (2014).
  65. Chockla, A. M., Klavetter, K. C., Mullins, C. B. & Korgel, B. A. Solution-grown germanium nanowire anodes for lithium-ion batteries. *ACS Appl. Mater. Interfaces* **4**, 4658–4664 (2012).
  66. Xiao, X. *et al.* Nanostructured Germanium Anode Materials for Advanced Rechargeable Batteries. *Adv. Mater. Interfaces* **4**, (2017).
  67. Yang, L. C., Gao, Q. S., Li, L., Tang, Y. & Wu, Y. P. Mesoporous germanium as anode material of high capacity and good cycling prepared by a mechanochemical reaction. *Electrochem. commun.* **12**, 418–421 (2010).
  68. Kennedy, T., Brandon, M. & Ryan, K. M. Advances in the Application of Silicon and Germanium Nanowires for High-Performance Lithium-Ion Batteries. *Adv. Mater.* **28**, 27 5696–5704 (2016).
  69. Li, X. *et al.* Germanium anode with excellent lithium storage performance in a germanium/lithium-cobalt oxide lithium-ion battery. *ACS Nano* **9**, 1858–1867 (2015).
  70. Bogart, T. D., Chockla, A. M. & Korgel, B. A. High capacity lithium ion battery anodes of silicon and germanium. *Curr. Opin. Chem. Eng.* **2**, 286–293 (2013).
  71. McNulty, D., Lonergan, A., O’Hanlon, S. & O’Dwyer, C. 3D open-worked inverse opal

TiO<sub>2</sub> and GeO<sub>2</sub> materials for long life, high capacity Li-ion battery anodes. *Solid State Ionics* **314**, 195–203 (2018).

## 6.6. Appendix

The appendix section of this chapter contains supplementary information relating to Chapter 6 (*e.g.* Experimental method and characterisation, SEM, EDX, TEM, *etc.*).

### 6.6.1. Experimental

For the catalysation of GeSn branched nanowires in a three phase bottom-up VLS growth dodecanethiol-stabilised, phase pure,  $\text{Au}_{0.80}\text{Ag}_{0.20}$  alloy nanoparticles were used. Colloidal nanoparticles were synthesised by co-reducing a mixture of chloroauric acid ( $\text{HAuCl}_4$ ) and silver nitrate ( $\text{AgNO}_3$ ) in a chloroform/water biphasic solution.<sup>1-4</sup> These metal nanoparticles were deposited onto a Si (001) substrate with native oxide by spin coating. A metal reaction vessel containing a nanoparticle-coated substrate was then left under vacuum at 180 °C for 12 hr to ensure a moisture free growth atmosphere and the desorption of the surfactant molecules from nanoparticle catalysts.

The Ge and Sn sources used were diphenylgermane (DPG) and tetraethyltin (TET) respectively. These precursors were dissolved in anhydrous toluene (10 mL) in an  $\text{N}_2$  filled glove box, with typical Ge and Sn precursor volumes of 0.025 mL and 0.0045 mL respectively. A solution containing both Ge and Sn precursors was loaded into a Hamilton sample-lock syringe inside a nitrogen-filled glovebox.

The  $\text{Au}_{0.80}\text{Ag}_{0.20}$  coated Si substrate was further annealed for 15 min at 440 °C under a flowing  $\text{H}_2/\text{Ar}$  atmosphere inside a tube furnace prior to the injection of precursors. The precursor solution was then injected into the metal reaction vessel using a Hamilton syringe pump at a rate of  $0.025 \text{ mL min}^{-1}$ . A  $\text{H}_2/\text{Ar}$  flow rate of 0.6 sccm was maintained during the entire growth period. Various growth times were employed to determine the growth rate, ranging from 15 – 120 min.

### 6.6.2. Characterisation

Bottom-up grown  $\text{Ge}_{1-x}\text{Sn}_x$  nanowires were imaged on a FEI Helios NanoLab 600i scanning electron microscope (SEM). All energy-dispersive X-ray (EDX) measurements were recorded in high-angle annular dark-field mode on a FEI Helios NanoLab 600i operating at 30 kV and 0.69 nA, with an attached Oxford X-Max 80 detector. EDX measurements had a standard error of 0.5 at. %. Transmission electron microscopy (TEM) analysis was performed on a JEOL JEM-2100 instrument operating at 200 kV in bright-field condition for imaging. High-resolution STEM imaging and electron energy loss spectroscopy (EELS) mapping was performed using a Nion UltraSTEM200 microscope, operated at 200 kV. Probe-forming optics were adjusted to deliver a 80 pm probe, with 40 pA beam current and 27 mrad convergence semi-angle. Electrochemical measurements were performed using a BioLogic VSP Potentiostat/Galvanostat. The electrochemical properties of branched GeSn nanowire samples were investigated in a half cell configuration against a pure Li counter electrode in a two electrode, stainless steel split cell (a coin cell assembly that can be disassembled for post-mortem analysis). The electrolyte used consisted of a  $1 \text{ mol dm}^{-3}$  solution of lithium hexafluorophosphate salt in a 1:1 (v/v) mixture of ethylene carbonate in dimethyl carbonate with 3 wt% vinylene carbonate. The separator used was a glass fiber separator (El-Cell ECC1-01-0012-A/L, 18 mm diameter, 0.65 mm thickness). The mass loading for anode samples was  $\sim 1.0 \text{ mg}$  and no additional conductive additives or binders were added. A Mettler Toledo XP2U ultra micro balance was used to determine the mass of GeSn nanowire material on the stainless steel substrates. Galvanostatic cycling was performed at 0.2 C in a potential window of 1.5 – 0.01 V (vs  $\text{Li/Li}^+$ ).

### 6.6.3. Figures

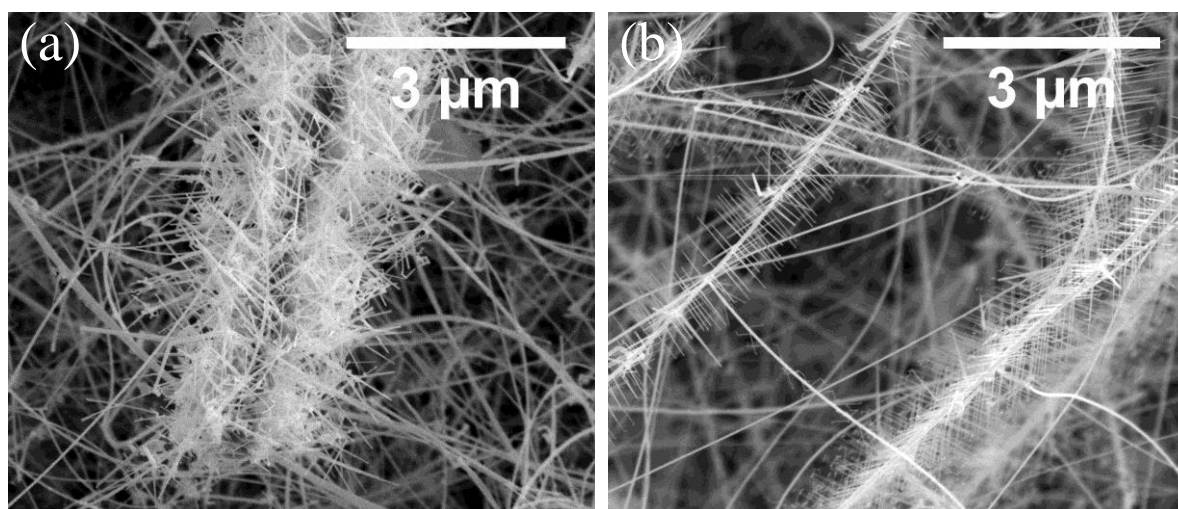


**Figure A6.1:** SEM images of the relative branch densities of (a) thick and (b) thin nanowire trunks. This trend was observed throughout the GeSn branched nanostructures.

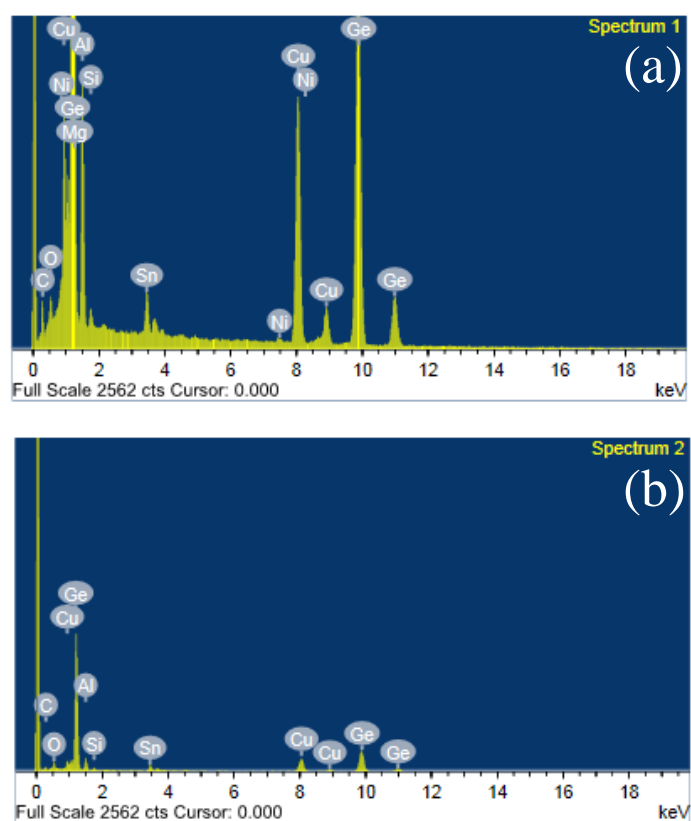


**Figure A6.2:** EDX Spectra of (a) a trunk (average 4.4 at. % Sn) and (b) branched nanowire (average 8.0 at. % Sn). Neither the trunk nor branch nanowire indicate the presence of Au or Ag metal.



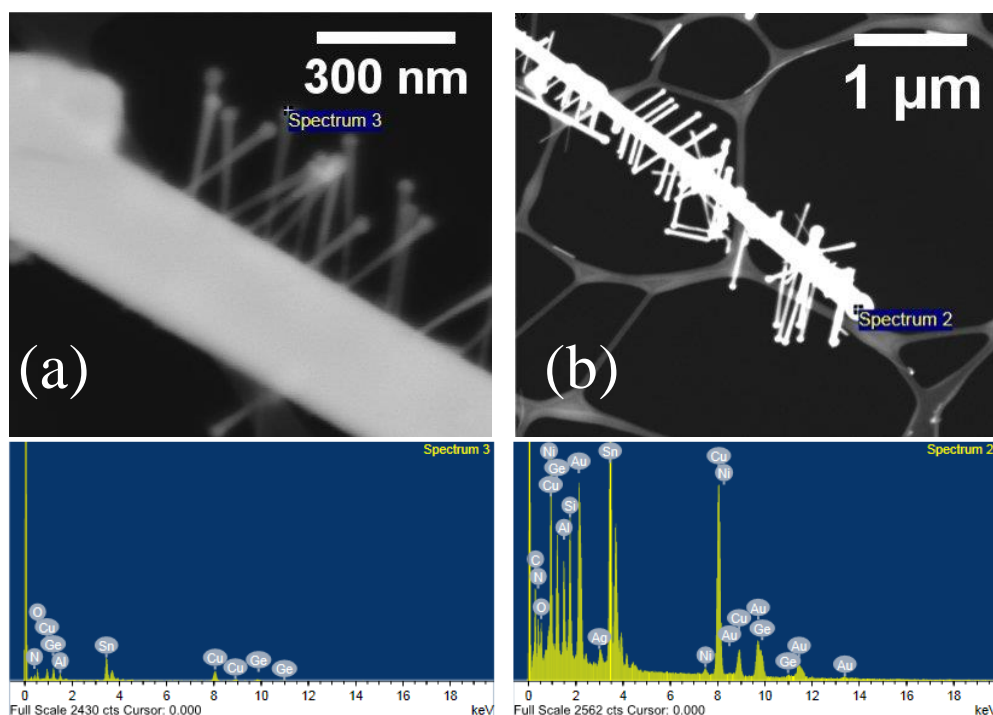


**Figure A6.3:** EDX analysis from the seed of (a) a branched nanowire and (b) a nanowire trunk. The seed on the branches in (a) does not indicate the presence of either Au or Ag, whereas Au and Ag are clearly apparent from an EDX spectrum of the trunk shown in (b).

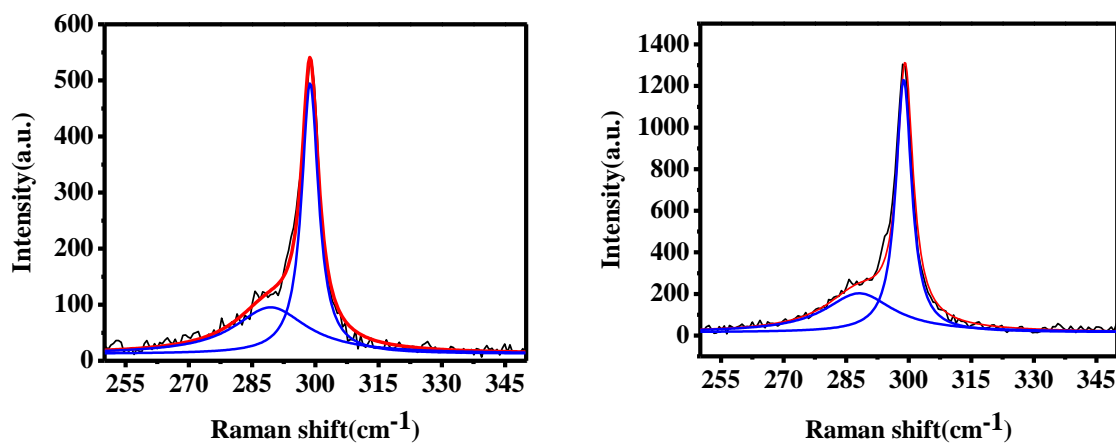


**Figure A6.4:** Room temperature Raman spectrum for two branched nanostructures recorded with an excitation wavelength of 488 nm. Raman spectrum displays two distinct peaks, relating to the varying Sn content between nanowire trunk (4.4 at. % Sn) and branch (8.0 at. % Sn).

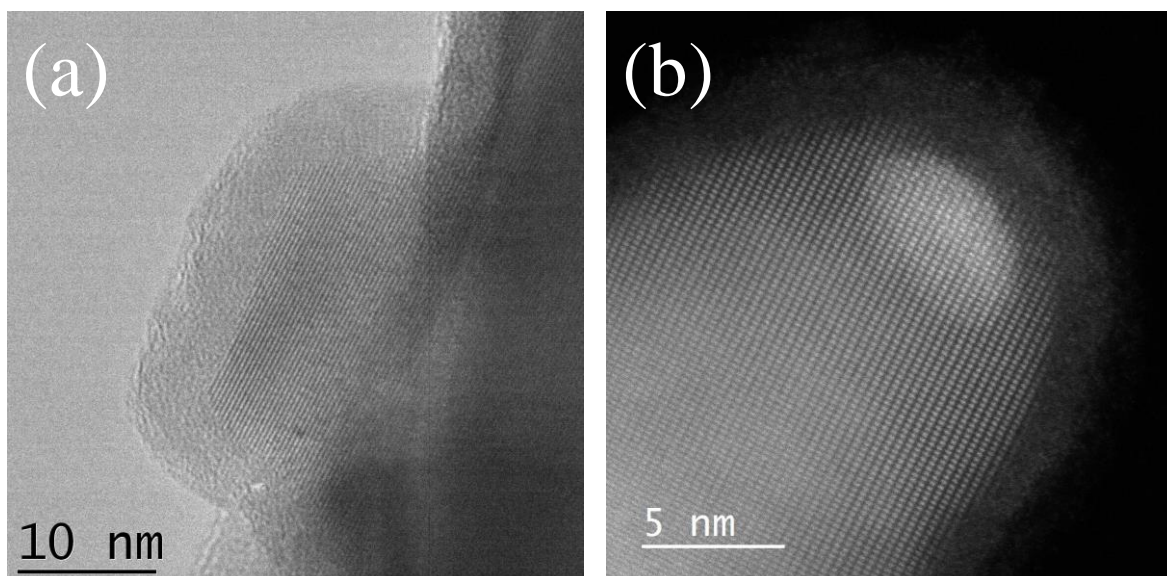


**Figure A6.5:** TEM analysis of the tips of nanowire branches showing (a) no apparent seed and (b) a small, diminished seed.

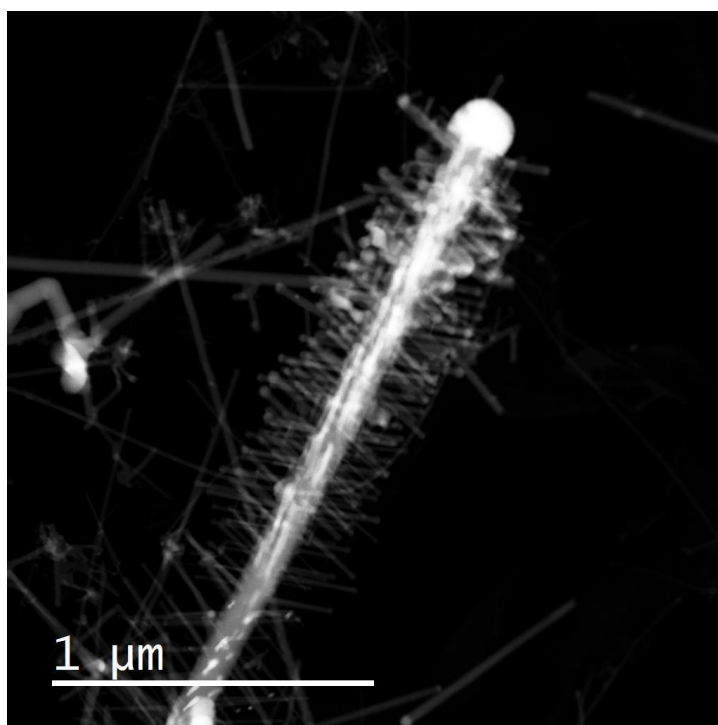


**Figure A6.6:** STEM image showing the decreasing length with increasing seed presence along the length of a nanowire trunk.

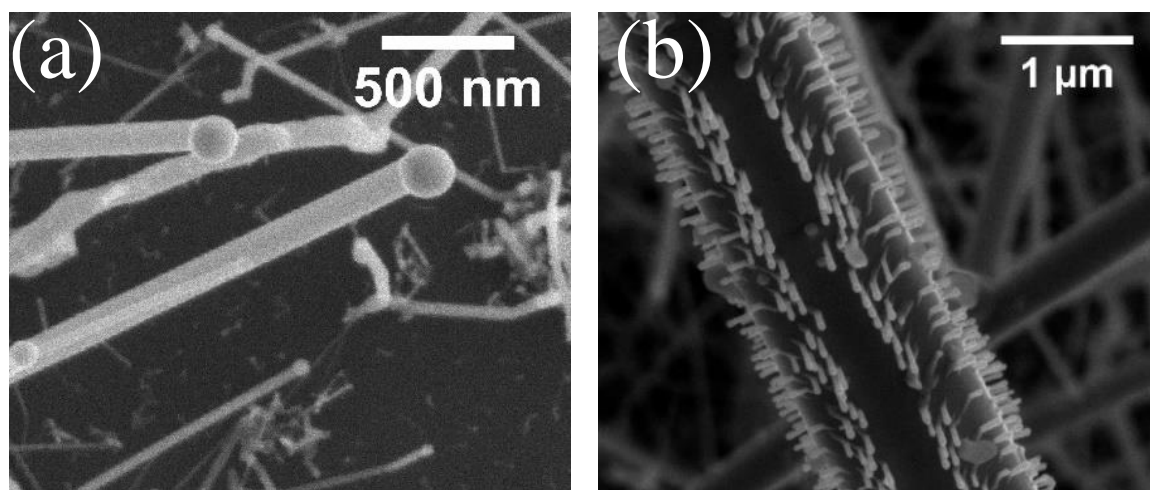


**Figure A6.7:** SEM images of GeSn branched nanowires growth after (a) 30 and (b) 80 min.

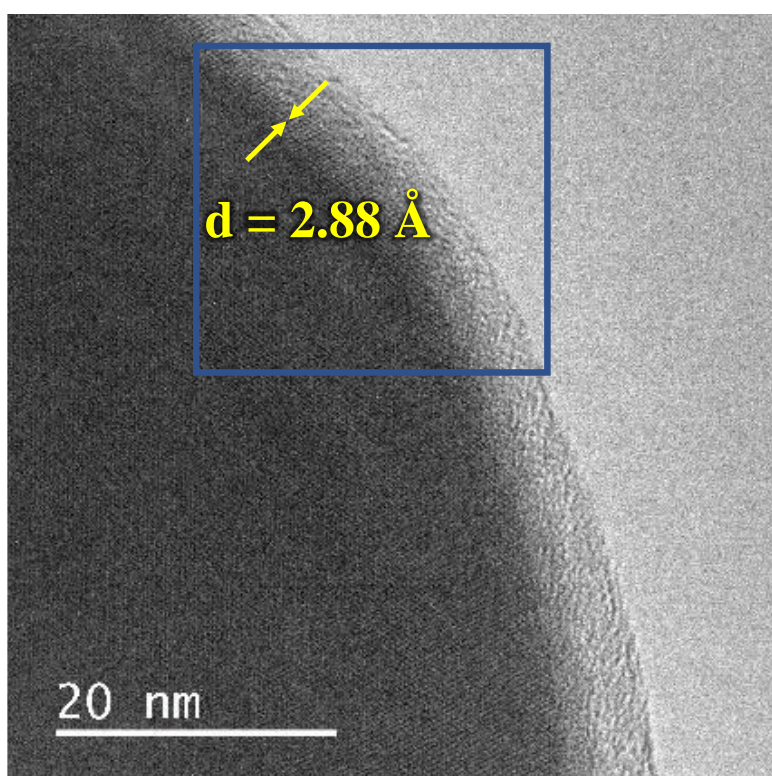


**Figure A6.8:** TEM image of the outer shell of a typical GeSn nanowire following an 80 min growth time. The lattice spacing of the outer edge of the nanowire sidewall matches well with metallic Sn (2.88 Å).

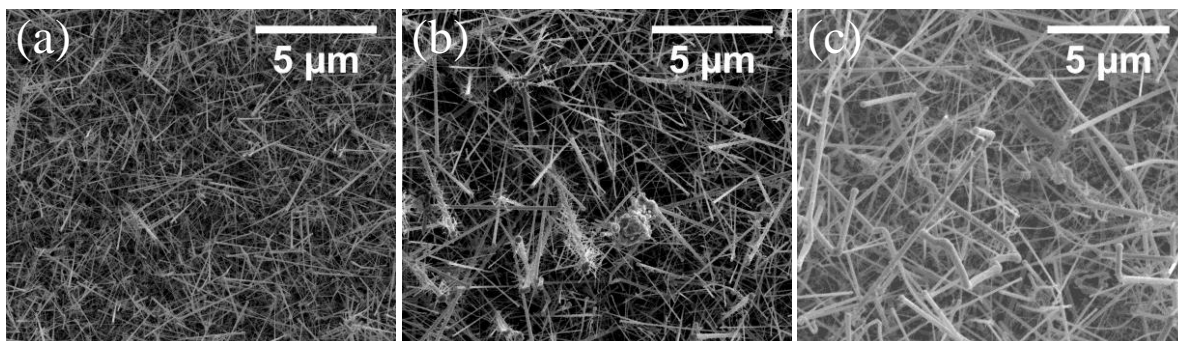


**Figure A6.9:** Branched nanowire growth catalysed by (a) Au, (b) Au<sub>0.90</sub>Ag<sub>0.10</sub> and (c) Au<sub>0.70</sub>Ag<sub>0.30</sub> nanoparticles with all other growth parameters fixed (4.5 μL TET, 440 °C, growth time 2 hr).

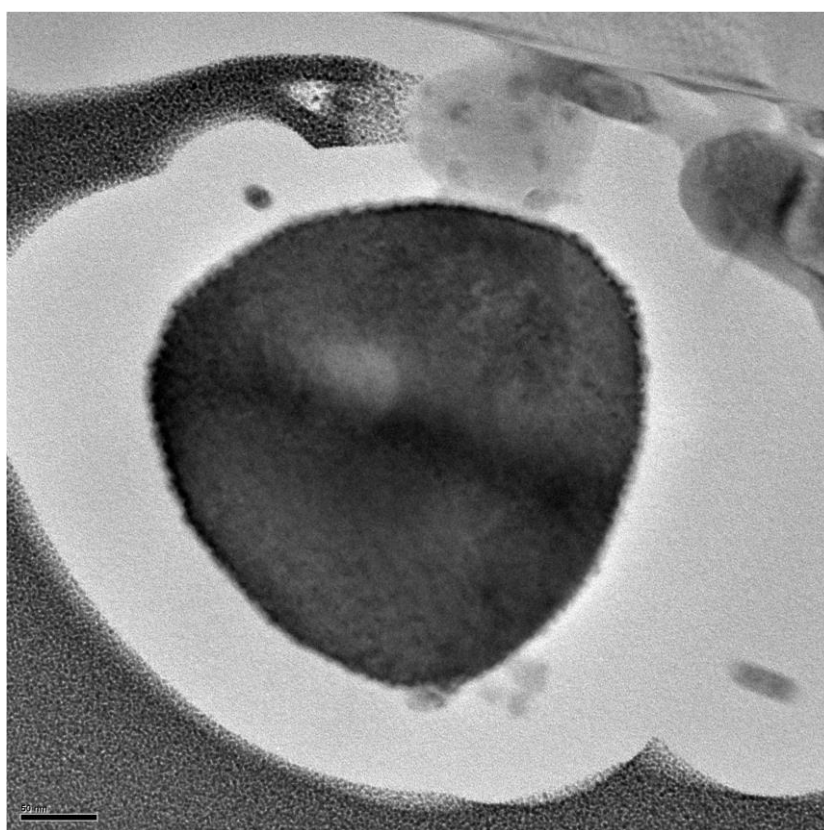


**Figure A6.10:** Cross-sectional TEM image of trunk nanowire showing nanowire facets. Scale bar represents 50 nm.

#### 6.6.4. References

1. Biswas, S. *et al.* Non-equilibrium induction of tin in germanium: Towards direct bandgap Ge  $1-x\text{Sn}$  nanowires. *Nat. Commun.* **7**, 11405 (2016).
2. Biswas, S., O'Regan, C., Morris, M. a. & Holmes, J. D. In-situ Observations of Nanoscale Effects in Germanium Nanowire Growth with Ternary Eutectic Alloys. *Small* **11**, 103–111 (2015).
3. Biswas, S., O'Regan, C., Petkov, N., Morris, M. a. & Holmes, J. D. Manipulating the growth kinetics of vapor-liquid-solid propagated ge nanowires. *Nano Lett.* **13**, 4044–4052 (2013).
4. He, S. T., Xie, S. S., Yao, J. N., Gao, H. J. & Pang, S. J. Self-assembled two-dimensional superlattice of Au-Ag alloy nanocrystals. *Appl. Phys. Lett.* **81**, 150–152 (2002).

# Chapter 7

## Supercritical Fluid Growth of High Sn Content $\text{Ge}_{1-x}\text{Sn}_x$ ( $x > 0.3$ ) Nanowires

This chapter is intended for submission in 2019. Consequently, sections of the chapter such as the abstract and introduction may contain repeating concepts and paragraphs. I co-wrote this paper with SB and JDH, and performed the nanowire synthesis. I carried out the elemental analysis with MC, KM and UB and performed and analysed the structural data.

Doherty, J.; Biswas, S.; Conroy, M.; Moore, K.; Bangert, U.; Holmes, J. D Supercritical Fluid Growth of High Sn Content  $\text{Ge}_{1-x}\text{Sn}_x$  ( $x > 0.3$ ) Nanowires (in preparation).

## 7. Supercritical Fluid Growth of High Sn Content $\text{Ge}_{1-x}\text{Sn}_x$ ( $x > 0.3$ ) Nanowires

---

### 7.1. Abstract

We report the catalytic fabrication of high Sn content  $\text{Ge}_{1-x}\text{Sn}_x$  nanowires from a supercritical fluid (SCF). The use of high pressure (21 MPa) toluene resulted in substantial Sn incorporation in the  $\text{Ge}_{1-x}\text{Sn}_x$  nanowires produced, with a Sn content ranging between  $0.1 \leq x \leq 0.35$ , *via* a supercritical fluid-liquid-solid (SFLS) growth mechanism. Sn incorporation in the  $\text{Ge}_{1-x}\text{Sn}_x$  nanowires was found to be strongly diameter dependence, with small diameter nanowires containing higher amounts of Sn relative to nanowires with larger diameters. A colossal Sn content of 35 at. % was achieved in  $\text{Ge}_{1-x}\text{Sn}_x$  nanowires with diameters of  $\sim 20$  nm. EDX analysis of the  $\text{Ge}_{1-x}\text{Sn}_x$  nanowires verified the homogeneous distribution of Sn throughout the nanowires, even for the high Sn content nanowires, without apparent clustering or segregation of Sn. The diameter dependent Sn inclusion observed has been attributed to the increased solubility at the metastable liquid-solid interface under high pressure. Even at a high Sn content, the  $\text{Ge}_{1-x}\text{Sn}_x$  nanowires retained their single crystalline nature with no apparent defects or twin boundaries.

## 7.2. Introduction

Alloying group IV semiconductors, such as Ge or Si with group IV metals such as Sn and Pb, can lead to a direct bandgap semiconductor<sup>1-3</sup> with the distinct advantage of being Si compatible, unlike direct bandgap III-V materials. The formation of a direct bandgap in Ge has been theoretically and experimentally reported by alloying the semiconductor with Sn.<sup>4,5</sup> As there is minimal separation between the L and  $\Gamma$  valleys in the band structure of Ge, adding Sn to the semiconductor at a concentration between 6 to 10 at.% causes a certain degree of  $\Gamma$ -L mixing.<sup>6,7</sup> In order to obtain a fully direct bandgap material, without the involvement of L valley mixing, a colossal incorporation of Sn is therefore required. The surge to incorporate higher Sn concentrations ( $x > 0.1$ ) can be attributed in part to the presence of band-mixing at lower Sn contents.<sup>6-9</sup> In the case of  $\text{Ge}_{1-x}\text{Sn}_x$ , the incorporation of higher amounts of Sn impurity into the  $\text{Ge}_{1-x}\text{Sn}_x$  nanowire result in an increase in the energy difference between  $\Gamma$  and L valleys.<sup>6,7</sup> This improves the efficiency of  $\text{Ge}_{1-x}\text{Sn}_x$ -based light sources in terms of lasing threshold and operating temperature and applicable for fully integrated Si optoelectronic and photonic systems used in mid- and far-infrared applications. A direct bandgap group IV semiconductor is imperative for the development of mid-IR optoelectronic devices such as photodetectors and photovoltaics.<sup>10-12</sup> This transition to a direct bandgap is required for the use of Ge optoelectronic materials, such as photodiodes, without the need for induced strain<sup>13,14</sup>. Theoretically, a semi-metallic bandgap is expected with Sn inclusion in excess of 40 at. %.<sup>15,16</sup> However, there have been few reports on  $\text{Ge}_{1-x}\text{Sn}_x$  nanowires with Sn incorporation greater than 10 at. %. In terms of high Sn incorporation,  $\text{Ge}_{1-x}\text{Sn}_x$  nanorods have been previously reported by Seifner et al. with  $x = 0.28$ ,<sup>15</sup> whilst Ramasamy et al. detailed their fabrication of  $\text{Ge}_{1-x}\text{Sn}_x$  nanoparticles with 40 at. % Sn.<sup>17</sup>



Ge<sub>1-x</sub>Sn<sub>x</sub> nanowires with a Sn content > 9 at. % have been recently reported *via* atmospheric pressure VLS growth where a kinetic dependent model; solute trapping; is responsible for non-equilibrium incorporation of Sn in Ge lattice.<sup>8,18</sup> High pressure (21 MPa) applied during the VLS growth could influence the solute trapping of the Sn impurities in Ge<sub>1-x</sub>Sn<sub>x</sub> by altering the metastable solubility of Sn at the growth interface. To the best of our knowledge, the reported theoretical literature surrounding solute trapping is presented at a constant temperature, so the exact effect of pressure on the solute trapping model is undescribed.<sup>19,20</sup> The introduction of pressure should influence the growth kinetics of the Ge<sub>1-x</sub>Sn<sub>x</sub> nanowires,<sup>21,22</sup> by increasing the decomposition rate of the precursors. This rapid precursor decomposition plays a significant role in the nanowire growth kinetics, as the growth kinetics may no longer be dominated by the crystallisation rate *i.e.* the liquid/solid interface between catalyst and nanowire, but rather have a non-trivial contribution from the incorporation of growth materials into the nanowire catalyst *i.e.* the SCF/liquid interface.<sup>22</sup>

To further extend the limits of Sn incorporation in the Ge nanowire lattice, without compromising the structural quality and crystallinity of the Ge<sub>1-x</sub>Sn<sub>x</sub>, we report the introduction of pressure as a growth parameter in the VLS growth protocol. In this report, supercritical toluene growth medium and AuAg alloy nanoparticle growth promoter is used for the growth of Ge<sub>1-x</sub>Sn<sub>x</sub> alloy nanowires with colossal Sn incorporation. Influence of high pressure results in the growth of Ge<sub>1-x</sub>Sn<sub>x</sub> nanowires with substantial Sn incorporation in the range between 0.1 ≤ *x* ≤ 0.35; much higher than the reported Sn incorporation in Ge 1-D lattice. We also communicate the apparent relationship between nanowire diameter and Sn inclusion in the nanowire; with smaller nanowire diameters relating to higher Sn incorporation in the Ge<sub>1-x</sub>Sn<sub>x</sub> nanowires.

## 7.3. Experimental

### 7.3.1. Method

Colloidal nanoparticles of  $\text{Au}_{0.90}\text{Ag}_{0.10}$  were synthesised by co-reducing a mixture of chloroauric acid ( $\text{HAuCl}_4$ ) and silver nitrate ( $\text{AgNO}_3$ ) in a chloroform/water biphasic solution.<sup>21,23–25</sup> These metal nanoparticles were deposited on to a Si(001) substrate with native oxide *via* spin coating and loaded into a stainless steel cell.  $\text{Ge}_{1-x}\text{Sn}_x$  nanowires were grown in 5 ml stainless steel cells (High Pressure Equipment Company) at a temperature of 405 °C. The handling of dry toluene, diphenylgermane (DPG) and allyltributylstannane (ATBS), as well as the filling of the reaction vessel and injection cell was carried out in a  $\text{N}_2$  glove box under stringent precautions against water. The reaction cell and injection equipment were dried under vacuum at 180 °C for 48 h and transferred into a glove box. 3 ml toluene was added into the 5 ml reaction cell and the assembly was heated to the desired temperature in a tube furnace for 1-2 h. After setting the pressure of the reaction cell to 21 MPa, the injection cell, filled with 20 ml of toluene/diphenylgermane/allyltributylstannane solution (25  $\mu\text{L}$  DPG and 7.5  $\mu\text{L}$  ATBS), was pressurised by an ISCO HPLC pump. The precursor solution was injected at a rate of  $0.025\text{ ml min}^{-1}$  over a time period of 120 min under constant pressure conditions in a flow through reaction. Finally, the reaction cell was cooled to room temperature, depressurised and disassembled to access the growth substrate.

### 7.3.2. Characterisation

Bottom-up grown  $\text{Ge}_{1-x}\text{Sn}_x$  nanowires were imaged on a FEI Helios NanoLab 600i scanning electron microscope (SEM). All energy-dispersive X-ray (EDX) measurements were recorded in high-angle annular dark-field mode in the FEI Helios NanoLab 600i operating at 30 kV and 0.69 nA with an attached Oxford X-Max 80 detector. Error in the EDX measurements indicates a standard error of 0.5 at. %. TEM analysis was performed on a JEOL JEM-2100 operating at

200 kV in bright-field condition for imaging. EDX mapping was performed on a Titan Themis double-corrected and monochromated Transmission Electron Microscope at 300kV with a Bruker Super X detector. Software for imaging and EDS mapping is FEI Velox.

#### 7.4. Results and Discussion

The optical properties of an alloy can be influenced by the alloy composition, as demonstrated both theoretically<sup>26</sup> and experimentally<sup>27–29</sup>. Thus, it is interesting to look into the unexplored region; i.e. beyond 25 at.% Sn; of the  $\text{Ge}_{1-x}\text{Sn}_x$  alloy nanowire where very high Sn content could have great impact on the crystal quality and stability of the alloy, along with the optical properties. To overcome the limitations in Sn incorporation ( $\approx 10$  at.% Sn)<sup>8,18,30</sup> in  $\text{Ge}_{1-x}\text{Sn}_x$  nanowires *via* atmospheric pressure chemical vapour deposition (CVD) growth, pressure was introduced as additional growth parameter in a SCF environment. The induction of pressure will encourage the decomposition of growth precursors and may influence the solute trapping<sup>20</sup> of the Sn adatoms in  $\text{Ge}_{1-x}\text{Sn}_x$  by altering the metastable solubility of Sn at the growth interface. A kinetic dependent solute trapping mechanism is believed to be liable for Sn incorporation in  $\text{Ge}_{1-x}\text{Sn}_x$  nanowires, where nanowires with faster growth rates have higher Sn incorporation in the nanowires.<sup>8,18</sup> Figure 7.1 shows SEM images of  $\text{Ge}_{1-x}\text{Sn}_x$  nanowires synthesised in a supercritical toluene environment from  $\text{Au}_{0.90}\text{Ag}_{0.10}$  seeds at a temperature of 405 °C and pressure of 20.7 MPa. The nanowires are deposited on a Si substrate and show the formation of small clusters consisting of individual nanowires (Figure 7.1(a)). Sn agglomeration and segregation can be seen clearly in Figure 7.1(a), with clusters of Sn apparent forming across the substrate. This Sn segregation, which was not apparent in CVD growth, could be attributed to the rapid decomposition of Sn source under high pressure. This rapid precursor decomposition, while beneficial for high Sn incorporation in the  $\text{Ge}_{1-x}\text{Sn}_x$  nanowires, instigated Sn aggregation across the substrate. The  $\text{Ge}_{1-x}\text{Sn}_x$  nanowires synthesised were relatively short,

compared to  $\text{Ge}_{1-x}\text{Sn}_x$  with a Sn content between 6 – 10 at. %, with typical lengths  $\leq 2 \mu\text{m}$  (Figure 7.1). The STEM image presented in Figure 7.1(c) provides further proof of the uniform morphology of the nanowires, without any bending, kinking and with negligible tapering. The hemispherical catalyst seed at the tips of the nanowire (visible in Figure 7.1(c)), verifies that these  $\text{Ge}_{1-x}\text{Sn}_x$  nanowires are grown *via* catalytic VLS like growth. Unlike previously reported CVD grown  $\text{Ge}_{1-x}\text{Sn}_x$  nanowires,<sup>8,18</sup> the  $\text{Ge}_{1-x}\text{Sn}_x$  nanowires grown using a SCF growth regime do not appear to contain a  $\text{Ge}_{1-x}\text{Sn}_x$  bulb ( $x \approx 0.5$ ) surrounding the nanowire catalyst seed.

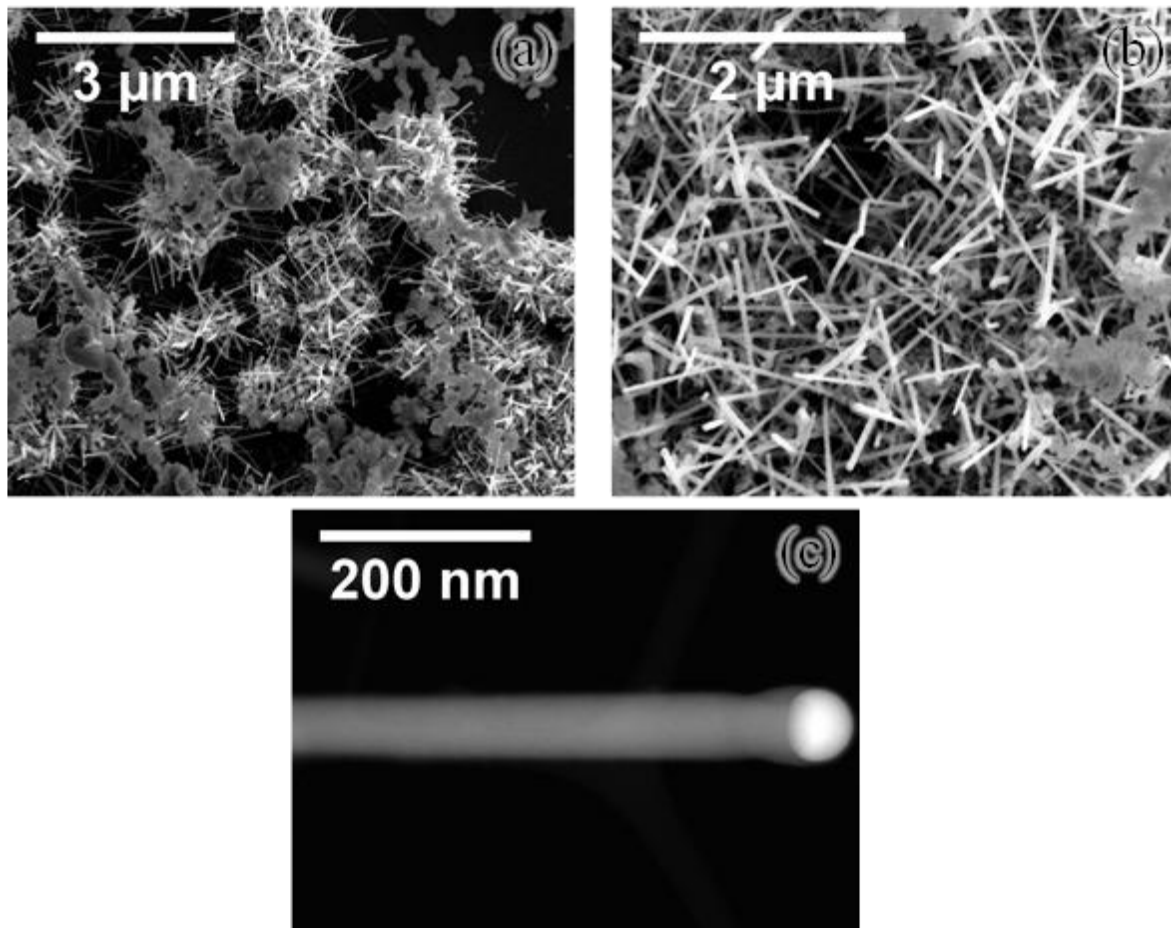


**Figure 7.1:** SEM/STEM Analysis of  $\text{Ge}_{1-x}\text{Sn}_x$  nanowires. SEM images of  $\text{Ge}_{1-x}\text{Sn}_x$  nanowires at low (a) and high (b) magnification are presented. The presence of Sn agglomerates can be seen in (a). (b) highlights the uniformity of the nanowires across the substrate. STEM images at low (c) and high (d) magnification are also shown. A single nanowire is presented in (c), displaying minimal tapering and the presence of a growth seed.

EDX point analysis on the  $\text{Ge}_{1-x}\text{Sn}_x$  nanowires revealed a mean Sn composition of  $\sim 17.1$  at. % (representative elemental spectrum, Figure 7.2(a)). The elemental spectrum also revealed no incorporation of Au or Ag into the nanowire body from the nanoparticle catalyst, which is an important factor when considering device; optoelectronic and nanoelectronic; implementation of  $\text{Ge}_{1-x}\text{Sn}_x$  nanowires seeded by metal catalysts. Sn incorporation in these SCF grown  $\text{Ge}_{1-x}\text{Sn}_x$  nanowires varies largely from nanowire to nanowire, from  $\sim 10 - 35$  at. %. Sn can be seen (in Figure 7.1) to cluster or agglomerate on the substrate at the high pressure used in the SCF assisted growth of  $\text{Ge}_{1-x}\text{Sn}_x$  nanowires. Notably, with greater than 20 at. % Sn incorporation, the solubility limit of Sn in Ge has also been overly stretched. Therefore, to ensure that the Sn is homogeneously distributed throughout the body in the  $\text{Ge}_{1-x}\text{Sn}_x$  nanowires, *i.e.* without Sn segregation in the bulk or surface of the nanowire or a gradual decrease in the Sn content from the seed to the end of a nanowire, EDX elemental maps (Figure 7.2(b)) were obtained for individual nanowires (Sn denoted by green, Ge by red and O by blue). Figure 7.2(b) displays a composite image of Ge, Sn and O; the individual elemental maps for each element is also provided for clarity. The lack of Sn segregation or clustering is verified by the absence of bright green spots (corresponding to Sn) in the elemental map in Figure 7.2(b). The formation of a Sn-rich seed is also clearly visible from the EDX elemental map, as was apparent in CVD grown  $\text{Ge}_{1-x}\text{Sn}_x$  nanowires at similar temperature.<sup>8,18</sup> An oxide rich layer can be observed in Figure 7.2(b) close to the nanowire seed. To ensure that there is no influence from this potentially S- rich oxide layer on the calculated Sn composition of the  $\text{Ge}_{1-x}\text{Sn}_x$  nanowires, EDX point analysis was conducted at a distance of  $> 200$  nm from the nanowire seed.

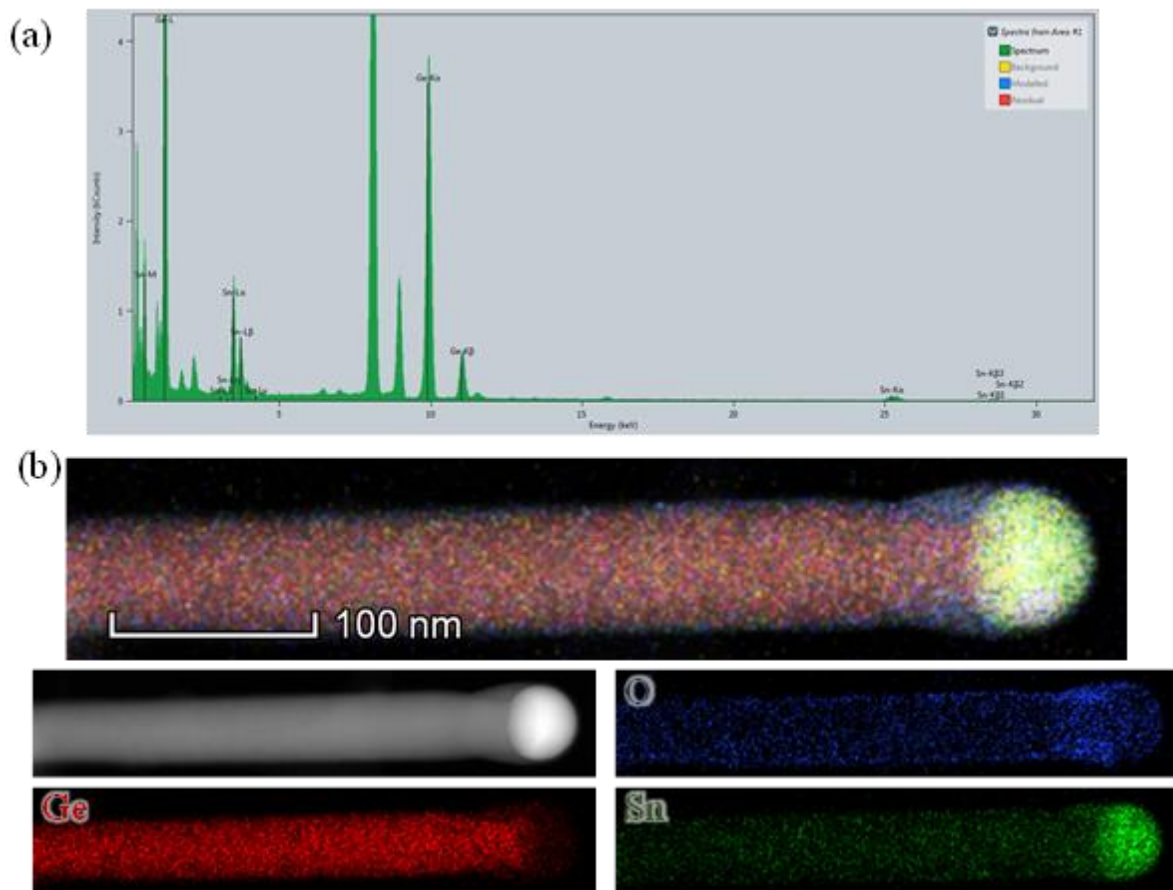


**Figure 7.2:** EDX elemental analysis of  $\text{Ge}_{1-x}\text{Sn}_x$  nanowires. The spectrum in (a) is representative of  $\text{Ge}_{1-x}\text{Sn}_x$  nanowires with  $x > 0.1$ . The high Sn incorporation is verified by point EDX analysis. (b) Elemental mapping indicates  $\text{Ge}_{1-x}\text{Sn}_x$  nanowires contain a colossal Sn incorporation of  $x \leq 0.35$  with the Sn distributed homogeneously throughout the body of the nanowire. Evidence of a Sn rich oxide layer at the seed/body interface is evident through EDX elemental mapping; O denoted by blue, Ge by red and Sn by green.

Despite the relatively narrow diameter range; average diameter of around 40 nm;  $\text{Ge}_{1-x}\text{Sn}_x$  nanowires have the tendency to remain clustered together, leading to difficulty in facile comparison between nanowires of different diameters. A dark field STEM image in Figure 3(a) clearly shows the diameter of  $\text{Ge}_{1-x}\text{Sn}_x$  nanowires between a lower ( $\sim 20$  nm) and higher ( $\sim 70$  nm) region of the diameter range (Figure 7.3(a)). Due to the clustered nature of the nanowires, it is difficult to precisely analyse the nanowire lengths. However, it is apparent from the STEM image in Figure 7.3(a) that the thinner nanowires seem to achieve greater

lengths than their thicker counterparts.  $\text{Ge}_{1-x}\text{Sn}_x$  nanowires with diameters above the mean ( $> 40.5 \text{ nm}$ ) have typical lengths less than  $1 \mu\text{m}$ , while nanowires with diameters below  $40.5 \text{ nm}$  above  $1 \mu\text{m}$  in length. This is contrary to the diameter dependence on length for the supersaturation limited VLS growth of Ge nanowire *via* CVD technique,<sup>21</sup> where thicker nanowires demonstrate faster growth kinetics. This discrepancy may be due to the faster decomposition rates of precursors in an SCF growth regime under high pressure compared to the CVD growth. The pressure component in the SCF based VLS-like growth may promote the kinetics of both the incorporation step at the catalyst surface and the crystallization step during the nanowire growth in the determination of the overall growth kinetics. In comparison, in a crystallisation limited process, the growth rate is influenced *via* the nucleation and crystal growth at the liquid/solid interface. In SCF assisted growth, due to faster precursor decomposition resulting large chemical potential in the vapour phase, both the crystallisation at the liquid-solid interface and the incorporation of growth material into the catalyst have influence on the final growth kinetics of nanowires. Hence, the diameter ( $d$ ) dependence on the growth rate ( $v$ ) does not follow the conventional Gibbs-Thompson size effect on growth kinetics, rather growth rate can be given by  $v = v_0 + \frac{\Gamma(4\Omega^S\sigma^S)}{d}$ , where  $v_0$  is the growth rate of the nanowire at infinite diameter ( $d$ ),  $\Omega^S$  is the molar volume in the solid phase and  $\sigma^S$  is the surface tension of the nanowires.<sup>22</sup> Hence, when  $d$  is infinity, the growth rate is restricted to  $v_0$ , but when  $d$  is minimal, the growth rate increases. This verifies the inverse relationship between the nanowire diameter and nanowire growth kinetics (Figure 7.3(a)) in  $\text{Ge}_{1-x}\text{Sn}_x$  nanowires with smaller diameter nanowires appear to have greater lengths than thicker  $\text{Ge}_{1-x}\text{Sn}_x$  nanowires. This further relates to the observation of diameter dependent Sn incorporation (Figure 7.3(b)) with thinner nanowires having larger Sn inclusion. A large set of nanowires at different diameter ranges were taken into account for the study on diameter dependent (and hence length dependent) Sn incorporation. In a kinetics dependent solute trapping model,<sup>20</sup>

faster growth rates lead to greater impurity incorporation, thus  $\text{Ge}_{1-x}\text{Sn}_x$  nanowires with smaller diameters and faster growth kinetics display higher Sn content.  $\text{Ge}_{1-x}\text{Sn}_x$  nanowires with the highest Sn contents ( $\sim 35$  at. %) were observed (Figure 7.3(b)) for those with the smallest diameters ( $\sim 20$  nm) whereas nanowires with larger diameters ( $> 50$  nm) contained only 10 – 15 at. % Sn. This large discrepancy of Sn inclusion in  $\text{Ge}_{1-x}\text{Sn}_x$  nanowires with different

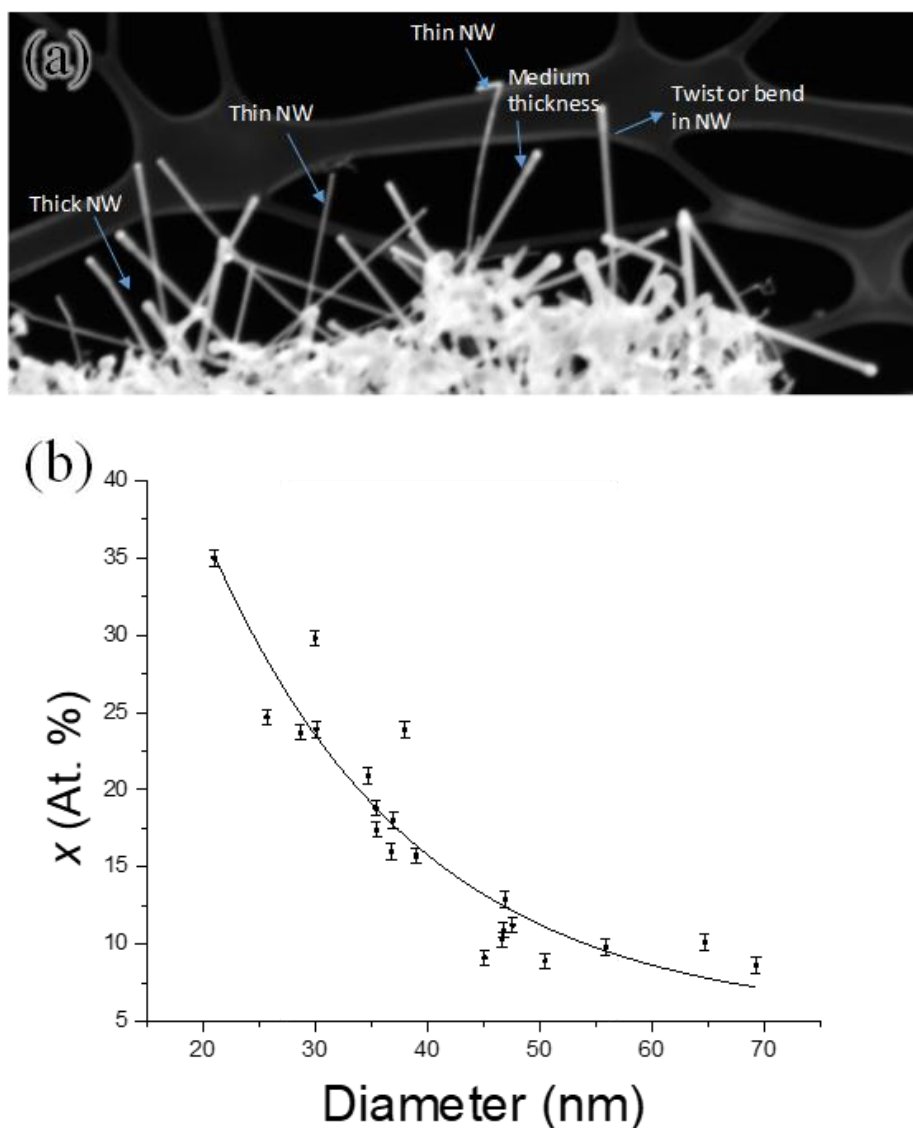


**Figure 7.3:** Diameter dependence of  $x$  in  $\text{Ge}_{1-x}\text{Sn}_x$  nanowires. The small variation in nanowire diameter appears to relate to a dramatic change in the Sn composition in the nanowire. The narrowest nanowires appear to have the highest Sn incorporation, with an apparent relationship observable between  $x$  and nanowire diameter.



diameter has not been previously observed for the CVD grown  $\text{Ge}_{1-x}\text{Sn}_x$  nanowires. But the impact of growth kinetics on the Sn incorporation was observed for CVD grown  $\text{Ge}_{1-x}\text{Sn}_x$  nanowires.<sup>18</sup> But an enormous increase in the amount of Sn incorporation is observed for high pressure SCF growth compared to CVD growth. This could be assigned to the change in solubility;<sup>31</sup> both or either solid solubility and eutectic solubility; of Sn in Ge under high pressure. We delegate a detailed model to a later study to explain large Sn inclusion on Ge nanowire under high pressure, by taking account of solute trapping and different solubility and interfaces.

Determining the structural quality (crystallinity, defects, *etc.*) without defects of the  $\text{Ge}_{1-x}\text{Sn}_x$  nanowires with a large Sn incorporation is imperative as high Sn content can produce a large lattice mismatch component in the alloy, resulting the formation of crystal defects such as twin boundaries or stacking fault. However, TEM analysis of these SCF grown  $\text{Ge}_{1-x}\text{Sn}_x$  nanowires was noted to be exceedingly difficult, as the high voltage electron beam caused the nanowires to amorphise and recrystallise (Figure 7.4). This damage was also observed at voltages as low as 30 kV. This may be due to increased instability in the nanowires due to the large impurity incorporation ( $x \leq 0.35$ ). Prior to damage, the  $\text{Ge}_{1-x}\text{Sn}_x$  nanowires showed no noticeable defects or twin boundaries, and are single crystalline (Figure 7.4(a), (c)). Focusing the electron beam on the  $\text{Ge}_{1-x}\text{Sn}_x$  nanowires results in irreparable deformation of the  $\text{Ge}_{1-x}\text{Sn}_x$  nanowires, rendering high resolution imaging unattainable (Figure 7.4(b), (d)). Sn incorporation in  $\text{Ge}_{1-x}\text{Sn}_x$  nanorods ( $x = 0.17$ ) have previously been demonstrated to segregate out at temperatures above 200 °C.<sup>15</sup>

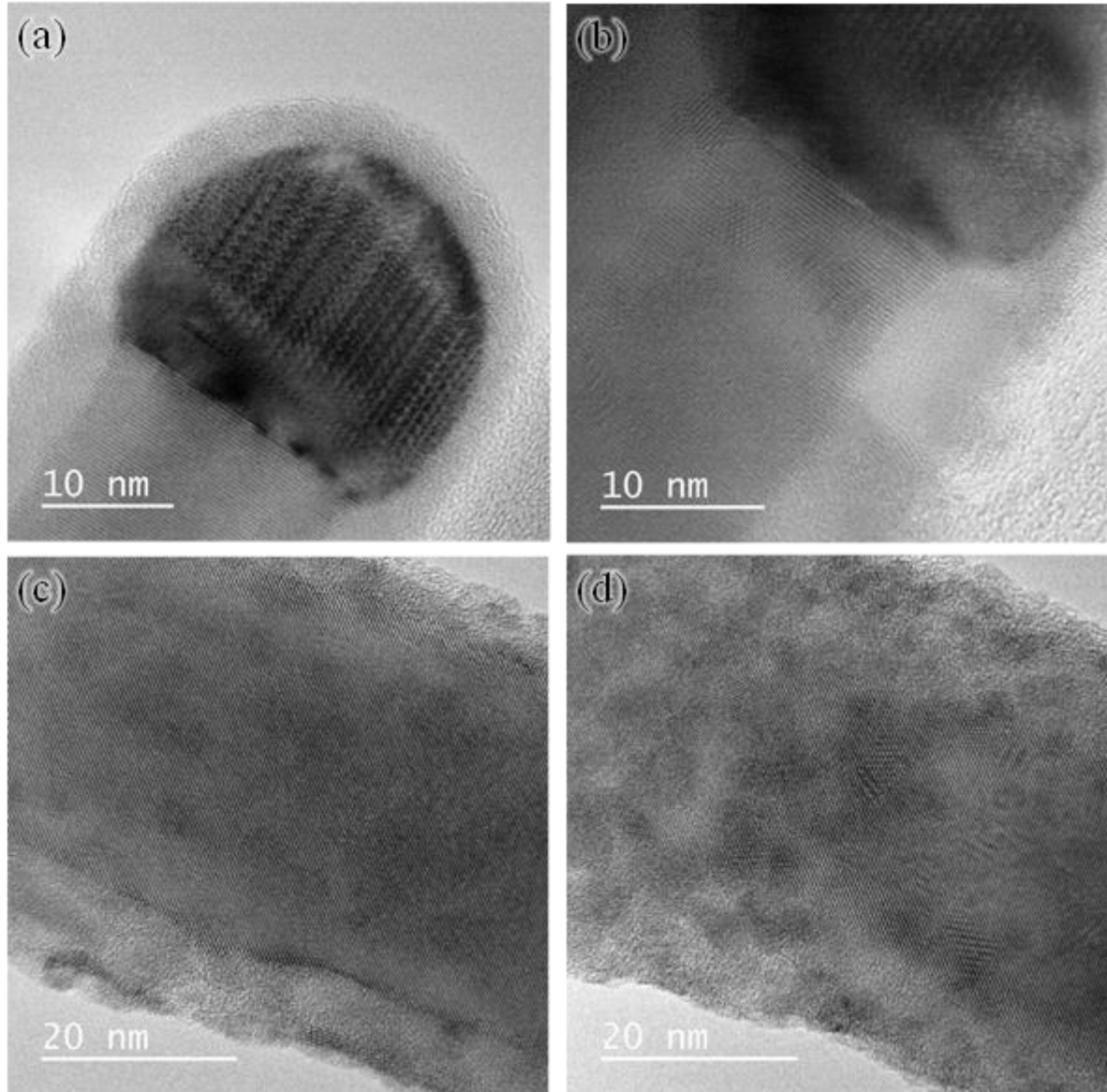


**Figure 7.4:** TEM analysis of  $\text{Ge}_{1-x}\text{Sn}_x$  nanowires. TEM images taken before (a) and after (b) amorphisation and recrystallization of the nanowire by the electron beam at the seed/body interface and before (c) and after (d) damage in the bulk of the  $\text{Ge}_{1-x}\text{Sn}_x$  nanowire.

## 7.5. Conclusion

We have reported the fabrication of  $\text{Ge}_{1-x}\text{Sn}_x$  nanowires by a SCF approach. The introduction of pressure resulted in a substantial increase in the Sn incorporation in the  $\text{Ge}_{1-x}\text{Sn}_x$  nanowires, with a mean  $x$  value of 0.17. Despite the large Sn inclusion, the  $\text{Ge}_{1-x}\text{Sn}_x$  nanowires did not display any apparent Sn segregation or clustering. EDX analysis of nanowires verified the homogeneous distribution of Sn throughout the nanowire body. The Sn rich nanowire seed, which has been observed in our previous CVD grown nanowires was also present in these SCF grown nanowires. Sn incorporation in the  $\text{Ge}_{1-x}\text{Sn}_x$  nanowires displayed a strong diameter dependence; narrower nanowires contained higher amounts of Sn relative to their broader counterparts. Up to  $x = 0.35$  was achieved in  $\text{Ge}_{1-x}\text{Sn}_x$  nanowires with diameters of approximately 20 nm. This diameter dependence can be attributed to the increased concentration of growth material in the SCF phase due to the fast decomposition of nanowire precursors. The high concentration of growth material in the SCF phase leads to a strong participation of the incorporation step at the catalyst interface on the growth rate of the nanowires.  $\text{Ge}_{1-x}\text{Sn}_x$  nanowires with a smaller diameter, and therefore a faster growth rate, result in a higher inclusion of Sn. Low resolution imaging, prior to nanowire amorphisation and recrystallisation, revealed single crystalline  $\text{Ge}_{1-x}\text{Sn}_x$  nanowires with no apparent defects or twin boundaries. As Sn incorporation has been shown to alter the  $d$  spacing of  $\text{Ge}_{1-x}\text{Sn}_x$  nanowires even in lower amounts,<sup>8,18</sup> the determination of the  $d$  spacing of these high Sn nanowires may prove an interesting aspect of their structural characterisation. However, the large Sn content results in increasing nanowire instability under the high voltage electron beam. Further investigation of  $\text{Ge}_{1-x}\text{Sn}_x$  nanowires with colossal Sn incorporation is required to determine the nature of the relationship between the Sn incorporation and diameter, and the structural quality of the nanowires. These  $\text{Ge}_{1-x}\text{Sn}_x$  nanowires ( $0.1 \leq x \leq 0.3$ ) could prove

themselves as potential candidates for implementation in photovoltaic and optical devices due to the predicted narrow and direct bandgap achieved with colossal Sn incorporation.

## 7.6. References

1. Kasper, E. *et al.* Growth of silicon based germanium tin alloys. *Thin Solid Films* **520**, 3195–3200 (2012).
2. Soref, R. A. & Friedman, L. Direct-gap Ge/GeSn/Si and GeSn/Ge/Si heterostructures. *Superlattices and Microstructures* **14**, 189–193 (1993).
3. Zaima, S. *et al.* Growth and applications of GeSn-related group-IV semiconductor materials. *2016 IEEE Photonics Soc. Summer Top. Meet. Ser. SUM 2016* **16**, 37–38 (2016).
4. Sau, J. D. & Cohen, M. L. Possibility of increased mobility in Ge-Sn alloy system. *Phys. Rev. B - Condens. Matter Mater. Phys.* **75**, 1–7 (2007).
5. Jenkins, D. W. & Dow, J. D. Electronic properties of metastable  $\text{Ge}_x\text{Sn}_{1-x}$  alloys. *Phys. Rev. B* **36**, 7994–8000 (1987).
6. Dutt, B. *et al.* Theoretical analysis of GeSn alloys as a gain medium for a Si-compatible laser. *IEEE J. Sel. Top. Quantum Electron.* **19**, (2013).
7. Polak, M. P., Scharoch, P. & Kudrawiec, R. The electronic band structure of  $\text{Ge}_{1-x}\text{Sn}_x$  in the full composition range: indirect, direct, and inverted gaps regimes, band offsets, and the Burstein–Moss effect. *J. Phys. D. Appl. Phys.* **50**, 195103 (2017).
8. Biswas, S. *et al.* Non-equilibrium induction of tin in germanium: Towards direct bandgap  $\text{Ge}_{1-x}\text{Sn}_x$  nanowires. *Nat. Commun.* **7**, (2016).
9. Saladukha, D., Doherty, J., Biswas, S., Ochalski, T. J. & Holmes, J. D. Optical study of strain-free GeSn nanowires. *Silicon Photonics XII* **10108**, 101081C (2017).
10. Soref, R. Mid-infrared photonics in silicon and germanium. *Nat. Photonics* **4**, 495–497

- (2010).
11. Xu, S. *et al.* GeSn lateral p-i-n photodetector on insulating substrate. *Opt. Express* **26**, 17312–17320 (2018).
  12. Mashanovich, G. Z. *et al.* Germanium Mid-Infrared Photonic Devices. *J. Light. Technol.* **35**, 624–630 (2017).
  13. Stange, D. *et al.* Optical Transitions in Direct-Bandgap Ge<sub>1-x</sub>Sn<sub>x</sub>Alloys. *ACS Photonics* **2**, 1539–1545 (2015).
  14. Ghetmiri, S. A. *et al.* Direct-bandgap GeSn grown on silicon with 2230 nm photoluminescence. *Appl. Phys. Lett.* **105**, 6–11 (2014).
  15. Seifner, M. S., Hernandez, S., Bernardi, J., Romano-Rodriguez, A. & Barth, S. Pushing the composition limit of anisotropic Ge<sub>1-x</sub>Sn<sub>x</sub> nanostructures and determination of their thermal stability. *Chem. Mater.* **29**, 9802–9813 (2017).
  16. Lan, H. S., Chang, S. T. & Liu, C. W. Semiconductor, topological semimetal, indirect semimetal, and topological Dirac semimetal phases of Ge<sub>1-x</sub>Sn<sub>x</sub> alloys. *Phys. Rev. B* **95**, 1–5 (2017).
  17. Ramasamy, K. *et al.* Sn<sub>x</sub>Ge<sub>1-x</sub>Alloy Nanocrystals: A First Step toward Solution-Processed Group IV Photovoltaics. *Chem. Mater.* **27**, 4640–4649 (2015).
  18. Doherty, J. *et al.* Influence of growth kinetics on Sn incorporation in direct band gap Ge<sub>1-x</sub>Sn<sub>x</sub> nanowires. *J. Mater. Chem. C* 8738–8750 (2018).
  19. Zentrum, D. PHASE-FIELD STUDY OF SOLUTE TRAPPING EFFECT IN RAPID SOLIDIFICATION P.K. Galenko, E.V. Abramova and D.M. Herlach. 457–466 (2011).

20. Galenko, P. Solute trapping and diffusionless solidification in a binary system. *Phys. Rev. E - Stat. Nonlinear, Soft Matter Phys.* **76**, 1–9 (2007).
21. Biswas, S., O'Regan, C., Petkov, N., Morris, M. a. & Holmes, J. D. Manipulating the growth kinetics of vapor-liquid-solid propagated ge nanowires. *Nano Lett.* **13**, 4044–4052 (2013).
22. Zhang, X., Lew, K. K., Nimmatoori, P., Redwing, J. M. & Dickey, E. C. Diameter-dependent composition of vapor-liquid-solid grown S i-xGe x nanowires. *Nano Lett.* **7**, 3241–3245 (2007).
23. Biswas, S. *et al.* Non-equilibrium induction of tin in germanium: Towards direct bandgap Ge 1-xSnxnanowires. *Nat. Commun.* **7**, 11405 (2016).
24. Biswas, S., O'Regan, C., Morris, M. a. & Holmes, J. D. In-situ Observations of Nanoscale Effects in Germanium Nanowire Growth with Ternary Eutectic Alloys. *Small* **11**, 103–111 (2015).
25. He, S. T., Xie, S. S., Yao, J. N., Gao, H. J. & Pang, S. J. Self-assembled two-dimensional superlattice of Au-Ag alloy nanocrystals. *Appl. Phys. Lett.* **81**, 150–152 (2002).
26. You, X. & Zhou, R. Electronic Structure and Optical Properties of GaAs 1 – Bi Alloy. **2014**, (2014).
27. Nabetani, Y. *et al.* Structure and optical properties of ZnSeO alloys with O composition up to 6.4%. *Mater. Sci. Semicond. Process.* **6**, 343–346 (2003).
28. Abdel-Rahim, M. A., Hafiz, M. M. & Alwany, A. E. B. The effect of composition on structural and optical properties of ZnSe alloys. *Opt. Laser Technol.* **47**, 88–94 (2013).
29. Shiraishi, T., Hisatsune, K., Tanaka, Y., Miura, E. & Takuma, Y. Optical properties of

- Au-Pt and Au-Pt-In alloys. *Gold Bull.* **34**, 129–133 (2001).
30. Haffner, T. *et al.* Growth of  $\text{Ge}_{1-x}\text{Sn}_x$  Nanowires by Chemical Vapor Deposition via Vapor-Liquid-Solid Mechanism Using  $\text{GeH}_4$  and  $\text{SnCl}_4$ . *Phys. Status Solidi* **215**, 1700743 (2017).
31. Mu, H., Senoo, M. & Fujishiro, I. Solid solubility of Si in Al under high pressure. *Jpn. J. Appl. Phys.* **15**, 777–783 (1976).



# **Chapter 8**

## **Conclusions and Future Outlook**

## 8. Conclusions and Future Outlook

### 8.1. Conclusions and Future Outlook

When I began my thesis in 2014, there was an abundance of publications of  $\text{Ge}_{1-x}\text{Sn}_x$  thin films, due to the compatibility of these group IV alloy materials with the well-established Si based electronic, optoelectronic and photonic platforms. These alloy materials further give the opportunity to achieve a direct and tuneable bandgap in group IV material system by alloying Ge with Sn.<sup>1-3</sup> However, back in 2014 there were a very limited number of reports on  $\text{Ge}_{1-x}\text{Sn}_x$  nanostructures; specially on nanowires.<sup>4-6</sup> 1D nanowire devices are expected to play an important role in the development of modern electronic devices (such as finFETs, GAA-FET *etc* ), particularly in single wire and multi-wire structures and the development of a Si compatible, direct bandgap 1D nanostructure is imperative for future scaling of current electronic/optoelectronic components. Thus, the under-representation of  $\text{Ge}_{1-x}\text{Sn}_x$  nanowires in the literature served as the motivation behind my thesis. Further, the nanowire morphology offer the unique advantage of strain relaxation compared to their thin film counterparts, giving greater opportunities for  $\text{Ge}_{1-x}\text{Sn}_x$ , materials engineering in terms of alloy composition, heterostructure formation *etc*. I focussed my research on the fabrication and characterisation of  $\text{Ge}_{1-x}\text{Sn}_x$  nanowires for future device implementation (*i.e.* optoelectronics, electronics, energy storage, *etc.*).

My research on this nanowire system began with the growth of  $\text{Ge}_{1-x}\text{Sn}_x$  nanowires via chemical vapour deposition (Chapters 2 & 3). The use of a post-growth step anneal resulted in direct bandgap  $\text{Ge}_{1-x}\text{Sn}_x$  nanowires with  $x = 0.09$  (Chapter 2). However, this two-step growth protocol induced a degree of disorder in the  $\text{Ge}_{1-x}\text{Sn}_x$  nanowires at the atomic scale as verified by Raman spectroscopy and high resolution TEM. In an effort to reduce the atomic “randomness” in the alloy, I exploited the nanowire growth kinetics manipulation in a single

step VLS growth for the large Sn impurity induction (Chapter 3). A kinetic dependent solute trapping mechanism is believed to be responsible for non-equilibrium Sn induction in Ge. By varying the growth kinetics of the  $\text{Ge}_{1-x}\text{Sn}_x$  nanowires with a set of growth parameters, I incorporated high Sn content (9.2 at. %) in  $\text{Ge}_{1-x}\text{Sn}_x$  nanowires without the use of the additional step anneal. These direct bandgap  $\text{Ge}_{1-x}\text{Sn}_x$  nanowires showed an increased degree of ordering relative to those grown with an added step anneal, verified by HRTEM imaging, Raman spectroscopy and PL measurements. In order to determine the functionality of these  $\text{Ge}_{1-x}\text{Sn}_x$  nanowires in optoelectronic application, I then fabricated  $\text{Ge}_{1-x}\text{Sn}_x$  nanowires with  $x > 0.1$  (Chapter 4). These nanowires with more than 10 at. % Sn were implemented in photodetector device.  $\text{Ge}_{1-x}\text{Sn}_x$  thin films had been previously reported as efficient photodetectors, but the  $\text{Ge}_{1-x}\text{Sn}_x$  nanowires show an increase in photosensitivity compared to thin films. Further to demonstrate the applicability of  $\text{Ge}_{1-x}\text{Sn}_x$  nanowires in alternative non-electronic device application, nanowires with lower Sn incorporation (4.8 at. %) were tested as anode materials for Li-ion batteries (Chapter 5).  $\text{Ge}_{1-x}\text{Sn}_x$  nanowires displayed high capacities ( $> 900 \text{ mAh/g}$ ) with excellent Coulombic efficiency over 100 cycles. Following this, I varied the growth parameters further to produce  $\text{Ge}_{1-x}\text{Sn}_x$  branched nanostructures (Chapter 6). These nanostructures were composed of  $\text{Ge}_{1-x}\text{Sn}_x$  nanowire trunks with low Sn ( $x = 0.04$ ) and Sn-rich  $\text{Ge}_{1-x}\text{Sn}_x$  nanowire branches ( $x = 0.08$ ). A growth mechanism for these novel nanostructures is also detailed in Chapter 6. The suitability of these  $\text{Ge}_{1-x}\text{Sn}_x$  branched nanostructures as anode materials for Li-ion batteries is also demonstrated. Finally, Chapter 7 introduces the new parameter of pressure to the  $\text{Ge}_{1-x}\text{Sn}_x$  nanowire growth system. The introduction of high pressure in a SCF fluid based growth results in colossal incorporation of Sn ( $x > 0.3$ ) in  $\text{Ge}_{1-x}\text{Sn}_x$  nanowires. Fabrication of  $\text{Ge}_{1-x}\text{Sn}_x$  nanowires with significant Sn incorporation ( $x > 0.1$ ) is imperative in optoelectronic and photonic applications as this would minimise band mixing effects, enabling the  $\text{Ge}_{1-x}\text{Sn}_x$  to behave as a fully direct bandgap material.

Ge<sub>1-x</sub>Sn<sub>x</sub> nanowires are suitable for future implementation in multiple devices (*e.g.* lasers, photodetectors, TFETS, batteries, *etc.*), and indeed in multiple fields; optics,<sup>7-9</sup> optoelectronic,<sup>10,11</sup> photonic,<sup>12-15</sup> electrical<sup>16-18</sup> and energy storage<sup>19,20</sup> to name a few. The tunability of the bandgap in Ge<sub>1-x</sub>Sn<sub>x</sub> nanowire can be highly controlled by the induction of various amounts of Sn *via* exploitation of the solute trapping of Sn impurities (Chapter 3). Ge<sub>1-x</sub>Sn<sub>x</sub> nanowires can be utilised in an array of devices depending on the specific Sn incorporation. Direct bandgap Ge<sub>1-x</sub>Sn<sub>x</sub> nanowires can be utilised in FET like devices, provided the bandgap is sufficiently wide.<sup>17,18,21</sup> Ge<sub>1-x</sub>Sn<sub>x</sub> nanowires with narrower bandgaps (*i.e.* with high Sn content) are suitable to optoelectronic devices such as photodetectors.<sup>11,22</sup> Going forward, the fabrication of a Ge<sub>1-x</sub>Sn<sub>x</sub>/Ge/Ge<sub>1-x</sub>Sn<sub>x</sub> or Ge<sub>1-x</sub>Sn<sub>x</sub>/Si<sub>y</sub>Ge<sub>1-y-x</sub>Sn<sub>x</sub> nanowire heterostructure is imperative to the continued implementation in electronic devices such as band-to-band tunnelling FET.<sup>23</sup> However, to ensure a sharp junction between different components, precise control over nanowire growth is required. Aligned and localised growth of Ge<sub>1-x</sub>Sn<sub>x</sub> nanowires by utilisation of a suitable growth substrate would also allow for facile device implementation. A transition to an alternative epitaxial growth substrate, *e.g.* Ge(111), or patterned growth substrate has potential to be a feasible solution to the unaligned growth of Ge<sub>1-x</sub>Sn<sub>x</sub> nanowires on Si substrates, requiring minimal alteration to the growth methods as laid out in this thesis. Ge<sub>1-x</sub>Sn<sub>x</sub> nanowires, with tunable bandgaps, minimal strain and single crystalline morphology are ideal candidates for numerous and varied applications.

## 8.2. References

1. Kasper, E. *et al.* Growth of silicon based germanium tin alloys. *Thin Solid Films* **520**, 3195–3200 (2012).
2. Yu, I. S. *et al.* Investigation of Ge<sub>1-x</sub>Sn<sub>x</sub>/Ge with high Sn composition grown at low-temperature. *AIP Adv.* **1**, (2011).
3. Conley, B. R. *et al.* CVD growth of Ge<sub>1-x</sub>Sn<sub>x</sub> using large scale Si process for higher efficient multi-junction solar cells. *2013 IEEE 39th Photovolt. Spec. Conf.* 1346–1349 (2013).
4. Gong, X. *et al.* Uniaxially Strained Germanium-Tin (GeSn) Gate-All-Around Nanowire PFETs Enabled by a Novel Top-Down Nanowire Formation Technology. *2013 Symp. VLSI Circuits* 34–35 (2013).
5. Noroozi, M., Hamawandi, B., Toprak, M. S. & Radamson, H. H. Fabrication and thermoelectric characterization of GeSn nanowires. *ULIS 2014 - 2014 15th Int. Conf. Ultim. Integr. Silicon* 125–128 (2014).
6. Ragan, R., Ahn, C. C. & Atwater, H. a. Nonlithographic epitaxial Sn<sub>x</sub>Ge<sub>1-x</sub> dense nanowire arrays grown on Ge(001). *Appl. Phys. Lett.* **82**, 3439–3441 (2003).
7. Assali, S. *et al.* Growth and Optical Properties of Direct Band Gap Ge/Ge<sub>0.87</sub>Sn<sub>0.13</sub> Core/Shell Nanowire Arrays. *Nano Lett.* **17**, 1538–1544 (2017).
8. Stange, D. *et al.* Optical Transitions in Direct-Bandgap Ge<sub>1-x</sub>Sn<sub>x</sub>Alloys. *ACS Photonics* **2**, 1539–1545 (2015).
9. Al-Kabi, S. *et al.* Optical Characterization of Si-Based Ge<sub>1-x</sub>Sn<sub>x</sub>Alloys with Sn Compositions up to 12%. *J. Electron. Mater.* **45**, 2133–2141 (2016).

10. Kim, S., Bhargava, N., Gupta, J., Coppinger, M. & Kolodzey, J. Infrared photoresponse of GeSn/n-Ge heterojunctions grown by molecular beam epitaxy. *Opt. Express* **22**, 11029 (2014).
11. Su, S. *et al.* GeSn p-i-n photodetector for all telecommunication bands detection. *Opt. Express* **19**, 6400 (2011).
12. Zheng, J. *et al.* Recent progress in GeSn growth and GeSn-based photonic devices. *J. Semicond.* **39**, 1–6 (2018).
13. Al-Kabi, S. *et al.* An optically pumped 2.5  $\mu\text{m}$  GeSn laser on Si operating at 110 K. *Appl. Phys. Lett.* **109**, (2016).
14. Stange, D. *et al.* Optically Pumped GeSn Microdisk Lasers on Si. *ACS Photonics* **3**, 1279–1285 (2016).
15. Wirths, S. *et al.* Lasing in direct-bandgap GeSn alloy grown on Si. *Nat. Photonics* **9**, 88–92 (2015).
16. Wang, H. *et al.* Performance Enhancement in Uniaxially Strained Germanium-Tin FinTFET: Fin Direction Dependence. *IEEE Trans. Electron Devices* **64**, 2804–2811 (2017).
17. Sant, S. & Schenk, A. Band-offset engineering for GeSn-SiGeSn hetero tunnel FETs and the role of strain. *IEEE J. Electron Devices Soc.* **3**, 164–175 (2015).
18. Schulte-Braucks, C. *et al.* Process modules for GeSn nanoelectronics with high Sn-contents. *Solid. State. Electron.* **128**, 54–59 (2017).
19. Cho, Y. J. *et al.* Germanium-tin alloy nanocrystals for high-performance lithium ion batteries. *Phys. Chem. Chem. Phys.* **15**, 11691–11695 (2013).

20. Bodnarchuk, M. I., Kravchyk, K. V., Krumeich, F., Wang, S. & Kovalenko, M. V. Colloidal tin-germanium nanorods and their Li-Ion storage properties. *ACS Nano* **8**, 2360–2368 (2014).
21. Weber, W. M. & Mikolajick, T. Silicon and germanium nanowire electronics: Physics of conventional and unconventional transistors. *Reports Prog. Phys.* **80**, (2017).
22. Oehme, M. *et al.* GeSn p-i-n detectors integrated on Si with up to 4% Sn. *Appl. Phys. Lett.* **101**, (2012).
23. Zhu, Z. *et al.* GeSn/Ge dual-nanowire heterostructure. *Summer Top. Meet. Ser. SUM 2017* 71–72 (2017).

# **Chapter 9**

## Appendix - Dissemination



## 9. Appendix - Dissemination

---

### 9.1. Publication List

#### 9.1.1. Publications arising directly from this thesis

1. Biswas, S.; **Doherty, J.**; Saladukha, D.; Ramasse, Q.; Majumdar, D.; Upmanyu, M.; Singha, A.; Ochalski, T. J.; Morris, M. A.; Holmes, J. D. Non-equilibrium Induction of Tin in Germanium: Towards Direct Bandgap  $\text{Ge}_{1-x}\text{Sn}_x$  Nanowires *Nature Comm.*, **2016**, 7, 11405.
2. **Doherty, J.**; Biswas, S.; Saladukha, D.; Ramasse, Q.; Bhattacharya, T. S.; Singha, A.; Ochalski, T. J.; Holmes, J. D. Influence of Growth Kinetics on Sn Incorporation in Direct Bandgap  $\text{Ge}_{1-x}\text{Sn}_x$  Nanowires *Mater. Chem. C*, **2018**, 6, 8738-8750.
3. **Doherty, J.**; Biswas, S.; Gallucio, E.; Broderick, C.; Duffy, R.; O'Reilly, E.; Holmes, J. D. Progress on GeSn Alloy Semiconductors: from Thin Films to the Nanoscale (in preparation).
4. **Doherty, J.**; Rao, M.; Saladukha, D.; Manning, H.; Conroy, M.; Moore, K.; Bangert, U.; Singha, A.; Ochalski, T. J.; Biswas, S.; Holmes, J. D Direct Bandgap  $\text{Ge}_{1-x}\text{Sn}_x$  ( $x = 0.10$ ) Nanowires in Photodetection (in preparation).
5. **Doherty, J.**; McNulty, D.; Conroy, M.; Moore, K.; Bangert, U.; Biswas, S.; O'Dwyer, C.; Holmes, J. D Germanium Tin Nanowires as Anode Materials for High Performance Li-Ion Batteries (in preparation).
6. **Doherty, J.**; Biswas, S.; McNulty, D.; O'Regan, C.; Downing, C.; Raha, S.; Singha, A.; O'Dwyer, C.; Holmes, J. D One-Step Fabrication of GeSn Branched Nanowires (in preparation).
7. **Doherty, J.**; Biswas, S.; Conroy, M.; Moore, K.; Bangert, U.; Holmes, J. D Supercritical Fluid Growth of High Sn Content  $\text{Ge}_{1-x}\text{Sn}_x$  ( $x > 0.3$ ) Nanowires (in preparation).

### 9.1.2. Co-authored Publications

8. Biswas, S.; **Doherty, J.**; Majumdar, D.; Ghoshal, T.; Rahme, K.; Conroy, M.; Singha, A.; Morris, M. A.; Holmes, J. D. Diameter-Controlled Germanium Nanowires with Lamellar Twinning and Polytypes *Chem. Mater.*, **2015**, 27 (9), pp 3408–3416
9. Saladukha, D.; Doherty, J.; Biswas, S.; Ochalskia, T.; Holmes, J. D.; Optical study of strain free GeSn nanowires, *Proc. of SPIE*, **10108**, 101081C-1-6
10. Kosmaca, J.; Meija, R.; Antsov, M.; Kunakova, G.; Sondors, R.; Sjomkane, M.; Iatsunskyi, I.; Coy, E.; **Doherty, J.**; Biswas, S.; Holmes, J. D.; Erts, D. Effect of tapering on mechanical and electrical properties of GeSn alloy nanowires (submitted to *Nano Research*, Nov. 2018)
11. Gallucio, E.; Mirabelli, G.; **Doherty, J.**; Petkov, N.; Holmes, J. D.; Duffy, R. Metallic Contacts on  $\text{Ge}_{0.92}\text{Sn}_{0.08}$  : systematic study of material and electrical features using Nickel, Platinum and Titanium (in preparation)
12. Buckley, D.; McNulty, D.; **Doherty, J.**; Holmes, J. D.; O'Dwyer, C. Sub-band gap photoconductivity in solution processed Al:ZnO quasi-superlattice materials (in preparation)

### 9.1.3. Conference Presentations

1. **Doherty, J.;** Biswas, S.; Rahme, K.; Ghoshal, T.; Holmes, J.D. 'Induction of Twinning and Polytypes in Diameter Controlled Germanium Nanowires'. Nanowires 2015, 26th - 30th October, Barcelona, Catalonia, Spain (Poster).
2. **Doherty, J.;** Biswas, S.; Saladukh, D.; Ramasse, Q.; Holmes, J.D. 'Direct bandgap Ge<sub>1-x</sub>Sn<sub>x</sub> nanowires'. Symposium O, EMRS Spring 2016, 2-6 May 2016, Lille, France (Invited Talk).
3. **Doherty, J.;** Biswas, S.; Saladukh, D.; Ramasse, Q.; Holmes, J.D. 'Direct bandgap Ge<sub>1-x</sub>Sn<sub>x</sub> nanowires'. 68th Irish Universities Chemistry Research Colloquium, 23-24 June 2016, Cork, Ireland (Poster).
4. **Doherty, J.;** Biswas, S.; Saladukh, D.; Ramasse, Q.; Holmes, J.D. 'Direct bandgap Ge<sub>1-x</sub>Sn<sub>x</sub> nanowires'. Annual Tyndall Student Poster Competition, 29 July 2016, Tyndall National Institute, Cork, Ireland (Poster).
5. **Doherty, J.;** Biswas, S.; Saladukh, D.; Ramasse, Q.; Holmes, J.D. 'Direct bandgap Ge<sub>1-x</sub>Sn<sub>x</sub> nanowires'. Tyndall Internal Conference, Tyndall National Institute, Cork, 5th April 2017 (Talk).
6. **Doherty, J.;** Biswas, S.; Saladukh, D.; Ramasse, Q.; Holmes, J.D. 'Influence of Growth Limiting Factors on the Morphology and Sn Incorporation of GeSn Alloy Nanowires '. Materials Research Society (MRS) Fall Meeting 2017, 27th November-01 December 2017, Boston, USA (Poster).